INL/EXT-10-20466

Microstructural Studies of Uranium-7Wt% Molybdenum/Aluminium-2Wt%Silicon Dispersion Fuel

Brandon D. Miller

November 2010

The INL is a U.S. Department of Energy National Laboratory
operated by Battelle Energy Alliance

INL/EXT-10-20466

Microstructural Studies of Uranium-7Wt% Molybdenum/Aluminium-2Wt%Silicon Dispersion Fuel

Brandon D. Miller

November 2010

Idaho National Laboratory
Idaho Falls, Idaho 83415

http://www.inl.gov

Prepared for the
U.S. Department of Energy
Office of National Nuclear Security Administration
Under DOE Idaho Operations Office
Contract DE-AC07-05ID14517

MICROSTRUCTURAL STUDIES OF

URANIUM-7WT%MOLYBDENUM/ALUMINUM-2WT%SILICON

DISPERSION FUEL

by

Brandon D. Miller

A dissertation submitted in partial fulfillment of

the requirements for the degree of

Doctor of Philosophy

(Nuclear Engineering and Engineering Physics)

at the

UNIVERSITY OF WISCONSIN-MADISON

2010

Table of Contents

List of Tables

List of Figures

List of Abbreviations

Elements

Ba ..... Barium
C ..... Carbon
Cl ..... Chloride
F ..... Fluorine
H ..... Hydrogen
He ..... Helium
Kr ..... Krypton
Mg ..... Magnesium
Mo ..... Molybdenum
Nd ..... Neodymium
O ..... Oxygen
Pd ..... Palladium
Rh ..... Rhodium
Ru ..... Ruthenium
Si ..... Silicon
Sr ..... Strontium
Tc ..... Technetium
Ti ..... Titanium
U ..... Uranium
DU ..... Depleted Uranium
Xe ..... Xenon
Y ..... Yttrium
Zr ..... Zirconium

Various

A. Rim ..... Amorphous Rim
AFIP ..... ATR Full-Size-Plate In Center Trap Position
At% ..... Atomic Percent
ATR ..... Advanced Test Reactor
BCC ..... Body Centered Cubic
BF ..... Bright Field
DOE ..... Department of Energy
Dpa ..... Displacements per atom
EBSD ..... Electron Back Scattered Diffraction
EDS ..... Energy Dispersive X-ray Spectroscopy
EML ..... Electron Microscopy Lab

eV ..... Electron Volt
FASB ..... Fuels and Science Building
FCC ..... Face Centered Cubic
FMI ..... Fuel Matrix Interaction
HEU ..... Highly Enriched Uranium
HFEF ..... Hot Fuel Examination Facility
HIP ..... Hot Isostatic Pressing
INL ..... Idaho National Laboratory
IVEM ..... Intermediate Voltage Electron Microscope
K-P ..... Kinchen Pease
LEU ..... Low Enriched Uranium
NRC ..... Nuclear Regulatory Commission
OM ..... Optical Microscopy
PFZ ..... Precipitate Free Zone
PIE ..... Post Irradiation Examination
PIPS ..... Precision Ion Polishing System
PKA ..... Primary Knock-on Atom
RIS ..... Radiation Induced Segregation
SAD ..... Selective Area Diffraction
SEM ..... Scanning Electron Microscopy
SIA ..... Self Interstitial Atom
SKA ..... Secondary Knock-on Atom
SRIM ..... Short Range Interaction in Matter
TEM ..... Transmission Electron Microscopy
WDS ..... Wavelength Dispersive Spectroscopy
Wt% ..... Weight %
XRD ..... X-Ray Diffraction

Chapter 1 Introduction

Steaming from the "Atoms for Peace" program of 1953, research reactors were developed to advance nuclear technology. Initially, reactors were fueled with low-enriched uranium (LEU) fuels. Acceleration of the nuclear technology led to the need for increasing power levels and neutron fluxes in research reactors. This required the use of highly enriched uranium (HEU) fuels. In the 1970's, the United State Department of Energy (DOE) recognized the need to reduce the use of HEU to mitigate proliferation. The Reduced Enrichment for Research and Test Reactors (RERTR) program was created to develop LEU fuels with comparable power levels/neutron fluxes to replace/lower the demand of HEU fuels.

During the process of developing new LEU fuels to replace HEU fuels, various fuel performance issues have arisen. The current fuel under development consists of U-Xwt%Mo (where X is wt%) fuel kernels surrounded by an aluminum matrix. A simple schematic of this fuel can be seen in Figure 1.1. In this figure, a single fuel particle is shown imbedded in the Al matrix. Additionally, key regions of interest that form during irradiation are shown. These four separate regions are: the fuel particle, an amorphous rim region between the crystalline fuel and the FMI layer, a fuel-matrix interaction (FMI) layer between the fuel and Al matrix, and the Si-modified Al matrix.

The FMI layer is formed during irradiation burnup and/or temperature treatments, and is composed of U-Mo-Al type phases. Additives that might be present in the Al matrix, such as Si, can interact with the FMI layer, making a complex multi-element FMI layer. In recent RERTR irradiation campaigns, using Si additives in the Al matrix has been shown to suppress the growth of the FMI layer and control bubble growth in the FMI layer. Many in-pile and out-of-pile experiments have been conducted to identify the phases that are present in this layer and will be discussed in detail in later chapters. Understanding how each one of these phases responds to irradiation is important in understanding how the FMI layers develop with increasing burnup.

The FMI layer affects the performance of the fuel in varying ways, ranging from increased fuel temperatures to increased swelling due to coalescence of fission gas bubbles. The FMI layer has been shown to be amorphous at a LEU burnup of 33% (1). The free volume of this amorphous material can affect the swelling in the fuel as well as fission gas retention. This is evident when comparing amorphous U_3Si_2 and U_3Si fuels (2). U_3Si_2 shows good fission gas retention and shows low swelling when compared to U_3Si. Understanding how the Si added to the matrix suppresses FMI layer and bubble growth is a key component to understanding U-Xwt%Mo/Al-modified dispersion fuel.

A Si rich amorphous rim region was discovered in this study and forms between the crystalline fuel particle and the FMI layer in U-7wt%Mo/Al-2wt%Si dispersion fuel.

Understanding this layer's irradiated microstructure is important for fuel qualification. This includes how this layer forms and its fission gas retention behavior.

The stability of the crystalline U-Xwt%Mo fuel kernels at high burnups (>50%) is another area of concern. Understanding how the fuel stores the gas it creates during fission is important in preventing porosity build up and potential breakaway swelling of the fuel. Fission gas bubbles have been shown to form a nano-sized ordered bubble superlattice structure in the grains of the U-Xwt%Mo fuel (1). Grain boundary bubbles also are present in the fuel. Additional information is needed to better understand the physical nature of this bubble superlattice. These parameters and experimental results will be examined within the context of a bubble size and distribution model created by Rest (3) to understand the importance of key parameters of the model, ie. grain size, resolution rate of the fission gas back into the bulk, and the diffusivity of fission gas in the fuel.

The four key needs/unknowns studied in this thesis are:

1: How does the Si added to the matrix affect the FMI layers' microstructure, i.e. bubble growth and sizes, FMI layer growth, and chemical composition?

2: How does the amorphous rim region form, what is its chemical composition, and what is its irradiation microstructure?

3: How does the bubble superlattice form in the crystal fuel region?

4: What are the key parameters/unknowns in the intragranular model by Rest (3) and how do the experimental results help better determine the correct parameters for this model?

Listed are key microstructural features that were analyzed in this study to help answer the above questions/unknowns:

-Non-irradiated microstructure of U-7wt%Mo dispersion fuel with varying fabrication processes

-Non-irradiated U-Xwt%Mo foil characterization with varying fabrication processes

-Defects present in the aluminum matrix

-Fission gas bubble formation in the FMI layer, the fuel grain boundaries, and the bulk of the fuel

-Bubble superlattice parameters including: size, spacing, and orientation

-Defects present in the fuel: such as voids, dislocations, and precipitates

-Crystal structure of the amorphous rim and its Si content in key locations

-Crystal structure of FMI layer

-FMI layer thickness

-FMI layer bubble evolution

-Si content around the bubbles in the FMI layer

The primary focus of this work is to study the microstructural development of U-Xwt%Mo/Al dispersion fuel. This includes studying in-pile irradiated fuel from previous RERTR mini-plate campaigns, heavy ion irradiations of the phases in the FMI and U-7wt%Mo foils to simulate fission product damage, and non-irradiated dispersion fuel analysis, focusing on fuel fabrication methods. By studying these conditions for the fuel, the irradiated microstructure development of the (U-Xwt%Mo)/Al dispersion fuel can be better characterized.

Fresh fuel analysis of unirradiated dispersion fuels from RERTR-9A and -9B is being used to understand how the fabrication process affects the pre-irradiation microstructure. Dispersion fuel from RERTR-9A underwent a hot isostatic pressing, HIP, step to help with bonding the fuel and the cladding. The focus of these tests was to study the pre-irradiated FMI layer that forms during fabrication and the appearance of the general microstructure. In addition to analyzing fuel from RERTR-9A and -9B, benchmark analysis was completed on the DU alloys and DU-7wt%Mo fuel pieces used for the heavy ion irradiation campaigns to better understand their pre-irradiation microstructure with varying fabrication processes. Analysis of a Al-2wt%Si alloy was performed to understand how the Si was distributed in the Al matrix prior to the fabrication process with the U-Mo fuels.

When trying to understand the irradiated microstructure of a material, in-pile reactor irradiations provide the most meaningful results. In reactor irradiations subject the fuel to

prototypic neutron and fission product damage. The primary difficulty with this method is the activity of the sample after irradiation. Samples need to be small to keep radiation levels low during sample preparation for scanning and transmission electron microscopy (SEM and TEM).

Neutron irradiated samples/punches came from mini-fuel plates irradiated in the RERTR-6 and -7 campaigns in the Advanced Test Reactor (ATR). One punch came from RERTR-6 on the high fluence end of the plate and two punches came from the RERTR-7 plate. Of these two, one punch came from the low fluence end and one from the high fluence end. These three punches will be known as RERTR-6, RERTR-L.Flux, and RERTR-H.Flux throughout the remainder of this work. Both plates were a (U-7wt%Mo)/Al-2wt%Si dispersion fuel. Due to their high radiation levels, 1-mm diameter punchings of the plates were used to create TEM samples. Punches were created at the Hot Fuel Examination Facility (HFEF) at the INL and sample preparation, SEM, and TEM analysis was performed at the Electron Microscopy Laboratory (EML).

Heavy ion irradiations are used to simulate fission product damage in a material. Most fission products have an energy on the range of 10-100 MeV and accelerators have been created to reach this energy. Additionally, lower energy accelerators (~1-10 MeV) are used to simulate fission products that have been slowed down by stopping. These accelerators can also be used to simulate reactor neutrons using light ions such as protons. Heavy ion irradiations progress rapidly, (~1 day to simulate life of the fuel), are

inexpensive when compared to neutron irradiations, and are safe due to their low radioactivity after irradiation. These irradiations are able to achieve lifetime damage doses within hours but present a challenge for TEM preparations. Heavy ions do not penetrate deep into the material, with most irradiations only penetrating 1-2 μm into the material. The damage profile over this range is not uniform and leads to an uncertainty in the total dose achieved in the sample.

Heavy ion irradiations using Kr and Xe were performed at Argonne National Laboratory at the Intermediate Voltage Electron Microscopy Laboratory (IVEM). IVEM offers a unique capability in that TEM analysis can be conducted at the same time as the irradiation, providing an opportunity to monitor defect development with increasing dose. Two separate irradiation campaigns were completed using the IVEM. The campaigns were focused on the FMI layer and the U-Xwt%Mo fuel region. Three separate depleted uranium alloys were cast to simulate the phases that are expected to form in the FMI layer. The alloys were irradiated at low doses (up to 10 dpa) to simulate the early microstructure of these phases and also to a dose of ~100 dpa to understand the end of life microstructure. The U-7wt%Mo fuel irradiation campaign was focused on creation of the ordered nano-sized bubble superlattice that was seen in earlier TEM results (1). This involved high doses to reach the fission gas inventory seen in the RERTR-6 irradiated fuel.

This thesis will be presented in the following chapters:

In Chapter 2, a current background of the RERTR program is presented and the issues of qualifying U-Xwt%Mo type dispersion fuel are addressed. Chapter 3 is focused on experimental setup, irradiation settings and parameters, TEM preparation, and TEM techniques. In Chapter 4, optical microscopy, scanning electron microscopy, and transmission electron microscopy results will be presented. Chapter 5 is focused on the modeling the intragranular bubble superlattice seen in the dispersion fuels. A background of the model, results, and discussion of the model results will be presented. Chapter 6 contains a discussion of the 4 key fuel performance questions presented above. Finally, chapter 7 is devoted to the conclusions and recommended future work.

a)

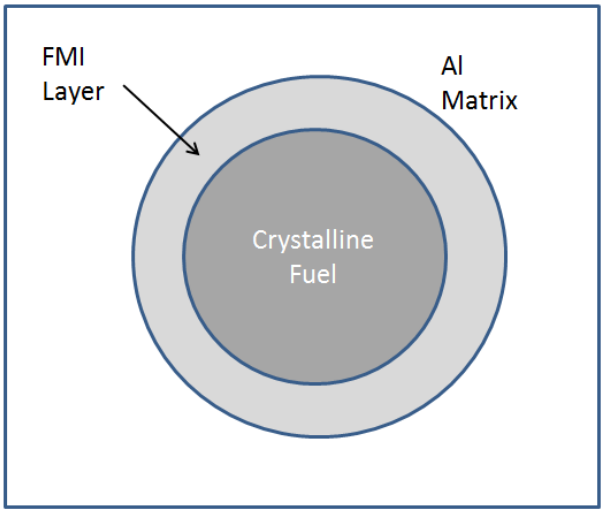

b)

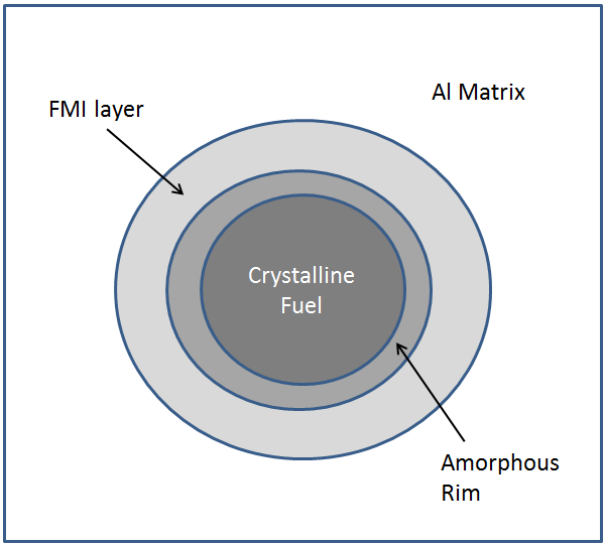

Figure 1.1: Simple schematic showing the typical microstructural regions formed in U-Mo (fuel)/Al-Si (matrix) modified dispersion fuel a) after fabrication and b) during irradiation. The fuel particle is roughly 300-500 μm is size. Note that TEM results will show that each region is non-uniform in thickness.

Chapter 2 : Background

Within the development and testing program for the Low Enriched Uranium, LEU, U-Xwt%Mo/Al dispersion fuels (X is generally 6-12 wt%) by the RERTR program, various microstructural issues that correspond to fuel degradation became evident after irradiation. Early RERTR fuel irradiations showed the formation of a fuel-matrix interaction (FMI) layer that affected fuel temperature, swelling, and fuel performance. In addition to the FMI layer, the fuel kernels themselves showed fission gas bubble formation at high burnups leading to increased swelling. The need to understand the effect of these issues became a major focus of the RERTR program. This chapter reviews the current understanding of irradiation-induced microstructural development, the history of the RERTR's work to understand these microstructural changes, and a review of the current understanding of U-Xwt%Mo/Al dispersion fuels.

2.1.1: Irradiation-Induced Microstructural Development

An irradiated microstructure consists of many defects. These defects may include vacancies, interstitials, grain boundaries, voids and dislocation loops, precipitates, and gas stabilized bubbles. The defects present in the material are governed by the irradiation conditions. The primary irradiation conditions are dose rate, dose, particle type, and operating temperature. The dose rate determines with how quickly defects can form. The total dose in the material reflects the total number of point defects produced in the material. The incoming particle type has a major effect on the damage cascade created in

the material. The operating temperature has varying effects on the microstructure: low temperature can lead to increased defect concentrations due to lack of diffusion capability in the material, as well as amorphization or lack of long range ordering in the crystal; high temperatures lead to increased diffusion and allow defects to diffuse to sinks much more readily, which can lead to dislocation loop formation or void formation in the material; very high temperatures will quickly anneal any radiation damage created. This section is focused on how point defects are created, what defect clusters form, and their effect on the microstructure. Additionally, fission gas bubble formation and a special microstructural condition called amorphization will be discussed.

Point Defects

When a high energy particle strikes an atom in the lattice, kinetic energy is transferred from the incoming atom to the lattice atom. The amount of energy transferred can be affected by the energy of the incoming particle, angle of interaction between the atoms, and charge of the particles. When enough energy is transferred to an atom to eject the atom from its lattice site into the interstices of the lattice, it is termed an interstitial atom. The vacant lattice site that is left is described as a vacancy. The vacancy and interstitial are termed as point defects, with the vacancy-interstitial pair being known as a Frenkel defect pair. A simple diagram of this process can be seen in
Figure 2.1. These point defects can recombine with each other, annihilating the point defect, find like defects and create defect clusters, or find sinks such as grain boundaries.

As mentioned above, energy is transferred during a particle-particle interaction. There are two possible actions that can occur with the lattice atom receiving energy from the incoming particle. The lattice atom can be displaced from its lattice site or it can remain in its location and de-excite by vibrating in its location and slowly removing excess energy by transferring it to its local neighbors through electronic interaction. There is a threshold energy above which atoms will be displaced from their lattice sites, defined as the displacement energy, E_d. This value varies throughout materials and incoming particle angles. Typical E_d values range from 15-90 eV (4). Displacement energy is also affected by the incoming particle angle relative to the lattice. In a Cu sample, the E_d can vary from 19 to 76 eV at a crystal orientation of [100] and [111] respectively (5). The E_d value has a major impact on the damage rate in the material. For example, the damage rate using an E_d of 25 eV is roughly twice the amount of a 40 eV material.

As the first lattice atom is removed from its lattice location as part of a collision, it is termed a “primary knock-on-atom” (PKA). The ejected PKA can interact with another lattice atom, creating a “secondary knock-on-atom” (SKA). This SKA can in turn interact with other atoms, creating more displaced atoms, as long as the transferred energy is greater than the required E_d to displace a lattice atom. This process can displace many atoms and is called a damage cascade. Figure 2.2 (6) shows how a typical cascade might look.

It is important to understand what happens to the damage cascade as a function of time. The time scale on how this process occurs can be seen in Figure 2.3 (4). This process can be broken up into two main regions: the PKA cascade region and the defect migration region. The PKA cascade region, $t<10^{-19}$ sec, is shown in Figure 2.3. In this region, the primary knock-on atom is created, causing the start of the cascade in the lattice. Additionally, the lattice local temperature spikes due to the energy transferred to the atoms, and, at the end of the time period ($\sim10^{-11}$ sec), the local lattice is quenched. In the defect migration region, $t>10^{-11}$ sec, the local lattice starts to anneal and defects can migrate. The lattice anneals by recombination of interstitials and vacancies. Remaining defects can diffuse to sinks or recombine by diffusion.

Incoming Particle Types:

Irradiation can occur in many different forms including: electrons, light ions (such as protons), heavy ions (such as fission products), gamma and x-rays, and neutrons. Each type of particle causes different crystal damage morphology. This can be seen in Figure 2.4 (4). Heavy ions and neutrons produce the largest sized cascades. Protons produce many smaller localized cascades and electrons, including electrons freed from gamma interactions with lattice electrons, produce a single vacancy and interstitial at a time. In typical nuclear reactor fuels, the two primary initiating interactions are the neutron and the heavy ion interactions, energized fission fragments.

When an atom fissions, it generally breaks into two large energized fission products and also releases high-energy neutrons. The two fission products are released with a combined energy up to 180 MeV (7). With the high energy of the fission products, the fission products have a range of up to 10 μm into the material. This is an important concept because the fission product damage is not confined to just the fuel itself. These fission products can produce high damage cascades in the materials surrounding the fuel, such as cladding or the matrix holding fuel kernels. Reactor neutrons are released with energies around 2 MeV (7). This high energy, combined with the fact that the neutron has no charge and only interacts via collision, leads to neutrons having a range that can reach all interior reactor core components.

Efforts have been made to model the defect production in a material. The most common model used is the Kinchin-Pease Model. This model calculates the number of displaced atoms that will occur in a cascade as a function of the primary knock on atom energy, PKA. A simple Kinchin-Pease model, K-P, can be seen in Figure 2.5 (4). The primary observation from the figure is that for most PKA energies, the number of displaced atoms is $T/(2E_d)$, where T is the PKA energy. Additional models, such as the NRT model (8), Norgett, Robinson, and Torrens, have been created that are modifications of the K-P model to better describe the total displaced atoms. Some of the modifications include, using potentials to describe the energy transfer instead of using the hard sphere approach and including losses due to electronic stopping. Due to the recombination factor in the

cascades created in the material during irradiations, the number of displaced atoms calculated by the NRT model should be multiplied by the displacement efficiency of the incoming particle. The displacement efficiency for specific particle types are shown in Figure 2.4 (9). The corrected value should estimate the total number of defects that should be present in the material prior to diffusion.

Defect Clusters in Materials:

Interstitial and vacancy point defects can recombine, diffuse to defect sinks, or combine with other like point defects to create clusters of point defects. The diffusion of point defects plays a major role in their ability to form large clusters or diffuse to sinks. The diffusion of the defects is highly dependent on the temperature of the system. At elevated temperatures, defects will more readily move throughout the system to the sinks or to recombine. At lower temperatures, the diffusion of defects is lowered and defects cannot readily move to the defect sinks and the defect concentrations will continue to grow until the concentration is high enough to interact with the sinks or recombine with their vacancy/interstitial counterpart. In addition to temperature, the diffusion of defects in a material is highly dependent on location in the material. Grain boundary diffusion is much higher than bulk diffusion through a material (10).

With vacancies and interstitials being produced in the material during irradiation, defects seek to form the lowest energy configuration possible. This can lead to recombination, loss to sinks, and, most importantly for irradiation study, combining with other interstitials or vacancies to form clusters of defects. The most commonly studied defects in irradiated fuel are dislocation loops. In an FCC material, dislocation loop defects form on the low energy plane of [111] and their slip direction is <110>. In an FCC perfect loop, the burgers vector is $b=a_o/2<110>$ and the faulted loop's burgers vector is $b=a_o/3<111>$. A perfect loop may dissociate to form two partial dislocations, creating a stacking fault in the material. As irradiation continues in the material, the dislocations will continue to grow until the size saturates. An important effect of faulted loops in a material is their ability to act as a pin or barrier, which suppresses dislocation motion in the material. These defects lead to increased radiation hardening in the material, which affects the material's mechanical properties, such as yield strength and ductility.

Voids are formed by vacancies in the material combining together. Voids tend to form in the temperature range of 0.3-0.55 T_m, where T_m is the melting temperature of the material (4). As the vacancies start to accumulate, stress accumulates in the void due to the material surrounding the void trying to collapse on it. Voids can become stabilized by the accumulation of gases in the material. In a reactor setting, fission or transmutation product gases can stabilize the voids and become fission gas bubbles. Bubbles can continue to grow with new vacancies and additional fission gases. A more detailed description of bubble formation will be provided later in this section.

In addition to voids and dislocations in the material, other defects can be present in the material, including grain boundaries, precipitates, and fission products. Grain boundaries offer sinks for defects to migrate toward. Additionally, they offer a mechanism for the material to have a different elemental composition than the bulk, called radiation induced segregation (RIS). RIS is evident in irradiated stainless steels, in which chromium tends to deplete around the grain boundaries leading to increased corrosion issues in the stainless steel parts (11). Precipitates tend to affect the material properties of the material, including hardness and yield strength. This is evident in oxide dispersed steels, where small nano-sized precipitates of yttrium oxides are added to the steel to act as defect sinks and barriers to increase the strength of the material at high temperatures (12).

2.1.2: Fission Products

One of the major challenges with nuclear fuel is the behavior of the fission products. Fission products are present in the fuel as solid and gaseous atoms. The solid and gaseous fission products can affect fuel properties such as melting temperature, thermal conductivity, and swelling. Fission gas can affect pressures in a fuel rod and can change the thermal conductance across the fuel rod gap. When the volume of the irradiated fuel is greater than the volume of the fresh fuel, the resulting is known as swelling. This background is focused on the swelling phenomena. Most of this section is summarized from (13) unless noted.

Solid Fission Product Swelling:

Excluding Xe and Kr, most of the fission products created during fission are in the form of a solid. In a UO_2, they can take form as solid metallic inclusions such as Ru, Tc, Rh, and Pd, or form oxides such as BaO and SrO. Additionally, fission products can remain in solution in the material. The volume change due to these fission products is related to the partial volume of the solid fission product and its associated oxygen atoms if an oxide forms. The partial volume of these compounds can be larger than the host material's partial volume leading to a swelling increase. Table 2.1 shows the swelling due to solid fission products in pure UO_2 fuel using partial volumes (13). The table shows the effect of the most probable solid fission products on the swelling in the fuel. From the Table 2.1 (13), it shows that UO_2 fuel will undergo 0.32% increase in swelling per atom percent burnup. This swelling increase due to solid fission products varies with different fuels due to their fission yields.

Fission Gas Bubbles:

The primary fission gases created from fission are Kr and Xe. These gases are insoluble in the fuel matrix. It is important to understand what affects the fission gas behavior in nuclear fuel. Table 2.2 (13) shows variables that can affect fission gas behavior in nuclear fuel. Important parameters will be discussed further below.

Bubble Formation:

During irradiation of the fuel, vacancies and interstitials are created by the collision of energetic particles with lattice atoms. The vacancies in the material can diffuse throughout the material and interact with other defects including other vacancies. This vacancy cluster can interact with fission gas throughout the fuel. The addition of the gas atoms is key to stabilizing the vacancy clusters. The clusters are under hydrostatic stresses and surface tension forces from the surrounding fuel. If the stress is high enough, it can collapse the cluster into smaller vacancy clusters. When fission gas is present in the vacancy clusters, it provides gas pressure to the cluster. This pressure acts against the hydrostatic stress from the bulk material and stabilizes the vacancy clusters/bubbles.

The bubbles can continue to grow by accumulation of additional gas atoms and vacancies. Another form of growth is coalescence. When a bubble collides with other bubble, the bubbles will coalescence into a larger bubble. It is driven towards forming one large bubble by the surface tensions of the bubbles. One larger bubble has a lower surface tension then two bubbles. In addition to increasing the bubble size, coalescence increases the fuel swelling. Following an example shown in (13) section 13.6, two similar bubbles that coalescence will show an increase in swelling of 40%.

As the bubbles grow, they can decrease in size by re-solution. This is the phenomenon where fission gas atoms in the bubbles are reintroduced into the fuel by irradiation. As

an energetic fission product is released by fission, it traverses throughout the fuel creating damage along its pathway. This area of damage is called a fission tract. The fission product can intersect with gas bubbles in the fuel and deposit some or all of the fission gas atoms back into the fuel. This process alleviates swelling in the material.

Bubble Mobility:

Bubble mobility is generally driven by two methods: random motion and gradient driven motion, such as stress or temperature. Without a gradient to drive the bubbles, bubbles will move in a random fashion. Matrix surface atoms randomly hop around in the inner surface of the bubble. The net displacement of these atoms will lead to a small displacement of the bubbles. In addition to matrix atoms displacing along the inner surface of the bubble, in an equilibrium bubble, vacancies will continue to enter the bubble volume and other bubble vacancies will be reintroduced into the matrix by resolution.

Bubbles can be moved by gradients such as temperature and stress. A temperature gradient across the bubble will lead to preferential motion along this gradient. Bulk surface atoms along the high temperature side of the bubble will preferentially diffuse towards the cool end of the bubble. This leads to bubble migration towards the hot end of the fuel. This is termed vapor transport or evaporation-condensation. Stress gradients in the bulk also affect bubble migration. Stress gradients could be from dislocations present in the material. Bubbles are driven towards these dislocations and are often pinned at

these dislocations. It has been shown that mobility from a stress gradient in the fuel is roughly ~1% of that of a temperature gradient (13).

Bubble Locations:

In general, the fission gases have three options as to where they can reside in the material. Gas can be dissolved in the matrix as small sub-nanometer sized gas clusters (in-solution), as bubbles in the matrix and grain boundaries, and as released gas. SEM, OM, and TEM analysis are the primary tools used to image the bubbles and their respective location.

TEM analysis is used to image bubbles that are on the nanometer scale size. Turnbull (14) has shown that nano sized bubbles have formed in UO_2 in the interior of the fuel grains. These bubbles are referred to as intragranular bubbles. These bubbles can be randomly distributed or as ordered bubbles. In the analysis of Turnbull (14), the intragranular bubbles have started to form an ordered structure. Many of the bubbles are situated in a straight line. This ordered structure has been seen by others (15) , (16), (17) for UO_2. Very little information is known about the ordered structure in fuel, outside of its existence. In addition to these small intragranular bubbles, larger intragranular bubbles ($\geq$5nm) can form in this region. This can be seen in Figure 2.6 (17). The UO_2 fuel was annealed at 1800°C for 5 hrs.

In addition to the intragranular bubbles, bubbles can form along the grain boundaries of the fuels. These bubbles are referred to as intergranular bubbles. With μm sized bubbles, SEM and OM imaging can used to see these bubbles. The intergranular bubbles are larger in size due to the enhanced diffusion of fission gas in this region. Figure 2.6 shows how μm sized bubbles have decorated the grain boundaries of UO_2 fuel. Fission gas that has been released by the fuel cannot be imaged but is evident by increased pressure in fuel pins.

Swelling due to Bubbles:

With bubbles residing in various locations throughout the fuel, swelling is a combination of the bubbles in these locations. These bubbles in the various locations are non-uniformly distributed. For a simple model of swelling, consider a $1cm^3$ of fresh fuel with a uniform distribution of N number of spherical bubbles with a radius of R. The fractional swelling from this condition is:

$$\frac{\Delta V}{V} = \left(\frac{4\pi R^3}{3}\right) N \tag{2.1}$$

If you assume a non-uniform bubble size, the fractional swelling becomes:

$$\frac{\Delta V}{V} = \frac{4\pi}{3} \int_0^\infty R^3 \, N(R) dR \tag{2.2}$$

These fractional swelling rates are for simple models. The swelling is affected by many reactor parameters including burnup, temperature, fission yield, etc. Many models have been created to simulate the swelling in reactor fuels including the DART code, the

BUBL code, and the PLATE code. These models can be complex and include parameters such as resolution, gas atom diffusion coefficients, bubble nucleation factors, coalescence, burnup, fission rate, etc. Swelling models that have been created for U-Xwt%Mo/Al dispersion fuels will be discussed in further detail later in section 2.5.8.

2.1.3 Amorphization:

A special condition in materials called amorphization occurs when irradiations are conducted at low temperatures. Amorphization occurs when a material loses all crystalline structure and becomes random or only consisting of short-range order (2-3 ordered neighbors). The concept behind amorphized materials is that the diffusion of point defects is low and the point defects are not allowed to recombine or reach sinks easily. The defect concentration continues to increase in the material until all of the ordered crystalline structure is consumed, leaving only a short ordering of crystalline structure. Amorphization in metal systems is often referred to as a metallic glass

Amorphization is highly dependent on dose and temperature. Above a critical temperature, amorphization cannot occur due to defects being able to reach sinks or recombine with each other. Additionally, a critical dose is needed to produce an amorphous material. Figure 2.7 (18) shows the amorphization curve of U_3Si, showing the dose and temperature dependence of an amorphous material. With increasing

temperature approaching the critical temperature, a high dose is needed to create an amorphous material.

When a material has transitioned to an amorphous state during irradiation, it is believed that it takes on a fluid like behavior (19). This leads to a decrease in viscosity and thus an increase in fission gas mobility. Doolittle (19) developed an expression for the fluidity or viscosity of an amorphous material.

$$\eta = \eta_0 \exp [C/V_f] \quad (2.3)$$

where η is the viscosity of the material, η_0 is the initial viscosity of the material prior to irradiation fission, C is a constant, and V_f is the free volume of the material. The V_f is believed to be proportional to the damage rate in the material. It is also highly related to the composition of the material

Materials undergoing an amorphous transition show changes in lattice parameter and volume fraction or free volume. Heavy ion studies of U_3Si and U_3Si_2 (20), (18) were completed to study the changes of lattice parameters and volume fractions with increasing dose. This was done to see how amorphization affects the free volume in these fuels. Neutron diffraction was used to measure the changes in lattice parameter at various doses. Figure 2.8 (20), (18) shows the changes in lattice parameters for U_3Si and U_3Si_2. The U_3Si experiment showed an increase in lattice parameter in the a-axis with a

slight decrease in the c-axis. Overall, the change in the a-axis was greater than the c-axis and thus leads to an increase in overall volume and thus an increase in swelling in the material. U_3Si_2 shows a decrease in both the a-axis and c-axis, and thus a decrease in volume fraction and swelling in the fuel.

2.2: The RERTR Program:

This section is focused on the RERTR program, focusing on its history, development of LEU fuels, and RERTR experiments and other international experiments

History of the RERTR Program:

The Reduced Enrichment for Research and Test Reactor was created in 1978 by the Department of Energy to reduce HEU usage throughout the world and to reduce nuclear proliferation. The program is composed of three main components: Development of advanced LEU fuels, design and safety analysis for research reactor conversion, and development of targets and process for the medical isotope Molybdenium-99 with LEU. The development of targets for Molybdenu-99 and reactor conversion will not be discussed in this thesis

The primary goal of the RERTR program is to convert reactors currently using HEU fuel to LEU fuel loadings. By lowering the HEU usage and creating new fuels that use LEU instead of HEU, proliferation risk can be minimized. The difference between HEU and

LEU is the percentage of U^{235} in the uranium that is present in the fuel in the same volume. LEU is defined as having a U^{235} percentage of less than 20 at% of the total uranium in the fuel, with U^{238} making up the rest of the total uranium. HEU is a loading above 20% U^{235} of the total U atoms present in the fuel.

In 1978, the RERTR program identified 106 reactors throughout the world that are targeted for conversion from HEU to LEU fuels (21). Most of these reactors are research and test reactors that operate at high powers and fluxes. These reactors often use HEU loadings to reach their required operating parameters. When converting the reactors from HEU to LEU loadings, it is imperative to not significantly change the operating parameters. When converting to LEU fuels, it became necessary to increase the density of the fuel to reach the same U^{235} loadings seen in HEU fuels.

In 2009, all but 19 of the targeted 106 research reactors have been or can be converted from HEU to LEU fuel using the RERTR qualified fuels discussed below (22). The other 19 reactors tend to have an exotic geometry and/or be high power/high flux reactors. These reactors require extremely high density LEU fuels to reach their original operating parameters. The high-density LEU fuels currently in development by the RERTR program are focused on providing LEU fuel options for these remaining 19 reactors.

The Development of Low Enriched Uranium Fuels:

The original fuels used in most HEU research and test reactors were one of three primary types: UAl_x-Al dispersion fuel, U_3O_8-Al dispersion fuel, and $UZrH_x$ fuels, with densities of 1.7 gm U/cm^3, 1.3 gm U/cm^3, and 0.5 gm U/cm^3 respectively. Dispersion fuels consist of fuel kernels surrounded by some matrix material. Aluminum is used as the matrix because it has a high thermal conductivity that helps with heat removal from the fuel. The initial fuel development in RERTR was focused on increasing the uranium densities of these fuels and the fuels were qualified at higher densities (2.3 gm U/cm^3 for UAl_x-Al, 3.2 gm U/cm^3 for U_3O_8, and 3.7g/cm^3 for $UZrH_x$). In addition to these three fuels, U_3Si_2 and U_3Si fuels were also studied. These qualified fuels offer uranium densities up to 4.8 g/cm^3. During initial screening of these fuels, it was found that U_3Si fuels failed at high burn-ups, primarily due to uncontrolled swelling in the fuel (22). This fuel was removed from consideration for converting reactors. The U_3Si_2 fuel showed acceptable performance and, with the qualification of this fuel and the original three fuels above, over 30 reactors were/could be converted from HEU loadings to LEU loadings (22). In addition to dispersion fuels, monolithic fuels can be used. These fuels consist of a fuel meat sandwiched between some cladding material. Figure 2.9 (22) shows the differences between monolithic and dispersion fuels.

With the development of these fuels, many of the HEU reactors in the world can be or were converted to LEU loadings. The remaining reactors throughout the world require fuels with higher uranium densities, (8 gm U/cm^3 or higher). This led to the need to find

new fuel designs to accommodate these densities. The two fuels that were selected were U-Mo dispersion fuels and U-Nb-Zr fuels. In addition to these fuels, a monolithic fuel using U-Xwt%Mo fuel foils sandwiched in Al cladding is being studied to reach U-loadings greater than 10 gm U/cm^3. These fuels are the starting basis of the current RERTR fuel development. The RERTR program is in the process of testing these fuels using the Advanced Test Reactor (ATR) at the INL. Mini-plate experiments have been conducted using U-Mo, U-Mo-Ternary, and U-Nb-Zr fuels. Included in these tests are different fuel designs, such as monolithic fuels and dispersion fuels. Additionally, four full plate irradiations and two fuel element tests have been or are in the process of being completed. Each test exposes the fuel to some predetermined irradiation condition and, from the results, the direction of future RERTR experiments will be or has been determined.

A brief description of the RERTR mini-plate irradiation and international campaigns are described below with the goals of each experiment and results from the completed irradiations. A key observation will be provided after each test as a summary of the results. Additionally, Table 2.3 provides an overview of all of the RERTR experiments and irradiation conditions conducted to Apr. 2009 and their key observations. Monolithic plates have been irradiated in many of these RERTR campaigns and their results will not be discussed. A detailed summary of the monolithic fuel plate campaigns can be found in the following references (22).

The RERTR and International Experiments:

Fuel failure mechanisms will be discussed later but to help follow the RERTR and International experiments, the definition of breakaway swelling and pillowing will be presented. Breakaway swelling is when fission gas bubbles coalescence together forming large micron sized bubbles. The bubbles will interlink and will continue to interlink together and eventually will cause the fuel particle to debond from Al matrix. This leads to high local swelling. Pillowing is where the swelling in the fuel causes the cladding to fail and separate.

RERTR-1 and RERTR-2 Tests:

The RERTR-1 and -2 experiments were the two pilot tests for the U-Xwt%Mo and U-Nb-Zr dispersion fuels. The main difference between the RERTR-1 test and the RERTR-2 test was the burnup of the fuel. The U^{235} equivalent burnups reached by the fuels were around 40% and 70% for RERTR-1 and RERTR-2 respectively. Burnups are reported as U^{235} burnups at a 20 at% enrichment. Designed operating temperature was set at 65°C. Each test consisted of many compositionally different dispersion fuels, i.e. U-7wt%Mo, U-10wt%Mo, etc., to test the response of each composition to high burnup and to provide a screening process for future fuel development.

Post Irradiation Examination (PIE) showed that the U-Nb-Zr fuels did not respond well to irradiation conditions and break-away swelling occurred in these materials. This fuel was abandoned after these tests. The U-Mo fuels showed promising behavior in fuels with

greater Mo loading of 6 wt%. The general observation of these fuels is that they respond to irradiation conditions much like the U_3Si_2. In the U_3Si_2 fuel development, a FMI layer formed between the U_3Si_2 fuel kernel and Al matrix. This layer was shown to be stable at high burnups (23).

Key observation: U-Xwt%Mo/Al dispersion fuels responded well to the designed burnup and are a candidate choice for high density LEU fuels.

RERTR-3 Test:

The RERTR-3 experiment had a higher operating temperature than the RERTR-1 and -2 tests. It consisted of a moderate burnup with fuels consisting of U-Xwt%Mo/Al alloys and U-Xwt%Mo/Mg fuel. The burnup of the fuel ranged from 25%-41% U^{235} burnup. PIE showed that a significant FMI layer formed around the U-Mo fuel kernel, which consisted of primarily $(U,Mo)Al_2$, $(U,Mo)Al_3$, and $(U,Mo)Al_4$ phases. These phases showed stable irradiation behavior at these burnups. In addition to the FMI layer, fission gas bubbles formed along the grain boundaries of the fuel, as seen in Figure 2.10 (24). This is consistent with what was seen in RERTR-1 and -2.

Key Observation: The fuels remained stable under the irradiation conditions.

RERTR-4 and RERTR-5 Tests:

The purpose of the RERTR-4 and -5 tests were to irradiate the U-Xwt%Mo/Al dispersion fuel to high burnup. The burnups achieved were 80 and 50% ^{235}U for RERTR-4 and -5 respectively. In addition, monolithic plates were irradiated in RERTR-4. PIE on the tests showed that the dispersion fuel responded much like the fuel in RERTR-3 except for the development of porosity between the FMI layer and the fuel, leading to increased swelling seen in Figure 2.11 (22). Results of the monolithic plates were very promising because the fuel responded well to the irradiation conditions.

Key Observations: The fuels show stable irradiation microstructures. Porosity has started to form in the higher burnup plates and can be a precursor for breakaway swelling. FMI layers are extensive in the fuels but have not affected the irradiation microstructure.

RERTR-6 Test:

The RERTR-6 test was conducted to further study the effects of the pore growth on the FMI layer boundary. As a result of RERTR-5, it was found that the porosity that formed at high burnup would lead to break-away swelling in the fuel. This ultimately leads to fuel failure. RERTR-6 was designed to test this issue. In addition, Si was added to the Al-matrix to try to help stabilize the growth of the FMI layer and control the breakaway swelling. This was done to try to form the FMI phase, $U(Al,Si)_3$, the phases found in FMI layer in U_3Si_2/Al dispersion fuel (23). This phase has been shown to stable be at high burnups.

Various wt% of Si (0.2%-5% Si) were added to the matrix of RERTR-6 to try to understand this FMI layer issue. The fuel was irradiated to roughly 50% U^{235} burnup. The dispersion fuel responded well to irradiation. In addition, the Si (above 2.0% Si) suppressed the growth of the FMI layer to an FMI layer thickness comparable to those seen in the U_3Si_2 fuel development campaign (22).

Key Observations: The use of Si additives above 0.2 wt% in the Al matrix decrease the FMI layer growth during irradiations.

RERTR-7A Test:

The RERTR-7A was conducted to test the U-Xwt%Mo/Al dispersion fuel at high operating power conditions. The fuel was irradiated to levels greater than 100% LEU burnup by using U^{235} enrichments greater than 20%. This was done to speed up the burnup seen by the fuel. PIE of the dispersion fuel shows bubble interlinking or porosity buildup around the fuel kernels. This bubble interlinking is the starting point of breakaway swelling which leads to fuel failure.

Key Observations: Fuels show porosity buildup around the fuel kernels at burnups up to 80%.

RERTR-7B Test:

The purpose of RERTR-7B test was to test the effects of adding Ti or Zr to the Al-matrix instead of Si. Out of pile diffusion couples show that Ti and Zr were effective in stabilizing the FMI growth. The burnup achieved by the fuel was roughly 30%. Results show that the fuel with the modified matrix responded well to low burnup. Swelling and FMI layer growth were minimal in the materials. The effect of Zr and Ti added to the fuel kernels has been shown to respond well to irradiation.

Key Observation: The effect of adding Ti and Zr to the Al matrix reduces the FMI growth to levels seen in the Si-modified matrix.

RERTR-8 Test:

The purpose of the RERTR-8 test is to understand the effects of the additives (Ti and Zr) to the fuel at high burnups (75% LEU equivalent). This test was designed to mimic RERTR-7B with the addition of Ti and Zr to the fuel kernel instead of the Al matrix in the dispersion fuels. The fuel responded well at the high burnups and was stable.

Key observation: The dispersion fuels show that the FMI layer between the fuel kernel and the matrix is stable level at these high burnups.

RERTR-9A and -9B Tests:

The RERTR 9 series of tests are designed to test the full fuel loading of 8 gU/cm^3 of U-Mo fuels with various levels of Si added. RERTR-9A is focused on dispersion fuel and -9B is focused on monolithic fuels. RERTR-9B was designed to look at different fabricated monolithic fuels. Porosity has formed in the dispersion fuel around the fuel kernels at a burnup of ~80%. Some interlinking of the porosity is evident at a burnup of ~120% but breakaway swelling has not occurred.

Key Observation: Porosity formation at high burnups but no breakaway swelling has occurred.

RERTR-10 Tests:

The goal of this test is to expose the dispersion plates to aggressive power conditions (550 W/cm^2). This test has gone through irradiation and no PIE results are available at the writing of this document. In addition to these RERTR mini-plate tests, additionally irradiations have been planned, are happening, or will happen in the near future to help guide the RERTR program.

These tests will help guide the selection of the final fuel.

AFIP Tests:

In addition to the mini fuel plate testing, the RERTR program will conduct full plate tests in the ATR. These have been designated as AFIP (ATR Full-Size-Plate In Center Trap

Position). There are four AFIP tests that are currently planned for testing in the ATR. AFIP-1 and -2 are tailored to study standard geometry fuel plates. AFIP-1 is being loaded with U-7wt%Mo fuel in a Si modified Al-matrix. AFIP-2 will be tested with monolithic plates as well as some dispersion plates. Monolithic plates in AFIP-2 will be subject to a LEU burnup of 2-800%. AFIP-3 and -4 are focused on fuel of varying complex geometry. Many of the reactors being targeted for conversion from HEU to LEU are of complex geometries, such as curved plates. In addition to subjecting the fuel to complex geometries, burnable poisons will be added to the fuel. Burnable poisons are being used to control the power of the fuel plates over their irradiation lifetime. Density zoning will be also incorporated in the fuel. Density loading is being used to increase/decrease power in specific locations on the fuel plates.

The primary focus of the AFIP tests is to provide feedback on large fuel plates that will be used when creating full-fuel test elements. To help monitor the fuel performance, the ATR has the capacity to monitor the plate swelling and thickness growth of each plate, as a function of burnup, by the use of an in-canal thickness measurement system. The plates will be under high power situations to demonstrate the fuels capability. Various AFIP tests are currently being conducted in the ATR at the time of this thesis.

FUEL ELEMENT Tests:

The ultimate goal of the RERTR program is to qualify a high density fuel, ~8 gm U/cm^3. The RERTR and AFIP tests are designed to lead the RERTR program towards the

selection of the fuel that will be used in a complete fuel element. With successful fuel element demonstrations under irradiation, RERTR will be able to provide a detailed package to the NRC for qualification as a new fuel. The current plan of the RERTR program is to qualify the fuel in two phases. The first phase is to qualify fuels to a loading of roughly 8.5 gm U/cm^3. The second phase is focused on fuels with loadings greater than 8.5 gm U/cm^3. Two fuel element tests are being designated for the phase one (ELEMENT-1 and -2). ELEMENT-3 is being used for phase two.

The focus of ELEMENT-1 is to test modified matrix dispersion fuels created by the RERTR program in the USA for qualification. Four fuel elements will be tested. Two will be in the ATR and two will be tested in Russia's MIR reactor. Both reactors are targeted for conversion in the RERTR program. PIE on the fuel will focus on deformation of the fuel, visual inspections, gamma scanning, thickness measurements, and some destructive analysis. The intention is that PIE can be completed by the end of 2009 or early 2010. A fuel qualification package can be provided to the NRC for qualification of the fuel of dispersion fuel by the end of 2010.

ELEMENT-2 is planned to be lagging behind the ELEMENT-1 test by a few months due to fabrication time. The ELEMENT-2 tests will consist of commercial vendor fuel. This test will be used to provide additional information to the ELEMENT-1 tests. This fuel will be subjected to less aggressive parameters than the ELEMENT-1 tests to provide a range of irradiation conditions. With the slight time lag from ELEMENT-1, PIE work for

Element-2 is not expected to be completed until late 2010. The information obtained from PIE when it becomes available will be used as supplementary information for NRC.

ELEMENT-3 will be loaded with fuel densities greater than 8.5 gm U/cm^3. This test will be conducted in the ATR in 2010 with four fuel elements. The fuel composition will be primarily monolithic fuels with a few high-density dispersion fuel plates. The fuel elements will be left in the reactor for 3-5 irradiation cycles. The planned removal date of the fuel is January 2011. Once cooled, the fuel will be transferred to the appropriate hot cells and PIE will be conducted.

KOMO and IRIS International Experiments:

In addition to the tests conducted by the U.S. RERTR program, other nations have tested U-Mo dispersion fuels. The two primary series of tests are the IRIS and KOMO tests. The French IRIS tests consisted of three full plate irradiations. The first two tests were U-7wt%Mo/Al tests. The Al matrix was not modified with Si. The results of these tests match the results seen in the early RERTR fuel tests. A large FMI layer formed, which lead to increased plate thickness and ultimately high swelling and failure rates. IRIS-3 was the first test to use a modified Si matrix and results from this test were promising. The fuel was able to achieve higher burnups than IRIS-1 and -2 without failing (22).

The KOMO tests were conducted by KAERI. The first two KOMO tests were similar to the first two IRIS tests, showing the typical FMI layer issue and the swelling and plate

thickness issues. KOMO-3 consisted of many different modifications of fuel of the U-Mo fuel, including U-Mo-X/Al (X=Ti, Si, and Zr) and Si modified matrix fuels. The additive modified fuel responded to irradiation much better than the non-modified fuel. The Si added fuel reduced the FMI layer thickness by half when compared to the standard U-Mo/Pure Al dispersion fuel (25).

Table 2.3 summarizes the RERTR and International U-Mo dispersion fuel experiments providing the Si content in the matrix, the reason for the tests, the maximum achieved burnup, and key observations of the PIE of each test.

2.3: Current Understanding of U-Xwt%Mo/Al Dispersion Fuel

The current advanced LEU fuel under development is U-Xwt%Mo/Al dispersion fuel. This fuel can be broken up into 3 main regions, the fuel kernel, the FMI layer, and Al matrix. The irradiation performance of the fuel kernel and FMI layer will be discussed in detail here starting with the U-Xwt%Mo fuel kernels.

2.3.1: Gamma Phase Stability and Fabrication

One of the criteria for the new high density fuels in the RERTR program was to design a fuel that was BCC in structure to limit swelling in the fuel plate. In general, BCC materials show lower swelling rates (0.2% swelling per dpa) compared to FCC materials (1.0% swelling per dpa) (26). The proposed reason for the lower swelling rate in BCC is

the relative bias for point defects at sinks. Pure uranium at typical research and test reactor temperatures is in a orthorhombic α-phase. The α-phase uranium fuel has been shown to have high swelling (27). Meyer (27) suggested adding an additional element to the uranium to stabilize the fuel into a γ-BCC phase at typical operating temperatures. To help stabilize the γ-phase of uranium, 4d and 5d elements from Group IV are being added to the uranium. These elements are soluble in uranium. By adding these elements to the uranium above 600°C, a metastable γ-phase of uranium can be created at typical operating temperatures by quenching the fuel. In particular, Mo has shown good solubility in uranium (~35%) and is being used to stabilize the uranium fuels into the γ-phase [19]. Figure 2.12 (28) shows the U-Mo phase diagram. It has been found in the RERTR-1 campaign that a molybdenum content greater than 5 wt% is needed to stabilize the metastable γ-phase during irradiation (29). The lattice parameter of the γ-phase as a function of the wt% Mo additive in the uranium is expressed in Equation 2.4 (28).

$$a_0 = 3.4808 - 0.00314 X_{mo} \qquad (2.4)$$

where X_{mo} is the Mo content in atomic %.

A thermodynamically stable γ-phase is not found at temperatures lower than ~520°C. To create the γ-phase below this temperature, the U-Xwt%Mo fuel needs to be quenched down to room temperature. U-Xwt%Mo ingots are heat treated in a vacuum at 950°C for an extended period and then quenched immediately down to room temperature (30). The quenched metastable γ-phase will decompose into the α phase and γ'phase (U_2Mo) at

elevated temperatures (above room temperature). Many studies have been done to show that the γ-phase decomposes at elevated temperatures and time (31), (32), (22), (33), (34)]. Most studies are at temperatures above 400°C, which is much higher than operational temperatures of the research reactors, ~200°C, but provide an idea of how the fuel kernels will decompose. It should be also noted that radiation will enhance diffusion throughout the fuel causing decomposition earlier and at lower temperatures (30).

2.3.2: Additives in the Fuel Kernels

Incorporating additional elements to the U-Xwt%Mo kernels to suppress the FMI layer growth is being investigated. There are 3 primary additives being explored at the current time: Mo, Zr, Ti, and Al. As mentioned, Mo is already added to the fuel to help stabilize the γ-phase in the fuel. The amount of Mo in the kernel directly impacts the growth rate of the FMI layer in the fuel. Figure 2.13 (35) shows the FMI layer growth in different compositional Mo contents. In this experiment, diffusion couples were created between U-Mo foils of varying Mo content and the Al-6061 matrix. The samples were heat treated at 580°C for 1.5 to 3 hours. At lower Mo content (less than 8 wt%), the FMI layer growth is much higher than those of greater Mo loadings.

Park, et al. (36) studied the effects of adding Zr to the fuel kernel with the addition of Si in the Al matrix. This study was composed of diffusion couples of U-7wt%Mo-Xwt%Zr, with Zr additions of x=0, 2, and 4 wt%. In each composition, three Al matrix diffusion

couples were compared. The diffusion couples showed that the Zr added to the U-Mo kernels decomposed into the α-phase and the γ-prime phase at the same rate of the standard U-Mo/Al kernels. The α-phase and the γ-prime phases are not desired due to their unwanted irradiation behavior such as swelling at high burnups.

Ti, as an additive to the fuel kernel, was also investigated to study its effect on the FMI layer microstructure. Park, et al. (37) found that Ti does suppress the FMI layer growth. The Ti addition to the kernel, much like the Zr addition, does lead to high decomposition of the γ-phase at elevated temperatures which is undesirable due to the new phase's irradiation stability. Additionally, it was found that the effectiveness of Ti in the kernel is limited to 1 wt%. Higher compositions led to dense precipitates in γ-phase, which affect the ability of the Ti to suppress the FMI layer. These precipitates can be seen in Figure 2.14 (38).

2.3.3: Fission Gas Bubbles in U-Xwt%Mo/Al Fuel Kernels

Fission gas bubbles have been seen in U-Xwt%Mo/Al dispersion fuels. These bubbles are evident as μm sized bubbles along the grain boundaries of the fuel kernels and as nm and μm sized bubbles in the grains. Provided is a brief summary of these bubbles in U-Xwt%Mo fuel kernels.

Intergranular Bubbles

SEM analysis shows that large μm sized bubbles have formed along grain boundaries of the fuel grains. This can be seen in Figure 2.15 at various burnups (39). At a burnup of roughly 35%, the bubbles decorate the grain boundaries. At a burnup of 65%, the bubbles have started to increase in size with the increase in fission gas inventory. Additionally, they have started to interlink with each other to form larger single bubbles. At 80%, the bubbles are evenly distributed across the grains of the fuel. At this point, the fuel has undergone recrystallization which will be discussed in section 2.3.4.

Intragranular Bubbles

A TEM study of U-Xwt%Mo/Al dispersion fuel (1) showed that a super ordered bubble lattice has formed in the bulk of the grain at a burnup of ~35%. These bubbles are roughly 2 nm in size and are spaced 6-7 nm apart. They are coherent with the host matrix and Figure 2.16 (1) shows these bubbles and the corresponding electron diffraction pattern. In addition to these bubbles, SEM images show that μm-sized bubbles start to form in the interior of the grains at high burnups. This can be seen in Figure 2.15b) in the middle image as small bubbles greater than 0.5 μm.

2.3.4: Recrystallization

The U-Xwt%Mo fuel kernels undergo a recrystallization step at burnups between 45-60% burnup. Recrystallization is the formation of smaller sub-grains out of the initial fuel

kernel grains. The driving force of recrystallization is the energy of defects provided to the grains. Rest describes when recrystallization occurs as "the energy per nucleus is high enough that the creation of grain-boundary surfaces is offset by the creation of strain-free volumes, with a resultant net decrease in free energy of the material" (40). Recrystallization of U-Xwt%Mo can be seen in Figure 2.15c) (39). Recrystallization creates more grain boundaries throughout the fuel kernels. This creates a larger sink to which fission gas can diffuse. Nogita et al. showed that in UO_2 fuel irradiated to high burnup, recrystallization occurred (41). They also showed that intragranular bubbles present before recrystallization have disappeared and larger sized bubbles have formed along the grain boundaries. Understanding how recrystallization affects the U-Xwt%Mo intragranular bubble evolution is unknown at the current time.

FMI Layer:

The growth of an FMI layer in dispersion fuels has become a major fuel performance issue. The FMI layer is formed between the matrix and fuel kernels in dispersion fuel and is composed of U-Mo-Al phases. Additionally, any additives in the fuel kernels and/or the matrix can affect the composition of the FMI layer. The FMI layer phases can lead to undesired fuel performance at high burnups. This includes decreases in thermal conductivity, and storage of fission gas that leads to bubbles and swelling. The formation of the FMI layer is affected by combinations of physical and irradiation parameters, which include: what phases formed, additives in the matrix and fuel kernel, burnup, and operating temperature.

2.3.5: Phases in the FMI Layer

To better understand the FMI layer's effect on fuel, it is important to know the physical composition of the FMI layer. There are two primary methods that can be used to study this: out-of-pile tests and in-pile-tests. The out-of-pile tests generally consist of diffusion couples conducted at high temperatures to promote FMI layer growth. This method has a disadvantage compared to in-pile-tests in that there is no radiation induced diffusion in the FMI layer. The in-pile-tests are irradiated in a reactor and simulate what will occur in a reactor. The major drawbacks of this method are the activity of the samples, cost, and time to complete these experiments.

There are three main techniques that have been used to identify phases present in the FMI layer: TEM, SEM including EBSD, and XRD. Van den Berghe, et al. (1)preformed TEM analysis on a neutron irradiated U-7wt%Mo dispersion fuel (burnup 33%) and found that the FMI layer was amorphous in character and no phase information was found. No additional information on TEM analysis of neutron irradiated U-7wt%Mo fuel beyond that in (1) has been found prior to this study.

SEM analysis has been conducted extensively on irradiated and non-irradiated dispersion fuels. The primary method used to determine the chemical composition of phases in SEM analysis is from EDS and WDS analysis. The chemical composition from EDS and WDS are used to determine the composition, and in combination with XRD could be used to identify the phase. By using the ratio of X=(Al+Si)/(U+Mo), an idea of what the

phases are present in the EDS location can be found. The ratio value X is used in UAl_x to determine the phase. It is assumed that the Si atoms are substitutional on the Al lattice sites and that Mo atoms are substitutional on U lattice sites.

The non-irradiated analysis has consisted of mostly diffusion couples to predict radiation induced diffusion. Diffusion couples involve sandwiching different types of materials together and heating the couple up to some designated temperature. The elevated temperature allows for thermal diffusion. At typical reactor operating temperatures, the radiation induced diffusion is the driving mechanism but by choosing a high temperature for the diffusion couples, it is hoped that the thermal diffusion is similar to the radiation induced diffusion rate. Diffusion couples produce an area between the sandwiched materials that is composed of a mixture of the two materials. This region can be composed of many different phases. Figure 2.17 (37)shows what a typical diffusion couple looks like in U-7wt%Mo/Al-0.2wt%Si after 2hrs at 580°C.

Park, et al. (36), (37), (42), (37) has conducted many diffusion couples experiments of varying fuel kernel and matrix compositions to help identify the phases in the FMI layer. The studies often included line scans over the FMI layer to determine the atomic percent of the elements present across the FMI layer. Once the atomic percent of the elements is determined, the atomic ratio across the FMI layer can be found (atomic ratio is defined as $x=(Al+Si)/(U+Mo+Ti/Zr)$ in UAl_x). Figure 2.18 shows an example of this analysis (43). Another observation from Park is the differences in material composition as a function of

position from the fuel kernel to the aluminum matrix. The atomic ratio value is the lowest on the kernel side and largest on the aluminum side. This is expected because there should be more Al available near the Al matrix than around the kernel. This also shows how FMI layer is not just one phase, but is composed of a mixture of many phases. This can be seen in Figure 2.19 (31). In the FMI region, there are two different contrast regions. Assuming that the sample was polished evenly, this would indicate a change in elemental composition in the area and thus a potential change in phase in this region.

Keiser, et al. (44) conducted diffusion couple experiments between U-Mo and Al-6061. The Al-6061 is composed of primary Al with additives, such as Si. The effect of these additives on the whole FMI layer is discussed later in section 2.5.2. In general, the phases take the form of UAl_x phases (i.e., $(U,Mo)(Al,Si)_x$). These complex phases are believed to be able to control the growth of the FMI layer and hopefully control the phases formed in the material. Two common phases seen are $(U,Mo)(Al,Si)_2$ and $(U,Mo)(Al,Si)_3$. The goal of the U-Mo vs. Al-6061 experiments was to see if the $(U,Mo)(Al,Si)_3$ phase responds to diffusion couples much like $U(Si,Al)_3$, a known phase that responds well to irradiation (23). The results of this experiment show that this phase does limit the FMI layer growth, much like the $U(Al,Si)_3$ phase.

Park, et al. (25) conducted PIE from the KOMO-3 irradiation test. Various phases formed in the fuel at varying conditions. Figure 2.20 (25) shows the FMI layer phases seen in the experiment in two different fuel types. An interesting observation from these

results is the effect of temperature on the phases that formed. In the high temperature locations (the center), the phases formed are of the UAl_3 type. At the periphery regions, high UAl_x phases form ($x \geq 4$), primarily UAl_4. In addition to UAl_x compounds, plates of Si-modified Al-matrix were irradiated in these tests. The phases formed are $(U,Mo)(Al,Si)_x$ phases. Observations showed that the $(U,Mo)(Si,Al)_3$ phase formed in the center of the fuel, much like the UAl_3 phase, whereas $(U,Mo)(Si,Al)_4$ was formed on the periphery regions.

The other primary method to determine the phases present in the FMI is XRD and neutron diffraction. Mirandou, et al. (31) conducted XRD on U-7wt%Mo/Al dispersion fuel. Figure 2.21 (31) shows the results of this analysis. Using the diffraction peaks from the XRD, the phases in the material can be identified. Mirandou found that three primary phases formed in the material, with $(U,Mo)Al_3$ and $(U,Mo)Al_4$ as the primary phases and a small amount of UMo_2Al_{20} also formed. In addition to the phases mentioned above, small amounts of $U_6Mo_4Al_{43}$ have also been seen in diffusion couples (31). Additional references on the phases in the FMI layer are provided. (45), (34), (46), (31), (47), (43), (48), (29), (49), (50), (1)

2.3.6: Effects of Additives in the FMI Layer

As the RERTR program progressed from the RERTR-1 through-5 tests, it became evident that the FMI layer would not be stable at high burnups. At high burnups, the fuel

developed porosity and this lead to break-away swelling in the fuel. This issue led the RERTR program to modify the dispersion fuel. The two primary options for modification of the fuel are modifying the Al-matrix or using additives within the fuel kernel itself. Combinations of these options are being considered as well.

Al-Matrix Modification:

There are two basic concepts for modifying the matrix. These are changing the matrix to another material, primarily Mg, or modifying the Al-matrix composition with the use of additional elements. The reason for selecting Mg for the matrix is to limit FMI layer growth. Mg does not interact with the fuel and form new phases (22). The concern with using a Mg matrix is the bonding between the fuel kernels and Mg matrix. Fuel fabrication was difficult in RERTR-1 showing that the fuel particles fall out of the matrix easily. Fuel was created using a lower density of particles so that more matrix can completely hold the particles.

Converting the matrix to Mg has not been explored in great detail. In RERTR-3, an Mg-matrix dispersion fuel was used and it showed no FMI layer between the fuel particles and behaved well under irradiation. The Mg-matrix fuel was not explored again until RERTR-8, when one fuel was loaded using a Mg-matrix. The fuel showed good irradiation behavior by not forming a FMI layer (22). Despite the irradiation success, PIE led to breakaway particles of the fuel kernels and matrix due to poor bonding.

Due to the fabrication issues with changing the matrix to Mg, Al-matrix modification is the primary option being studied. The focus of Al-matrix modification includes adding Si to the Al-matrix. The goal of Si addition to the FMI layer is to drive the layer towards the $U(Al,Si)_3$ phase. $U(Al,Si)_3$ is present in the FMI layer in the U_3Si_2 dispersion fuels that have been shown to be stable at high burnups (23).

As burnup starts to occur at an elevated temperature, the FMI layer will begin to grow. This is due to Al and Si diffusing into the fuel kernel due to the atoms higher diffusion mobility. As Si enters the FMI layer, it drives the FMI layer to form the $(U,Mo)(Al,Si)_3$ phase due to the Si bonds. With this stable phase formed, additional Al will diffuse into this area at a much more slower rate due to the strong bonding of the $U(Al,Si)_3$ phase. It should be noted that the FMI layer will still grow, to an extent due to two effects. The primary mechanism that helps aid the Al diffusion into the fuel is radiation induced diffusion. The other effect concerns the Si content in the FMI layer. As the FMI layer increases in thickness, the finite Si content in the area is distributed across this layer. This reduces the Si bonding in the area and can drive the system to $U(Al,Si)_x$ phases where x is ≥ 3.

The compositional makeup of the matrix affects the growth of the FMI layer. In RERTR-6, four different compositional Al-matrices were used. These include an Al-Xwt%Si matrix with 0.2 and 2.0 wt% Si and commercial Al-6061 and Al-4043. The primary results from this experiment show that the composition of the Si in the matrix affects the FMI layer growth. In Figure 2.22 (51), optical microscopy of the 0.2% Si and 2.0% Si

matrix fuels is shown. The 0.2% Si fuel formed an FMI layer ~12μm thick. This is about the same thickness seen in a pure Al matrix. The 2% Si scenario shows a reduction of the FMI layer thickness when compared to a pure matrix, ~2μm. The same results were seen for the Al-4043 matrix, which contains ~5%Si. It is believed that the FMI thickness was reduced due to the formation of $U(Al,Si)_3$ type phases. These results led the RERTR program to use Al-2.0wt%Si, A-6061, and Al-4043 matrices for the future experiments.

With the PIE results from RERTR-6,-7, and -8 and the KOMO-3 test becoming available, the FMI layer in the Si modified Al-matrix has shown good irradiation behavior at high burnups with Si loadings between 0.2 and 5 wt% (25). The preliminary results from all of the tests have shown that FMI layer growth has been stunted by the Si addition. The major fuel limitations that were identified by these tests are Si distribution in the matrix, porosity buildup at the FMI layer interface, and fission gas accumulation in the material. The irradiated Si modified dispersion fuels have shown irregular FMI layer growth in some of the kernels. The primary driving force for this is Si content in the surrounding areas. Figure 2.23 (50) shows a secondary electron SEM image and its accompanying Si x-ray map. In the areas where there are abundant Si precipitates prior to fabrication and irradiation, the fuel kernels show very little FMI layer thickness. Areas with minimal Si precipitates distribution show a much higher FMI layer thickness. With the Si being insoluble in pure aluminum, finding a method to evenly disperse the Si precipitates in the material is needed to provide a uniform FMI layer. In addition to Si modified matrices,

Ti and Zr have been added to the matrix to stabilize the FMI at high burnups. Additional information on these tests can be found in the following references (37) (36), (42), (52).

2.3.7: Temperature Effects on the FMI Layer

Fuel temperature plays a major role in the performance of the fuel. Dispersion fuel is constructed by placing fuel kernels in a matrix. The matrix provides a mechanism to help remove heat from the fuel by nature of a high thermal conductivity. Typically, Al is used as the matrix material due to its high thermal conductivity. By having a matrix material that has a high thermal conductivity, the fuel temperature remains low and in turn minimizes diffusion effects in the material. With the formation of the FMI with increasing burnup, the Al matrix is consumed. The phases formed in the FMI have a thermal conductivity much lower than the Al-matrix, less than a third of the value of Al (53). The lower thermal conductivity leads to the inability of the matrix to remove the heat as efficiently and thus increases the fuel temperature. This increases thermal diffusion and leads to FMI growth, which lowers the total thermal conductivity of the meat of the fuel. This cycle repeats itself and eventually the process leads to complete Al transformation to an FMI layer, which could lead to potential fuel failure. By controlling the FMI growth, primarily by adding Si to the Al matrix, the fuel temperature can be controlled and lead to a decreased chance for fuel failure.

Operational temperature of the fuel affects how the FMI layer will grow in the matrix. This can be seen for heat-treated U-10wt%Mo/Al dispersion fuels in Figure 2.24 (53). Three different matrix microstructures are shown in the figure each developed at various temperatures. These samples were heat treated for the same time. With increasing temperature, it is evident that the FMI layer is expanding. At 215°C, the Al matrix is almost completely consumed, leading to a much lower total thermal conductivity for the fuel plates. At 145°C, the FMI layer is negligible.

2.3.8: Fission Gas Bubbles in the FMI layer

Fission gas bubbles can form in the FMI layer. Outside of SEM images showing sporadic fission bubbles in the FMI, no information has been provided about bubbles present in the FMI layer. The TEM study by Van de Burghe (1)showed no nano-sized bubbles present in the FMI layer. With the FMI being amorphous (1), bubble studies of other amorphous materials might be pertinent. U_3Si and U_3Si_2 dispersion fuels underwent an amorphous transformation at RERTR temperature conditions. Figure 2.25 shows a micrograph comparing the bubble formation in U_3Si and U_3Si_2 amorphous fuels at the same burnup (2). It is important to notice the size of the scale bar in both images. In the U_3Si image, the scale bar is 10 μm. For U_3Si_2, the scale bar is 1 μm. The U_3Si fuel developed large non-uniform bubbles while U_3Si_2 produced much smaller uniform bubble distributions. The swelling in the U_3Si fuel was deemed undesirable while the swelling in the U_3Si_2 was within an acceptable limit.

2.3.9: Fuel Performance Issues

As seen in the section 2.2 (RERTR History Section) many irradiations have been performed on U-Xwt%Mo dispersion fuels. While most irradiations were successful during irradiations, some experiments showed undesirable irradiation behavior (22), (54). These behaviors include: overheating of the cladding, corrosion attack on the cladding, unacceptable swelling of the fuel plates, growth of unacceptable FMI layers, porosity buildup around the fuel kernels, and delamination of the fuel kernels from the matrix. A brief summary of these effects on the fuel are provided here.

In the RERTR-5 irradiation campaign, excess activity over background was noticed in the ATR reactor coolant after 10 days of irradiation (22). Upon experiment removal from the reactor, it was noticed that one plate had breached its cladding. Figure 2.26 (22) shows a cross-section micrograph of the failed fuel plate. It was determined that the Al cladding in the breached area was thinner than in the surrounding areas. This was due to the plate fabrication process. After the failure of this plate, addition screening was used to make sure that the Al cladding was at the proper thickness before insertion into ATR.

The UMUS experiments in France's HFR showed a similar cladding breach in one plate (54). It was determined that a low thermal conductivity oxide layer had formed in the Al cladding due to corrosion from the pH level of the reactor coolant. It was found that the HFR reactor was operated at a pH greater than 5. This led to the enhanced formation of boehmite which has a much-lower thermal conductivity when compared with Al. The

decrease in the thermal conductivity led to an increase in the fuel temperature that in turn affected the fuel region and the Al cladding. The fuel region showed that the Al matrix was completely consumed by the FMI layer. In addition, the fuel region became delaminated from the Al cladding. The delamination of the fuel region from the matrix can be seen in Figure 2.27 (22) as well as the complete consumption of the Al matrix by the FMI.

Another key undesirable fuel defect is swelling of the fuel plates. In the FUTURE, IRIS-1 and -2, and KOMO-1 and -2 tests, the fuel exhibited swelling rates between 10-20% (22). This excessive swelling led to removal of many of these experiments from their respective reactor before reaching their target burnup. These swelling values are about twice the values observed in U_3Si_2 dispersion fuels (22). The main source of this swelling in the fuel plates is due to gas porosity buildup in the fuel region. Figure 2.28 (19), shows an example of porosity buildup in the fuel region. The figures show three different locations and how the burnup affects the porosity. In addition, the plate thickness is provided and shows how the porosity affects the swelling in the fuel. In areas of high burnup, the porosity is high thus leading to higher swelling. The porosity can continue to grow and interlink with increasing burnup and lead to delamination in the center region of the fuel. This is often described as pillowing and can led to fuel failure. This can be seen in Figure 2.29 (55).

The burnup of the fuel has a major effect on the swelling. Figure 2.30 shows the swelling rate vs. burnup for various U-10wt%Mo/Al dispersion fuels (19). Included are some SEM images showing the general microstructure of fuel with increasing burnup. It should be noted that there is an elbow in the swelling rate of U-10wt%Mo/Al dispersion fuel. At the elbow, the fuel is starting to recrystallize and at this elbow, the swelling rate of the fuel is higher than the region before the recrystallization zone. It should be noted that the swelling data reported here is for fuels that are in a pure Al matrix with no additives.

The effect of Si in the matrix on the swelling of the fuel plates can be seen in Figure 2.31 (51). The results show the comparison of fuel plates from RERTR-5 and -6 as a function of plate position in the reactor. RERTR-5 and -6 underwent ~50% burnup. Additionally for RERTR-6, varying Si contents are shown and their effect on the swelling can be seen. Figure 2.31 shows how for Si content 2 wt% and higher, the swelling is reduced by a factor of 2 when compared to a pure Al matrix.

2.3.10: Modeling Efforts of the RERTR Fuel

With qualifying the fuel, a modeling code to predict how the fuel will react during its irradiation is needed. This helps determine what the fuel's irradiation parameters are in specific locations in a fuel plate. The RERTR program is focusing on one such code called the Plate Lifetime Accurate Thermal Evaluation, or PLATE for short. The primary

focus of the code is to evaluate the thermal conditions of the U-Mo/Al dispersion fuels during their irradiation lifetime. This includes determining temperatures, heat fluxes, fission rates, and fission densities at specific locations on a fuel plate. This model can also predict other parameters and more information on this modeling effort can be found in (53).

In addition to the PLATE code, Rest has developed a model to help predict intergranular and intragranular bubbles in a fuel (3). This model will be used to model the intragranular bubbles seen in this study. More information about this model will be provided in Chapter 5.

2.3.11: Heavy Ion Irradiations of RERTR Fuels

Due to the difficulty of performing microstructure analysis on highly radioactive materials, several heavy ion irradiations have been conducted to support neutron irradiated samples. Heavy ion irradiations are useful because they can be used to simulate fission product damage in the material. Heavy ion irradiations provided fast, cheap, and minimally radioactive samples compared to neutron irradiated samples that can be quickly analyzed when compared to neutron irradiations. The main drawback to heavy ion irradiations is the penetration depth of the heavy ions. Depending on the energy and ion type, the heavy ions typically only penetrate a few μms.

The primary heavy ion irradiations on U-Xwt%Mo fuel have been conducted in Germany. The German group chose I^{127} at 80 and 120 MeV for irradiations (56), (57) (58), (59). This ion and energy level were chosen since together they resemble a typical fission product. The energies correspond to those typically seen in the fission products in a nuclear reaction (7).

Wieschalla, et al. (56) performed iodine irradiations on U-6wt%Mo/Al and U-10wt%Mo/Al dispersion fuels to a fluence of $1x10^{17}$ ions/cm^2 at 200°C. This experiment was conducted to mimic the in-pile fuel behavior seen in this fuel. The FMI layer created resembled the typical FMI layer seen in neutron irradiated fuel. EDX and XRD confirmed that the FMI layer formed was composed of roughly the same phases that occur in fuel. This experiment showed that heavy ion irradiations could be used as a method to study the radiation response of fuel.

Palancher, et al. (57) conducted I^{127} 80MeV bombardments at 170°C up to a fluence of $2.0x10^{17}$ on four U-Xwt%Mo compositions. The four compositions were (U-7wt%Mo/Al), (U-7wt%Mo/Al-Si), (U-10wt%Mo/Al), and (U-10wt%Mo/Al-Si). The focus of the Palancher study is the FMI layer. Irradiations showed Al matrix with Si added showed little to no FMI layer growth during the irradiations. The pure Al based matrices showed a substantial FMI layer growth during the irradiation. EDX on the samples showed that in the (U-7wt%Mo/Al-Si) sample, an FMI layer did form non-

uniformly around the U-7wt%Mo fuel kernel. XRD data confirmed that a $U(Al,Si)_3$ FMI layer phase was formed in the pure Al matrix based samples.

Listed below are the key questions/unknowns that this study was completed for:

1: How does the Si added to the matrix affect the FMI layers' microstructure, i.e. bubble growth and sizes, FMI layer growth, and chemical composition?

2: How does the amorphous rim region form, what is its chemical composition, and what is its irradiation microstructure?

3: How does the bubble superlattice form in the crystal fuel region?

Table 2.1: Swelling rate of UO_2 from solid fission products using partial volumes (13)

Fission-Product Group	Yi	vi/vU	Yi vi/vU
Nb+Soluable Zr	0.149		
Y+ rare Earths	0.534		
Total Soluble Fission Products	0.683	1	0.683
Mo	0.24		
Ru+Tc+Rh+Pd	0.263		
Total Metallic Inclusions	0.503	0.36	0.181
Ba+Sr (as Zirconates)	0.149	1.74	0.258
Cs+Rb+I+Te	0.238	0.76	0.181
Other Fission Products	0.027	0.76	0.021
		Total	1.324

Table 2.2: Variables that can affect fission gas behavior (13)

Variables that affect fission-gas behavior
Temperature
Temperature Gradient
Matrix Stress
Matrix Stress Gradient
Fission Rate
Irradiation Time or Burnup
Fuel Properties
Vapor Pressure
Surface Tension
Creep Strength
Coefficients of thermal surface and bulk diffusion
Fission Gas Properties
Nuclear Yield
Equation of State
Diffusion Coefficient in the Solid Fuel
Diffusion Coefficient of the Gaseous Fuel
Fuel Microstructure
Dislocation Density
Grain Size
Restructuring
Crack Pattern

Table 2.3: Overview of RERTR and International Experiments

Campaign	Fuel Type	Si Content Matrix-Range	Basis of Test Dispersion	Maximum Burnup	Observations
RERTR-1	U,Mo and U,Nb,Zr	-	Test Different Mo Content in Fuel	40	U,Mo Fuel Stable and U,Nb,Zr Unstable
RERTR-2	U,Mo and U,Nb,Zr	-	Test Different Mo Content in Fuel	70	U,Mo Fuel Stable and U,Nb,Zr Unstable
RERTR-3	U,Mo	-	High Operating Temps	40	Stable Response
RERTR-4	U,Mo	-	High Burnups	80	Porosity at high burnups
RERTR-5	U,Mo	-	High Burnups	50	Extreme FMI Layers
RERTR-6	U,Mo	0.2-5wt%	Test Varying Si Contents	50	Si suppresses FMI growth
RERTR-7A	U,Mo	0.2-5wt%	Very High Burnups	100	Porosity buildup at 80% BU
RERTR-7B	U,Mo	-	Test Ti and Zr Additives in Matrix	30	Porosity at high burnups
RERTR-8	U,Mo,X Modified	2-5 wt%	Test Ti and Zr Additives in Fuel	75	Porosity at high burnups
RERTR-9A	U,Mo	2-5 wt%	Full Fuel Loadings	30	NA
RERTR-9B	U,Mo	2-5 wt%	Full Fuel Loadings	30	NA
RERTR-10	U,Mo	2-5 wt%	Aggressive Power Conditions	50	NA
AFIP-1	U,Mo	2-5 wt%	Test Full Sized Plates	NA	NA
AFIB-2	U,Mo	Under Design	Test Full Sized Plates	NA	NA
AFIB-3	U,Mo	Under Design	Varying Plate Geometries	NA	NA
AFIB-4	U,Mo	Under Design	Varying Plate Geometries	NA	NA
ELEMENT-1	U,Mo	Under Design	Full Fuel Loadings	NA	NA
ELEMENT-2	U,Mo	Under Design	Full Fuel Loadings	NA	NA
ELEMENT-3	U,Mo	Under Design	Full Fuel Loadings	NA	NA
KOMO-1	U,Mo	-	Pin Type Fuels	13	Unstable Response
KOMO-2	U,Mo	-	Pin Type Fuels	71	Unstable Response
KOMO-3	U,Mo	0-2wt%	Pin Type Fuels	65	Stable Response
ISIS-1	U,Mo	-	Test Full Sized Plates	80	Unstable Response
ISIS-2	U,Mo	-	Test Full Sized Plates	58	Unstable Response
ISIS-3	U,Mo	0.3-2.1 wt%	Test Full Sized Plates-Si Modified	50	Stable Response

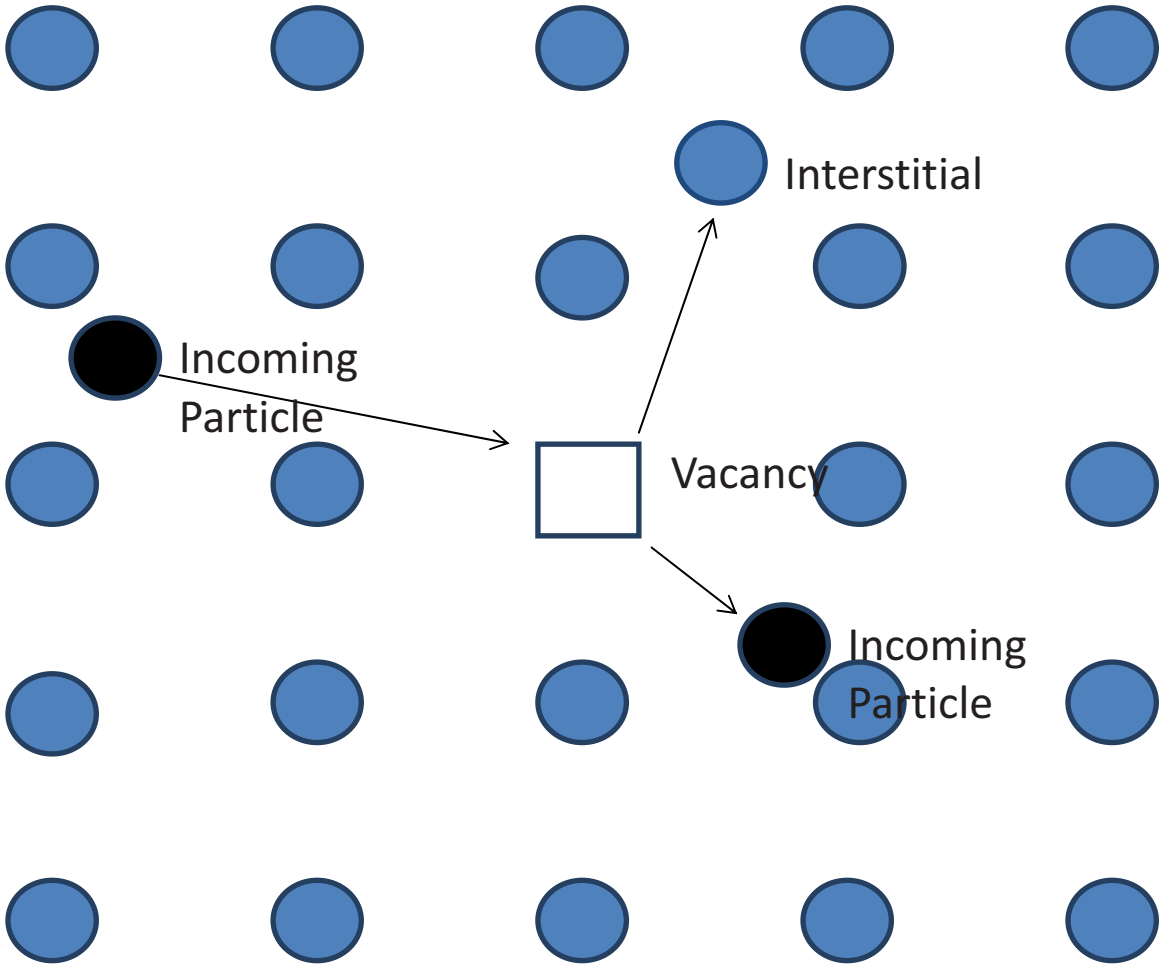

Figure 2.1: A simple diagram showing an incoming particle striking a lattice atom and displacing it from its lattice location.

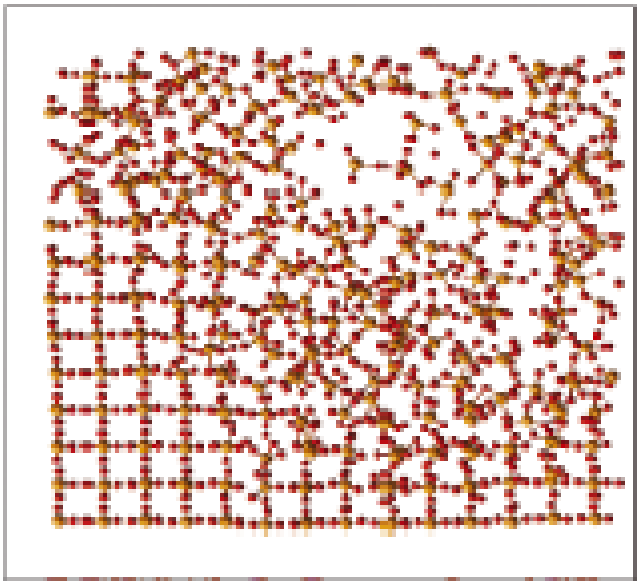

Figure 2.2: Simulation of what a damage cascade might look like (6)

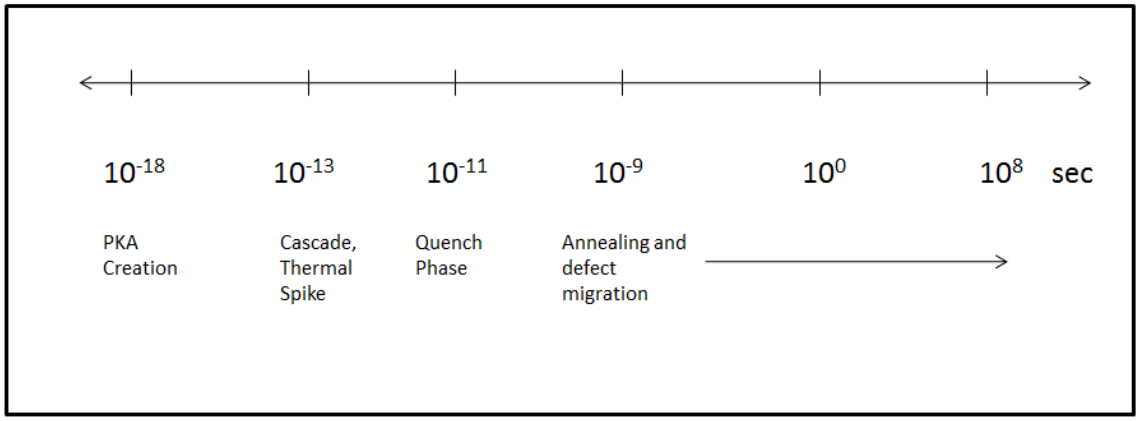

Figure 2.3: Time scale of a damage cascade (4)

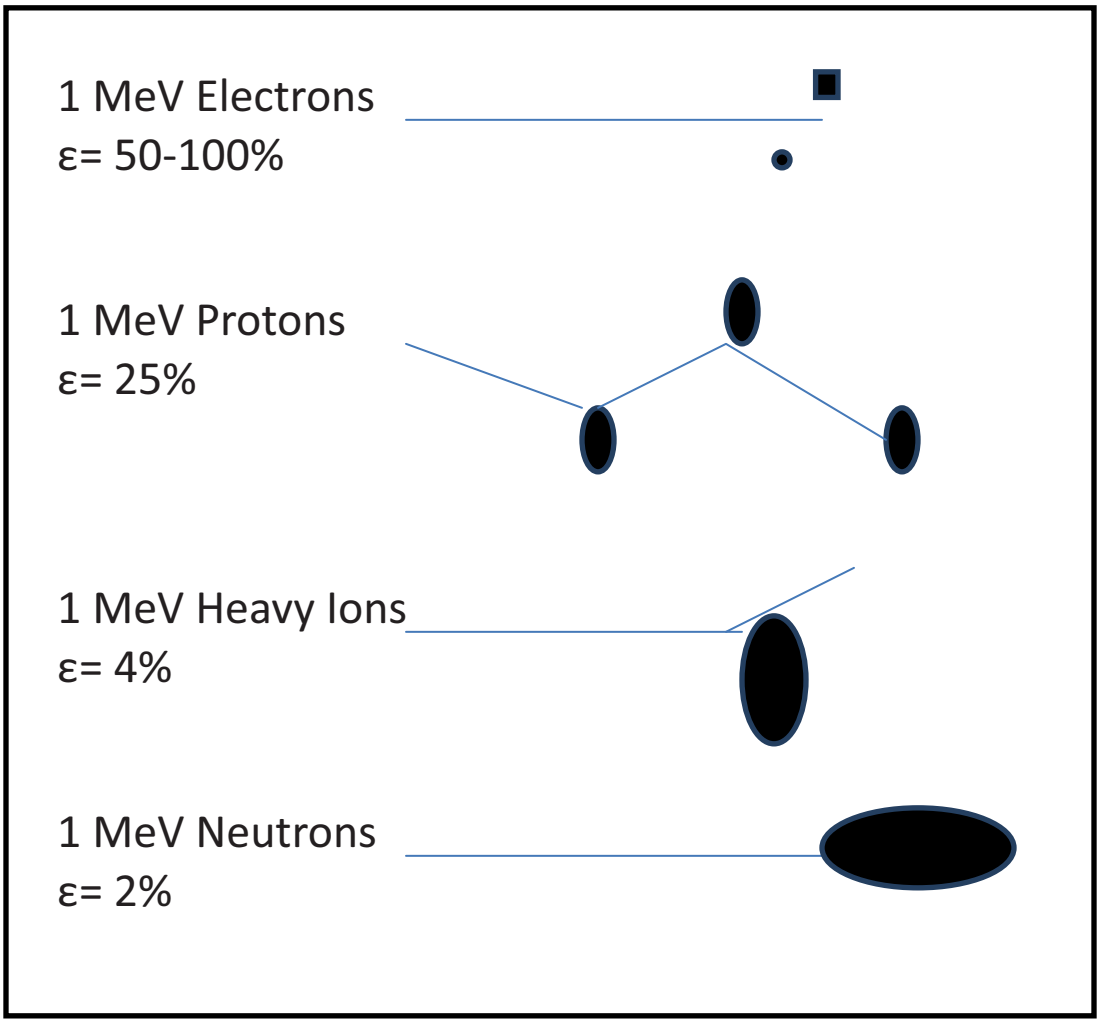

Figure 2.4: Damage cascades vs. ion type with their displacement efficiency (4)

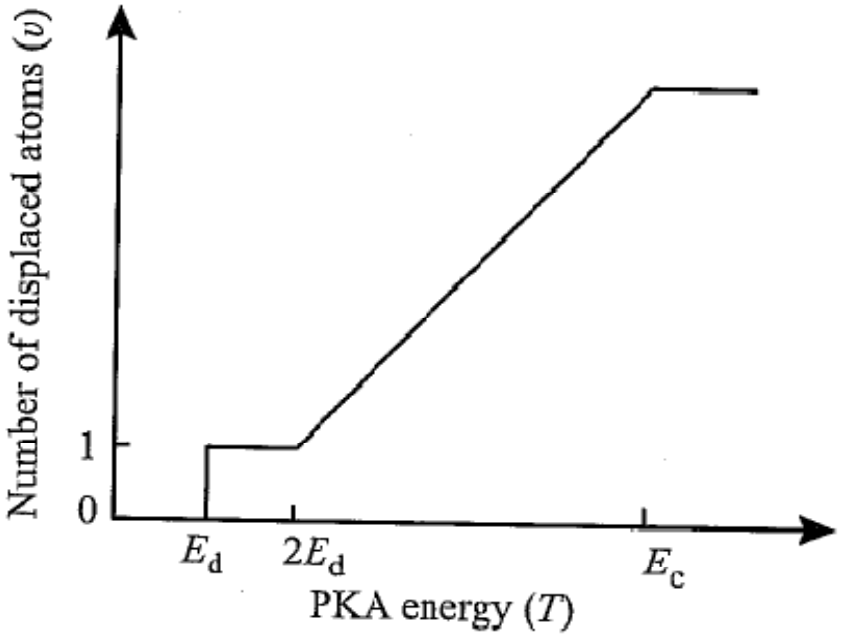

Figure 2.5: Simple K-P model (4)

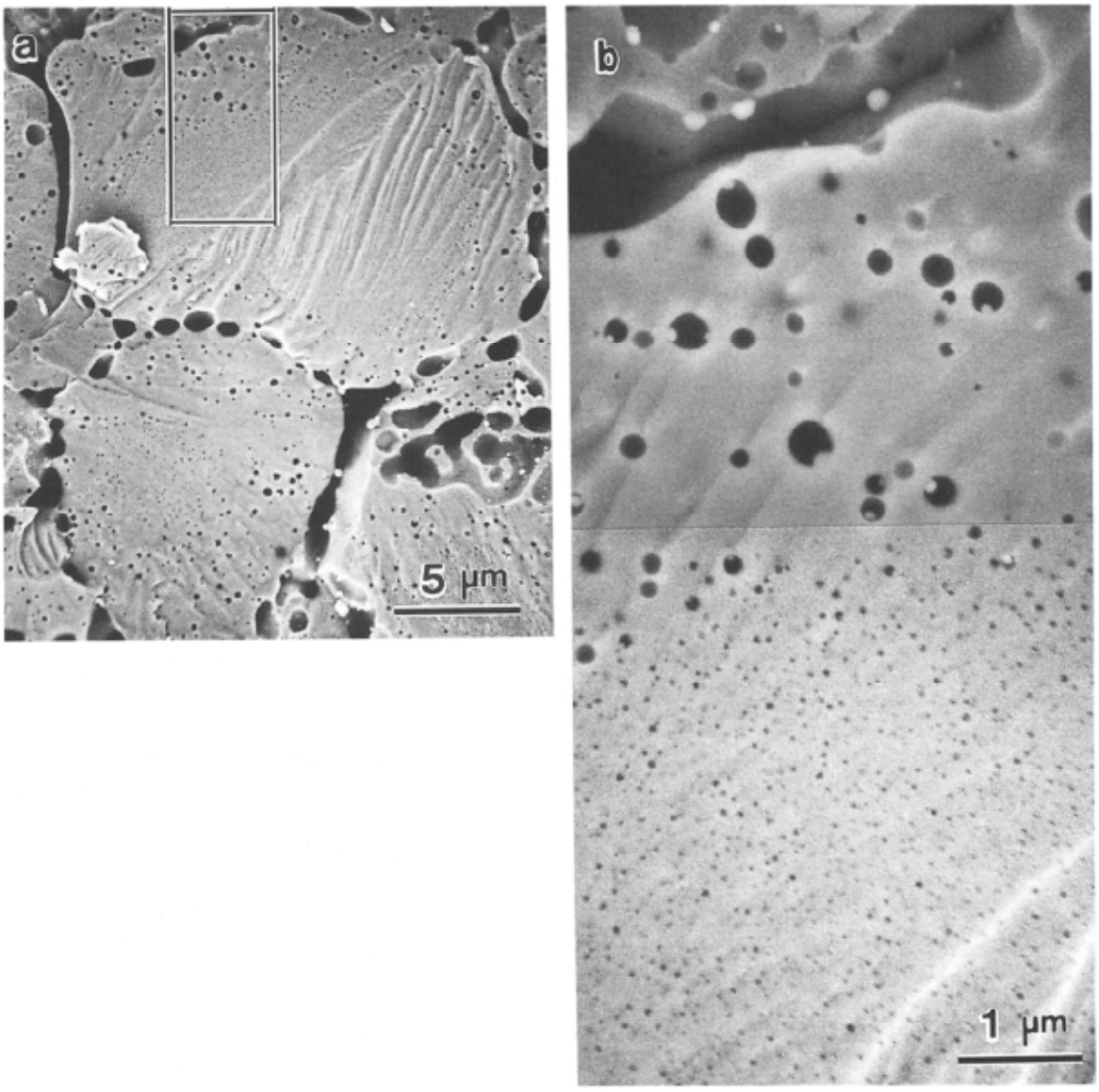

Figure 2.6: SEM micrographs of UO_2 showing an overview of bubble growth in various locations (17)

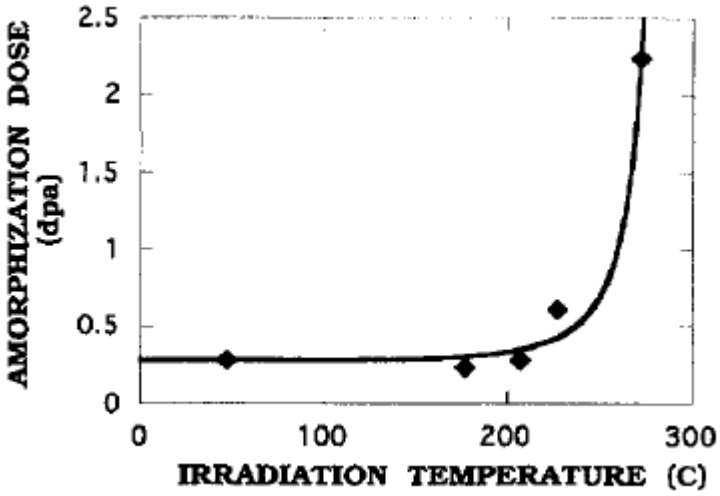

Figure 2.7: Amorphization curve for U_3Si (18)

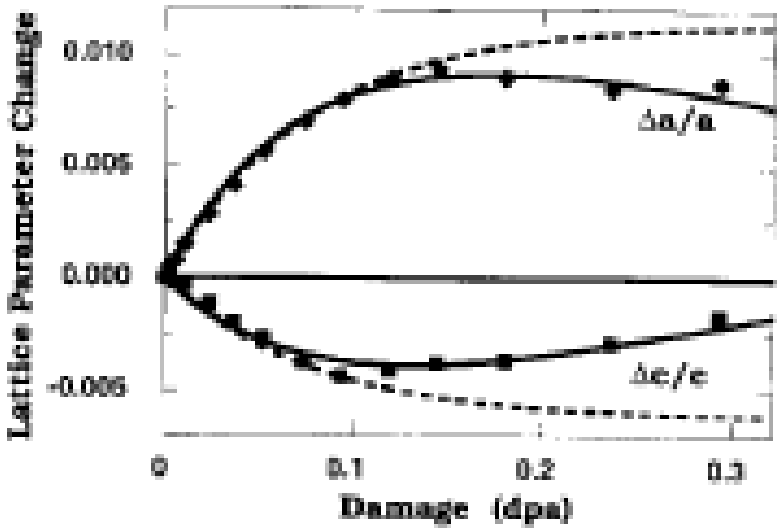

a)

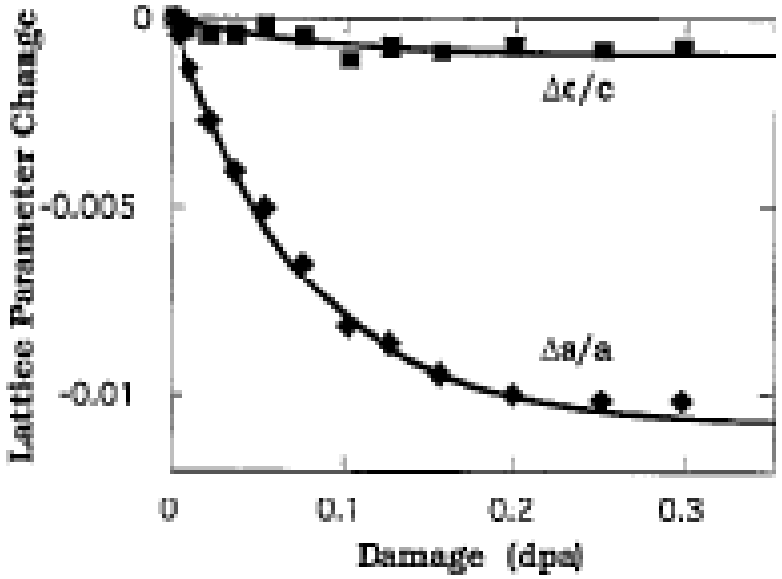

b)

Figure 2.8: Changes in lattice parameter for U_3Si and U_3Si_2 with increasing dose. Note the structures of U_3Si_2 and U_3Si are tetragonal and the a and c directions are the lattice parameters in specific directions (20), (18).

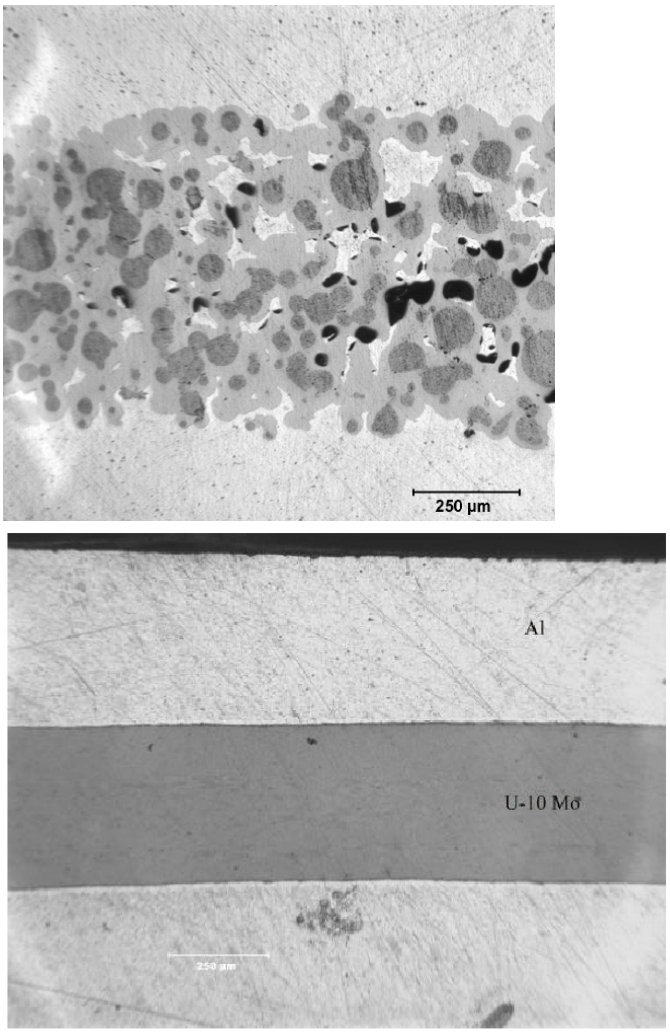

Figure 2.9: Micrographs showing irradiated U-6wt%Mo/Al dispersion fuel and U-10wt%Mo monolithic fuel. The medium gray phase in the dispersion fuel is the FMI layer. The dark phase is the U-6wt%Mo fuel kernels in the Al matrix. (22)

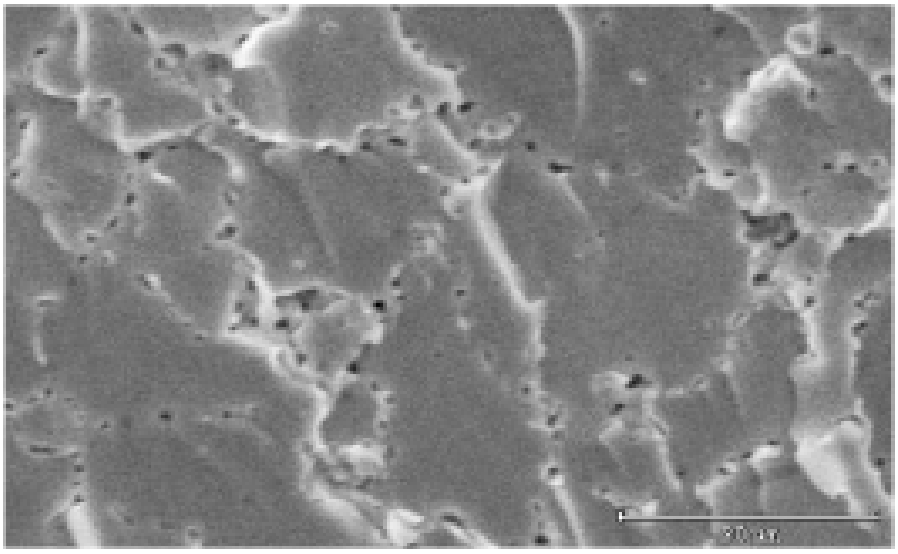

Figure 2.10: Fission gas bubbles decorating the grain boundaries of the U,Mo fuel kernels (24)

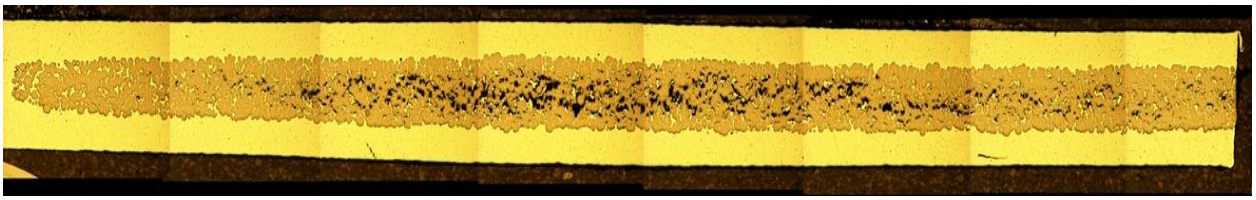

Figure 2.11: Porosity build-up between the fuel and the FMI layer (22)

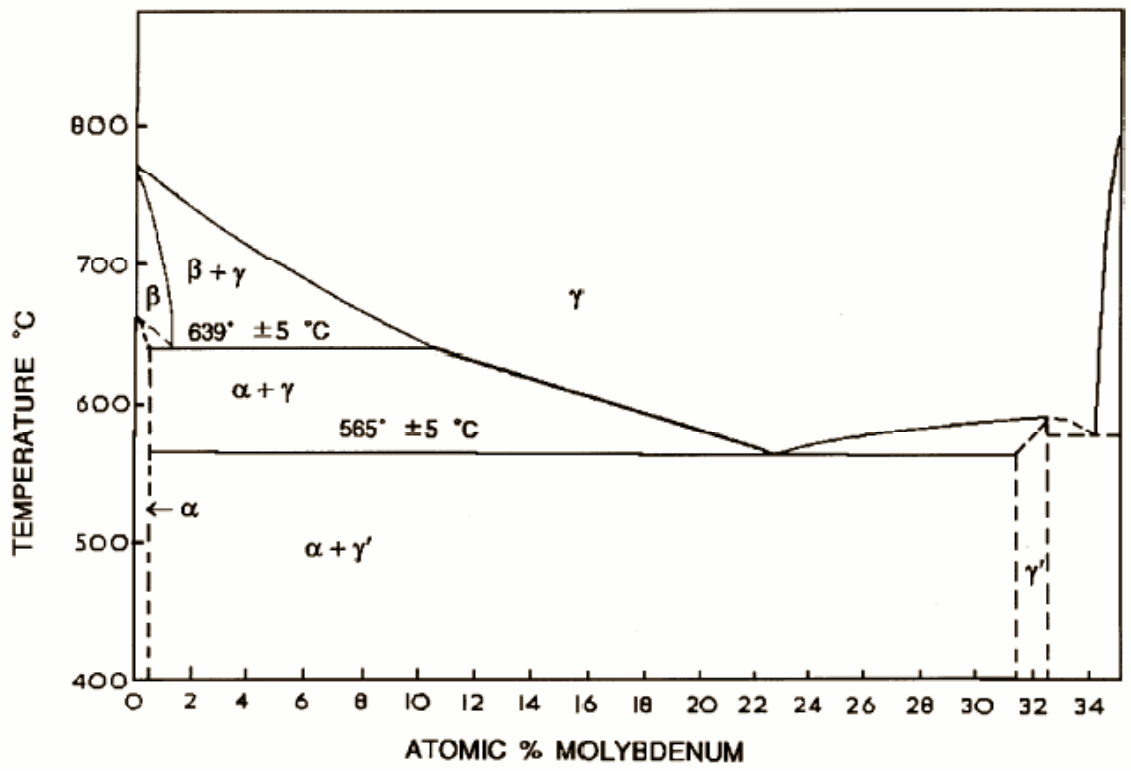

Figure 2.12: U-Mo phase diagram (28)

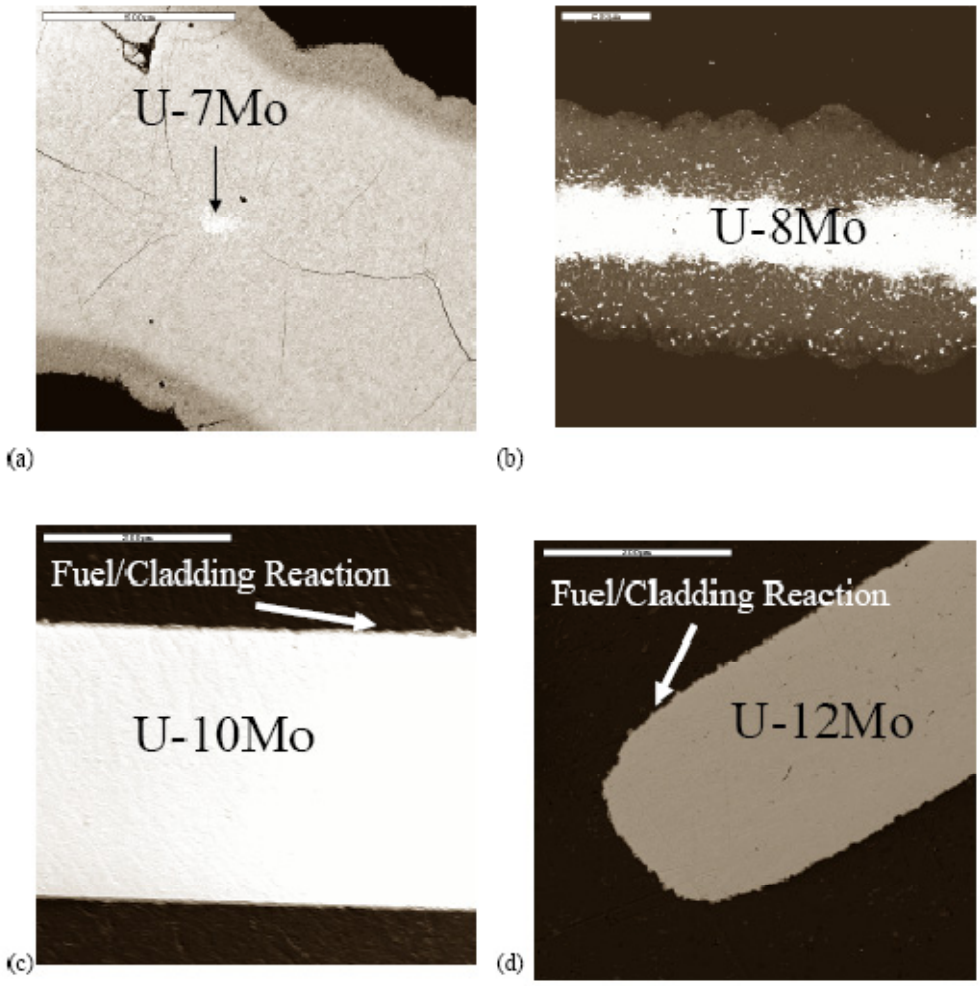

Figure 2.13: Optical microscopy images of various Mo loaded monolithic fuel plates showing the effect of Mo content on the FMI layer growth rate. (35)

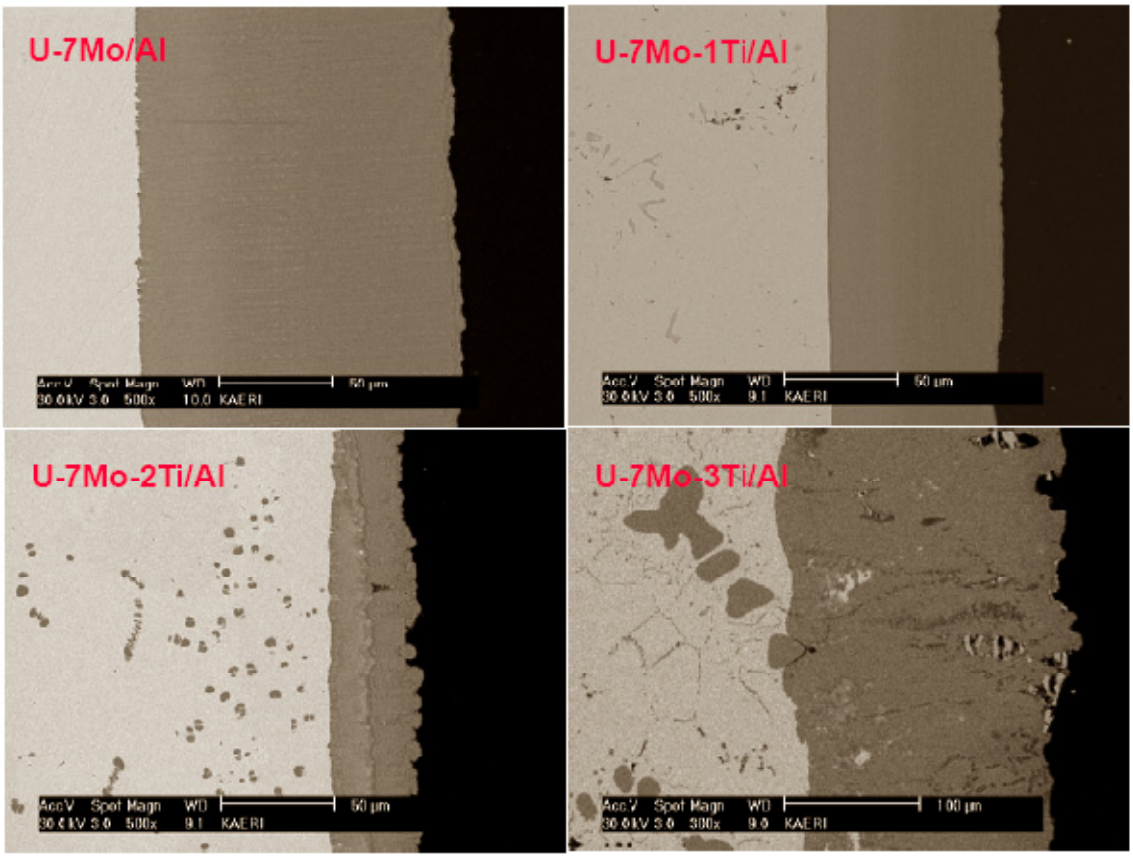

Figure 2.14: Precipitate growth with increasing Ti content (38)

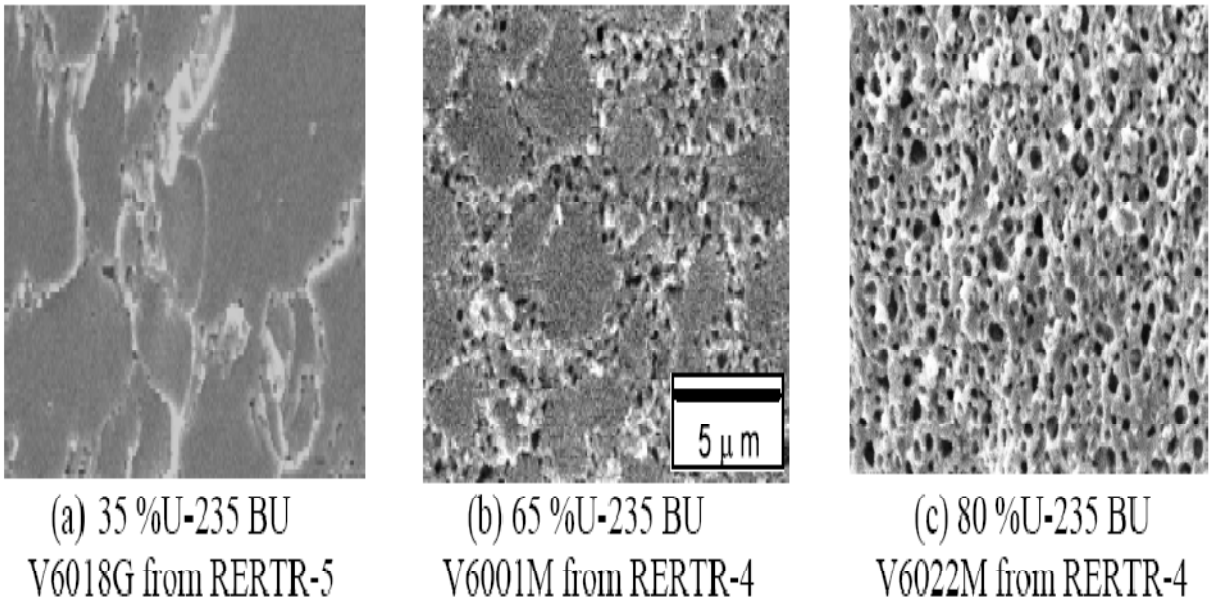

Figure 2.15: Micrographs showing how the intergranular bubble density varies with increasing burnups (39)

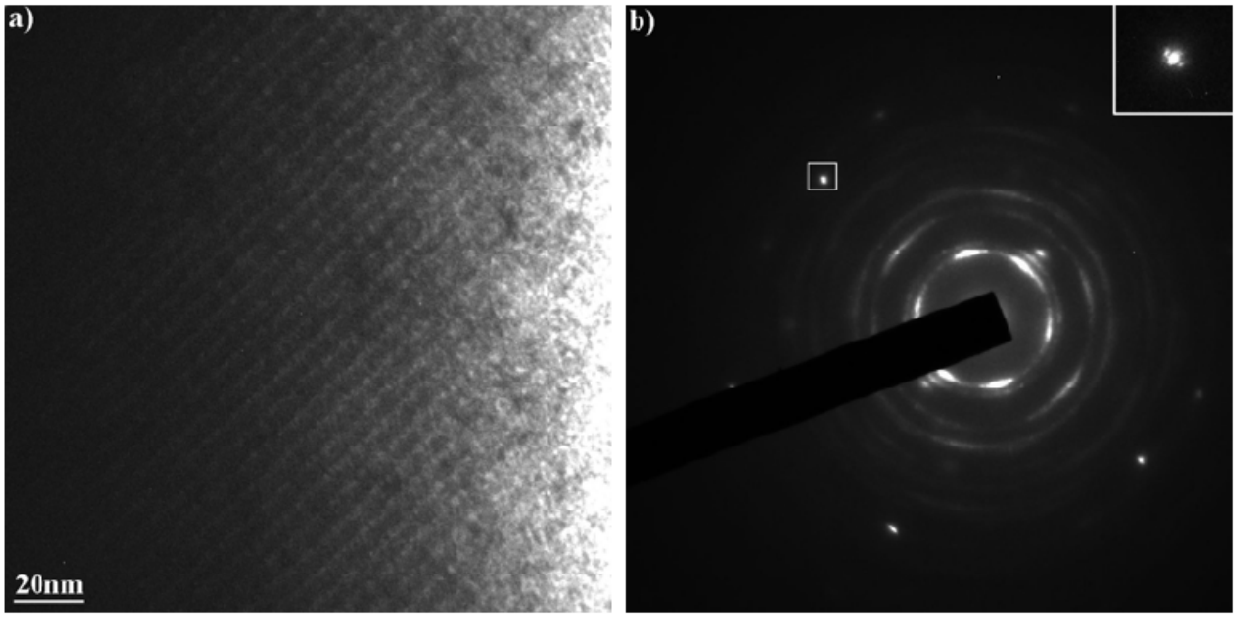

Figure 2.16: TEM image of super-ordered bubble lattice and its corresponding coherent electron diffraction (1)

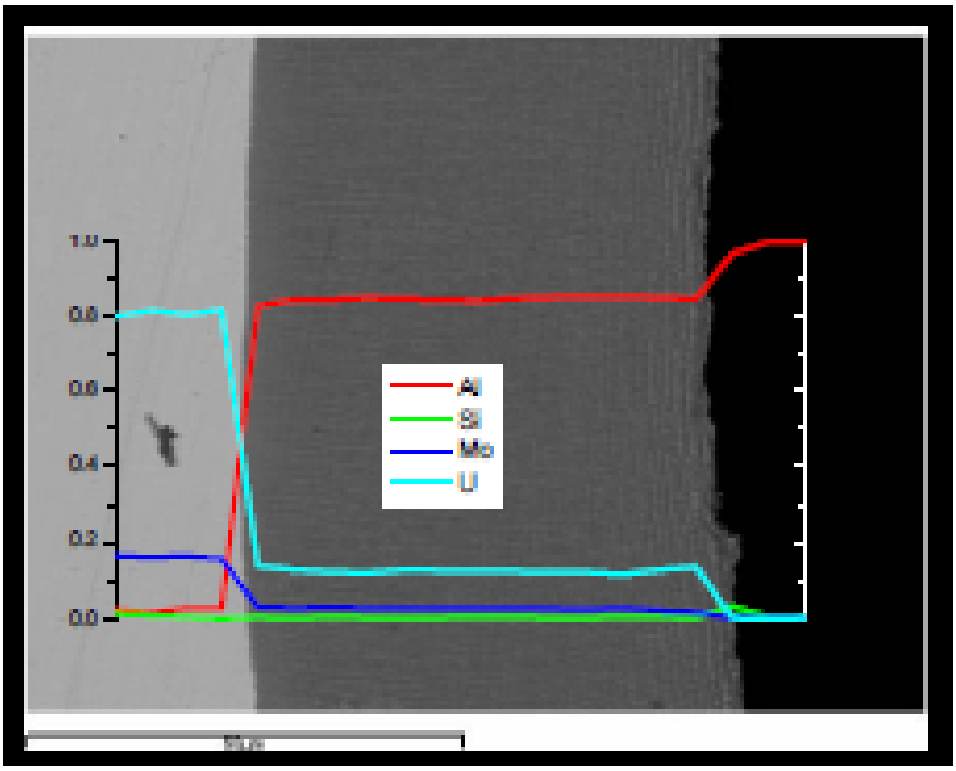

Figure 2.17: Typical diffusion couple of U-7wt%Mo vs Al-0.2wt%Si dispersion fuel after a temperature treatment of 580˚C for 2 hrs. (36)

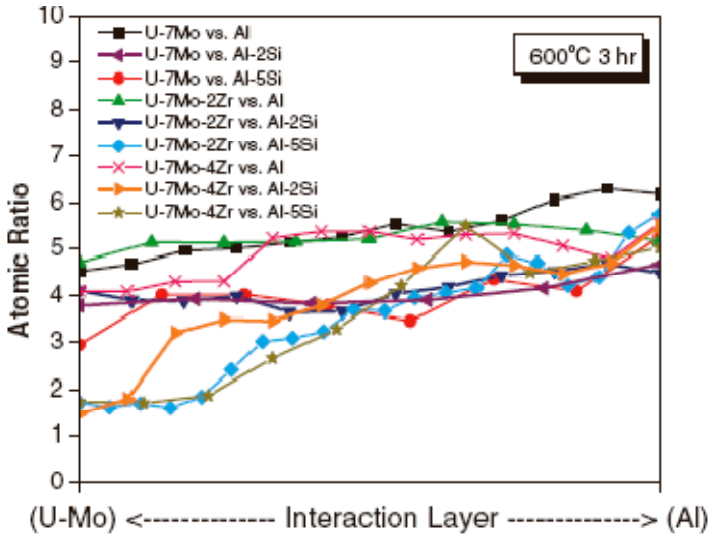

Figure 2.18: Example of how the atomic ratio varies across the FMI layer. Note that the atomic ration, x, is placed into UAl_x to help determine what phase the specific area would be in if it was crystalline. (43)

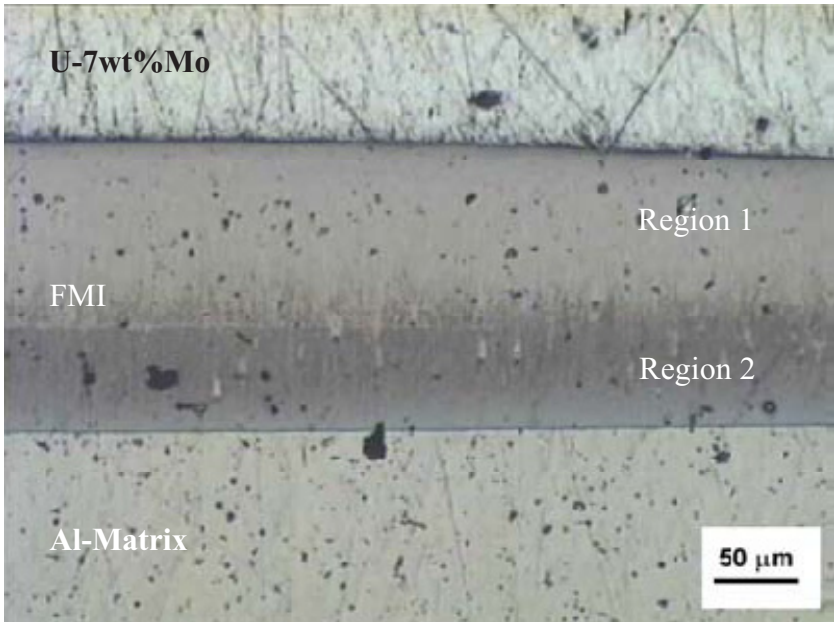

Figure 2.19: U-7wt%Mo/Al Matrix diffusion couple at 580°C for 2 hours (31)

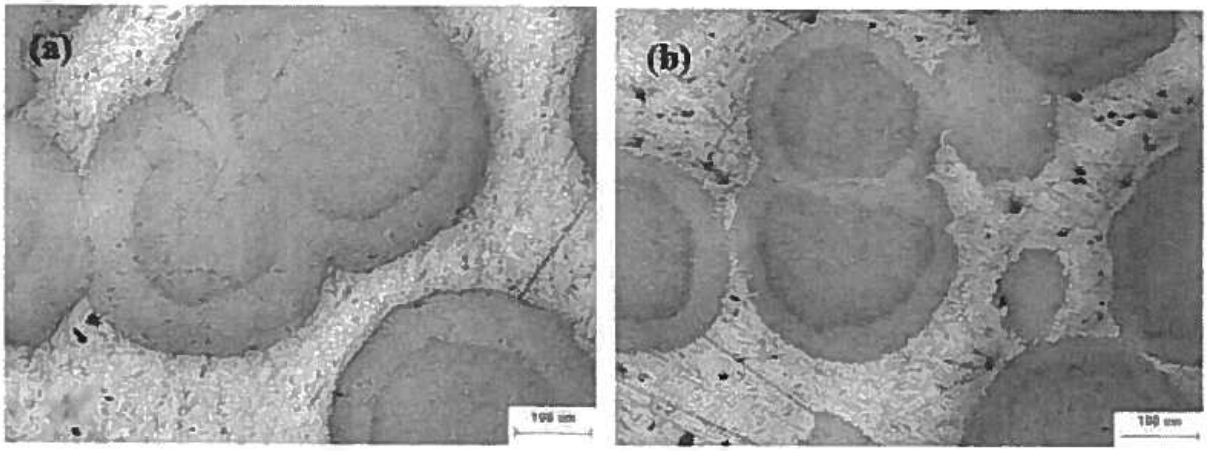

	BU(%)	Fuel Meat Location	Composition of observed IL phases (at.%)	Phase Type
U-7Mo/Al (557-MD1)	63.2	center	$U_{19}Mo_3Al_{78}$	$(U,Mo)Al_3$
	44.7	periphery	$U_{15}Mo_2Al_{83}$	$(U,Mo)Al_4$
U-7Mo/Al-2Si (557-HS1)	64.8	Center	$U_{21}Mo_3Al_{76}$	$(U,Mo)Al_3$
			$U_{21}Mo_3Al_{65}Si_{11}$ (at Si max.)	$(U,Mo)(Al,Si)_3$
	47.3	periphery	$U_{15}Mo_3Al_{82}$	$(U,Mo)Al_4$
			$U_{12}Mo_2Al_{82}Si_4$ (at Si max.)	$(U,Mo)(Al,Si)_{4+}$

Figure 2.20: Optical Microscopy of Fuel Kernels from KOMO-3 to burnups of ~64% showing the FMI layer thickness. a) U-7wt%Mo/Al and b) U-7wt%Mo/Al-2Si. Table contains the EDS compositions at various locations on the fuel plate with the phase type present in the location (25)

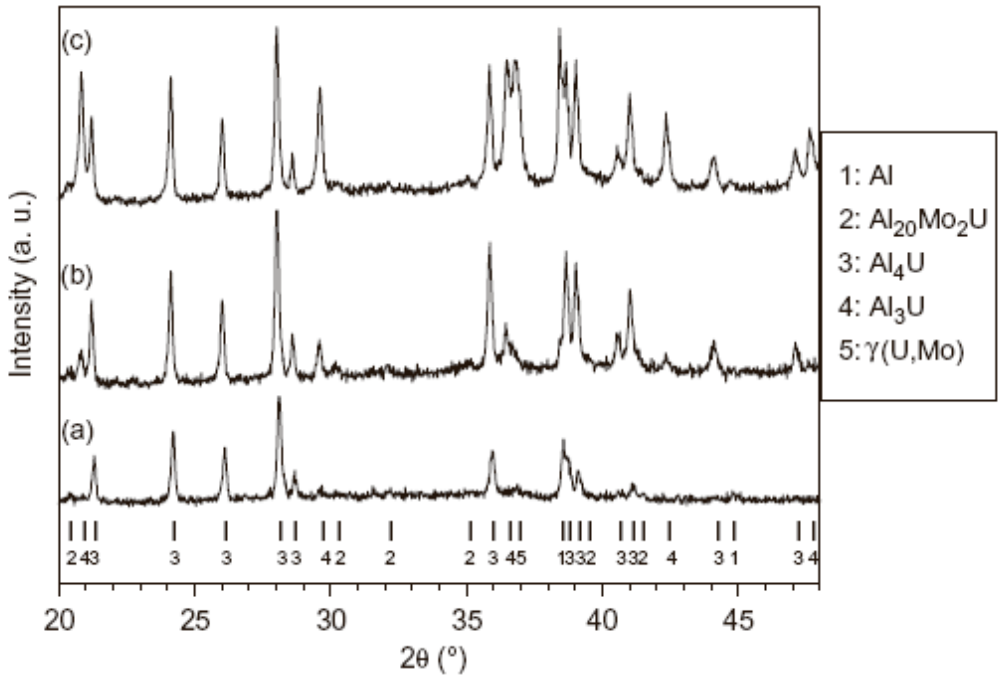

Figure 2.21: XRD Pattern of U-7wt%Mo after 2 hr. Heat Treatment at 580°C. (a) XRD conducted near the Al side of the FMI layer, (b) XRD conducted around middle of layer, and (c) XRD conducted near the U-Mo interface (31)

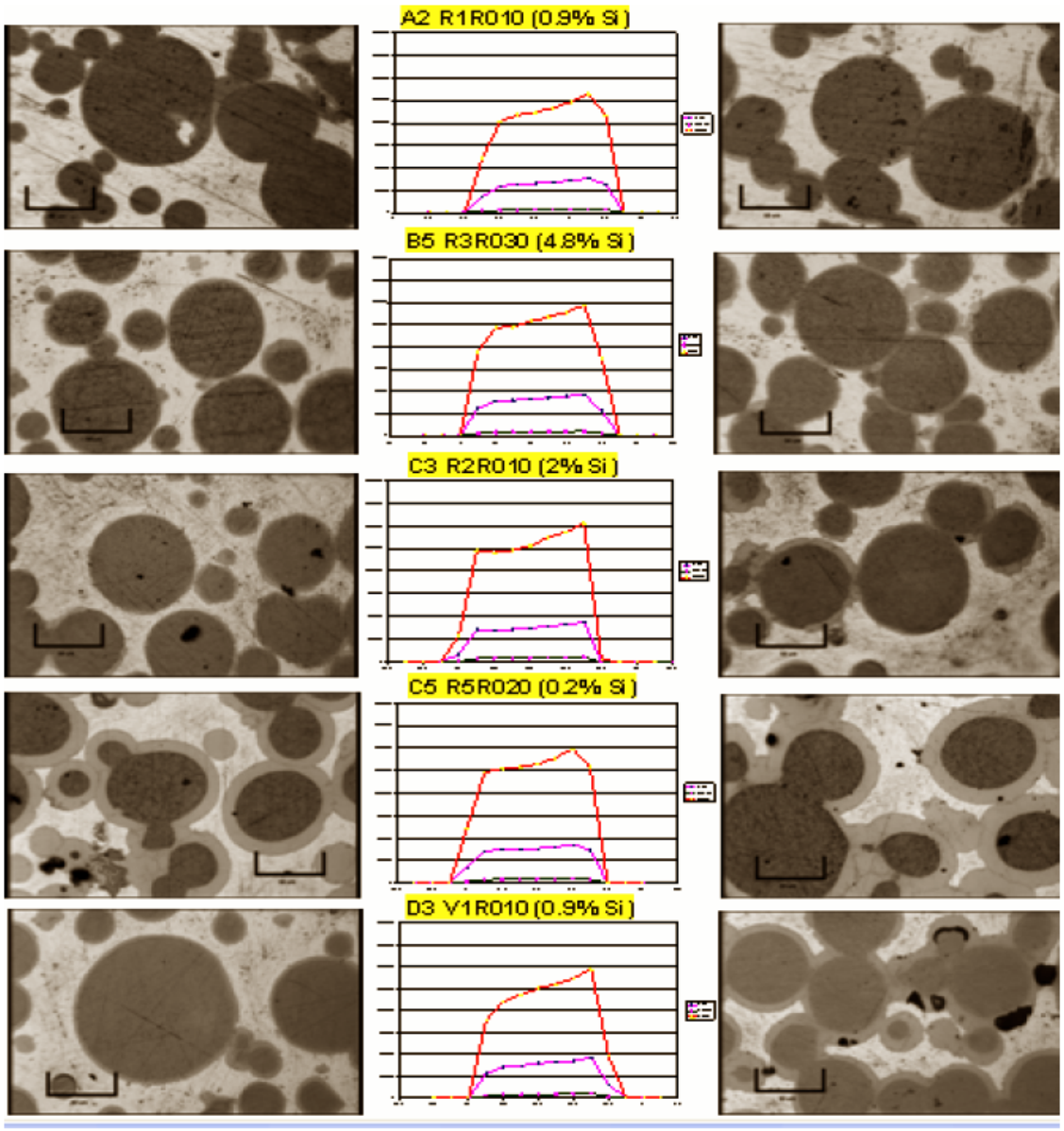

Figure 2.22: FMI layer growth with various Si content. Left side images are from the low flux side of the plates. Right side images are from the high flux side. The middle column contains the RERTR plate the OM images were obtained from, its Si content, and its gamma activity spectrum for burnup calculations (51).

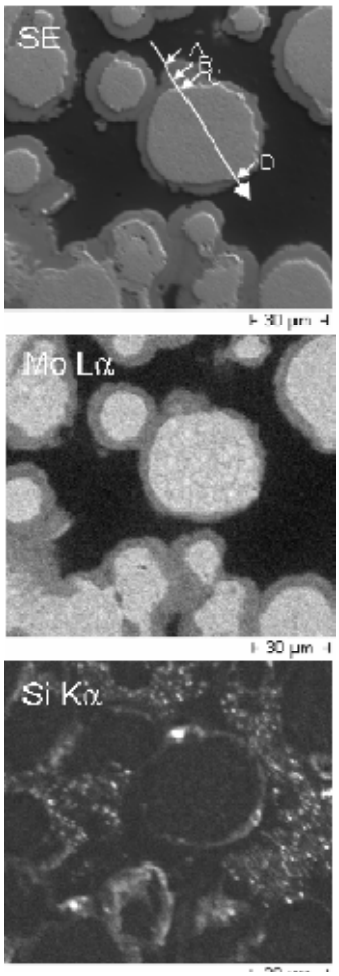

Figure 2.23: Secondary image SEM image and its accompanying Mo and Si x-ray map (60)

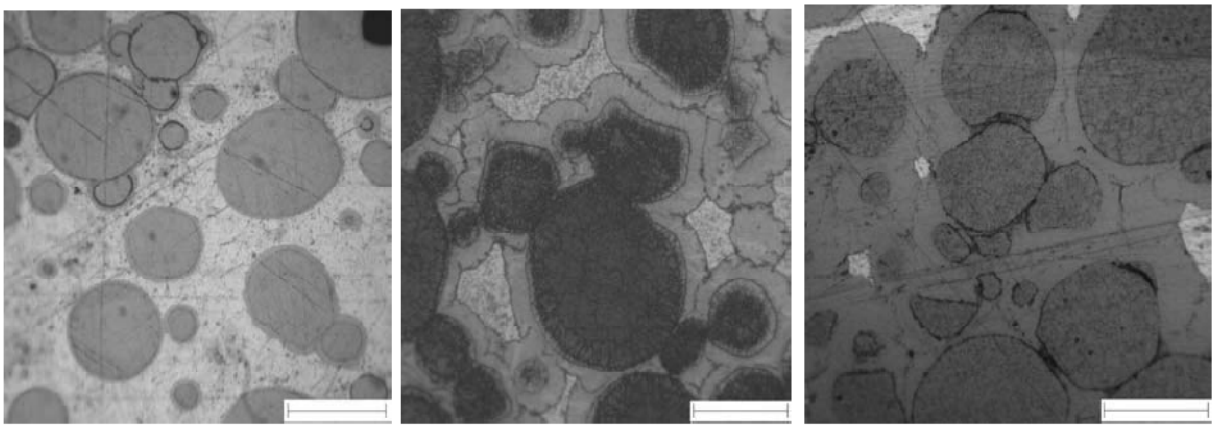

Figure 2.24: Irradiated U-10wt%Mo/Al dispersion fuel at an irradiation temperature of a) 145°C, b) 200°C, and c) 215°C (scale bar=100 μm) (53)

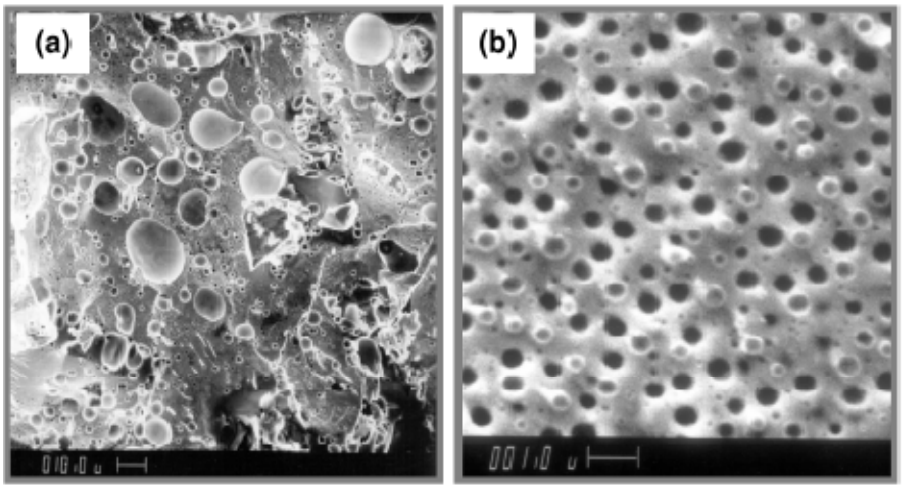

Figure 2.25: Bubble formation in amorphous (a) U_3Si and (b) U_3Si_2 (2)

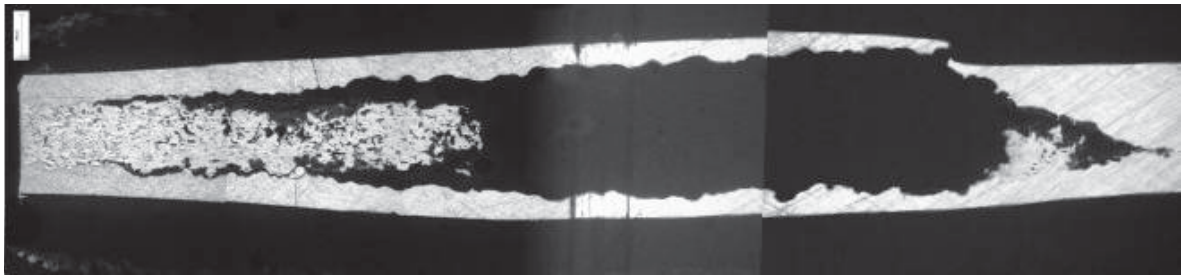

Figure 2.26: Breached fuel plate from RERTR-5 (22)

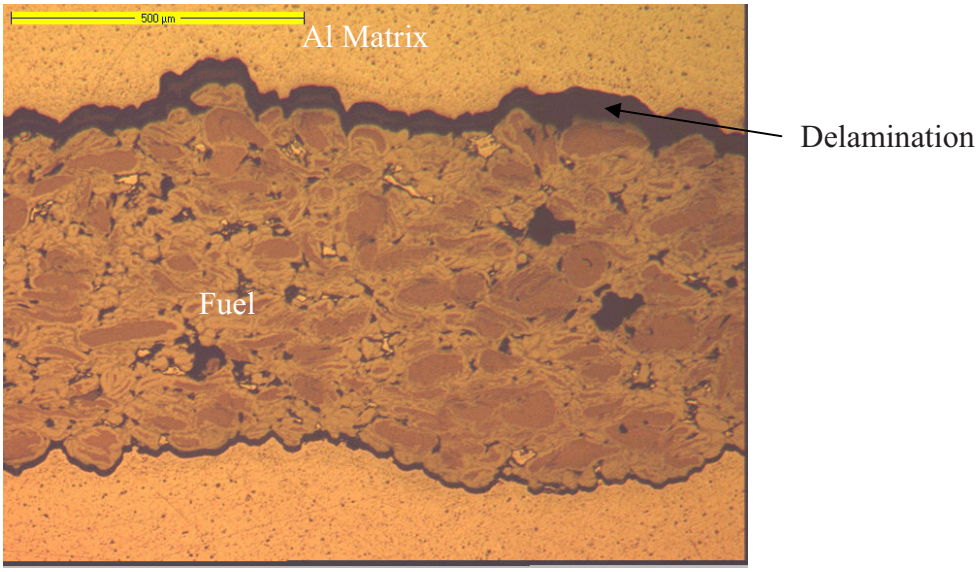

Figure 2.27: Delamination of the fuel region from the matrix from the UMUS experiment (22)

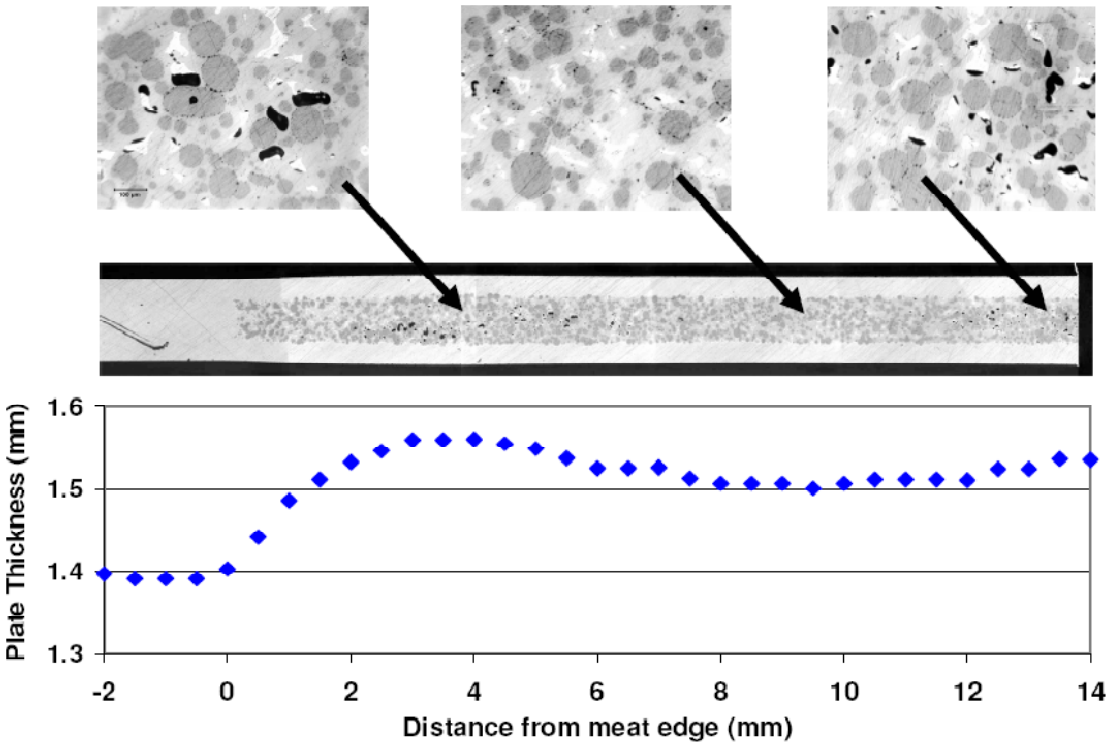

Figure 2.28: Optical microscopy images of a fuel plate from RERTR-4 showing the effect of burnup on the microstructure across a fuel plate. Included is the plate thickness across the plate showing the effect of burnup on the swelling in the plate. (19)

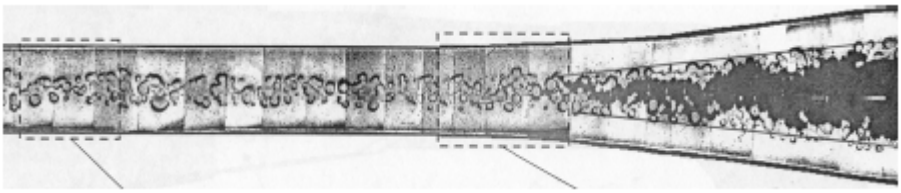

Figure 2.29: Pillowing in a fuel plate from the FUTURE experiment (22)

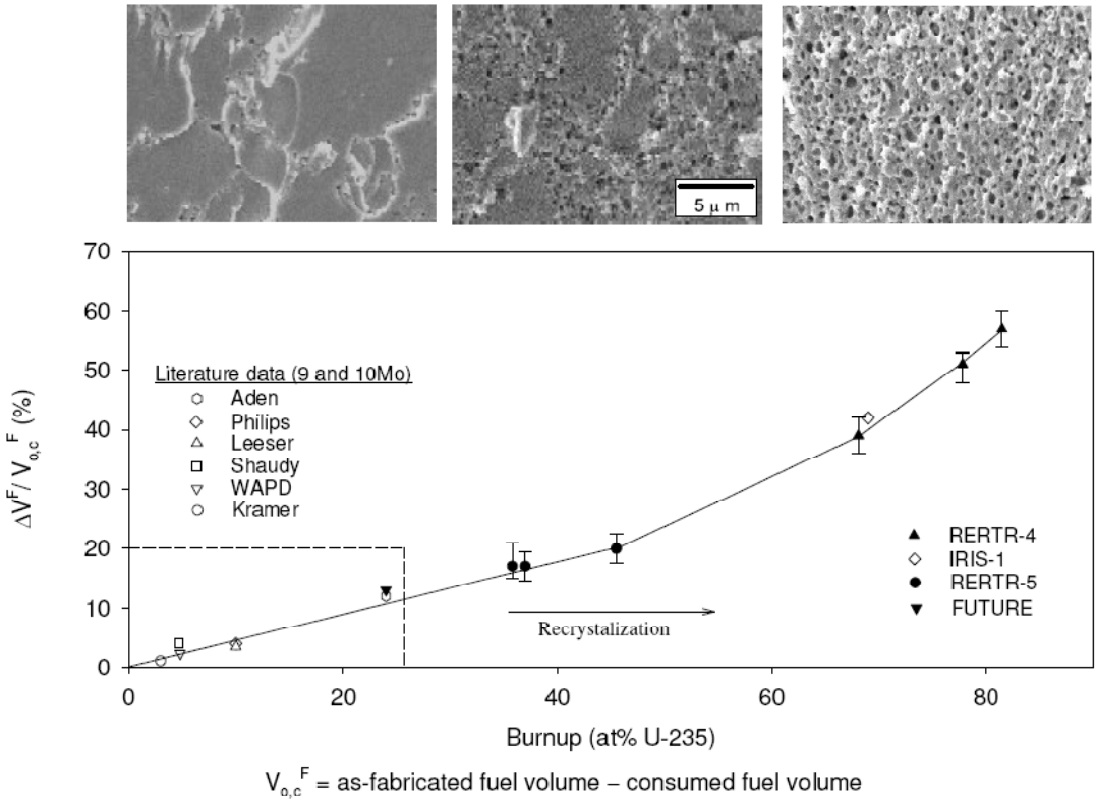

Figure 2.30: Swelling behavior of U-10wt%Mo/Al dispersion fuels vs. burnup (19)

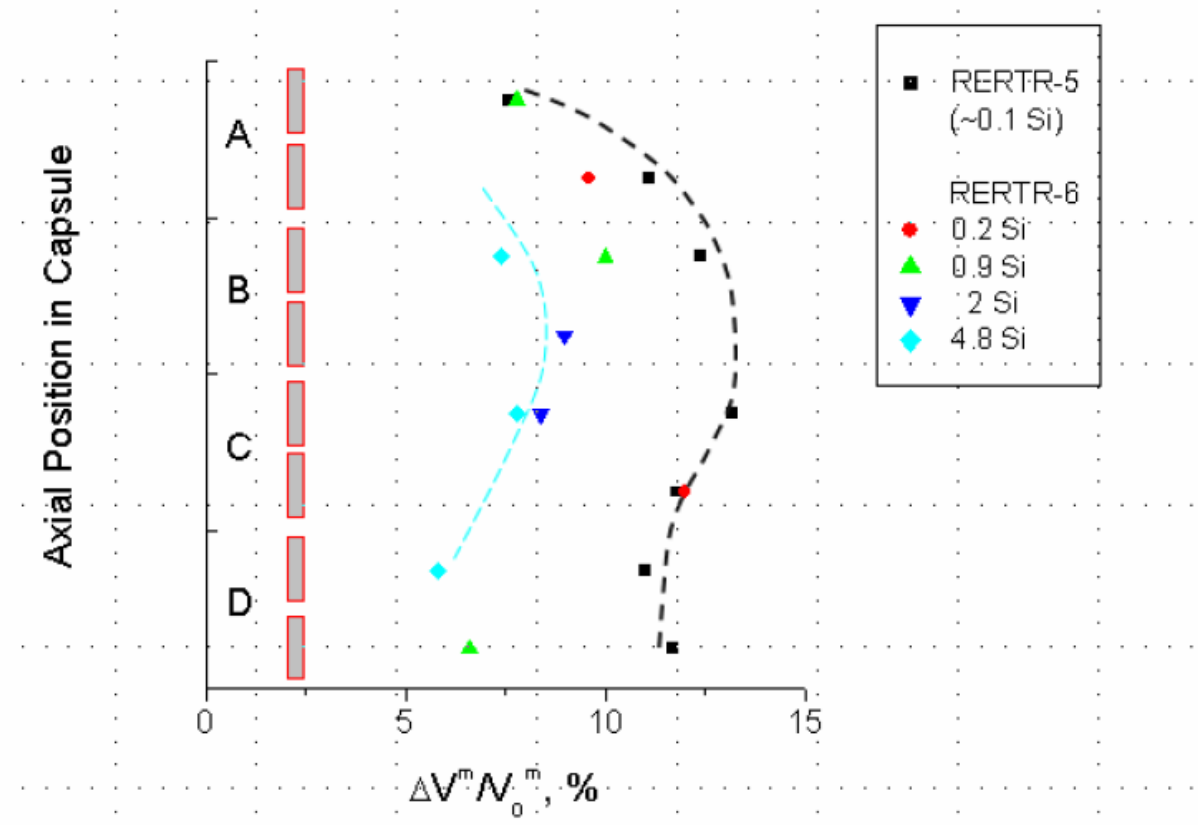

Figure 2.31: The effect of Si content in the matrix vs. swelling from RERTR-5 and -6 (51)

Chapter 3 : Experimental Procedure

The experimental procedure was chosen to gain a better understanding of the microstructure of U-Xwt%Mo dispersion fuels after fabrication and during irradiation. Experiments were chosen to support the three main questions/unknowns of this study:

- How does the Si content in the FMI layer affect the growth rate of the FMI layer, how does it affect the FMI's microstructure which goes amorphous, and how does it suppress the bubble growth in the FMI layer?
- Why does the rim between the FMI layer and the crystalline fuel region go amorphous, how is its microstructure affected by irradiation, and how the amorphous rim region differs from the amorphous FMI layer?
- How does the bubble superlattice form in the crystalline fuel region?

Table 3.1: List of the experiments and the unknown that it supports

Experiment	Supports
TEM studies of Al-2wt%Si powder	Si Modified FMI Layer
TEM DU Alloys-Unirradiated	Si Modified FMI Layer
TEM DU Alloys-Proton Irradiated	Si Modified FMI Layer
TEM DU Alloys-Kr Irradiated	Si Modified FMI Layer
TEM DU-7wt% Foils-Unirradiated	Bubble Superlattice
TEM DU-7wt% Foils-Xe Irradiated	Bubble Superlattice
TEM RERTR-9A and -9B	Si Modified FMI Layer
OM, SEM, TEM RERTR-6	Si Modified FMI Layer, Amorphous Rim, Bubble Superlattice
OM, SEM, TEM RERTR-7 L.Flux	Si Modified FMI Layer, Amorphous Rim, Bubble

	Superlattice
OM, SEM, TEM RERTR-7 H. Flux	Si Modified FMI Layer, Amorphous Rim, Bubble Superlattice

Table 3.2 shows a list of the experiments conducted in this study and how they support the three main questions listed above.

The experimental procedure is described in the following sections: 1) Fabrication of the fuels, 2) Irradiation parameters of the experiments, 3) Sample Preparation for TEM Analysis, and 4) TEM techniques for microstructural analysis.

3.1: Fabrication of Materials

Prior to this study, it was known that irradiated dispersion fuels were composed of three primary regions of interest: the Al-modified matrix, the FMI layer region, and the crystalline fuel region, as seen in Figure 1.1. In this work, reactor irradiated U-7wt%Mo/Al-2wt%Si dispersion fuels from the RERTR-6, RERTR-7 Low Flux, and RERTR-7 High Flux were used to study all three regions of interest. Inter-metallic alloys using depleted uranium were cast to study the anticipated FMI layer phases (UAl_4, $U_6Mo_4Al_{43}$, UMo_2Al_{20}, $U(Al,Si)_3$, and $(U,Mo)(Al,Si)_3$). DU-7wt%Mo foils were created to show the effect of fabrication on the pre-irradiated microstructure of the crystalline fuel region and how the foil's microstructure changes with heavy ion irradiations. An Al-2wt%Si sample was cast to understand the pre-fabrication microstructure of the matrix prior to adding fuel kernels. The fabrication processes of these fuels are discussed below.

3.1.1: U-7wt%Mo/Al-2wt%Si Dispersion Fuels

The common method to create the U-7wt%Mo spherical fuel is to first create an ingot of U-7wt%Mo fuel. This ingot is then loaded onto a centrifuge and heated to an elevated temperature. At the elevated temperature, the ingot is spun at a high rotation and U-7wt%Mo fuel spheres are spalled off the fuel. By setting the operation temperature and rotation speed, specific sized U-7wt%Mo fuel kernels can be made. These particles are mixed Si modified Al matrix powder and compacted in a press and dye. The compact is then loaded into Al cladding plates, one of which is recessed to hold the compact. Next, the fuel plate is hot-rolled into a foil of some desired thickness to bond the fuel-matrix powder to the Al cladding. This hot rolling operation is performed at a temperature of 500˚C for about 60 min. Finally, the completed foil can be cold-rolled to a final designated foil thickness if needed.

3.1.2: Intermetallic FMI Phases

Three separate depleted uranium alloys were cast to simulate the target FMI phases that are known to form during neutron irradiations and diffusion couple experiments. Table 3.1: List of the experiments and the unknown that it supports

Experiment	Supports
TEM studies of Al-2wt%Si powder	Si Modified FMI Layer
TEM DU Alloys-Unirradiated	Si Modified FMI Layer
TEM DU Alloys-Proton Irradiated	Si Modified FMI Layer
TEM DU Alloys-Kr Irradiated	Si Modified FMI Layer
TEM DU-7wt% Foils-Unirradiated	Bubble Superlattice
TEM DU-7wt% Foils-Xe Irradiated	Bubble Superlattice
TEM RERTR-9A and -9B	Si Modified FMI Layer

OM, SEM, TEM RERTR-6	Si Modified FMI Layer, Amorphous Rim, Bubble Superlattice
OM, SEM, TEM RERTR-7 L.Flux	Si Modified FMI Layer, Amorphous Rim, Bubble Superlattice
OM, SEM, TEM RERTR-7 H. Flux	Si Modified FMI Layer, Amorphous Rim, Bubble Superlattice

Table 3.2 lists the material information for each cast alloy and the planned phases. The three alloys were cast using arc melting. High purity Al, Mo, and Si at 99.999% were used for alloy fabrication. The cast ingots were wrapped in a Ta foil, sealed in a stainless steel tube, and homogenized at 500ºC for 200 hours. Each ingot weighed approximately 15 grams. Note some alloys contain more than one target FMI phase in its microstructure. SEM and EDS analysis was conducted on these alloys prior to TEM analysis. SEM was used to gain a better understanding of the general microstructure of the alloys and EDS analysis was used to determine chemical compositions of the target FMI phases in each alloy. Results of this analysis will be provided in Chapter 4.

3.1.3: DU-7wt%Mo Alloys

Three different fabrication methods were used to see how various treatments affect the unirradiated microstructure of U-Xwt%Mo dispersion fuel. Additionally, the foils created were used for the Xe heavy ion irradiation campaign. All three fabrication methods utilized arc melting of DU and Mo scraps to form a button of DU-7wt%Mo. Buttons were arc melted several times to ensure homogeneity.

For the first fabrication method, the DU-7wt%Mo button was cast into a ¼" diameter rod for sample preparation. For the other two fabrication methods, the DU-7wt%Mo buttons underwent hot rolling at 650ºC to create foils of roughly 250 μm thickness; some foils were in this condition. For the final fabrication method, the hot-rolled foil was then

annealed in a furnace at 900ºC for an hour to relieve the stress from hot-rolling. This sample was quenched immediately after removal from the furnace to lock in the meta-stable γ-phase of U,Mo while hopefully avoiding the α and γ' U-phases. This final fabrication method was used for the Xe heavy ion irradiation campaign where a stress free microstructure was desired.

3.1.4: Al-2wt%Si powder sample

The Al-2wt%Si powder was received from CERCA company. This Al-2wt%Si powder came from an Al-2wt%Si alloy that was atomized into a fine powder.

3.2: Irradiation Parameters

3.2.1: RERTR-6 Sample

The neutron irradiated fuel punch from the RERTR-6 ATR irradiation campaign came from plate R2R010, a U-7wt%Mo/Al-2wt%Si dispersion plate. The plate was enriched to 19.7% U^{235} and had an average fission density, average fission rate, and peak heat flux of 3.2×10^{20} f/cm^3, 2.7×10^{14} f/cm^3·sec, and 1.48×10^6 W/m^2, respectively. Using the PLATE code, a peak fuel temperature of 109°C was calculated. The fuel punch used for TEM analysis came from the side of the plate with the highest neutron flux. The calculated local fission density, local fission rate, and local heat flux at the location of the fuel punch was 4.5×10^{20} f/cm^3, 3.8×10^{14} f/cm^3·sec, and 1.48×10^6 W/m^2, respectively.

3.2.2: RERTR-7 Low Flux Sample

Two punches were obtained from plate R2R040 for TEM analysis. One punch (designated as RERTR-7 low flux), came from the low flux side of the plate. The other punch (designated as RERTR-7 high flux), came from the high flux side of the plate. The low flux irradiation conditions determined from the PLATE code was a fission density of $3.3x10^{21}$f/cm^3, a fission rate of $4.3x10^{14}$ f/cm^3-sec, and an irradiation temperature of 90-91ºC

3.2.3: RERTR-7 High Flux

This punch was taken from the high flux end of the R2R040 plate. The irradiation parameters for this punch as calculated by the PLATE code are: a fission density of $6.3x10^{21}$ f/cm^3 , a fission rate of $8.11x10^{14}$ f/cm^3-sec, a heat flux of 307-337 W/cm^2, and an irradiation temperature of 119-121˚C At this fission density, it is believed the fuel has undergone radiation induced recrystallization (19).

Heavy Ion Irradiations at the IVEM:

Heavy ion irradiations were conducted at the Intermediate Voltage Electron Microscope (IVEM) facility at the ANL. This facility uses a Hitachi H-9000NAR 300 keV transmission electron microscope attached to a NEC tandem accelerator. The incoming ion beam of the accelerator has a diameter of 1.5 mm and an ion angle of incident of 30°

from the sample. The vacuum of the system holds a pressure less than $4x10^{-7}$ torr. Samples were mounted on a heated double tilt holder to control temperature during irradiation.

3.2.4: Heavy Ion Irradiations of DU-Alloys

The DU-FMI alloys were irradiated using 500 keV Kr atoms to potentially form Kr bubbles and cause radiation damage. Using the INL's JEOL 2010 TEM, the electron transparent thickness of the fuel is roughly 100 nm. The heavy ion experiment was designed so that a portion of the Kr atoms are deposited into the DU-alloys to create bubble formation. At 500 keV, less than half of the Kr atoms are injected at a depth of 100 nm or less into the alloys, allowing bubble formation to occur. The incoming Kr beam from the accelerator had a flux of 10^{12} ion/cm^2·sec. The DU-FMI alloys were irradiated at 200 ±10°C to mimic the temperatures seen in typical reactor conditions for dispersion fuel. The target doses for the DU-FMI alloys were 1.0, 4.0, 10.0, and 100.0 dpa. SRIM simulations of damage rates for the DU-FMI alloys are shown in Figure 3.1. The displacement energies used for SRIM (61)calculations of Al, Si, Mo, and U are 25, 25, 40, and 60 eV, respectively. Using the damage rates calculated for the DU-FMI alloy using SRIN, Kr fluences of $2.3x10^{14}$, $2.4x10^{14}$, $2.8x10^{14}$, and $2.5x10^{14}$ ion/cm^2 were calculated as necessary to achieve 1 dpa damage for the UAl_3-type phases $(U(Si,Al)_3$ and $(U,Mo)(Al,Si)_3)$, UAl_4, UMo_2Al_{20}, and $U_6Mo_4Al_{43}$.

3.2.5: Heavy Ion Irradiations of DU-7wt%Mo Foils

The DU-7wt%Mo foils were irradiated using 500 keV Xe atoms with the goal of forming Xe bubbles. This energy was chosen so that 85% of the Xe atoms are implanted 100 nm or less into the foils, allowing potential bubbles to form. Xe was chosen because being a primary fission gas. The average Xe ion flux from the accelerator was 1.5×10^{12} ion/cm^2-sec. Table 3.3 shows the irradiations that were conducted. Irradiations were conducted at 100, 200, and 300°C and fluences up to 2.5×10^{16} ion/cm^2-sec. The DU-7wt%Mo foils were irradiated at various temperatures and different fluences to better understand the bubble growth at various conditions. The SRIM damage calculations for the DU-7wt%Mo foils can be seen in Figure 3.2. The displacement energies used in SRIM calculations were 40 eV for U and 60 eV for Mo. Note that the DU-7wt%Mo foils underwent extreme oxidation during irradiation, preventing in-situ TEM analysis at higher irradiation doses. This oxidation layer was removed using a PIPS ion mill.

3.2.6: Proton irradiations of DU-alloys

Proton irradiations on the DU-alloys were conducted at the University of Wisconsin-Madison using its 1.7 MeV tandem accelerator. The DU-alloys were irradiated at 200˚C. Each target phase will have different damage rates when compared to each other and due to this the final achieved doses for the DU-alloys can be seen in Table 3.4.

3.2.7: Al-2wt%Si Powder Sample

This sample was not irradiated and is being used for pre-irradiation microstructure study only.

3.3: Sample Preparation for TEM Analysis

Sample geometries for TEM analysis varied across experiments. The neutron irradiated RERTR-6, -7 L.Flux, -7 H.Flux, -9A, and -9B were in the form of 1-mm diameter punches roughly 1.5 mm thick. They were 1-mm diameter punches to lower the radiation levels to which personnel were exposed when compared to radiation levels of a standard 3-mm TEM disc. The Al-2wt%Si powder sample was in small micron sized powder and was mixed with epoxy in a 3-mm diameter Mo ring that had a 1-mm diameter hole in the center. All other fuel samples were in the form of 3-mm diameter discs. With the exception of the Al-2wt%Si sample, a primary method was used for TEM preparation for both the 1-mm and 3-mm diameter fuel samples although the 1-mm diameter sized samples required an extra step due to the geometry of the individual sample. Once this additional step is performed on the necessary samples, TEM preparation was identical for both 1-mm and 3-mm diameter geometries. The Al-2wt%Si powder sample TEM preparation process will be discussed last.

1-mm Diameter Punch Mounting:

The fresh fuel dispersion samples from RERTR-9A and -9B and the neutron irradiated samples from RERTR-6, -7 L.Flux, and -7 H.Flux were 1-mm punches. This required the need of the punches to be mounted to a 3-mm diameter ring for TEM analysis. These fuel samples were roughly 1.5 mm in thickness, with 0.5 mm of dispersion fuel sandwiched between Al cladding. A 3-mm Mo rod was fabricated as the support disc for the 1-mm diameter punches. The Mo rod had a 1-mm diameter hole bored out of the center and was then sectioned lengthwise into disks about 500 μm thick. The 1-mm diameter punches were secured into the Mo disks with G1-epoxy and cured. The punches were oriented such that the fuel region was within the Mo ring and the Al cladding protruded from the ends of the Mo punch. The sample was then polished from both sides through 1200 grit, using silicon carbide paper, to a thickness of 150 μm, such that the fuel region was exposed on both sides. Figure 3.3 shows how the 1-mm punches were mounted into the 3-mm Mo ring.

TEM Preparation:

The following steps were used for all of the samples (1-mm punches mounted as previously described and 3-mm punches). The samples were wet-polished bilaterally to a thickness of roughly 150 μm, using 320 through 1200 grit with silicon carbide (SiC) paper. For the 1-mm fuel samples, the sample was polished down to ~150 μm making sure that fuel was present on both sides of the sample before proceeding. Samples were then jet-polished using a South Bay single jet-polisher with a 5% perchloric acid in

methanol solution at -40°C. Samples were polished equally on both sides to produce a thin area in the center of the sample.

Jet polishing proved challenging with the FMI alloys and dispersion fuels due to their multi-phase nature. The Al phase preferentially polishes at a faster rate than the U-phases in the materials. This leads to premature perforation of the samples before the U-phases are polished down to a useable TEM thickness (~100 nm). The preferential polishing in some samples/phases led to the need to ion mill the samples (in addition to jet-polishing), using a Gatan Precession Ion Polishing System (PIPS). The PIPS milled the samples with 4 keV argon atoms at 8° until a perforation was present in the middle of the sample. A larger perforation, roughly visible by eye, in the center of the sample was preferable, allowing more area to analyze in the TEM. Once an acceptable-sized hole was present in the center of the sample, the PIPS gun angle was reduced in 1° steps for 15 min, until a final gun angle of 4° was established. Samples were quickly removed from the PIPS system and transferred into the TEM to reduce oxidation of the samples. Whenever significant oxidation occurred, samples were ion milled at a 4° angle for a short time period to remove the oxidation.

For the Al-2wt%Si powder sample, the powder was mixed with epoxy and placed into a Mo ring with a 1-mm hole bored out of the center. The sample was polished on both sides, through 1200 grit, down to a thickness of roughly 100 μm. The sample was loaded

into a dimpler and was dimpled down until perforation in the center of the sample. The PIPS was used to help thin the center of the sample to a final TEM transparent thickness.

3.4 TEM Techniques for Microstructural Analysis

TEM microstructural analysis was conducted using two TEMs. Benchmark analysis and post irradiation analysis was conducted using the INL's JEOL 2010, operating at 200 keV. This microscope is equipped with an EDS system and a high resolution CCD camera for imaging. In-situ TEM analysis was conducted on the heavy ion irradiated samples at Argonne's IVEM facility. This microscope is a Hitachi H-9000NAR, operating at 300keV, and is equipped with an EDS system and a CCD camera for imaging. Using these microscopes, the following microstructural features were studied: examination of the general sample microstructure before and after irradiation; imaging of any defects present in the various materials; imaging of voids/bubbles, if present; electron diffraction of the materials, focusing on crystal structure and ordered bubble orientation, if present; and EDS analysis of the FMI layer, focusing on Si content.

Defect Imaging:

General overview images of the microstructure of a material were captured using 2-beam conditions. Setting up a specific 2-beam condition can be used to image defects present in the material, such as dislocations. For examples, in an FCC material, such as Al, using a g= [200] 2-beam condition, dislocations present in the material can be imaged. When

using this setting, all of the faulted loops ($b=a_o/3<111>$) and two-thirds of the perfect loops ($b=a_0/2<100>$) are imaged. Another special condition, called rel-rod imaging, is used to look at Frank faulted loops. By setting up a g= [113] condition near the <110> zone, the electron diffraction pattern will show small streaks perpendicular to the diffraction spots. Small faulted loops (<5 nm) can be imaged by setting up a WBDF image using one of these small streaks. The faulted loops displayed will be one-fourth of the total number of faulted loops.

Due to the multiphase aspect of all of the materials studied, many different conditions were needed to image the dislocations present in the materials. Due to the unknown crystal structures of the DU-FMI alloys prior to TEM analysis, 2-beam image conditions were obtained at all low g-beams, such as g=[100], g=[110], g=[111], to show any microstructural features present. Specific 2-beam conditions used for dislocation analysis for each phase will be discussed in Chapter 4.

Stacking Faults:

Stacking faults are defects in the ordering of planes in a material. For example, a material may have three separate planes of atoms vertically stacked and repeating, creating the crystalline structure. This can represented as ABCABCABCABC, where each letter represents a plane of atoms. When a stacking fault is present, the ordering of ABC will be changed, such as in ABCACABC, where a “B” plane of atoms has been

removed. This will appear in the TEM as a change in diffraction contrast. Materials with stacking faults are discussed in Chapter 4.

Precipitates:

Precipitates may be evident in the materials, and are distinguished from voids based on diffraction condition. Precipitates are highly dependent on diffraction contrast whereas voids are dependent on absorption contrast. By tilting a sample through large angles, the precipitates will change contrast while the voids will not. Depending on the size of the precipitates and the spot size of the TEM used, crystal structure and chemical composition of the precipitates can be determined.

Voids/Bubbles:

Voids and or bubbles of irradiated samples can be imaged by tilting the sample away from strong diffraction conditions. Over-focus and under-focus conditions, useful for smaller sized bubbles, were applied to see any feature changes present in the voids/bubbles. The materials were also tilted through large angles to verify that the bubbles were not precipitates. In addition to tilting the sample away from strong diffraction conditions, BF images were obtained at primary diffraction zones. This condition is used to image the super-ordered bubble lattice structure that is present in the U-7wt%Mo fuel kernels.

Bubble sizes were measured across the longest direction of a bubble. To determine the bubble density in the super-ordered bubble lattice, the volume was determined using bubble lattice spacing. As it will be seen later, the bubble superlattice is in a FCC orientation. There are 4 atoms, or in this case bubbles, in a FCC unit cell. Knowing the lattice spacing and that there are 4 bubbles per a cell, the bubble density can be calculated. For obtaining a bubble distribution, bubble sizes need to be obtained and a bin sizes for the bubbles need to be created. After determining a size and the range of each bin-array, bubble size distributions of an area were calculated by dividing the number of bubbles in each specific bin by the total number of counted bubbles in that bin-array. The bin sizes remained the same for all analysis to provide a useful comparison.

Crystal Structure

Electron diffraction patterns of the major zones were used to determine the crystal structure of the materials. In addition to determining the crystal structure, electron diffraction patterns can roughly determine the lattice parameter of the crystalline materials. Using aluminum as a reference phase, the lattice parameters of the materials are calculated. This is done by finding the crystal structure and measuring the diffraction spacing to a known lattice spot. This is then compared to the reference Al phase and a ratio between the two is applied to find the lattice parameter.

EDS/Spot Analysis:

EDS analysis determines elemental composition in specific locations, along with atomic and weight percentage. Measured compositions from EDS analysis can be compared to literature compositions to hypothesize the phase. In addition to determining spot elemental compositions, many EDS measurements can be made across a line or area to determine elemental composition changes. In the amorphous regions, the FMI atomic ratio (Al+Si)/(U+Mo) is determined using the spot EDS atomic elemental composition. The resulting ratio can be substituted into x in UAl_x to conjecture the phase of the amorphous material and to monitor Si content throughout the FMI layer.

Note that EDS measurements are semi-quantitative in that the measurement in a specific area can be affected by different factors. First, the spot size of the TEM on the INL's JEOL 2010 is roughly 10-20 nm. When EDS is conducted on an area of interest smaller than the spot size, counts from the surrounding area will occur. This leads to inaccurate EDS results. Additionally, bulk material above or below a target feature can lead to undesired counts that affect the results of the EDS measurement. Another issue that occur during EDS analysis is the high radiation field from the sample and how it affects the EDS measurement. When conducting EDS in a thin area, the EDS count rate of interest is low and the background radiation field starts to dominate the EDS spectrum and makes the results of the EDS analysis flawed.

Principles of Statistics:

In the results section of the study, bubble distributions will be provided. In the distributions, the number of bubbles were counted, the average size, the skewness of the distribution, and the kurtosis of the distribution will be provided. In the average size calculation, the plus/minus added to the results is the standard deviation of the measurements. The skewness is the measure of symmetry of the distribution. If the distribution was symmetric on both the left side and the right side of distribution, the skewness is defined as zero. If the distribution is skewed to the left, the tail is longer compared to the right, it is defined as a negative value. If it is skewed to the right, it is a positive value. The kurtosis value is related to if the distribution is peaked or flat relative to a normal distribution. High kurtosis corresponds to a distinct peak that is near the mean and decreases in intensity rapidly the further you move from the mean. A low kurtosis corresponds to more of a broad peak rather than a sharp peak.

Table 3.1: List of the experiments and the unknown that it supports

Experiment	Supports
TEM studies of Al-2wt%Si powder	Si Modified FMI Layer
TEM DU Alloys-Unirradiated	Si Modified FMI Layer
TEM DU Alloys-Proton Irradiated	Si Modified FMI Layer
TEM DU Alloys-Kr Irradiated	Si Modified FMI Layer
TEM DU-7wt% Foils-Unirradiated	Bubble Superlattice
TEM DU-7wt% Foils-Xe Irradiated	Bubble Superlattice
TEM RERTR-9A and -9B	Si Modified FMI Layer
OM, SEM, TEM RERTR-6	Si Modified FMI Layer, Amorphous Rim, Bubble Superlattice
OM, SEM, TEM RERTR-7 L.Flux	Si Modified FMI Layer, Amorphous Rim, Bubble Superlattice
OM, SEM, TEM RERTR-7 H. Flux	Si Modified FMI Layer, Amorphous Rim, Bubble Superlattice

Table 3.2: DU-Alloy Compositions and the phases present in each alloy

Alloy Designation	**A**	**B**	**D**
Composition (wt%)	67U-5Si-28Al	48U-5Mo-47Al	69U-4Mo-20Al-7Si
Composition (at%)	$U_{19}Si_{12}Al_{69}$	$U_{10}Mo_3Al_{87}$	$U_{22}Mo_3Al_{56}Si_{19}$
Phases Present	$U(Al,Si)_3$	UMo_2Al_{20}, UAl_4, $U_6Mo_4Al_{43}$	$(U,Mo)(Al,Si)_3$, UMo_2Al_{20}
Found in Dispersion Fuel Type	(U,Si)/Al Fuel	(U,Mo)/Al Fuel	(U,Mo)/(Al,Si) Fuel

Table 3.3: DU-7wt%Mo foils Xe-irradiation parameters

Sample	Final Dose Ion/cm^2	Dose Rate Ion/cm^2-sec	Temperature ˚C
1	1.25x10^{16}	1.5x10^{12}	200
2	2.5x10^{16}	1.5x10^{12}	200
4	2.5x10^{16}	1.25x10^{12}	100
5	6.25x10^{15}	1.25x10^{12}	300
6	6.25x10^{15}	1.25x10^{12}	200

Table 3.4: Final achieved doses for the proton irradiated DU-alloys. The 0.05, 0.37, and 1.17 dpa columns correspond to the maximum damage seen by the $(U,Mo)(Al,Si)_3$ phase.

Phase	**0.05 dpa**	**0.37 dpa**	**1.17 dpa**
UAl_4	0.03	0.27	0.86
UMo_2Al_{20}	0.02	0.20	0.63
$U_6Mo_4Al_{43}$	0.02	0.19	0.60
$U(Al,Si)_3$	0.04	0.32	1.02
$(U,Mo)(Al,Si)_3$	0.05	0.37	1.17
Al	0.02	0.16	0.50

a)

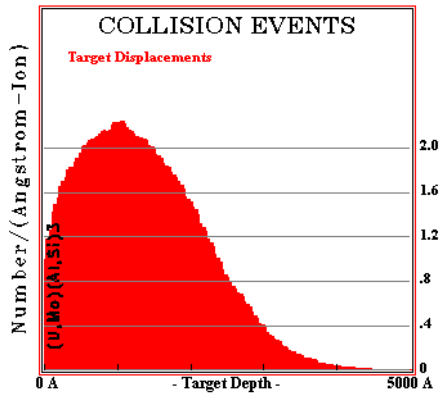
COLLISION EVENTS
Target Displacements
Number/(Angstrom-Ion)
(U,Mo)(Al,Si)3
2.0
1.6
1.2
.8
.4
0
0 A
- Target Depth -
5000 A

b)

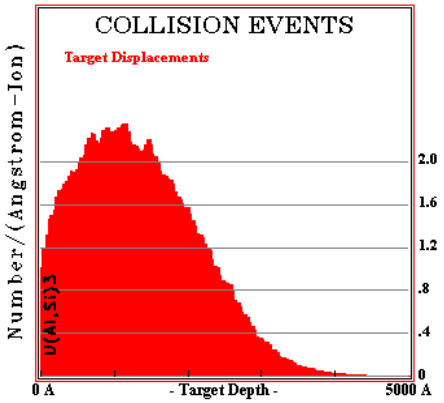
COLLISION EVENTS
Target Displacements
Number/(Angstrom-Ion)
U(Al,Si)3
2.0
1.6
1.2
.8
.4
0
0 A
- Target Depth -
5000 A

c)

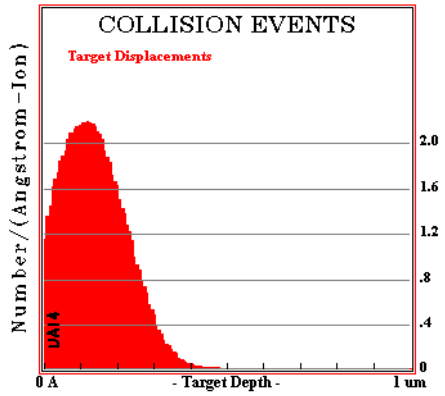
COLLISION EVENTS
Target Displacements
Number/(Angstrom-Ion)
UAl4
2.0
1.6
1.2
.8
.4
0
0 A
- Target Depth -
1 um

d)

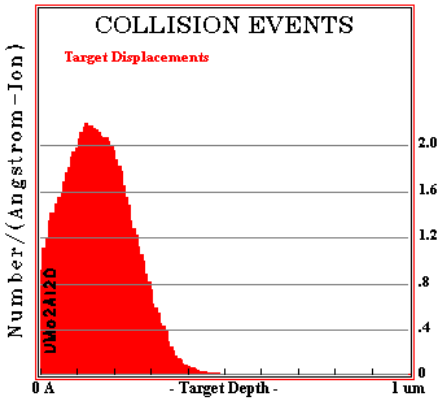
COLLISION EVENTS
Target Displacements
Number/(Angstrom-Ion)
UMo2Al20
2.0
1.6
1.2
.8
.4
0
0 A
- Target Depth -
1 um

e)

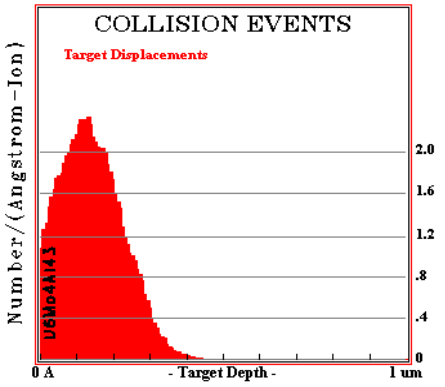
COLLISION EVENTS
Target Displacements
Number/(Angstrom-Ion)
UGMo4Al43
2.0
1.6
1.2
.8
.4
0
0 A
- Target Depth -
1 um

Figure 3.1: SRIM simulations for the DU-Alloys: a) $(U,Mo)(Al,Si)_3$, b) $U(Al,Si)_3$, c) UAl_4, d)UMo_2Al_{20}, and e) $U_6Mo_4Al_{43}$

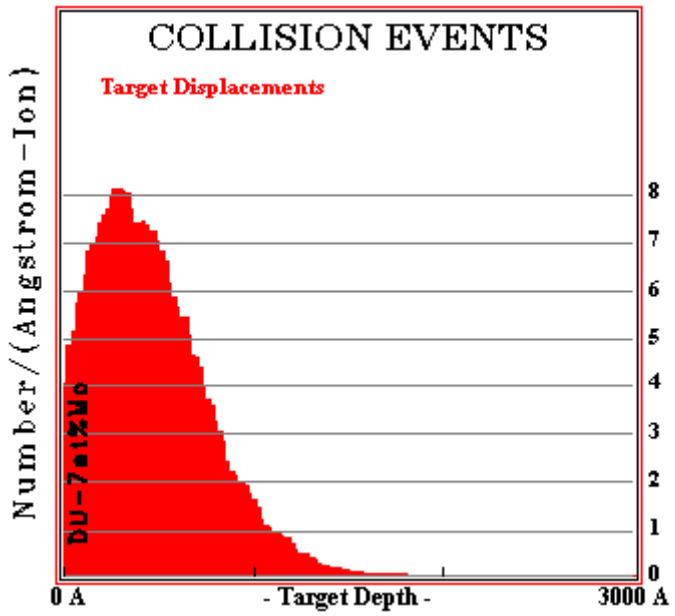

Figure 3.2: SRIM calculation for the DU-7wt%Mo foils

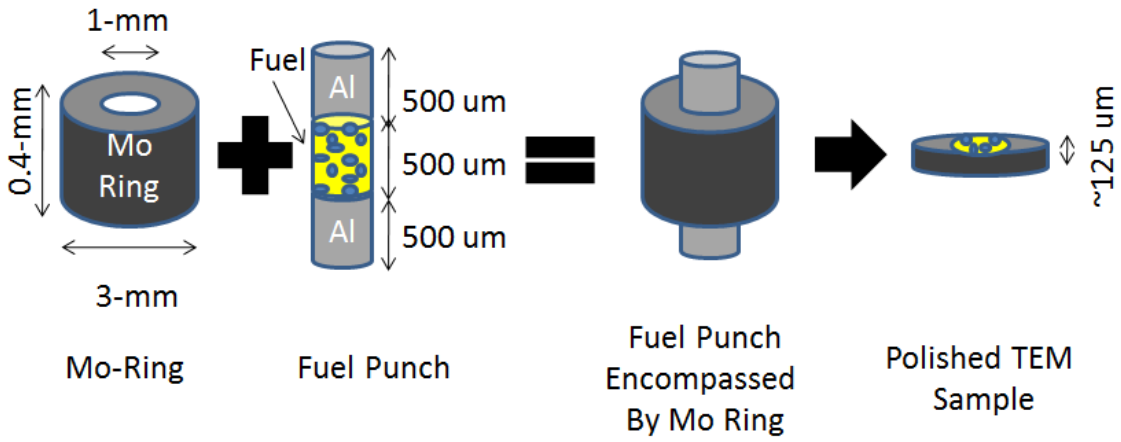

Figure 3.3: 1-mm punch mounting in a Mo ring

Chapter 4 : Experimental Results

Experimental results will be discussed as follows: TEM analysis of the Al-2wt%Si powder used for fabricating the Al-matrix of the dispersion fuel, TEM benchmark of the DU-alloys fabricated to simulate target FMI phases known to form during diffusion couples, TEM analysis of proton irradiated DU-alloys, TEM analysis of Kr irradiated DU-alloys, TEM benchmark of DU-7wt%Mo foils with varying fabrication methods, TEM analysis of Xe irradiated DU-7wt%Mo foils, TEM analysis of unirradiated RERTR-9A and -9B archive fuel, OM, SEM, and TEM analysis of a neutron irradiated punch of RERTR-6, OM, SEM, and TEM analysis of a neutron irradiated punch of RERTR-7, and a calculation of the fission gas inventory of both RERTR-6 and 7- L. Flux used in the intragranular bubble model presented in Chapter 5.

The three main purposes of the experiments were:

1: How does the Si added to the matrix affect the FMI layers' microstructure, i.e. bubble growth and sizes, FMI layer growth, and chemical composition?

2: How does the amorphous rim region form, what is its chemical composition, and what is its irradiation microstructure?

3: How does the bubble superlattice form in the crystal fuel region?

Table 4.1 lists how each experiment supports addressing the questions posed above.

4.1: TEM analysis of Al-2wt%Si Powder

TEM analysis was performed on atomized Al-2wt%Si granules to better understand where the Si was distributed prior to fuel plate fabrication. Analysis showed that the Si was found in three particular locations: as small nano-sized precipitates in the bulk, decorated along Al grain boundaries, and as Si string precipitates. Figure 4.1shows TEM micrographs showing the general microstructure of these Si locations. Figure 4.1 a) shows circular Si precipitates, as well as string like Si precipitates and Figure 4.1b) shows an Al grain boundary, which is decorated by Si precipitates. Note that in Figure 4.1b) string precipitates are present with some protruding off the Al grain boundary.

EDS chemical compositions were used to verify the Si content. It should be noted that the Si content in a specific area is likely higher than the measured EDS value due to the EDS sample volume being larger than the precipitate thus increasing signal from the surrounding matrix.

The small individual Si precipitates were present as nano-sized circular/facetted precipitates ranging in size from 14 to 192 nm. The general microstructure shows that the precipitates were present as either small clusters of precipitates (with sizes near the 14.9 nm) or as larger precipitates near 192 nm in size. The circular individual precipitates are not evident in all areas. The maximum Si content measured in the circular precipitates was ~68 at% while most had an average Si content between 10-20 at%. The Si decorated grain boundaries are found in various areas but the majority of the grain boundaries are Si free.

The Si string precipitates are evident in almost all areas and can range in length up to several μm. EDS analysis on the string precipitates show that the maximum Si content measured was ~38 at% with the majority of the precipitates having concentration around 20-30 at%. SAD at these string precipitates show a ring pattern is present, indicating a nano-crystalline structure. Figure 4.2a) shows the diffraction pattern from the string Si precipitates, Figure 4.2b) shows the WBDF image using a portion of the ring portion of the electron pattern, and Figure 4.2c) shows a BF image of the area where Figure 4.2b) was obtained. Figure 4.2b) shows that the string precipitates are composed of clusters of nano-sized Si precipitates (<10 nm in size).

4.2: TEM benchmark of DU-alloys

Three DU-alloys were cast to simulate phases that are known to form in the FMI layer in diffusion couples. The target phases are $U(Al,Si)_3$, $(U,Mo)(Al,Si)_3$, UAl_4, UMo_2Al_{20}, and $U_6Mo_4Al_{43}$. These phases were studied using SEM and TEM to understand their microstructural changes with irradiation and the results are discussed below.

SEM Results

SEM analysis was performed to get a better understanding of the DU-alloy's microstructures and to verify target phase formation in the respective DU-alloy. A ZEISS Model 960A SEM with an Oxford wavelength dispersive spectrometer (WDS) and an energy dispersive spectrometer (EDS) that employed the ISIS LINK software was used for analysis. Secondary electron images were obtained to show the overall microstructures of the alloys and can be seen below in

Figure 4.3. In addition, WDS and EDS were used to provide X-ray maps and point elemental compositions in the DU-alloys to verify if the chemical composition is of that of the target phases. Measured EDS chemical compositions are of the target phase's chemical composition in their respective DU-alloy. Table 4.2 shows the phases present in each DU-alloy and a summary of the defect microstructures from the TEM analysis discussed below.

TEM Results

TEM analysis was used to: verify the structural information of the target DU-alloys using major diffraction zone patterns, understand the defect microstructures of the fabricated DU-alloys prior to irradiation, and, using EDS, verify chemical compositions. The three DU-alloys can contain more than one phase with some specific phases being present in multiple DU-alloys, see Table 4.2. TEM results will be discussed by individual phases, not by specific DU-alloy.

Lattice parameters reported in the literature for the target phases will be provided for each phase and are assumed the value measured in the TEM unless the value of the lattice parameter measured in the TEM exceeds a 5% difference from the literature value. This assumption is made due to the relative error in determining lattice parameters from SAD patterns (up to 10% depending on microscope conditions). JEMS, a crystal model program (62), was used to simulate the target DU-phases electron diffraction pattern from literature values. JEMS simulated diffraction patterns were compared to the measured TEM diffraction patterns to help verify the crystal structures.

The structure of $U(Al,Si)_3$ was found to be a cubic $L1_2$ ordered Cu_3Au type structure. The lattice parameter is roughly the same as UAl_3, indicating that the minimal Si concentration, up to 13 at%, has no measurable effect on the lattice parameter at the $U(Al,Si)_3$ composition of this DU-alloy. Note that the Si does affect the lattice parameter but due to the error in measuring lattice parameters using the TEM SAD technique, the difference in lattice parameter is within the 10% error value. $U(Al,Si)_3$ has a Pearson symbol of cP4 and it has a space group of 221. Figure 4.4 shows a SAD pattern of the z=[011] of $U(Al,Si)_3$. The diffraction pattern shows extra ordered satellite spots, indicating that a superlattice is present with Si atoms sitting on an Al corner lattice spot every 4 lattices. Figure 4.5 shows a JEMS model of $U(Al,Si)_3$ at z=[011] showing a superlattice box with individual atom locations. The diffraction pattern shows extra ordered satellite spots, on top of the ordered spots from the ordered Cu_3Au type structure. $U(Al,Si)_3$ was tilted through many two-beam conditions to image any defects in the fabricated microstructure. No defects were seen in $U(Al,Si)_3$, indicating a clean pre-irradiation microstructure.

$(U,Mo)(Al,Si)_3$ is an FCC ordered ($L1_2$) structure like $U(Al,Si)_3$. This phase doesn't include the superlattice spots seen in $U(Al,Si)_3$ diffraction patterns, indicating that the Si in this system is randomly sitting on Al sites. The measured lattice parameter is in good agreement with the anticipated UAl_3 value of 0.426 nm. Chemical compositions measured by EDS are the expected values for $(U,Mo)(Al,Si)_3$. The pre-irradiation microstructure is defect free.

The UAl_4 phase in DU-alloy B has an Imma body-centered orthorhombic structure with a Pearson's symbol of ol20 and a space group of 74. The measured lattice parameter is in agreement with the literature value of a=0.627, b=1.371, and c=0.441 nm. Chemical composition measured by EDS shows that the expected composition is present. The general microstructure consists of only small precipitates which can be seen in Figure 4.6. Due to the small size of the precipitates and the spot size of the TEM, no crystal structure information could be obtained. EDS analysis of the precipitates shows that Mo is present in various amounts. Other than the Mo-rich precipitates, no other major defects are present in the pre-irradiated UAl_4 microstructure.

$U_6Mo_4Al_{43}$, present in DU-alloy B, has a P63mcm hexagonal structure with a measured lattice parameter consistent with literature values, a=b=1.097, and c=1.769 nm. Its Pearson's symbol is hP106 and a space group of 193. Chemical analysis measured by EDS of this phase indicates the anticipated composition. Tilting through all major two-beam conditions, no defects were seen, indicating a clean pre-irradiation microstructure.

UMo_2Al_{20}, which is present in DU-alloy B and D, is an Fd-3m large cubic structure with a literature lattice parameter of a=1.451 nm. Its Pearson's symbol is cF184 and its space group is 227. The measured TEM lattice parameter is consistent with literature value. EDS chemical analysis shows the anticipated values. The general microstructure of UMo_2Al_{20} contains a high

density of stacking faults which can be seen in Figure 4.7. EDS chemical analysis shows the anticipated values.

4:3: TEM analysis of proton irradiated DU-alloys

Proton irradiations were conducted at the University of Wisconsin-Madison at 200°C to doses of up to 1.5 dpa. TEM analysis of the proton irradiated DU-alloys shows little change in the irradiated microstructure compared to the unirradiated microstructure in the DU-alloys. UAl_4 and the Al phases were the only phases showing any significant change. The unidentified Mo precipitates seen in UAl_4 showed coarsening with increasing dose. It is not clear if this is thermal or radiation induced. Figure 4.8 contains TEM micrographs showing the coarsening evolution of the precipitates in the unirradiated, 0.27, and 0.86 dpa irradiations. The Al phase showed voids, indicating irradiation occurred but not enough voids were seen to allow statistical analysis.

It is believed that proton irradiations could be useful to simulate radiation damage in fuels but fission products are likely the largest source of damage in fuels. Future proton irradiations are not a direction the RERTR program is focused on due to the success of the heavy ion irradiations discussed below.

4.4: TEM analysis of Kr irradiated DU-alloys

Kr irradiations were conducted at 200°C to target doses of 1, 10, and 100 dpa. Kr was chosen due to it being a typical fission gas. Kr irradiations were completed through various doses up to

100 dpa to better understand how the specific phase's microstructure would respond to irradiation at specific target doses, specifically bubble growth in specific phases. Note that the minimum resolution of fission gas bubbles that can be resolved by the INL's JEOL 2010 is around 2nm.

$U(Al,Si)_3$ underwent significant changes at an early dose (<0.2 dpa) as evidenced by its SAD pattern. The fine superlattice spots seen in the non-irradiated microstructure have disappeared, indicating that Si atoms are randomly distributed on Al lattice sites. The SAD pattern shows no other changes through a dose of 100 dpa. The progression of the $U(Al,Si)_3$ SAD pattern with increasing dose can be seen in Figure 4.9. The Kikuchi lines remain visible at 100 dpa and the phase does not undergo amorphization. At 0.25 dpa, small defects become evident in the microstructure. The small features become dislocation loops by 10 dpa. As the dose increases, the loops start to interact with each other and form larger loops. Also, the loops can dissolve into dislocation line segments. The dislocation evolution of $U(Al,Si)_3$ at 10, 50, 80, and 100 dpa can be seen in Figure 4.10.

At doses greater than 80 dpa, the dislocations start to form ribbon-like superdislocations along with a defect spot feature. The ribbon-like dislocations and spot features can be seen in Figure 4.11. The spot features are often attached to a dislocation line or as part of the super dislocations. The average size of the spot features is 11 ± 3 nm and their density is ~2.7×10^{16} cm^{-3}. Due to the size of these spot features and the TEM's spot size capability, no chemical compositions were obtained.

The microstructure of $(U,Mo)(Al,Si)_3$ differs from $U(Al,Si)_3$ significantly. Figure 4.12 shows the evolution of the SAD pattern of $(U,Mo)(Al,Si)_3$ with increasing dose. At a dose of 0.25 dpa, a diffuse ring has started to form indicating that amorphization is starting to occur. Small "black spot" defects were seen at this dose. By 1 dpa, a significant diffuse ring has formed and almost all diffraction spots have disappeared. Additionally, the black spot defects have disappeared. At a dose of ~2 dpa, the $(U,Mo)(Al,Si)_3$ phase has completely turned amorphous and remains in this state up to a final dose of 100dpa.

Figure 4.13 shows the defect microstructure evolution of $(U,Mo)(Al,Si)_3$ with increasing dose up to 100 dpa. At 0.25 dpa, small defects have started to form in $(U,Mo)(Al,Si)_3$. At 0.50 dpa, the size of these defects has increased significantly. At 1 dpa, the defect contrast has almost disappeared and the defects have almost vanished. Above 1 dpa, no visible defects are present. No large bubble growth (>5 nm) or defects were seen at 100 dpa.

Figure 4.14 shows the SAD evolution of UMo_2Al_{20} with increasing dose. At 4 dpa, UMo_2Al_{20} has started to transform into an amorphous state and this phase undergoes a complete amorphous transformation by 10 dpa. At 100 dpa, UMo_2Al_{20} remains in an amorphous state. The defect microstructure evolution of UMo_2Al_{20} with increasing dose can be seen in Figure 4.15. The pre-irradiated microstructure was dominated by high density stacking faults. By 1 dpa, the density of the stacking faults is significantly lower and by 4 dpa, the stack faults are nonexistent. No other radiation defects were seen in UMo_2Al_{20} through 100 dpa.

The SAD evolution of UAl_4 with increasing dose can be seen in Figure 4.16. UAl_4 remains crystalline up to a dose of 100 dpa but at this dose, the Kikuchi line pattern visibility is reduced to zero and the clarity of the diffraction pattern is reduced significantly. One interesting observation is the streaky nature of the diffraction spots at 1 and 10 dpa in the SAD pattern of UAl_4 with increasing dose. Figure 4.17 shows the defect microstructure of UAl_4 with increasing dose. At 1 dpa, small defects have developed in UAl_4. The sizes of these defects continue to grow with dose and are still seen at 100 dpa. The small plate like defects are believed to be the reason for the streaky nature of the diffraction pattern. Additionally, the streaking can be from bending due to extreme stresses in the phase.

In addition to small defects in the microstructure, small bubbles/voids (2-3 nm) were seen above 1 dpa but do not develop into larger voids/bubbles at a dose of 100 dpa. The unknown Mo precipitates seen in the pre-irradiated microstructure dissolve with increasing dose and are almost complete dissolved at a dose of 100 dpa. Note that in the proton irradiation, these precipitates were shown to grow with increasing dose.

The evolution of the SAD pattern with increasing dose of $U_6Mo_4Al_{43}$ can be seen in Figure 4.18. At a dose of 1 dpa, $U_6Mo_4Al_{43}$ is completely amorphous and remains in this state up to 100 dpa. The defect microstructure of $U_6Mo_4Al_{43}$ with increasing dose can be seen in Figure 4.19. The pre-irradiated microstructure is defect free and by 1 dpa, only small ~2-3 nm sized bubbles have formed. The defect microstructure at 100 dpa is dominated by large gas bubbles. The

distribution of these bubbles at 100 dpa can be seen in Figure 4.20. The bubble microstructure is consistent throughout all of the $U_6Mo_4Al_{43}$ microstructure.

The defect microstructure of the pure Al phase at 100 dpa shows a high density of small (2-5 nm) sized bubbles, along with dislocation loops, and dislocation networks. No faulted loop analysis was conducted on the Al phase with the focus of the work being directed on the DU-alloys.

As a reminder, Table 4.3 shows a summary of irradiated microstructures of all of the DU-alloys along with Al.

4.5: TEM Benchmark of DU-7wt%Mo Foils

DU-7wt%Mo fuel foils were fabricated in three different ways to understand how the fabrication process affects the DU-7wt%Mo fuel. It should be noted that monolithic fuels and dispersion fuels are created by a different fabrication process and have different microstructures. The three fabrication process analyzed were a fuel after hot-rolling, an as fabricated sample prior to sample rolling, and an annealed hot-rolled sample that was quenched in water immediately to help lock in the γ-phase. The ultimate goal of the analysis was to find a low-stressed microstructure of the DU-7wt%Mo for Xe irradiation/implantation.

The hot-rolled fuel showed that it was heavily damaged from the rolling process, showing bending contours from the heavily stressed microstructure. Additionally, α-U was found

indicating that the fuel has started to decompose due to the fabrication process. This can be seen in Figure 4.21. The as-cast fuel showed large pockets of U_2Mo and α-U in the host γ-U-7wt%Mo. This can be seen in Figure 4.22. The annealed hot-rolled plate shows a stressed microstructure as seen in Figure 4.23. There is some small U_2Mo and α-U decomposition but these samples were used for the Xe irradiated foils.

4.6: TEM analysis of Xe irradiated DU-7wt%Mo Foils

Xe irradiation of the DU-7wt%Mo foils was challenging due to the U-7wt%Mo fuel oxidizing easily. The DU alloys did not form the same oxide density like the DU-7wt%Mo foils. The foils oxidized during shipment of the foils to the IVEM facility. TEM analysis of the fuel at IVEM showed that some TEM transparent areas were present but it was unknown if the oxide layer would affect the results of the Xe irradiation. The experiment was designed such that 85% of the Xe would be implanted into the assumed TEM transparent thickness of 75 nm. Irradiations were completed at various fluencies, up to $2.5x10^{16}$ Xe ions/cm^2, and various temperatures, 100 to 300°C, to try to create a bubble superlattice. Note that the goal of this experiment is create fission gas bubbles, not to achieve specific target dpa values.

Most transparent TEM areas became too TEM thick during irradiation, indicating that the fuel was either bending, the TEM transparent area was being sputtered off, and/or a new thicker oxidation layer was forming. The foil was shown to form a dislocation microstructure and a typical image of this microstructure can be seen in Figure 4.24. Bubbles were seen in the fuel at

a fluence of $2.5x10^{16}$ Xe ions/cm^2. This can be seen in Figure 4.25. The bubbles are roughly 20-40 nm in size, larger than the expected 3-6 nm sized bubbles expected in a bubble superlattice. No bubble superlattices were seen throughout the irradiations. It is unknown why it didn't form, but one reason could be the oxidation layer formed on the samples during shipment and irradiation.

4.7: TEM analysis of RERTR-9A and -9B fuel

TEM analysis of RERTR-9A and -9B was conducted to better understand the pre-irradiation microstructure of the fuel. One of the key questions prior to analysis of RERTR-9A and -9B was what was the nature of the microstructure of the FMI layer created during fabrication and was this FMI layer amorphous.

TEM Analysis of RERTR-9A:

TEM analysis shows that an FMI layer has formed at the elevated temperature during hot-rolling and HIP fabrication. In addition to the hot-rolling step that both RERTR-9A and -9B underwent, -9A was HIP'd at 450°C for 45 min. TEM analysis shows that this layer is ~2 µm in thickness. This interaction layer is nano-crystalline in structure as seen in ring diffraction pattern and using the JEMS program (62), the pattern matched up with a ring pattern of a UAl_3-type phase. This can be seen in Figure 4.26. By using a section of the ring pattern, the grain distribution on the FMI can be seen in Figure 4.27a). It was determined that average grain size was 35 ±1 nm.

EDS analysis in the FMI region shows that the chemical composition of nano-crystals is consistent with a UAl_3- type phase. It should be noted that the FMI layer can vary in chemical composition primarily due to the Si concentration that was present adjacent to the FMI layer prior to fabrication. Si is insoluble in Al as seen in the Al-2wt%Si powder analysis and forms precipitates. The density of these precipitates around the fuel particles has a major impact on the EDS composition of the FMI layer. Areas that are Si enriched or depleted show Si concentrations ranging from 0-51 at%. In determining that the FMI layer is a UAl_3 type, the Si and the Al at% are added up together and the U and Mo at% are added together to figure the UAl_3-type composition.

The microstructure of the FMI layer in the RERTR-9A archive fuel shows a laminar structure as seen in Figure 4.28. In RERTR-9A, the FMI layer formed is/has transitioned from the decomposed phases into the UAl_3-type phases as seen in Figure 4.28. EDS spot compositions are marked in Figure 4.28. The light shaded areas in Figure 4.28 correspond to areas that have a $(U,Mo)(Al,Si)_3$ EDS chemical composition. The dark shaded areas are U and Mo enriched areas that have not completely decomposed or transitioned into the expected UAl_3 phase but have transitioned out of the γ-(U,Mo). EDS compositions show this phase has an elemental composition that is expected in the U_2Mo phase. No crystallographic information is available due to not being able to achieve a small enough spot size in the TEM.

TEM Analysis of RERTR-9B:

TEM analysis of RERTR-9B shows a FMI layer has formed to a thickness of roughly 1.5 µm due to the elevated hot-rolling fabrication temperatures. Note that this sample did not undergo HIP'ing and showed a smaller FMI layer thickness compared to the HIP'd FMI layer in RERTR-9A. The FMI layer in this fuel is nano-crystalline as seen in diffraction ring pattern and image in Figure 4.29. The average grain size is 29 ±1 nm. The grain distribution can be seen in Figure 4.27 b). EDS compositions of RERTR-9B show that the average Si (28 at%) in the FMI is enriched above the anticipated 19 at% for $(U,Mo)(Al,Si)_3$. The summation of the Al and Si at% is consistent with the UAl_3-type phases (~68 at%). It is believed that with elevated temperature rolling step, the Si will diffuse into the U,Mo phases at a faster rate than the Al atoms as evident by the enriched Si at% in the FMI layer. The general microstructure of the grains, as seen in Figure 4.30, is consistent with those seen in RERTR-9A.

TEM Analysis of RERTR-6 ,-7 L. Flux, and -7 H.Flux

TEM analysis of RERTR-6, -7 L. Flux, and -7 H.Flux were conducted to understand the effects of irradiation on the microstructure of the fuel. With the RERTR-6 and -7 L.Flux experiments and the work conducted by Van de Berghe (1), the irradiation microstructure of U-7wt%Mo dispersion fuel, prior the transient swelling regime, can be characterized. RERTR-7 H.Flux will provide the fuel microstructure after the transient swelling regime.

4.8: OM, SEM, and TEM analysis of RERTR-6:

Experimental results of plate R2R010 from the RERTR-6 experiment are described in the following sections: Optical Microscopy (OM) of plate R2R010, SEM analysis of plate R2R010, TEM characterization of the U-7wt%Mo fuel kernel, TEM characterization of the FMI layer, and TEM characterization of the Al-2wt%Si matrix. Plate R2R010 is a U-7wt%Mo/Al-2wt%Si dispersion fuel.

Optical Microscopy:

OM images of the cross-section of plate R2R010 are shown in Figure 4.31 (63). The figure shows the overall microstructure of the fuel on the Figure 4.31a) low fission density side (4.0 $x10^{21}$ f/cm^3) and 4.31.b) the high fission density side of the plate ($2.5x10^{21}$ f/cm^3). The cross-section shows that the fuel is stable with no large porosity forming in the fuel plate. Figure 4.31a) of the low neutron flux side of the plate shows that a very minimal sized FMI layer has formed around the fuel particles (~1 μm). Figure 4.31b) of the high neutron flux side of the plate shows that a larger stable FMI layer has formed around the fuel kernels ranging in size from 1-10 μm. This FMI layer is non-uniform around the fuel kernels, indicating that the Si content in the surrounding area was non-uniform. In the U-Mo/pure Al dispersion fuel, the FMI layers were consistent around the fuel particles showing little to no difference in thickness.

SEM Results:

SEM results of plate R2R010 will be summarized from reported SEM analysis completed by D. Keiser at the INL (64). Two punches were obtained from plate R2R010 at the low and high

neutron fluence sides of the plate and will be referred to as punch A and B. Fission densities of punch A and B were 2.4 x10^{21} and 4.5 x10^{21} f/cm^3 respectively. Peak temperatures were 94 and 109°C for punch A and B. Punch A shows that the nominal FMI layer thickness was 1-2 μm and can be seen in image a) in Figure 4.32. Figure 4.33 shows X-ray maps from punch B indicating where individual elements were distributed throughout the irradiated dispersion fuel. The Si X-ray map shows that Si has enriched along the boundary of the fuel kernels or in the FMI layer. Some Si-rich precipitates can be seen in the interior of the Al-2wt%Si matrix but very few precipitates are evident near fuel kernels outside of the FMI layer.

Punch B on the high neutron flux side of the plate shows that a much thicker non-uniform FMI layer has formed around the fuel kernels which can be seen in Figure 4.32 b). A high magnification image of this area shows that fission gas bubbles can be seen in specific parts of the FMI layer and can be seen Figure 4.32 c). An EDS line scan (seen as the white line in image b) in Figure 4.32 shows that in the FMI region 1, Si content was high and no visible bubbles were seen in the FMI layer. FMI region 2 shows a much lower Si content and visible bubbles could be seen. Note that due to the SEM's resolution, this was the only area that visible fission gas bubbles could be seen in the FMI layer.

Crystal and Amorphous Fuel Regions

TEM analysis showed that the U-7wt%Mo fuel kernels readily formed an oxide layer after removal from the PIPS system. This led for the need to quickly move the sample from the PIPS system into the TEM to reduce oxide build up. TEM analysis showed that a small oxide layer

formed but did not impede with producing high-quality TEM images in most areas. The fuel region shows two different microstructures: an amorphous fuel region and the crystalline fuel region. Figure 4.34 shows a montage of overlapping TEM images of a typical fuel kernel in RERTR-6 and -7 L. Flux, showing key areas of interest. Marked on the montage is where the fuel transitions from amorphous to a crystalline state.

The amorphous rim is present in all fuel kernels and has a thickness range of 0.7 to 3.7 μm. It should be noted that only three measurements of thickness were made and the thickness could be more or less then the values presented. Another key observation of the amorphous rim is the presence of a high concentration of Si atoms in the region. Figure 4.35 shows an image of the amorphous rim, the crystalline fuel region, and the FMI layer with EDS spot measurements in various locations. The highest Si content is seen in the FMI layer and this is expected given the results seen in the SEM analysis. The amorphous rim shows Si contents around 10% indicating that a high amount of Si is diffusing into the fuel during irradiation. The highest Si seen in the amorphous rim in other areas was 31 at% with the majority of the readings falling between 10 and 20 at%.

The ratio of the x=(U+Mo)/(Al+Si) in $(U,Mo)_x(Al,Si)$, was calculated and presented in Figure 4.35 to get an idea of what phase composition would be present if the fuel was crystalline. One reason for obtaining these values is to see if the fuel composition is close to those of U_3Si and U_3Si_2, known phases that turn amorphous during irradiation (23). Results from the area show

that the fuel is around the $(U,Mo)_3(Al,Si)$ to $(U,Mo)_4(Al,Si)$ range with the $(U,Mo)_3(Al,Si)$ composition residing along the FMI/amorphous rim interface.

Selective area diffraction (SAD) images show that the crystalline U-7wt%Mo fuel kernels remain in a BCC crystal structure. Figure 4.36 shows SAD images at all the major diffraction zones. Using the SAD patterns, the lattice parameter of the fuel kernels was determined to be ~0.340 nm. EDS analysis of the fuel kernel shows that the elemental composition of the fuel is (wt%): ~10 and 90 at% for Mo, and U respectively. The pre-irradiation EDS elemental compositions from RERTR-9A were (wt%): 7 and 93% for Mo and U, respectively.

In the crystalline fuel region, bright field imaging of the U-7wt%Mo fuel kernels shows that the major defect present is fission gas bubbles and dislocations. The bubbles appear in two primary areas. They appear as nano-sized intragranular bubbles in an ordered super-lattice in the bulk of the grains (<10 nm) and as large (>10 nm) sized bubbles (intergranular type) that are along the fuel grain boundaries.

Bright field imaging shows that bubble superlattice has formed in the bulk of the fuel kernels. These bubbles are referred to as intragranular bubbles. This feature occurs throughout all electron transparent fuel regions. Figure 4.37 shows BF images of the intragranular bubbles at their respective diffraction zones at all of the major U-7wt% BCC zones. In addition, high magnification images of SAD satellite spots are shown in Figure 4.38. The sample is preferentially oriented in the [011] direction requiring high tilt to image the [100] and [111]

zones. This lead to poor quality images of these zones. From the BF images, the average bubble size and density were determined to be 3.48± 0.03 nm and $2.75x10^{18}$ bubbles/cm^3. The intragranular bubble distribution can be seen in Figure 4.39. The bubble superlattice is parallel to the host U-7wt%Mo BCC structure, indicating coherency. From the satellite spots at the major BCC U-7wt% diffraction zones and corresponding bright-field images, the bubble superlattice is determined to be FCC in orientation. The swelling contribution of the intragranular bubbles was 6.75%. The swelling contribution was found by finding the volume of the intragranular bubbles in a unit cell of the bubble superlattice.

Bubble lattice spacing of the superlattice was found using the measured planar spacing from major electron diffraction patterns and from BF images of the superlattice at major diffraction zones. The lattice constant of the bubble superlattice was found to be 11.06 ± 0.04 nm. Figure 4.39 shows a picture of the FCC superlattice on top of the host U-7wt%Mo BCC matrix.

A typical image of the larger bubbles (>100 nm) seen along the grain boundaries of the fuel kernels can be seen in Figure 4.40. These bubbles are referred to as intergranular bubbles. In SEM images, these bubbles tend to decorate the grain boundaries of the fuel. Note that bubbles that are present along the interface of the FMI layer and the amorphous rim region are assumed in this analysis to be FMI layer bubbles and will be discussed in the FMI layer characterization below.

Dislocation images were obtained at g=200 and g=110 types around the [011] zone to find the dislocation density in the fuel. The dislocation density is important to understanding if the fuel undergoes recrystallization or is transitioning to this state. Figure 4.41shows a BF image of U-7wt%Mo using a g=200 condition. There are dislocations present with the superlattice bubble formation still present. This is the observed general dislocation microstructure of the fuel though very little dislocation analysis was completed due to limitations from not having large areas of crystalline fuel to analyze due to sample preparation. In addition to not having large areas of crystalline fuel, tilting the sample to a 2-beam condition introduces scattering from the bubbles which affects the ability to properly image dislocations that might be present between two bubbles.

In the microstructure of the amorphous rim and crystalline fuel, small pockets of irregular shaped precipitates/features are present in the intergranular bubbles. Figure 4.42 shows a) an area which has a high density of these features and b) a close up BF image of a feature with locations of EDS spot measurement. Included are the EDS measurements at the indicated spot locations. Mo, Ba, Y, Sr, and Nd are expected fission products. Comparing EDS measurement A to B, it appears that theses fission products like to reside in the fission gas bubbles. Mo and Y are expected to remain in solution in the fuel. Ba and Sr are expected to form oxides readily in the UO_2 fuel but due to no to little oxygen present in this metallic fuel, it is believed that it will seek another location in the fuel. This is likely the fission gas bubbles in the U-Mo fuel. Additional work is needed to fully understand where the fission products are residing in U-Mo metallic fuel.

Electron diffraction of the fission gas bubbles/fission product features show that it is amorphous in character. EDS conducted in the feature shows a high concentration of fission products as seen in the EDS spectrum. EDS of the fuel region adjacent to the feature (spot B) shows little to no fission products when compared to the feature (spot A). These high concentrations of fission products are present in most features measured, indicating that the features are sinks for fission products. Some of the fission products include Xe, Kr, Sr, Y, Nd, Mo, and Ba.

FMI Layer Region:

SAD analysis of the FMI layer shows that it is amorphous in character. This is consistent in all areas of the fuel. Figure 4.43 shows a typical SAD pattern of the FMI layer. Using the FMI diffraction patterns, the nearest neighbor was determined to be 0.24±0.03 nm.

Bright field imaging was used to find the variation in thickness across the FMI layer. As was seen in the SEM analysis of the dispersion fuel, the FMI layer is not consistent around the U-7wt%Mo fuel kernels due to the non-uniform distribution of Si. Measurements of the thickness of the FMI layer were obtained by taking BF images of the FMI layer that included the Al-2wt%Si and fuel regions. From the images, the maximum and minimum thicknesses of the FMI layer were measured. The maximum value obtained was 2.00 μm. The minimum thickness was determined to be 0.68 μm.

As seen in the Si non-uniformity in the Al-matrix observed in SEM analysis, the Si values vary across each FMI layer. In addition, Si will vary from point to point in the same FMI layer

region. Figure 4.44 shows an FMI layer with various spot EDS compositions. The key observation is the Si is generally the lowest on the Al interface side and the greatest along the amorphous rim interface. There is a sharp increase in Si at the FMI/amorphous rim interface, indicating the Si is preferentially attracted to the U and Mo compared to Al. The maximum Si value seen in the FMI layer was 23.2 at%. Point composition EDS analysis across the FMI layer was used to help determine the FMI layer atomic ratio discussed in the background section 2.5.1. The atomic ratio is defined as x=(Al+Si)/(U+Mo). The value "x" is placed into UAl_x to determine what phase would likely be present if the FMI layer was crystalline. Figure 4.45a) shows a typical FMI layer atomic ratio calculation, its Si content across the FMI layer, and the BF image of the FMI layer being measured. Figure 4.45b) shows an area with fuel kernels that are close to each other. The key observations to make from Figure 4.45b) to make is how the Si concentrations can vary from kernel to kernel.

Bubble size distributions were found for specific regions of the FMI layer to understand the effect of location on bubble evolution. The regions of interest were: the FMI layer/fuel kernel interface, the bulk of the FMI layer, and the FMI layer/Al-matrix interface. The bubble sizes and distributions can be seen in Figure 4.46. The FMI/fuel kernel and FMI layer/Al matrix regions were defined as roughly the first 100nm of the interface. In addition, an overall distribution of the bubbles including all regions of the FMI layer can be seen in Figure 4.47.

EDS measurements were conducted in areas where fission gas bubbles were evident in the FMI layer to understand the effect of Si on bubbles size. Point EDS compositions were obtained to

show the relationship of Si content to bubble size. Figure 4.48 shows the effect of Si vs. bubble size throughout the sample.

Al matrix:

The typical irradiated microstructure of the Al-2wt%Si matrix can be seen in Figure 4.49. Image a) and b) show an under and over focus condition and c) shows faulted loops present in the matrix. As seen in the over and under focus images, a high density of voids/bubbles is present in the matrix. Faulted loops were seen in the matrix and their density and sizes were not measured. In addition to the bubble defects in the Al matrix, dislocation networks are present but are typically of those seen in the fabrication process. Small Si precipitates were seen in the Al matrix from neutron capture in Al.

4.9: OM, SEM, and TEM analysis of RERTR-7 L.Flux

Results of the analysis of the low fluence side of plate R2R040 of the RERTR-7 irradiation campaign (sample designation is RERTR-7 L. Flux) will be discussed as follows: OM cross section results, SEM analysis conducted by Dr. Jan Fong of the INL, TEM results of the fuel region, and TEM results of the FMI region. No TEM results for the Al-2wt% Si matrix will be provided as the results show a general microstructure that is similar to the microstructure seen in RERTR-6.

Optical Microscopy:

Optical Microscopy was performed for the RERTR-7 campaign and observations of plate R2R040 are discussed (63). The low flux end of the plate, shown in Figure 4.50a), shows a stable microstructure with FMI layers up to ~4 μm. The fuel particles are saturated with fission gas bubbles. Surrounding the fuel particles a light colored halo can be seen. This is the typical microstructure seen for the Si precipitate free zone (PFZ). EDS of this region is needed to verify this phenomenon. Outside of the PFZ, the region where the scale bar is located on the image, typical Si precipitates features can be seen.

Figure 4.50b) shows the fuel particles at the high flux portion of the plate. This area is at a burnup of ~113% LEU equivalent, far beyond the desired operating limit of this fuel. The fuel particles show large fission gas bubbles at the FMI/fuel interface, a typical failure interface for U,Mo/Al dispersion. These bubbles appear to have started to interlink, one of the indicators that the fuel is starting to fail. Some fuel/FMI interfaces show no bubbles indicating that some other microstructure is forming in this area and TEM and/or SEM analysis is needed to see how these areas differ from the areas that show large fission gas bubbles.

SEM Results:

The SEM results of RERTR-7 L. Flux differ from RERTR-6 with the fracture surface of RERTR-7 L. Flux showing more intergranular type bubbles along the grain boundaries. Figure 4.51 shows a fracture surface of the fuel particles. The key observation is the overall intergranular bubble distribution throughout the fuel. In the RERTR-7 L. Flux SEM analysis, the

fuel grains are smaller compared to RERTR-6. The surrounding material around the grain boundaries shows a high density of intergranular bubbles. This area is likely the FMI layer and/or the amorphous rim of the fuel particles. The high density of intergranular bubbles is significantly higher than that seen in RERTR-6 indicating that either the fission density of RERTR-7 or the different grain sizes plays a major part of the irradiation microstructure in RERTR-7 L. Flux.

Figure 4.52 shows an SEI image and a WDS spectrum of a fuel particle. The key point to notice is the high concentration of Si that is present in the FMI layer and into the fuel particle. Another key observation is the difference between the Si EDS and WDS spectrums of the same area. EDS shows some counts deep into the fuel particle while the WDS shows no counts deep in to the fuel particle. This indicates that WDS would likely be the best option to obtain semi-quantitative elemental compositions for Si and Al in irradiated fuels.

Crystalline and Amorphous Fuel Region:

Analysis of the fuel region shows that the fuel is in a crystalline state in the center of the fuel particles and an amorphous rim, like the one seen in RERTR-6, has formed along the outer edge of the fuel particles. Figure 4.53a) shows a BF image of the crystal and amorphous interface. Figure 4.53b) and c) show the crystalline electron and amorphous diffraction pattern in this area. The thickness of the amorphous rim ranges from 2.4-6.0 μm.

EDS of the amorphous region shows that a significant Si is present. Up to 10 at% Al is present in the TEM EDS analysis of the amorphous rim while SEM EDS shows 1-2 at% Al. The crystalline fuel region shows no significant Si or Al content. The maximum Si content in the amorphous region was 23.9 at%. The average ratio of the heavy elements (U and Mo) to the light elements (Al and Si) in the entire amorphous rim was found to be 4.11 ± 1.75. The ratio for the amorphous rim nearest the FMI layer was found to be 3.06 ± 0.83 for 14 measurements. For future experiments, a greater sampling of this area will be conducted to verify ratio values reported here.

The crystalline fuel is in a BCC structure as was seen in RERTR-6. From the electron diffraction patterns, the crystal fuel's lattice parameter is 3.432 nm with a standard deviation of 0.055 nm. The lattice parameter found in literature for U-7wt%Mo is 3.427 nm [U,Mo Handbook]. Dislocation analysis provided no new information due to lack of a large electron transparent in the crystalline fuel region.

A fission product precipitate is found in the fission gas bubbles in both the crystalline fuel and amorphous fuel rim. These features can be seen in Figure 4.54 and are consistent with those seen in RERTR-6, Figure 4.42. The features are of various sizes and geometries. Electron diffraction of this phase shows that it is amorphous in character. EDS spectra of this phase show high concentrations of fission products when compared to the bulk crystal U-7wt%Mo fuel. The EDS spectrum in this region can be seen in Figure 4.54. In particular, Nb, Y, Sr, and Ba can be seen in high concentrations.

Both intragranular and intergranular bubbles are present in the fuel and are very similar to those seen in RERTR-6. It should be noted that in RERTR-7 L. Flux, much clearer intergranular bubbles were seen compared to RERTR-6. RERTR-6 provided a much clearer intragranular region. These observations could be related to the microstructure seen in the SEM analysis. As was seen in the SEM analysis, the general microstructure of RERTR-7 shows a higher amount of intergranular bubbles when compared to RERTR-6. Another key point to mention is the size of the intergranular bubbles in the fuel region. Micron sized bubbles can be seen along the grain boundaries of the fuel in SEM analysis. Due to the large size of some of these bubbles, some intergranular bubbles will be too large to see in the TEM or will have preferentially polished away during ion polishing. Thus to perform a detailed bubble analysis of the intergranular bubbles, the SEM and TEM techniques would be both required.

Figure 4.54 shows an area of a fuel particle that contains fission gas bubbles. It should be noted the bubbles are not present in all areas. These bubbles are consistent with SEM analysis with large intergranular bubbles being present along the grain boundaries with few in the bulk of the fuel grains. It also should be noted that fission gas bubbles are present in the amorphous rim region of the fuel and roughly the same size as the intergranular bubbles. Figure 4.55 shows the intergranular bubble distribution from the TEM analysis of RERTR-7 L. Flux. This distribution includes bubbles that are present in both the amorphous and crystalline areas.

In the crystalline fuel region, intragranular bubbles are present. Figure 4.56 shows a) a BF image of the intragranular bubbles at a [011] zone and b) a close up of the satellite spots at a [011] zone. The satellite spots correspond to a large spaced ordered structure or the intragranular bubble superlattice. Note that the diffraction pattern is not the corresponding diffraction pattern for the BF images from that area and is being shown due to its quality. The BF image shows that the bubbles are in a superlattice much like the superlattice seen by (1) and those seen in the TEM analysis of RERTR-6. BF images at all major zones indicate that the intragranular bubble superlattice is in a FCC orientation. The satellite spots and BF images of the bubbles show that the superlattice bubbles are coherent with the host BCC U-7wt%Mo matrix. The average bubble size and its standard deviation is 3.10 ± 0.43 nm. The intragranular bubble size distribution can be seen in Figure 4.57. From the BF images, the lattice constant of the bubble superlattice is 11.71 ± 0.32 nm. The swelling contribution of intragranular bubbles in RERTR-7 L. Flux is 4.7%.

The bubble spacing from the BF images of the intragranular bubbles were compared to the satellite diffraction spacing to verify that the two were related. The BF image spacing in the g=200 and g=110 direction was 8.40 ± 0.26 nm and 7.24 ± 0.32 nm compared to the satellite diffraction spacings of 8.40 ± 0.31 nm and 6.85 ±0.33 nm. The values are close in value in both directions indicating that the satellite diffraction spots are indeed from the intragranular bubble superlattice.

Small, intragranular like fission gas bubbles (>2 nm) are found in the amorphous rim that are randomly distributed throughout the rim. They are not present as an ordered superlattice bubble structure due to the amorphous rim being amorphous but indicate that fission gas is being stored in this region. The bubbles are present in all areas of the rim.

FMI Layer Region:

The entire FMI layer is amorphous in structure as seen its election diffraction patter in Figure 4.58. Using the amorphous ring pattern, the nearest neighbor spacing and standard deviation was determined to be 2.38 ± 0.05 nm. The FMI layer thickness varies from fuel kernel to fuel kernel and also varies along individual fuel kernels. Figure 4.59 shows a micrograph showing the varying thickness in the FMI layer. The minimum and maximum FMI layer thickness measured was 0.71 and 4.6 μm.

Using EDS, Si content was measured across the FMI layers and varies up to 14.9 at. %. EDS line scans were completed across various FMI layers. Atomic ratios, x=(Al+Si)/(U+Mo), were calculated using the results of the line scans and two representative atomic ratio profiles can be seen in Figure 4.60. As expected the highest ratio is along the Al/FMI interface with the lowest ratio along the fuel/FMI interface. The bulk FMI layer atomic ratio was found to be $(U,Mo)(Al,Si)_{3.7}$. The Al/FMI interface has an atomic ratio of $(U,Mo)(Al,Si)_{6.65}$ and the FMI/Fuel interface has a ratio of $(U,Mo)(Al,Si)_{2.68}$.

Fission gas bubbles were seen in various regions throughout the FMI layer. It should be noted that not all areas in the FMI region show bubbles. Bubble sizes were measured in the FMI layer. In addition, the location of the bubbles were noted with the specific locations being the first 100 nm near the fuel/FMI layer interface, the bulk of the FMI layer, and the first 100 nm of the Al/FMI interface. Figure 4.61shows the bubble distributions of the FMI/fuel interface, the bulk, and FMI/Al interface. In addition to bubble distributions in specific locations, Figure 4.62 shows the bubble distribution of all FMI bubbles regardless of location.

4.10: TEM Analysis of RERTR-7 H.Flux

Key observations of TEM analysis of RERTR-7 H.Flux are provided and discussed in reference to the analysis of RERTR-6 and -7 L.Flux. A review of the irradiation parameters for RERTR-7 H.Flux are provided and examination of the following regions are presented: the crystal fuel region, the amorphous rim region, the FMI layer, and the Al-2wt%Si matrix.

Irradiation Parameters:

As a reminder, the irradiation parameters for this punch taken from the high flux end of plate R2R040 calculated by the PLATE code are: an irradiation temperature of 119-121˚C, fission rate of 8.11×10^{14} f/cm^3-sec, fission density of 6.3×10^{21} f/cm^3, and a heat flux of 307-337 W/cm^2. At this fission density, it is believed the fuel has undergone recrystallization (19). It is expected that the bubble superlattice will have transformed, leading to larger (>10 nm) sized bubbles distributed throughout the grains.

Crystal Fuel Region:

SEM analysis of RERTR-7 H.Flux shows that in the crystal fuel region, the grain sizes are sub-micron, with much higher density of intergranular type bubbles present when compared to RERTR-7 L.Flux. SEM comparison of RERTR-7 H.Flux vs. L.Flux can be seen in Figure 4.63a) and b) respectively. Additionally, TEM analysis shows an increase in density of these bubbles, which can be seen in Figure 4.63c) for RERTR-7 H.Flux and L. Flux. These bubbles are uniformly distributed throughout the fuel particles.

Most of the center of the fuel particles remains in a crystalline form. Pockets of amorphous material were seen around the large intergranular type bubbles in the crystal fuel. The crystal grains in the fuel have shrunk considerably from the low flux end of the plate and show a width of roughly 100-500 nm. This can be seen in Figure 4.64a). RERTR-7 L.Flux showed grain sizes on the range of 4 μm. In addition to the decreased size of the crystal grains, most of the intragranular type bubbles have disappeared, with some pockets of residual intragranular type bubbles remaining. This can be seen in Figure 4.64b).

An interesting discovery was seen in the crystal fuel pertaining to the intragranular bubbles and the recrystallization process. Figure 4.65 shows an area in the crystal fuel region where a grain has undergone amorphization but the bubble superlattice is still partially intact. This suggests that the superlattice might drive the grain amorphous prior to reaching a maximum bubble size. This is likely due to the significant damage imparted into the crystal grain from the irradiation

and the bubble superlattice. Lawson (65) showed that a bubble superlattice collapses at a diameter of roughly 6 nm with the bubbles coalescence with each other. The bubbles seen in RERTR-7 H.Flux are smaller than 6 nm. Another key observation in this figure is how the small gas bubbles are starting to migrate towards the large bubble, causing bubble growth, and forming a larger bubble similar to the intergranular type bubbles seen in Figure 4.63c).

Amorphous Rim:

The amorphous rim microstructure seen in RERTR-7 L.Flux is still present in the fuel particle and a typical amorphous rim can be seen in Figure 4.66. The amorphous rim thickness is greater, around 4 μm in RERTR-7 L.Flux compared to 8 μm in RERTR-7 H.Flux. This indicates that the Si is continually diffusing into the crystalline fuel region with increasing dose. EDS analysis showed that the Si content in the amorphous rim region has decreased to a range of 4 at% to 17 at% when compared to RERTR-7 L.Flux. In RERTR-7 L.Flux, the Si content can reach up 32 at% with most values ranging from 10-20 at%. This decrease is expected as there is a finite amount of Si in the system. This Si resides in the FMI layer and the amorphous rim. With little size growth in the FMI layer and an increase in the amorphous rim region thickness of up to two times, the Si will be distributed over a larger volume. This increased volume will decrease the Si concentration in the amorphous rim region and the FMI layer. In addition, at the crystal fuel/amorphous rim interface, the Si content is around 2-3 at%, indicating that some Si is present in the crystalline fuel region. Note that Si will still enter the FMI layer from the matrix due to Al transmutation into Si and from Si precipitates that were originally ou side of the PFZ zone.

FMI layer:

The FMI layer's microstructure, i.e. the bubble microstructure and layer thickness, does not change greatly from RERTR-7 L.Flux to H.Flux. A key observation in the FMI layer is the formation of cracking along the FMI layer/Al matrix interface in some locations. This can be seen in Figure 4.67. This cracking is not desirable as it can help with diffusion of gas bubbles, which can coalescence into large bubbles. This can lead to pillowing and breakaway swelling (22).

Al-2wt%Si Matrix:

The Al matrix showed an increase in the size of the Si precipitates developed by Al transmutation, ~10 nm when compared to those seen in RERTR-6 and -7 L.Flux (28). With no Si precipitates being seen in RERTR-9A and -9B, the Si precipitates seen are from transmutation of Al. The Si precipitates can be seen in Figure 4.68 as the small dark circular features. Additionally, larger voids, ~50 nm, were present in the matrix in various locations and these can be seen in Figure 4.68.

Key differences and similarities between RERTR-6, -7 L.Flux, and -7 H.Flux are:

- RERTR-6 and -7 L.Flux show bubble superlattices throughout the entire bulk of the fuel grains while -7 H.Flux shows some residual bubble superlattice in a few regions but the general microstructure is lacking of long range bubble superlattices
- Bubble sizes in the superlattices in -6 and -7 L.Flux are 3.5 and 3.1 nm respectively

- RERTR-7 H.Flux shows a higher density of intergranular bubbles when compared to -6 and -7 L.Flux.
- An amorphous rim is present between the crystalline fuel particles and the FMI layers in all three experiments but -7 H.Flux shows a thicker amorphous rim region when compared to -6 and -7 L.Flux, ~8 to 4 μm, respectively.
- The FMI layers are similar in all experiments
- The Al matrix shows small ~10 nm sized Si rich precipitates in each sample and RERTR-7 H.Flux shows large voids, ~50 nm.

As a reminder, Table 4.1 summarizes the key observations from each experiment pertaining to the three key questions/unknowns of this study.

4.11: Bubble Yield Calculation

A calculation was done to find the ideal diameter of the intragranular bubbles if all of the fission gases produced during irradiation was stored in the bubbles. This is being done to figure out how much of the fission gas is residing as intragranular bubble and as fission gas along the grain boundaries. The calculated intragranular bubble size can be compared to the measured TEM intragranular bubbles to find the percentage of fission gas that is likely in the form of intergranular bubbles and in-solution in the bulk. Below is the step by step of how the calculated bubble diameters were found:

Local fission densities for the TEM punches were found using the PLATE code. The fission densities for RERTR-6, RERTR-7 L. Flux, and RERTR-7 H. Flux are shown below:

Punch ID	Fission Density Fission/cm^3
RERTR-6	$4.5x10^{21}$
RERTR-7 L.Flux	$3.3x10^{21}$

Kr and Xe are the primary gases formed from fission. Fission yields for these gases were found for U^{235} in the thermal neutron spectrum (66). Only the stable isotopes for Kr and Xe were used in determining the fission yields for each element. The summation of the stable fission yields for Kr and Xe are 0.03756 and 0.21006 atoms/fission respectively. The total yield for the fission gases is 0.24762 atoms/fission (67). Using the total yields and fission densities for the designated punches, the total gas atoms created in a cm^3 can be found and is shown below for each punch. This was done by taking the fission density of each punch and multiplying it by the total fission gas yield.

Punch ID	Gas Density atom/cm^3
RERTR-6	$1.11x10^{21}$
RERTR-7 L.Flux	$8.17x10^{21}$

From the TEM images, the intragranular bubbles were shown to be in a FCC structure. The number of atoms, or bubbles in this case, per a FCC unit cell is 4 atoms. The lattice constant for the intragranular superlattice was measured for each punch condition and is listed below.

Punch ID	Lattice Parameter nm
RERTR-6	12.01
RERTR-7 L.Flux	11.71

The volume of the unit cubic cell and the number of atoms/bubbles in a FCC unit cell can be used to find the number of bubbles/cm^3. The volume of a unit cubic cell is the bubble lattice parameter cubed. The number of bubbles in a FCC unit cell is 4 and by taking this value and dividing it by the volume of the cube, the bubble density was found.

Punch ID	Bubble Density bubble/cm^3
RERTR-6	$2.5x10^{18}$
RERTR-7 L.Flux	$2.26x10^{18}$

Using the bubble densities and gas densities, the number of gas atoms in a bubble can be found. This was found by taking the gas density and dividing it by the bubble density.

Punch ID	Gas atoms per bubble atoms/bubble
RERTR-6	446
RERTR-7 L.Flux	362

A gas atom is assumed to have a volume of 0.085 nm^3 (13). Using this value and the gas atoms per a bubble, the total volume of an intragranular bubble can be found. This is done by taking the gas atoms in a bubble and multiplying it by the gas atom volume of 0.085 nm^3. This is shown below.

Punch ID	Volume Bubble nm^3
RERTR-6	37.9
RERTR-7 L.Flux	30.7

Assuming that the bubbles are spheres and knowing that the volume of a sphere is $4/3\pi r^3$, the calculated diameter of the bubble can be found and is shown below. Additionally, the experimental TEM value is provided for each punch and the difference between the measured and calculated value is shown.

Punch ID	Measured Diameter nm	Calculated Diameter nm	Percent Difference %
RERTR-6	4.27	3.53	17.33
RERTR-7 L.Flux	3.76	3.1	17.55

Note that this analysis does not take into effect any external effect that might be affecting the bubble sizes. Using Olander's (13) analysis on the amount of gas in a bubble in section 13.2.4 in his book, it is noticed that bubble size plays an effect on the gas atoms present in a bubble. Olander uses the Van der Waals correction to describe the gas-atoms in a bubble. This correction is shown below.

$$m = \frac{8\pi r^2 \gamma}{3(RT + \frac{2B\gamma}{r})} \text{ or } = \frac{8\pi r^2 \gamma}{3RT} + \frac{4\pi r^3}{3B}$$

where m is the moles of gas, r is the radius of the bubble, B is Van der Waals constant for a gas, R is the gas constant, T is the temperature, and γ is the surface tension.

Olander proposed that the for bubble radius's under 1 nm, the first term in the equation above does not affect the number of gas atoms. This shows that the surface tension doesn't play a major factor on the number of gas atoms when the bubble radius is around 1 nm. For bubbles greater than 100 nm, the 1st term in the equation above is the dominating factor and the 2nd term can be ignored. For bubble greater than 100 nm, the surface tension is the major driving force. Knowing that the bubble radius's in RERTR-6 and -7 L.Flux are ~1.75 nm in size, the first term

was used to find the gas-atoms in a bubble. For RERTR-6, the gas-atoms in bubble was found to be ~264 atoms. This is assuming that B is equal to 0.085 nm^3.

This 264 atoms is lower than the 446 atoms per bubble calculated in the bubble yield calculation. The proposed reason for the difference is that the Van der Waals constant is temperature dependent. Olander reported it as a constant and this assumption is not true. Cost (68) noted that to properly find the Van der Waals constant, virial coefficients should be used to find the temperature dependence on the Van der Waals constant. The use of the virial coefficients on the Van der Waals equation can be seen below.

$$\frac{pV}{m} = RT + Bp + Cp^2$$

where p is the pressure of the bubble, V is the volume of the bubble, m is the moles of gas in a bubble, R is the gas constant, T is the temperature, and B and C are the virial coefficients.
To find the proper viral coefficients, a combination of 80% Xe and 20% Kr gas needs to be analyzed to find the viral coefficients. No literature data on this analysis was found at the time of this writing. One key observation noted by Cost is that the when comparing the standard Van der Waals with the virial coefficient modified Van der Waals equation, the standard Van der Waals predicts that the gas atom in a bubble are 50% less than the viral coefficient modified Van der Waals equation. Adding the 50% difference to the calculated Van der Waals gas-atom calculation of 264 atoms for RERTR-6, the number of gas atoms in a virial coefficient modified Van der Waals calculation is 396 atoms. This is within 88% of the gas atoms in a bubble in the bubble yield calculation.

To best determine the correct gas-atoms in bubble, the virial coefficients for an 80%Xe and 20% Kr gas needs to be found. Once knowing these coefficients, the better idea of the gas atoms in a bubble can be found and this will improve the accuracy of the model that will be presented in Chapter 6.

Table 4.1: List of experiments conducted, the key observations of the experiment pertaining to the three questions/unknowns, and which question/unknown the experiment supports

Experiment	Key Observations	Supports Key Question
TEM studies of Al-2wt%Si powder	Si forms precipitates in the Al Matrix	Si Modified FMI Layer
TEM DU Alloys-Unirradiated	No major observations	Si Modified FMI Layer
TEM DU Alloys-Proton Irradiated	Stable Microstructures of the DU Alloys	Si Modified FMI Layer
TEM DU Alloys-Kr Irradiated	$U_6Mo_4Al_{43}$ forms large gas bubbles. $(U,Mo)(Al,Si)_3$ doesn't form bubbles up to a dose of 100 dpa	Si Modified FMI Layer
TEM DU-7wt% Foils-Unirradiated	Fuel shows signs of decomposition into U_2Mo and alpha U	Bubble Superlattice
TEM DU-7wt% Foils-Xe Irradiated	Experiment unsuccessful	Bubble Superlattice
TEM RERTR-9A and -9B	FMI layer is nano-crystalline and forms $(U,Mo)(Al,Si)_3$ type grains	Si Modified FMI Layer
OM, SEM, TEM RERTR-6	FMI amorphous, Si rich amorphous rim forms, bubble superlattice is FCC in orientation	Si Modified FMI Layer, Amorphous Rim, Bubble Superlattice
OM, SEM, TEM RERTR-7 L.Flux	FMI amorphous, Si rich amorphous rim forms, bubble superlattice is FCC in orientation	Si Modified FMI Layer, Amorphous Rim, Bubble Superlattice
OM, SEM, TEM RERTR-7 H. Flux	Bubble superlattice virtually gone, large density of intergranular bubbles, larger amorphous rim	Si Modified FMI Layer, Amorphous Rim, Bubble Superlattice

Table 4.2: Target phase composition, the DU-alloy in which the target phases is present, and the pre-irradiation microstructure of the target phases.

Target Phase	DU-Alloy	Pre-irradiation Defect Microstructure
$U(Al,Si)_3$	A	Extra diffraction spots from superlattice
$(U,Mo)(Al,Si)_3$	D	Clean
UAl_4	B	Mo-rich Precipitates
$U_6Mo_4Al_{43}$	B	Clean
UMo_2Al_{20}	B and D	High density stacking faults

Table 4.3: Summary of the irradiated microstructures of the DU-Alloys and Al

Phase	Dose to Amorphization (dpa)	Microstructure at 10 dpa	Microstructure at 100 dpa
$U(Al,Si)_3$	>100 dpa	Dislocation line and loop defects, clear SAD pattern	Clear SAD pattern, superdislocation and spots evident, no voids
$(U,Mo)(Al,Si)_3$	2	Amorphous, no defects, no voids	Amorphous, no defects, no voids
UMo_2Al_{20}	5	Amorphous, no defects, no voids	Amorphous, no defects, no voids
UAl_4	>100	Small defects, small bubbles (2-3 nm), preexisting precipitates dissolving	Degradation of SAD and kikuchi pattern, small bubbles (2-3 nm), complex defect microstructure, no voids
$U_6Mo_4Al_{43}$	<1	Amorphous, small bubbles (2-3 nm)	Amorphous, large bubbles (>5 nm)
Al	>100	Not available	Small voids (2-5 nm), dislocation loops and networks

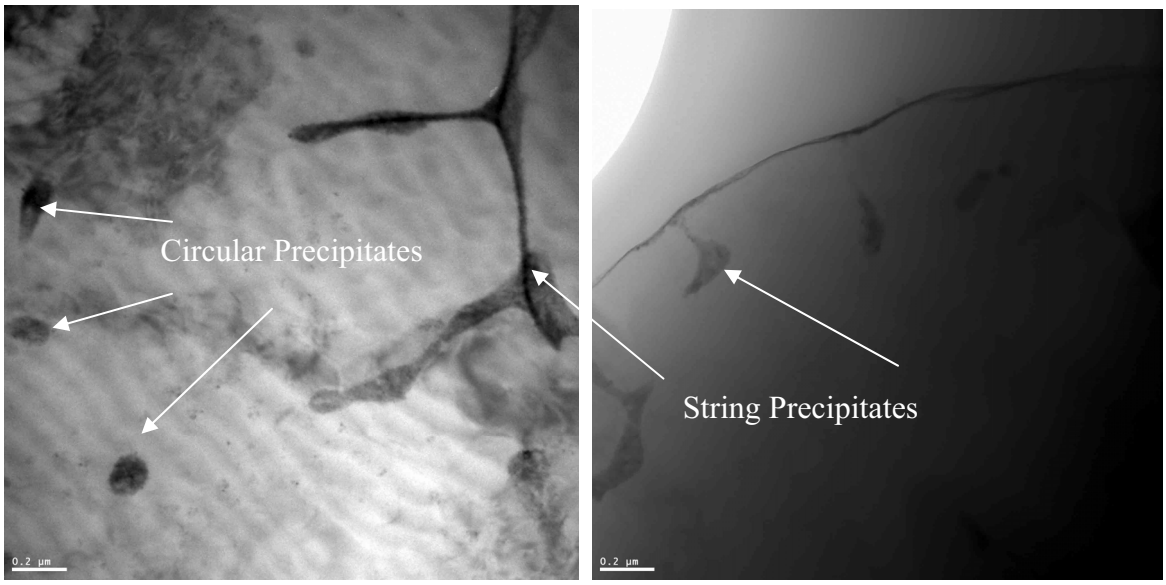

Figure 4.1: BF images showing Si precipitates in an Al-2wt%Si powder sample: a) BF image showing Si circular precipitates and Si string precipitates and b) BF image showing Si decorating an Al grain boundary and Si string precipitates.

a) 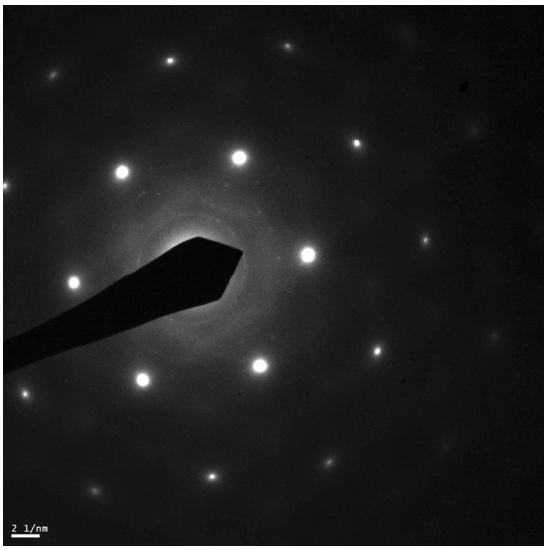

b) 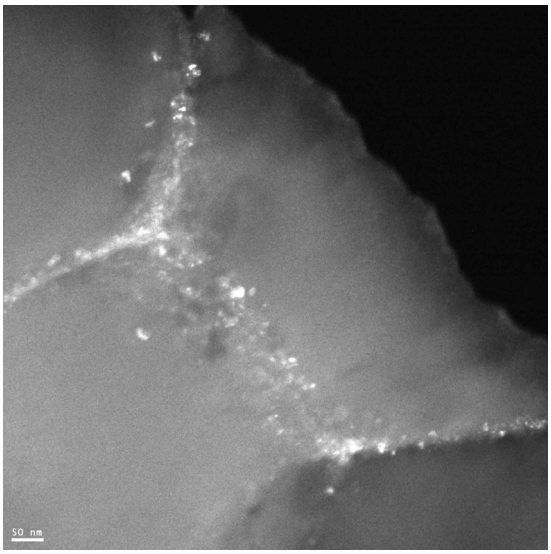

c) 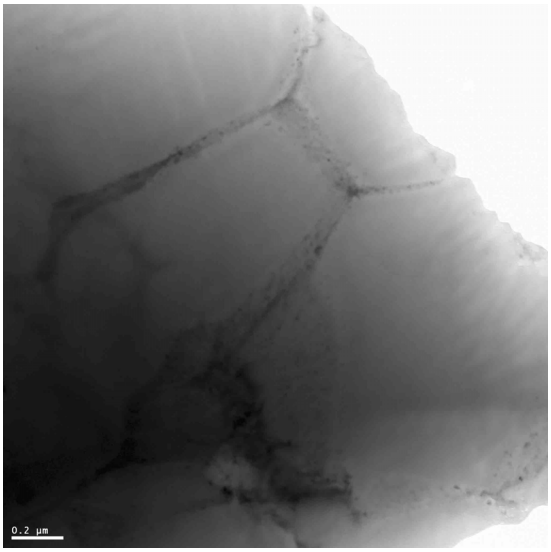

Figure 4.2: a) Electron diffraction pattern over a Si string precipitate showing a faint ring pattern indicating nano-crystals, b) WBDF image of the Si string precipitates using a portion of the ring pattern in a), and c) BF image of the Si string precipitate.

a) 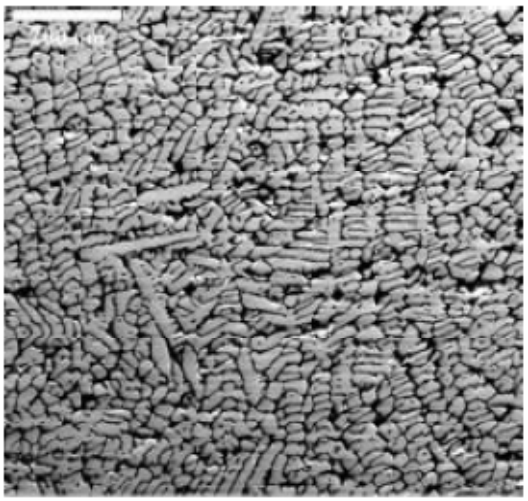 b) 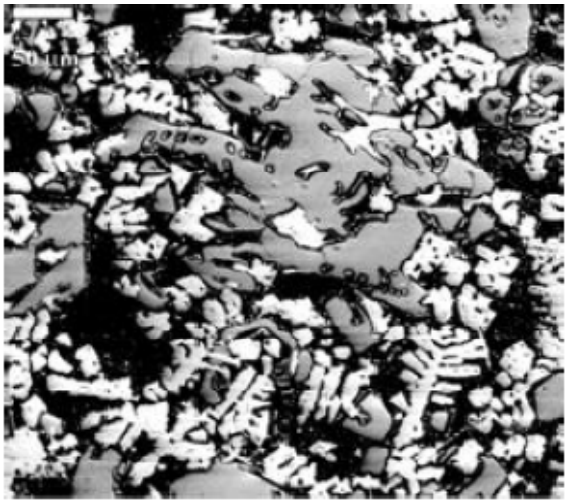

c) 

Figure 4.3: SEM images of the DU-alloys microstructures for a) Alloy A, b) Alloy B, and c) Alloy D. In a) the dark phase is Al and the light grey phase is $U(Al,Si)_3$. In b) the dark phase is Al, the dark grey phase is $U_6Mo_4Al_{43}$, and the white phase is UAl_4. In c) the dark phase is Al with pockets of UMo_2Al_{20} and the light phase is $(U,Mo)(Al,Si)_3$.

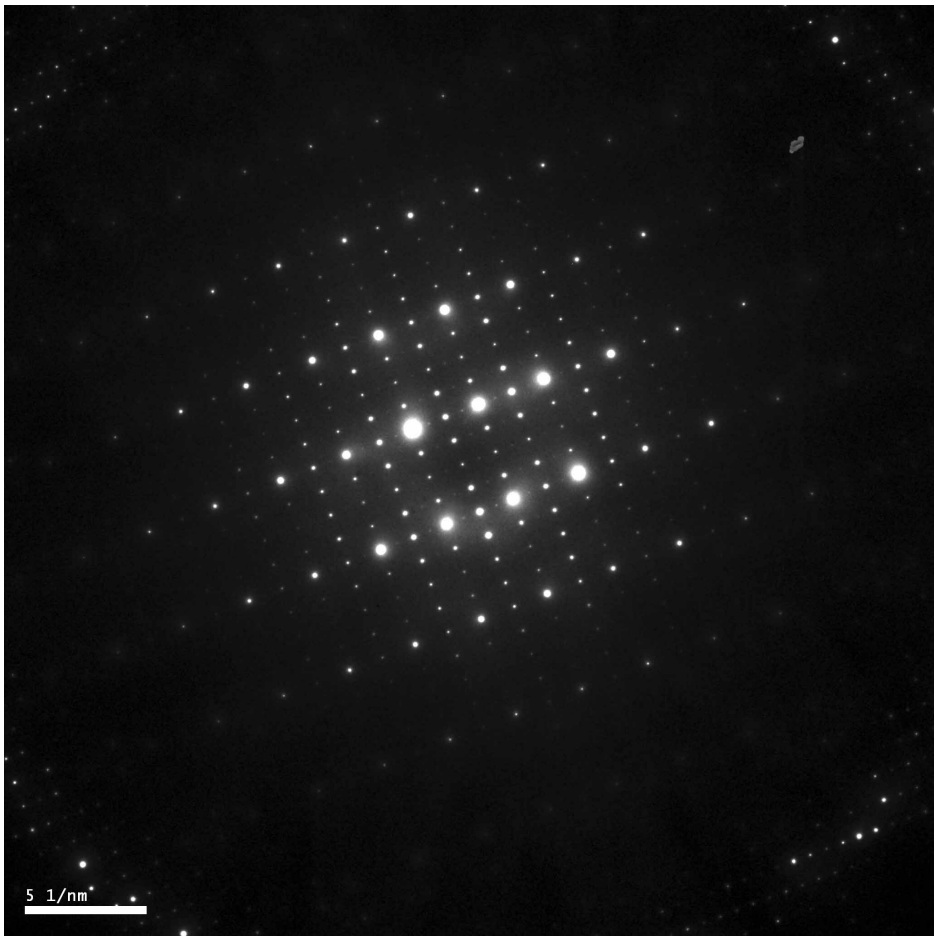

Figure 4.4: SAD pattern of $U(Al,Si)_3$ at z=[110] showing the extra superlattice spots with the addition of the extra diffraction spots for the ordered structure.

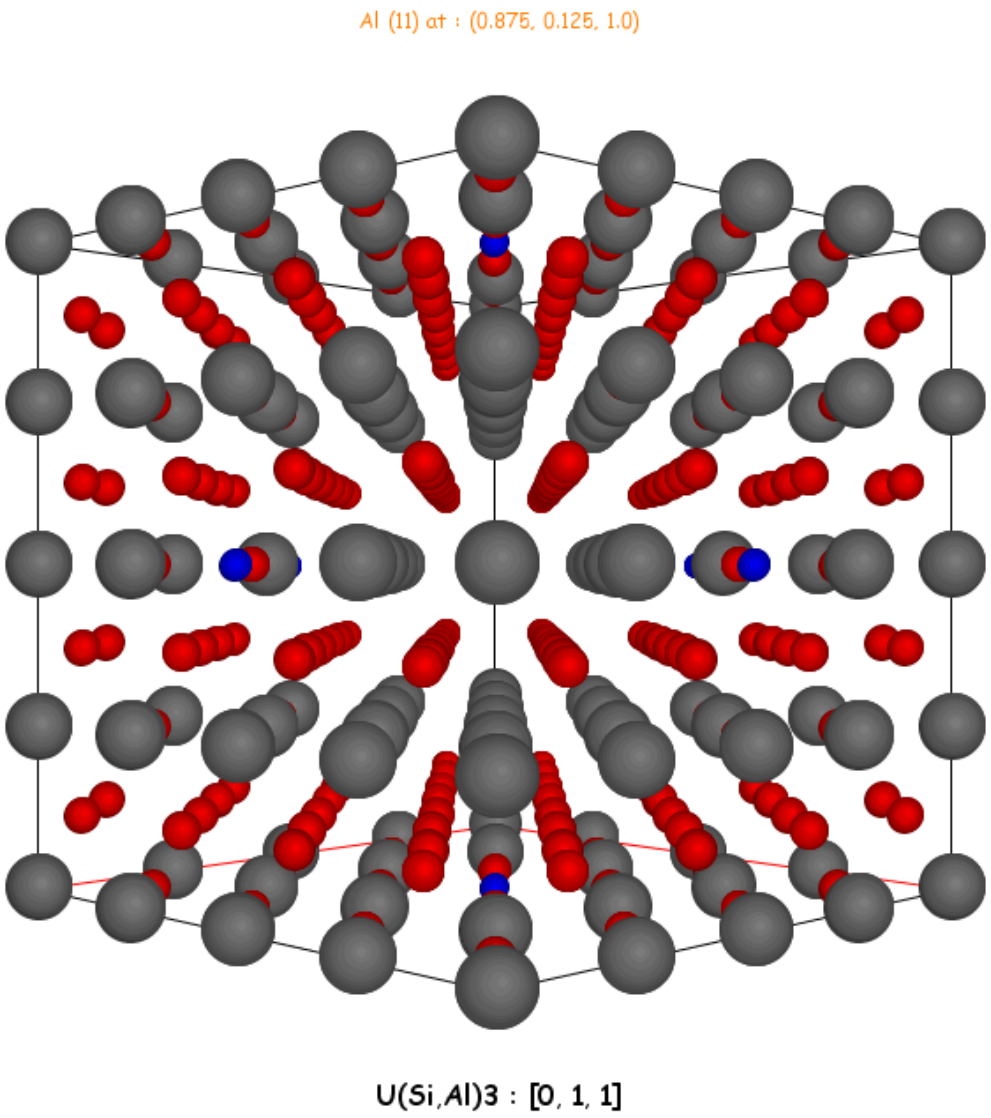

Figure 4.5: Superlattice box of $U(Al,Si)_3$ at z=[011] showing the location of specific atoms. Grey atoms represent U, red atoms represent Al, and the blue atoms represent Si atoms.

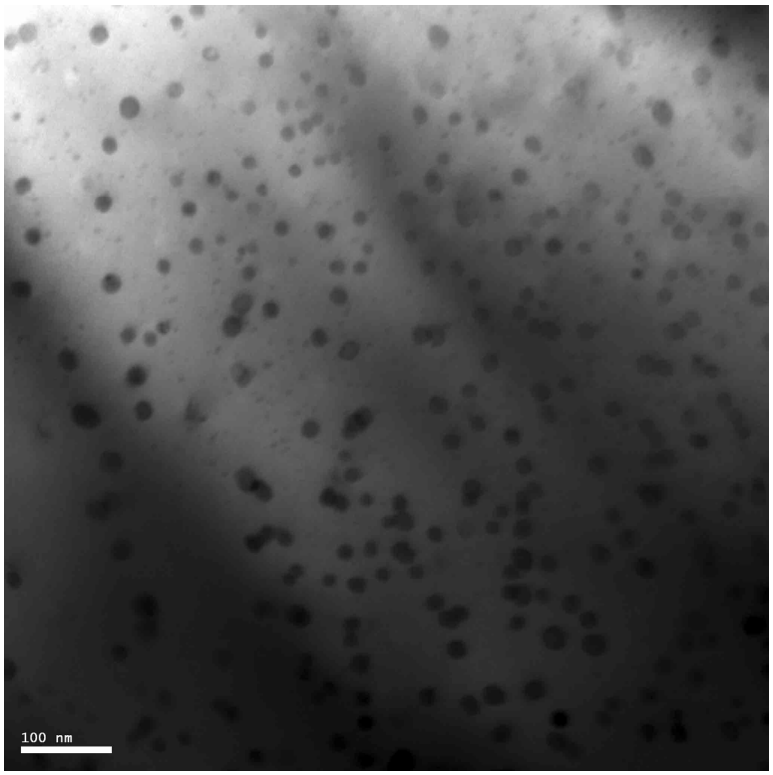

Figure 4.6: Molybdenum rich precipitates in UAl_4

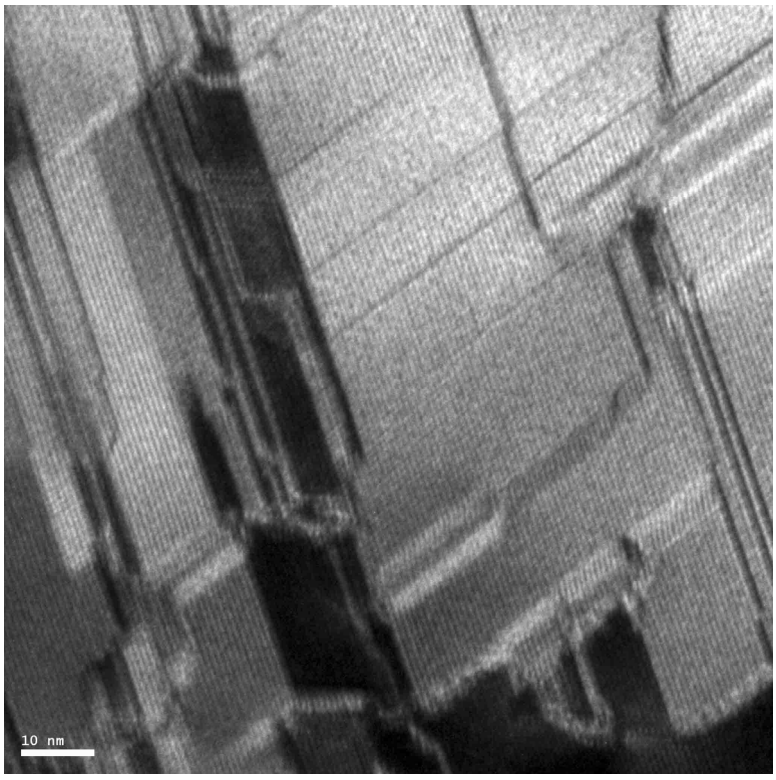

Figure 4.7: BF images of UMo_2Al_{20} showing a high density of stacking faults

a) 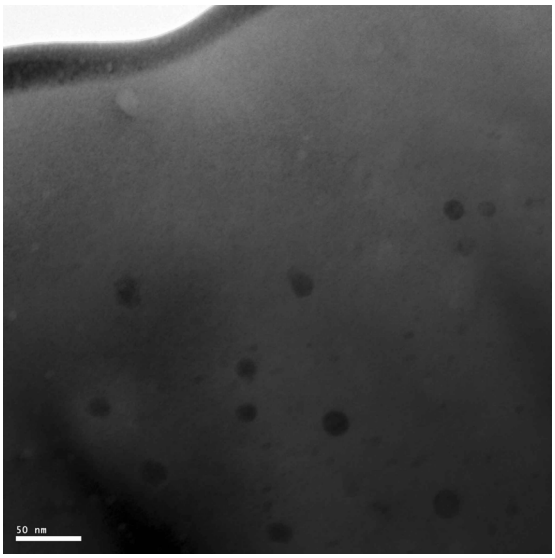

b) 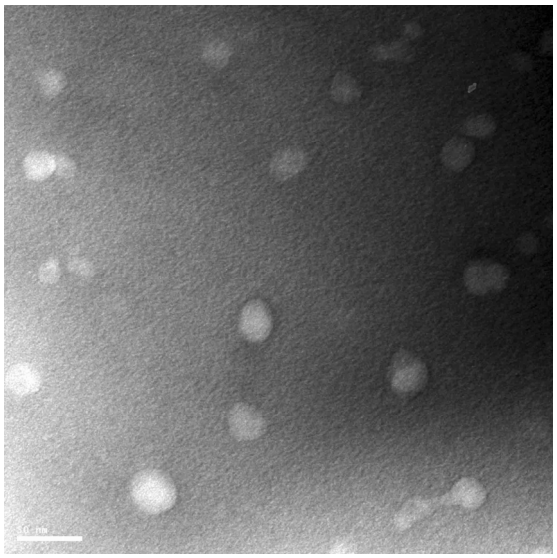

c) 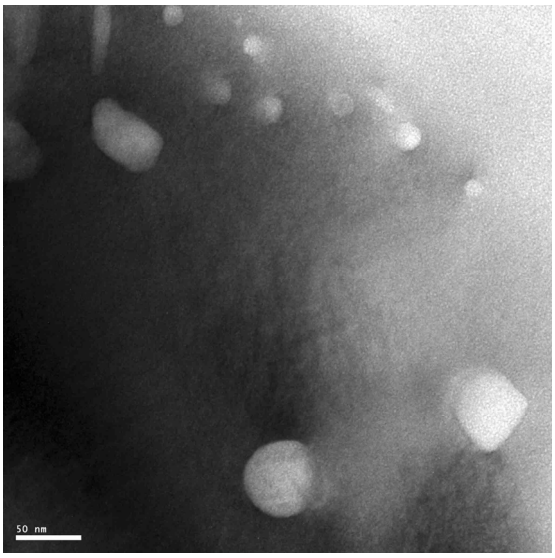

Figure 4.8: BF images showing the Mo precipitate coarsening with increasing doses: a) unirradiated, b) 0.27 dpa, and c) 0.86 dpa. Scale=50 nm.

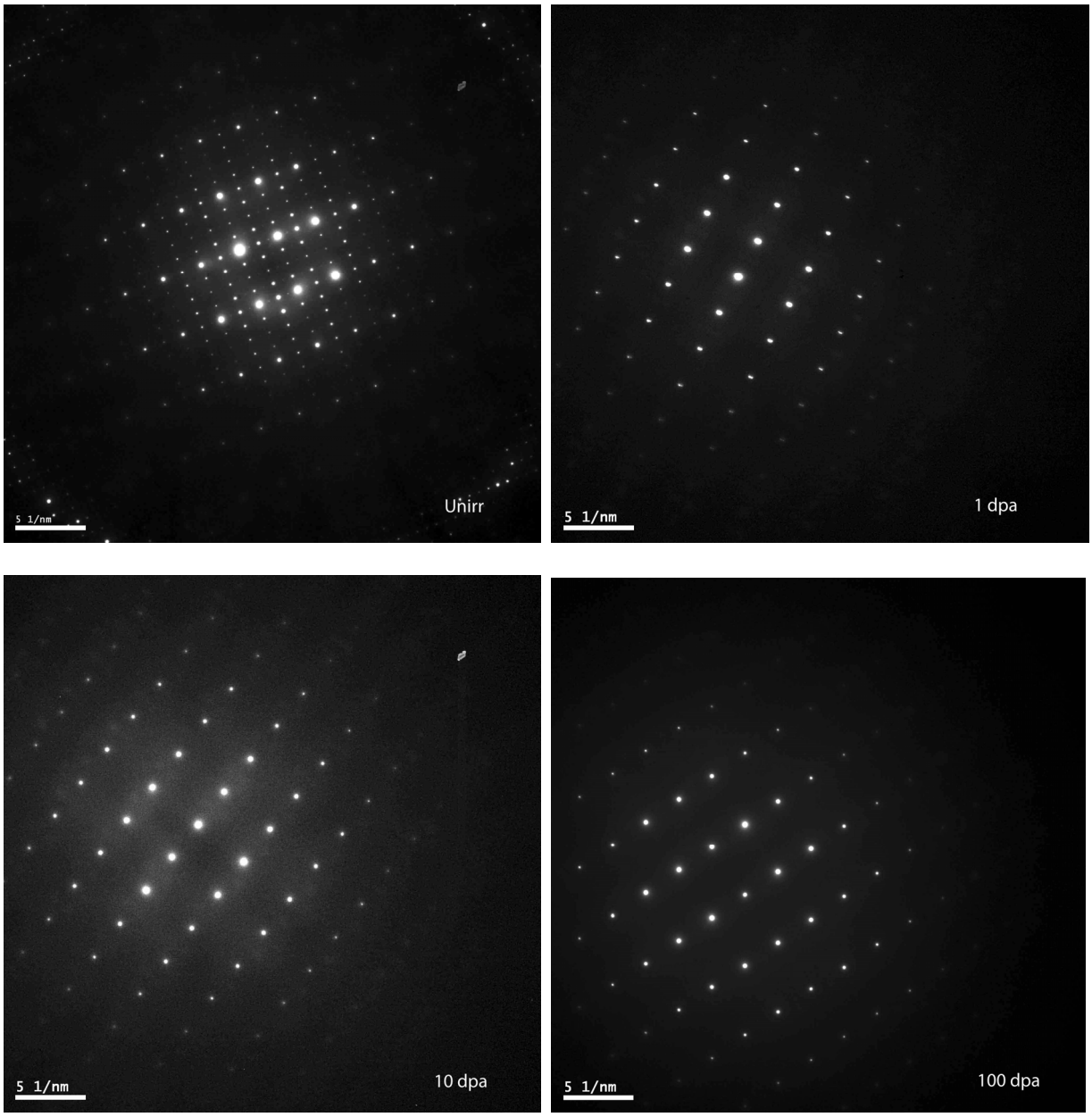

Figure 4.9: SAD patterns of $U(Al,Si)_3$ at z=[011] at irradiation doses of unirradiated, 1, 10, and 100 dpa

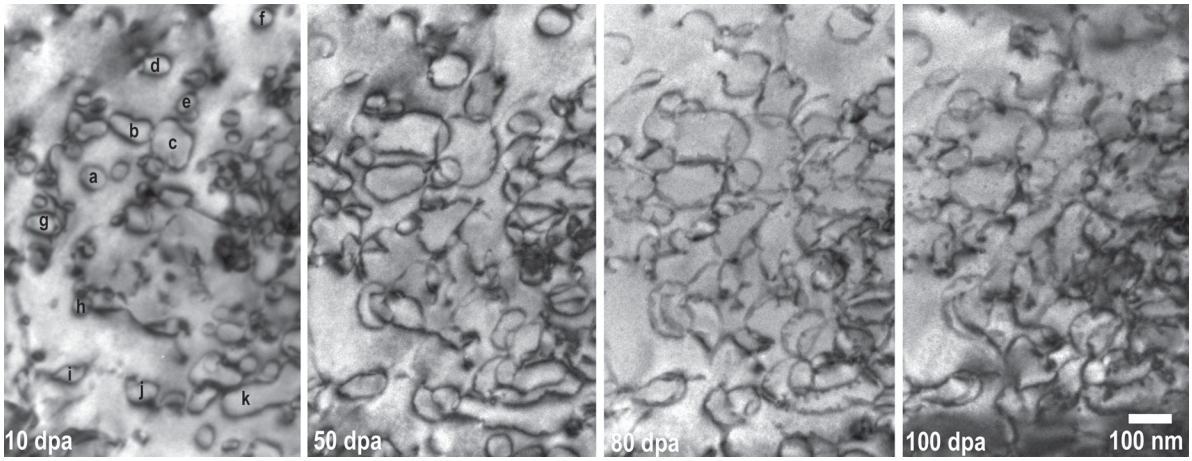

Figure 4.10: Dislocation evolution of $U(Al,Si)_3$ with increasing dose at a g=-1, 1,-1 two-beam condition. Images were obtained at 10, 50, 80, and 100 dpa.

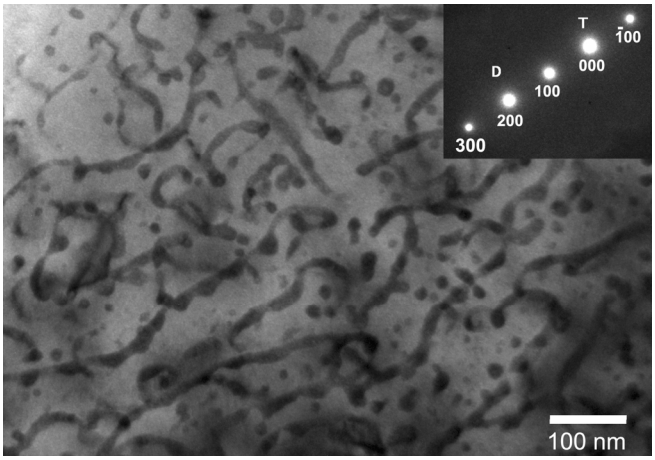

Figure 4.11: Ribbon-dislocations and spot features of $U(Al,Si)_3$ at 100 dpa

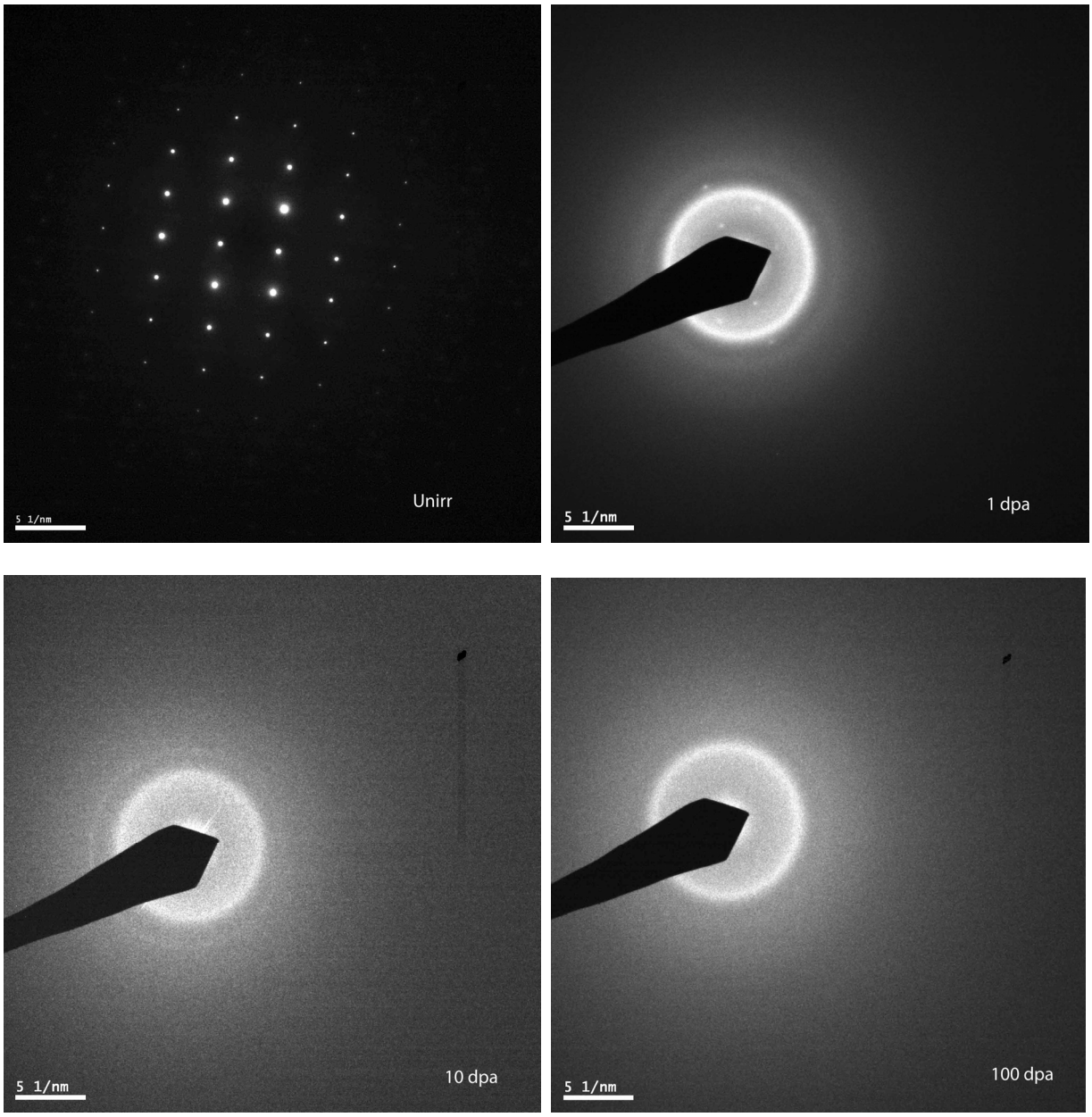

Figure 4.12: SAD pattern evolution of $(U,Mo)(Al,Si)_3$ with increasing irradiation dose: unirradiated, 1, 4, and 100 dpa.

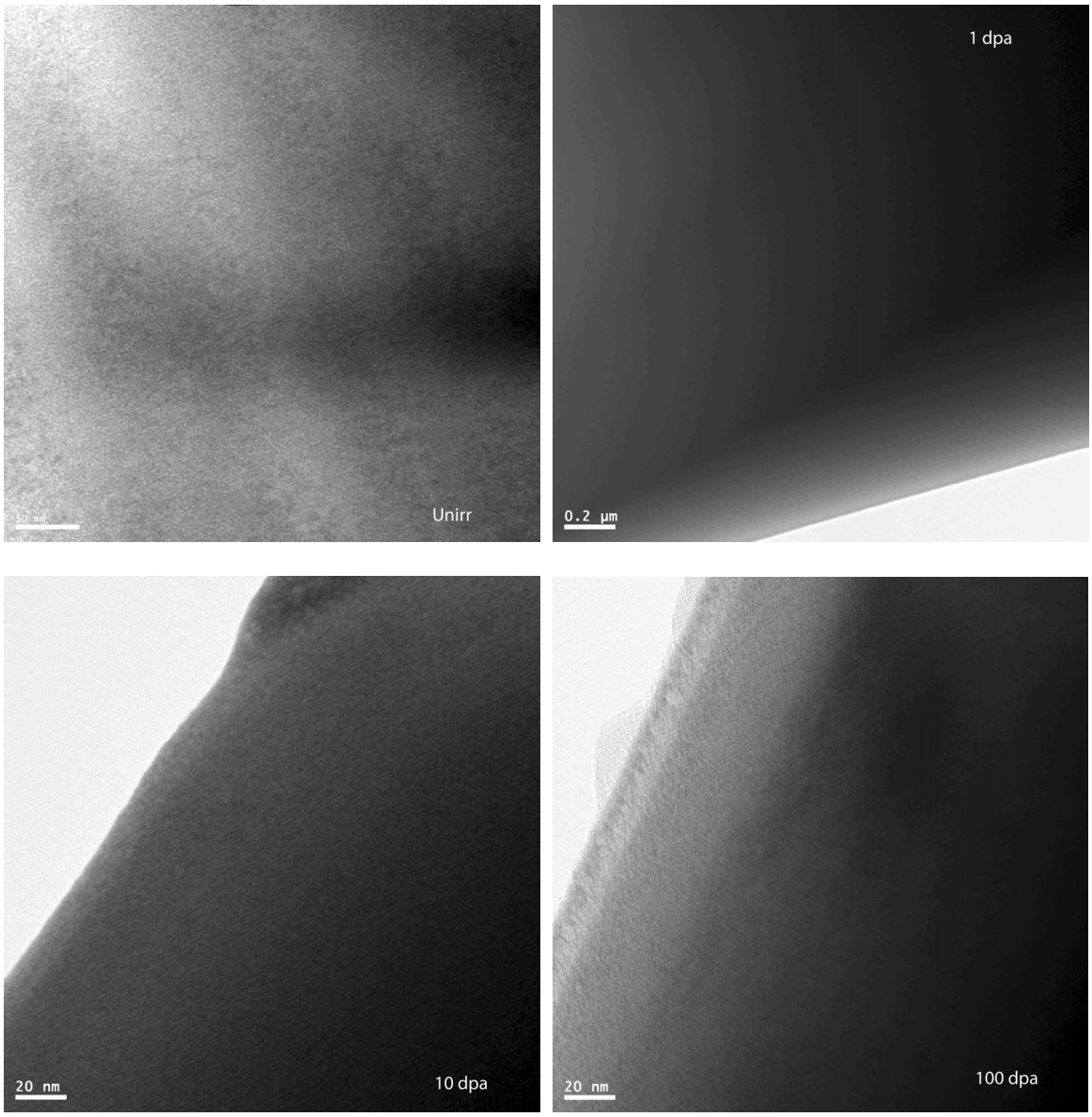

Figure 4.13: Defect microstructure evolution of $(U,Mo)(Al,Si)_3$ with increasing doses of unirradiated, 1, 4, and 100 dpa. Unirradiated image is at a g=111 two-beam condition. Note that the images are at different magnifications.

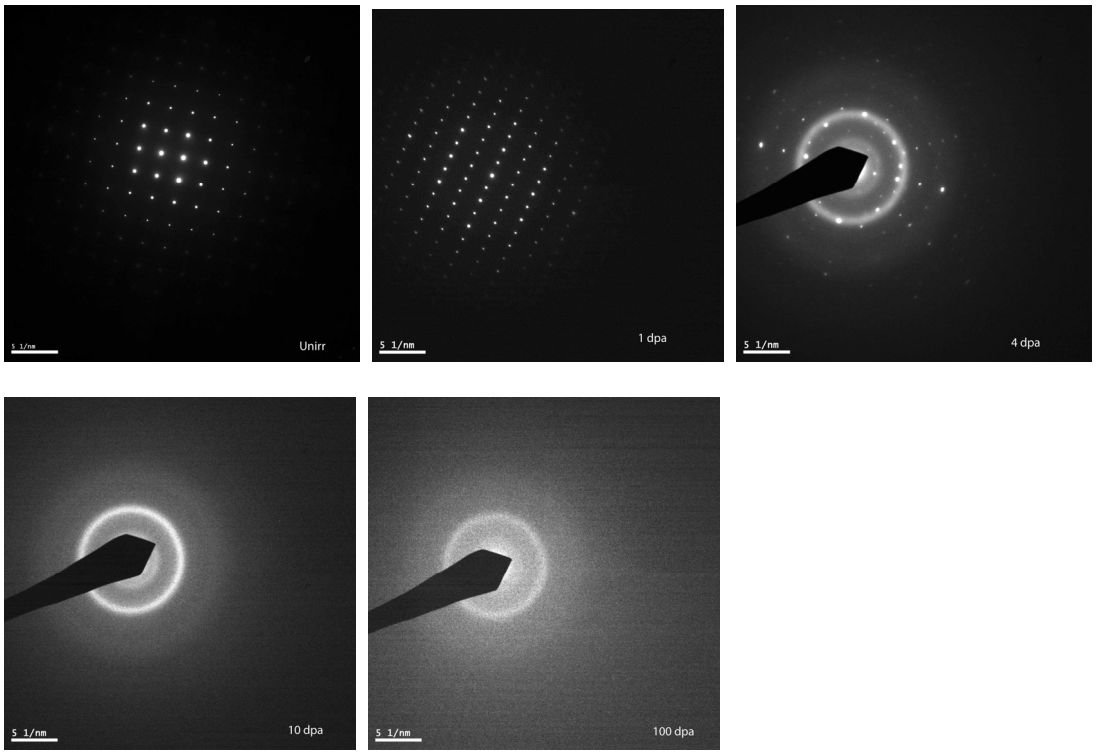

Figure 4.14: SAD pattern evolution of UMo_2Al_{20} with increasing doses of unirradiated, 1, 4, 10, and 100 dpa.

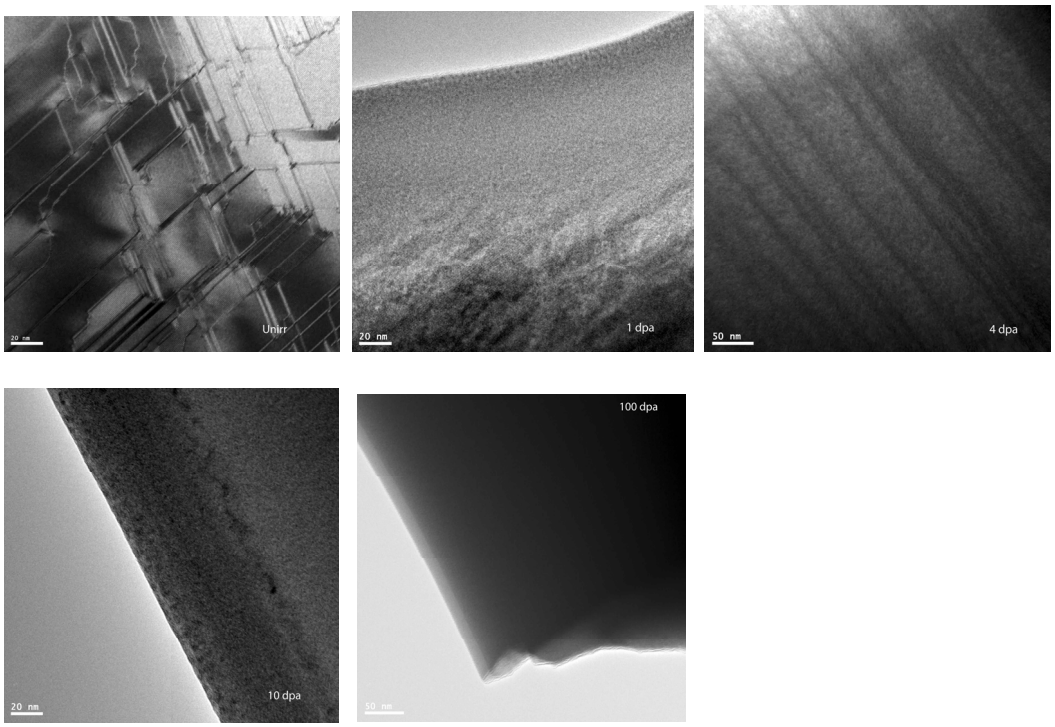

Figure 4.15: Defect microstructure evolution of UMo_2Al_{20} with increasing doses of unirradiated, 1, 4, 10, and 100 dpa. Note that the images are at different magnifications.

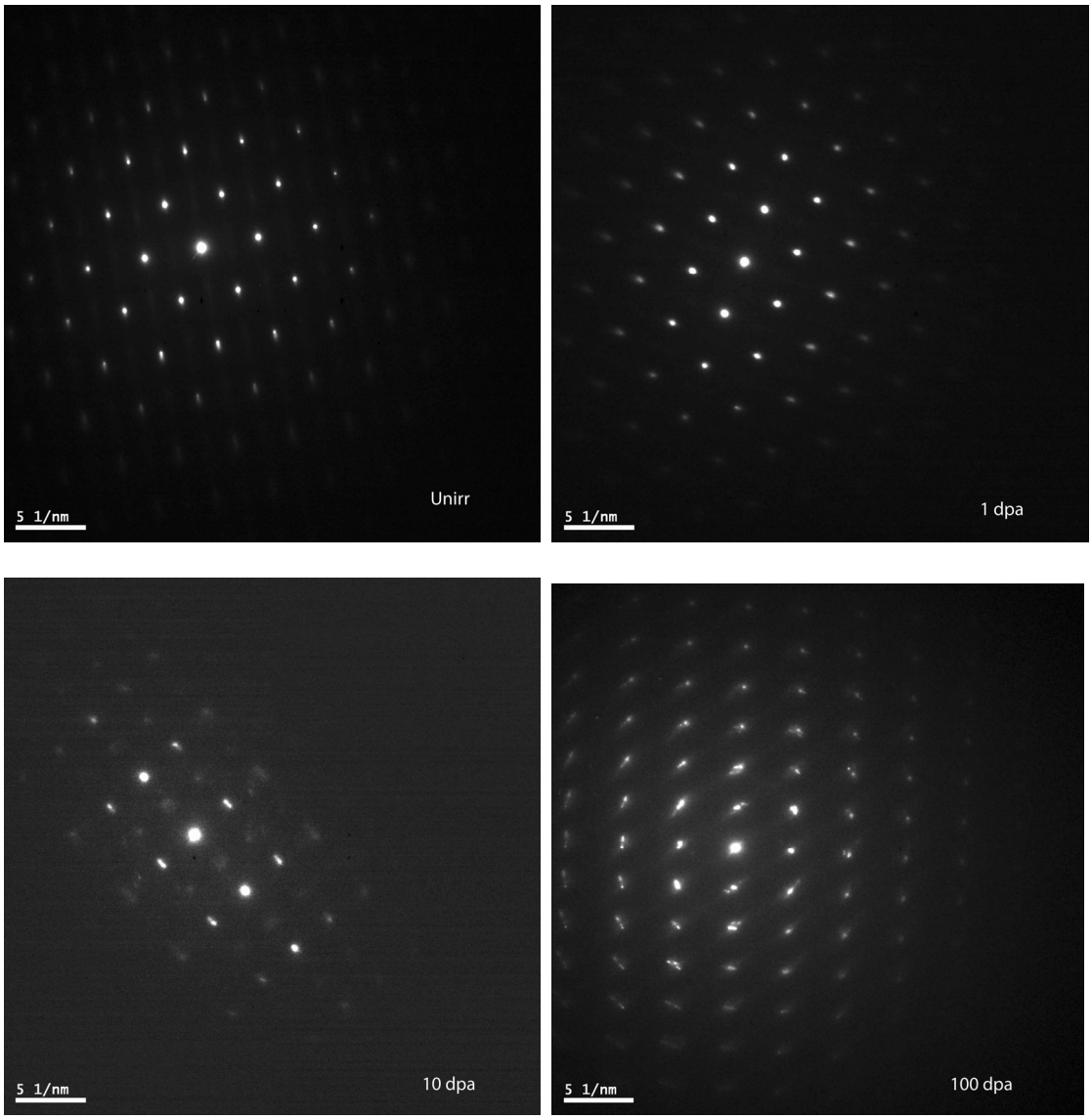

Figure 4.16: SAD pattern evolution of UAl_4 with increasing doses of unirradiated, 1, 10, and 100 dpa.

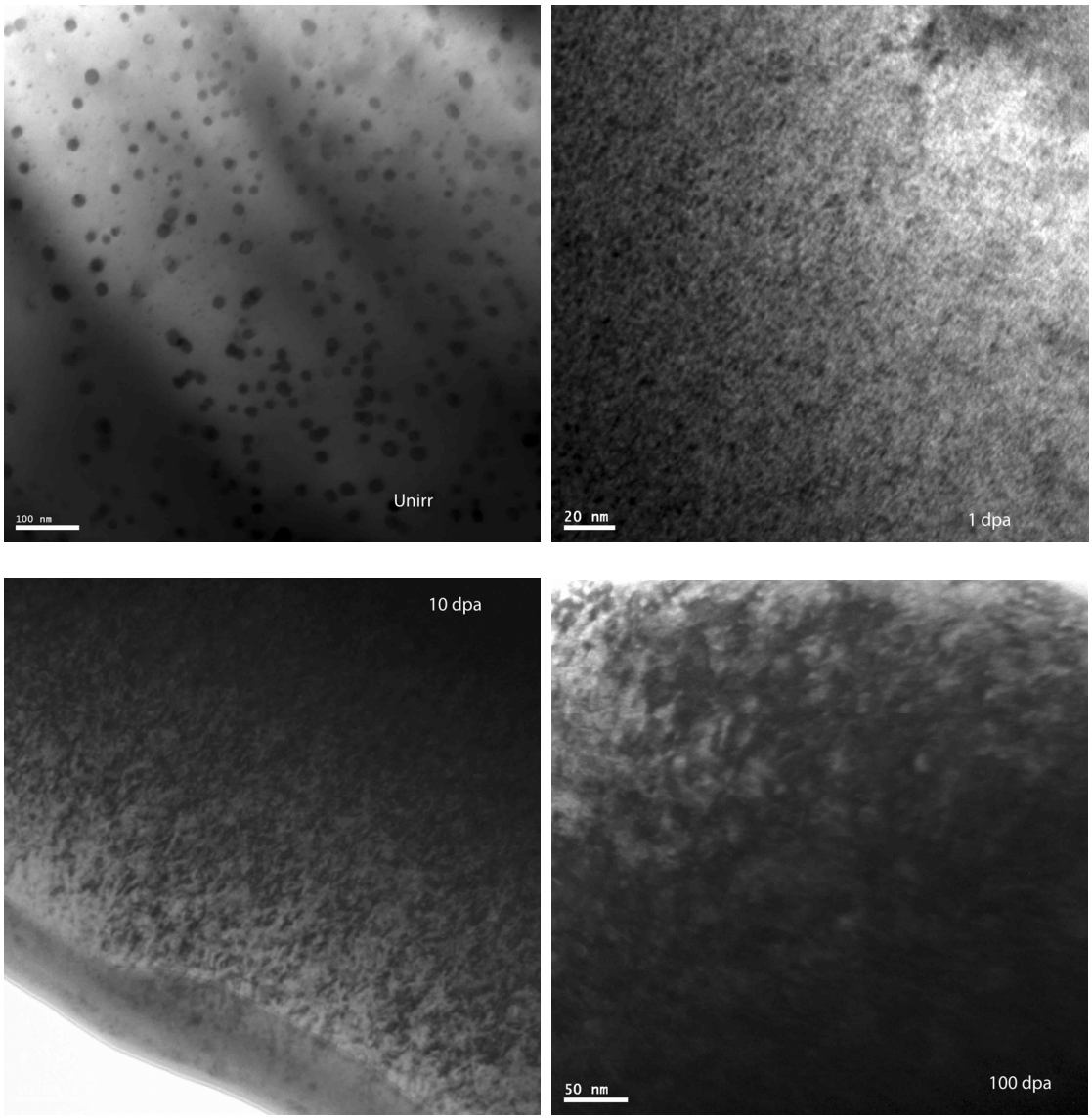

Figure 4.17: Defect microstructure evolution of UAl_4 with increasing doses of unirradiated, 1, 10, and 100 dpa. Note that the images are at different magnifications.

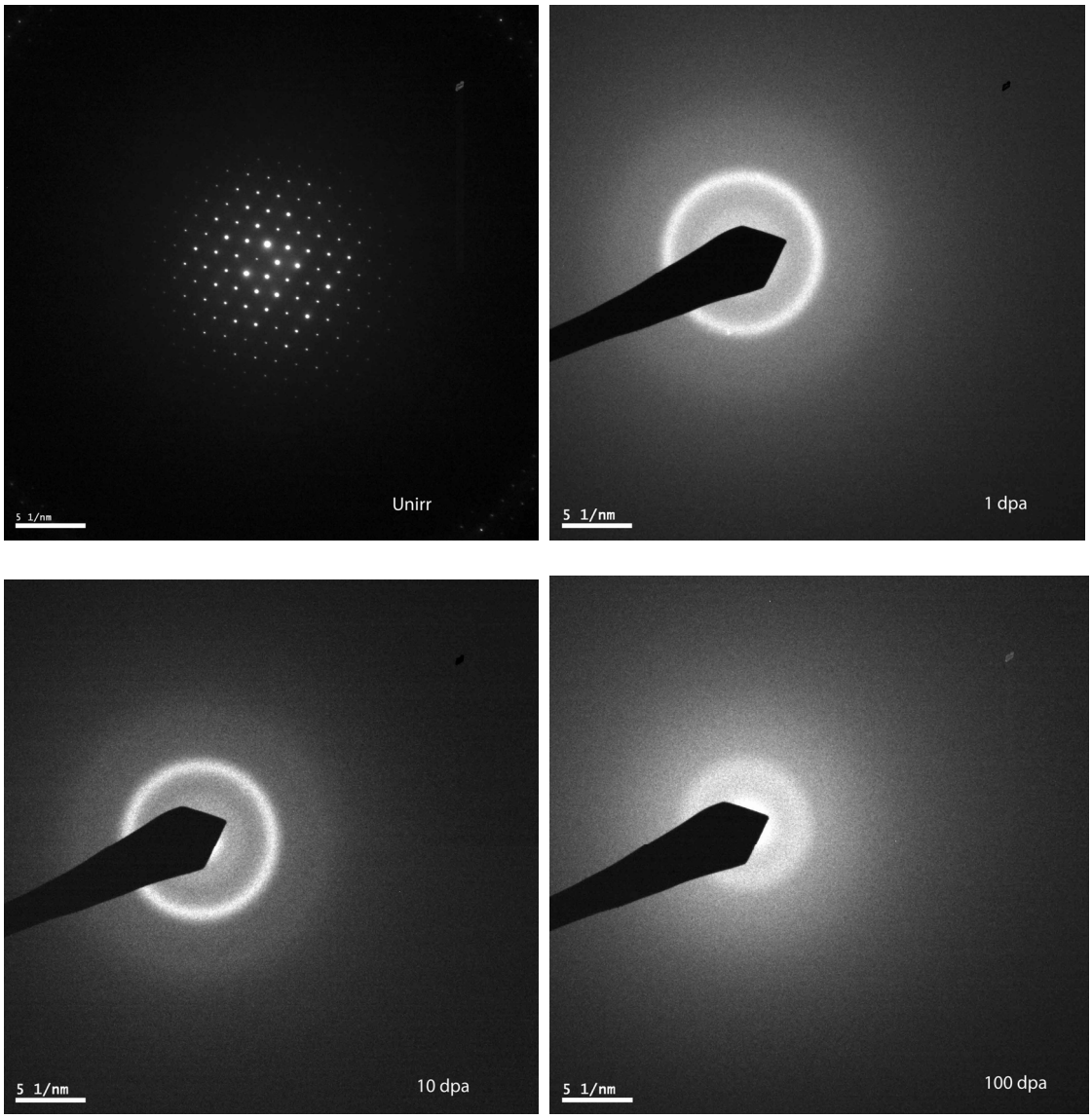

Figure 4.18: SAD pattern evolution of $U_6Mo_4Al_{43}$ with increasing doses of unirradiated, 1, 10, and 100 dpa.

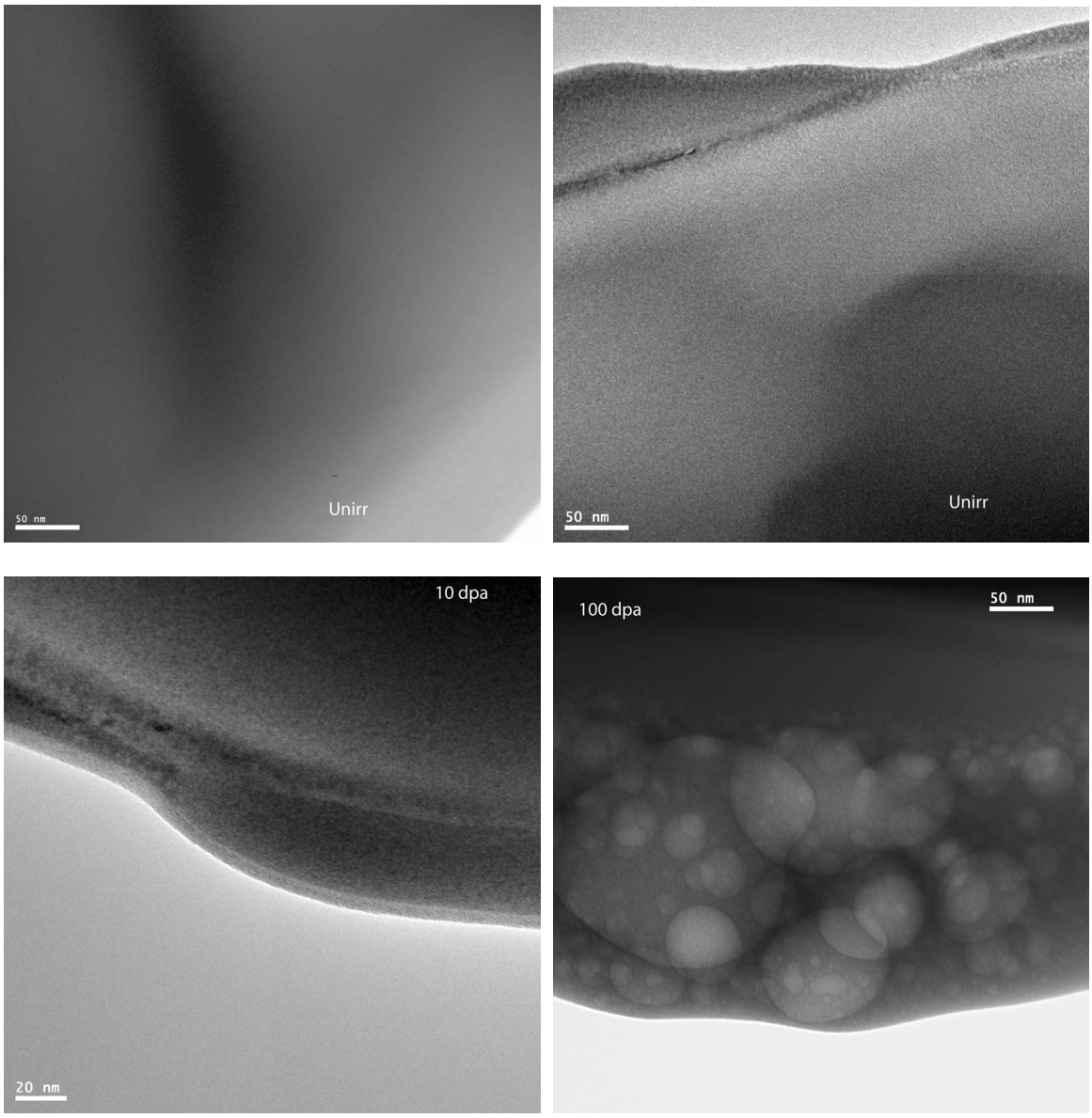

Figure 4.19: Defect microstructure evolution of $U_6Mo_4Al_{43}$ with increasing doses of unirradiated, 1, 10, and 100 dpa. Note that the magnifications vary throughout the images.

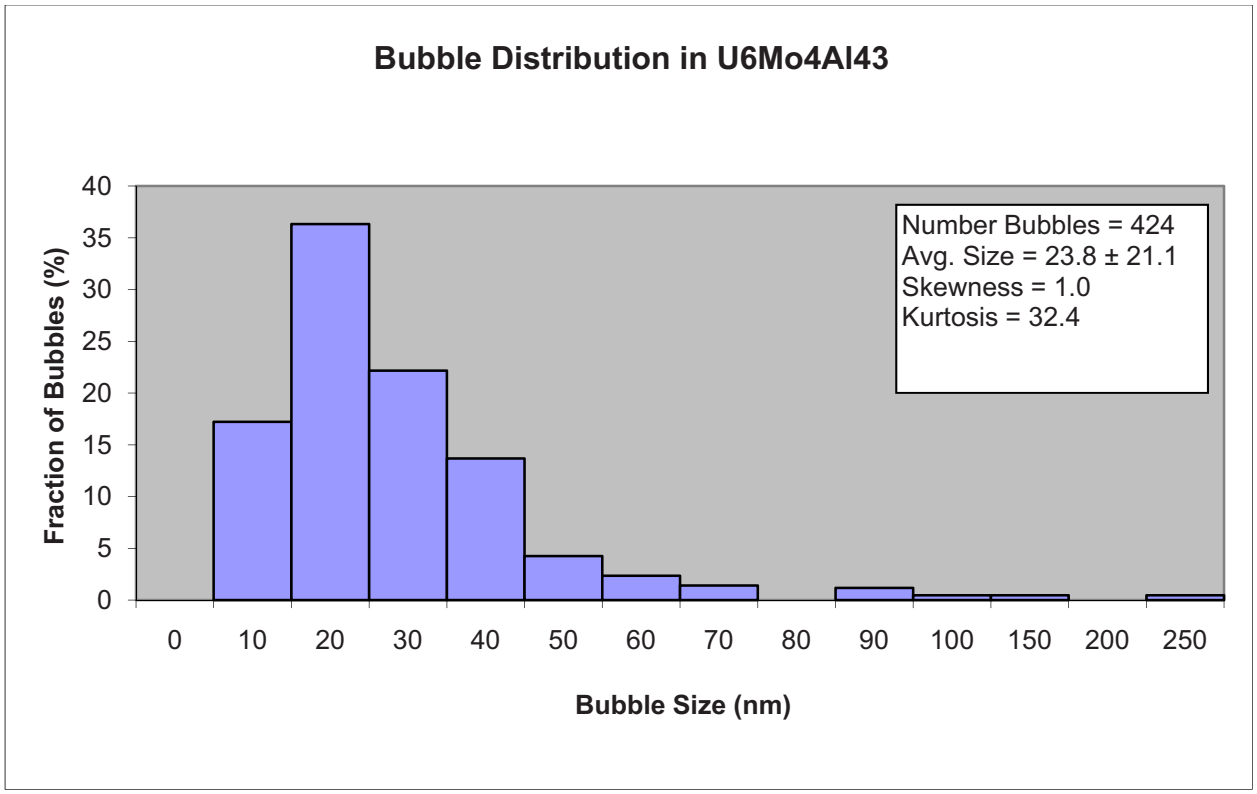

Figure 4.20: Gas bubble distribution of $U_6Mo_4Al_{43}$ at 100 dpa.

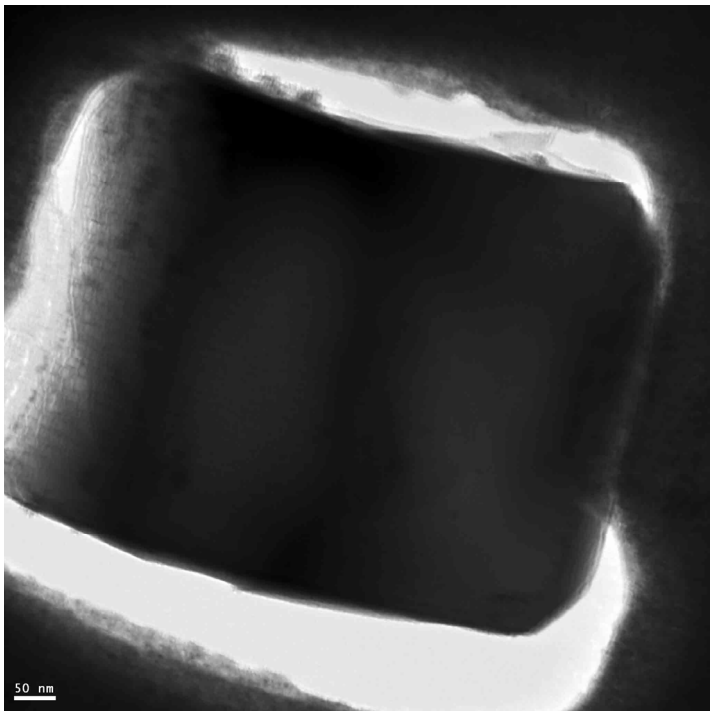

Figure 4.21: α-U precipitate in the as-fabricated hot-rolled DU-7wt%Mo foil

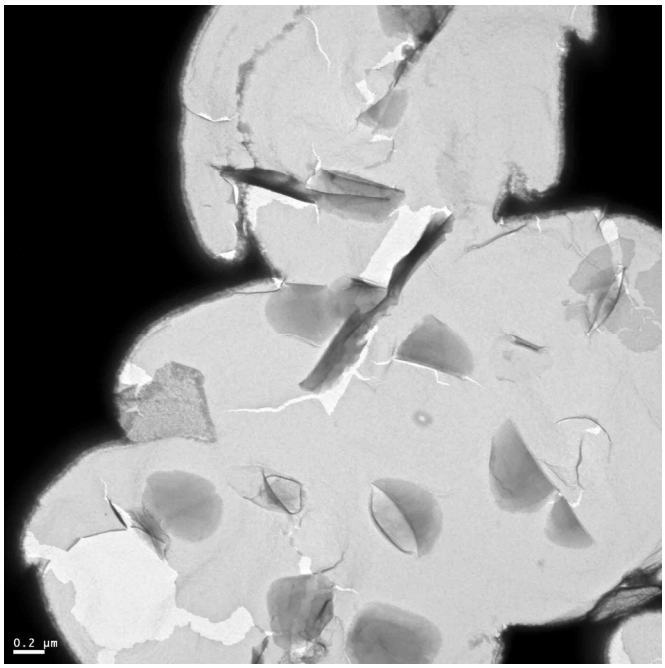

Figure 4.22: Decomposition of the DU-7wt%Mo in the as-cast sample showing U_2Mo (light phase), α-U (grey phase), and the thick DU-7wt%Mo phase (Black phase)

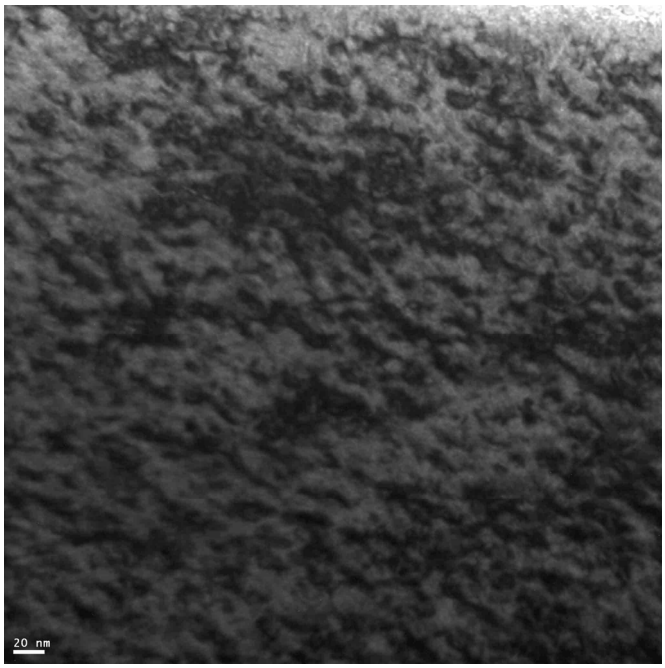

Figure 4.23: Defect microstructure of DU-7wt%Mo after thermal annealing and water quench.

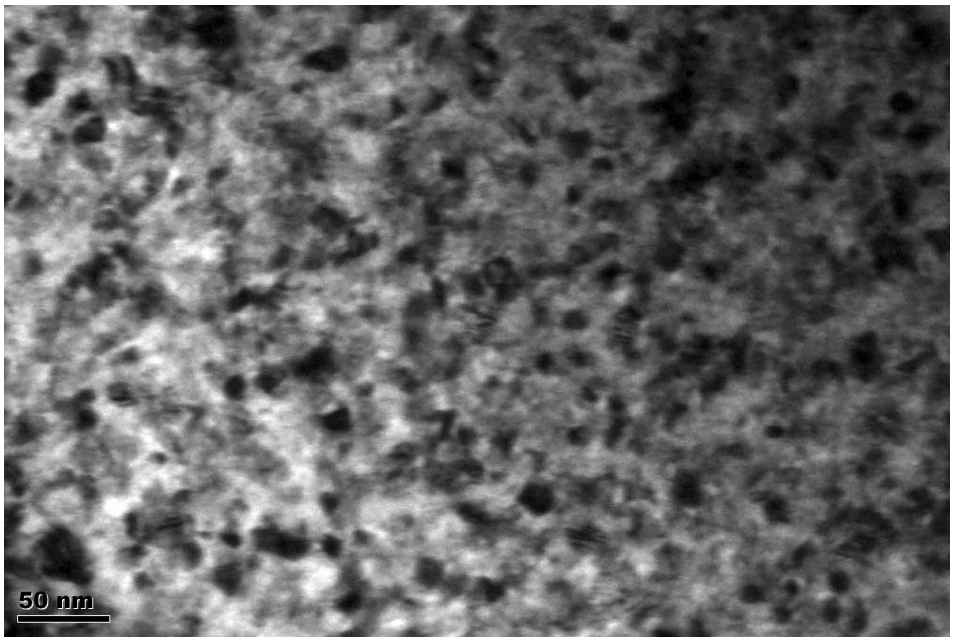

Figure 4.24: Defect microstructure of DU-7wt%Mo at a fluence of 2.5×10^{16} Xe ions/cm^2

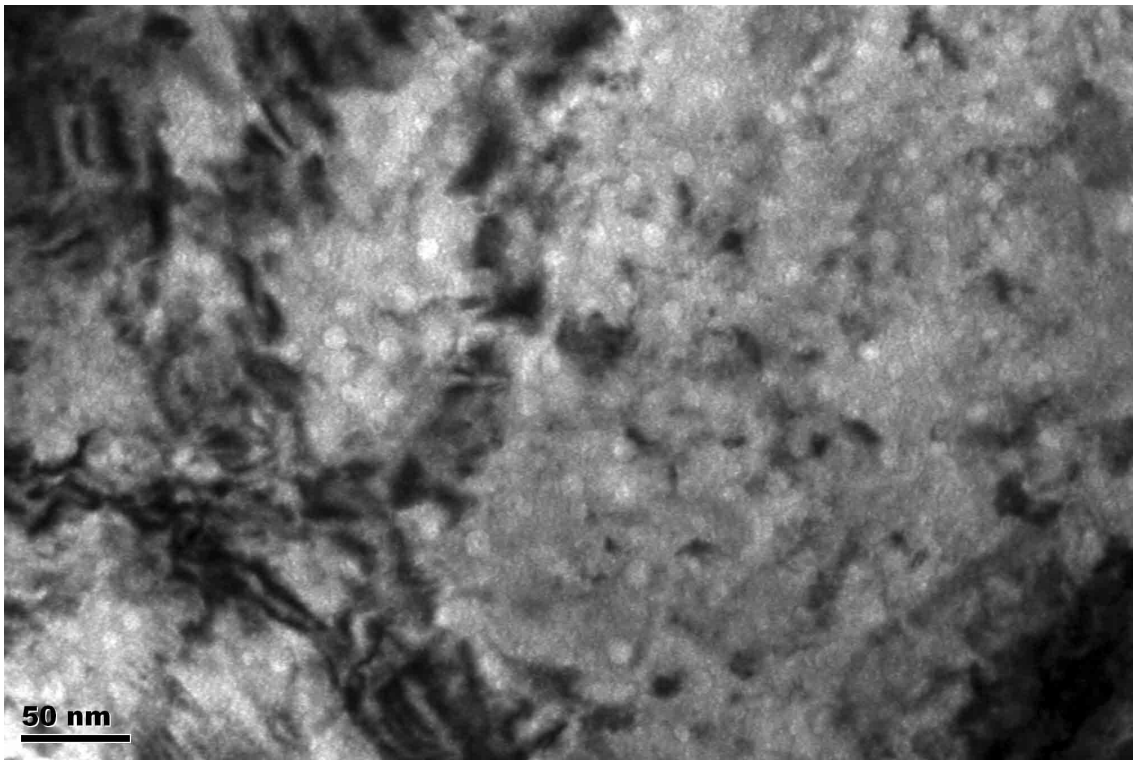

Figure 4.25: Fission gas bubbles in DU-7wt%Mo irradiated to a Xe fluence of 2.5×10^{16} Xe ions/cm^2

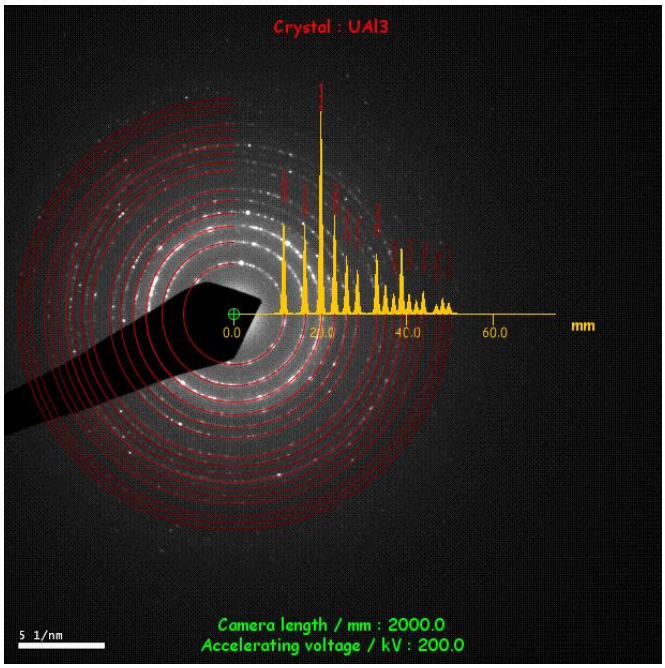

Figure 4.26: SAD pattern of the FMI layer in RERTR-9B and a JEM's simulated SAD pattern showing the nano-crystalline structure

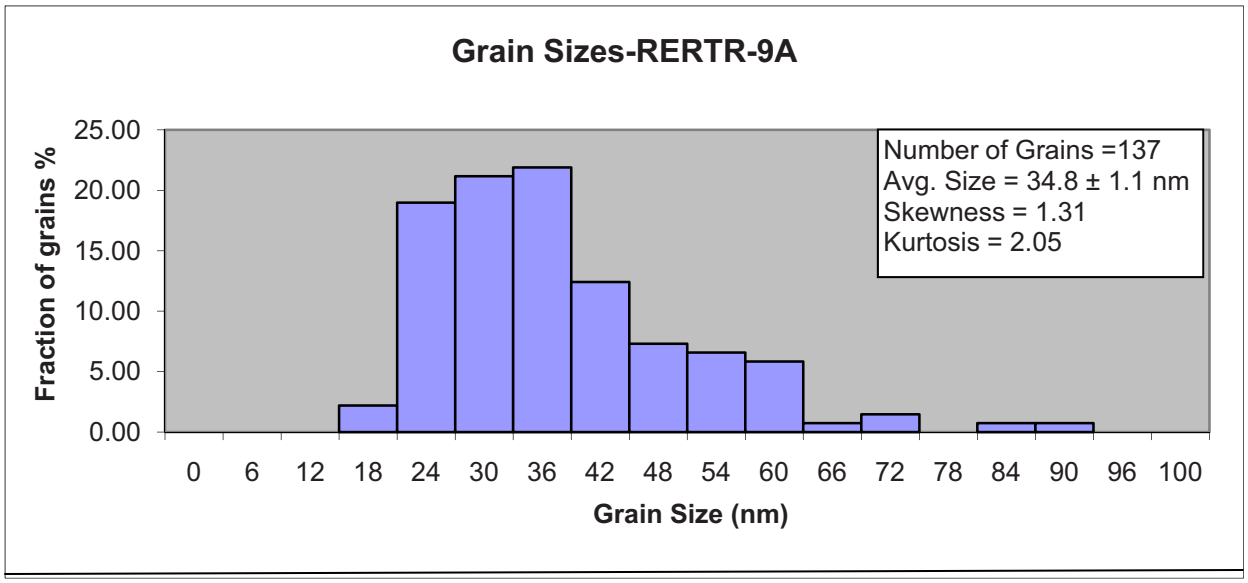

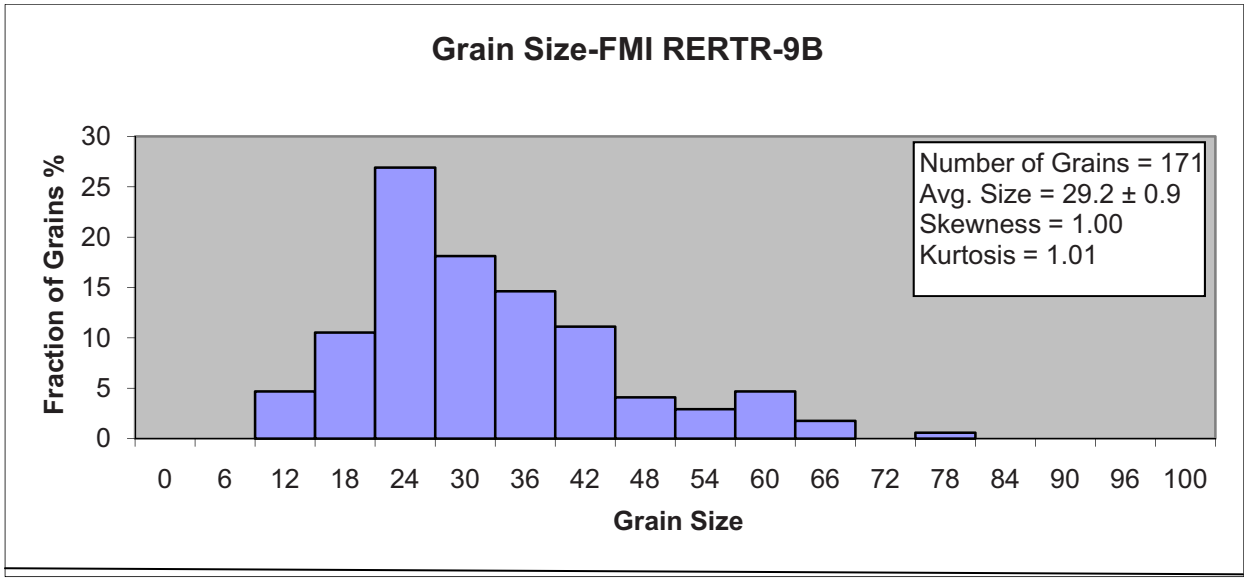

Figure 4.27: FMI grain size distribution in a) RERTR-9A and b) -9B

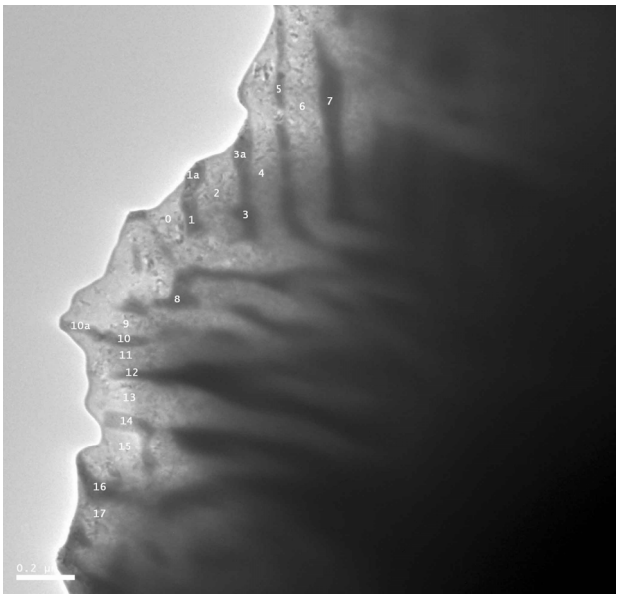

Spot	Al	Si	Mo	U	Atomic Ratio
0	53	20	3	24	2.70
1	13	7	18	63	0.24
1a	11	2	22	65	0.14
2	48	25	3	24	2.70
3	16	17	19	48	0.49
3a	10	10	22	58	0.25
4	31	37	4	28	2.12
5	11	12	21	56	0.29
6	53	20	3	23	2.80
9	18	48	5	29	1.94
10	11	16	12	61	0.36
11	12	51	3	35	1.65
12	11	8	22	59	0.23
13	39	32	3	27	2.36
14	10	2	26	63	0.13
15	57	18	2	23	3.00
16	11	5	21	63	0.19
17	16	49	3	31	1.91

Figure 4.28: General microstructure of RERTR-9A showing a laminar structure. Included is EDS spot compositions in the microstructure and their according atomic ratio value. EDS values are in at%

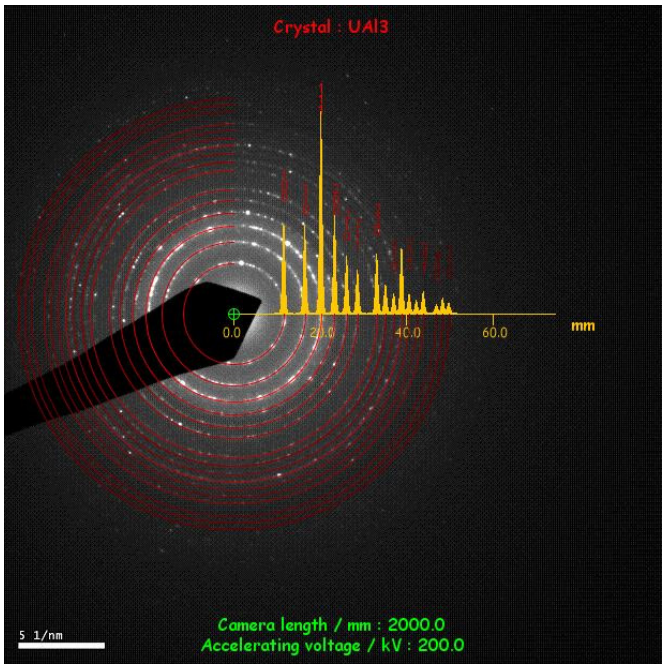

Figure 4.29: SAD pattern of the FMI layer in RERTR-9B and a JEM's simulated SAD pattern showing the nano-crystalline structure.

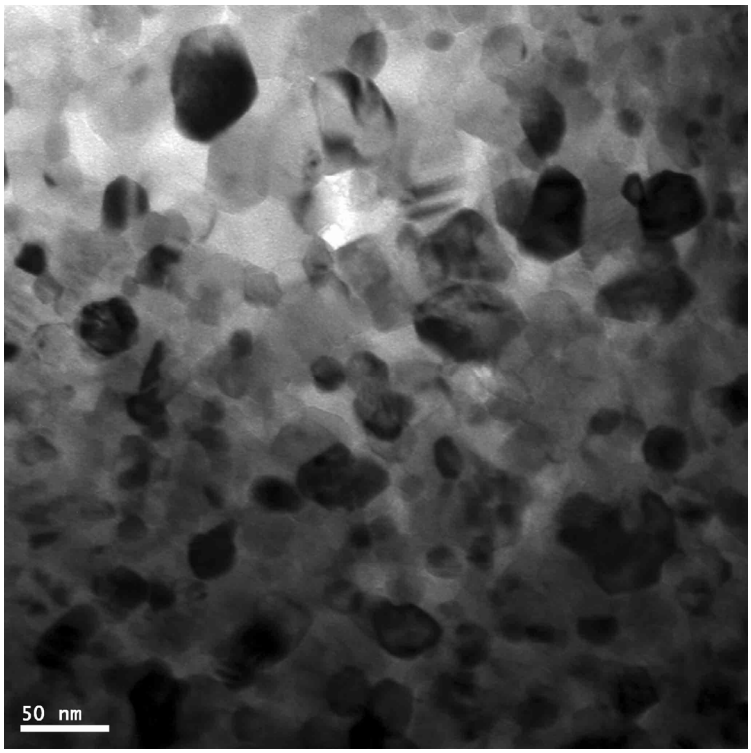

Figure 4.30: General microstructure of the FMI layer in RERTR-9B showing the FMI grains

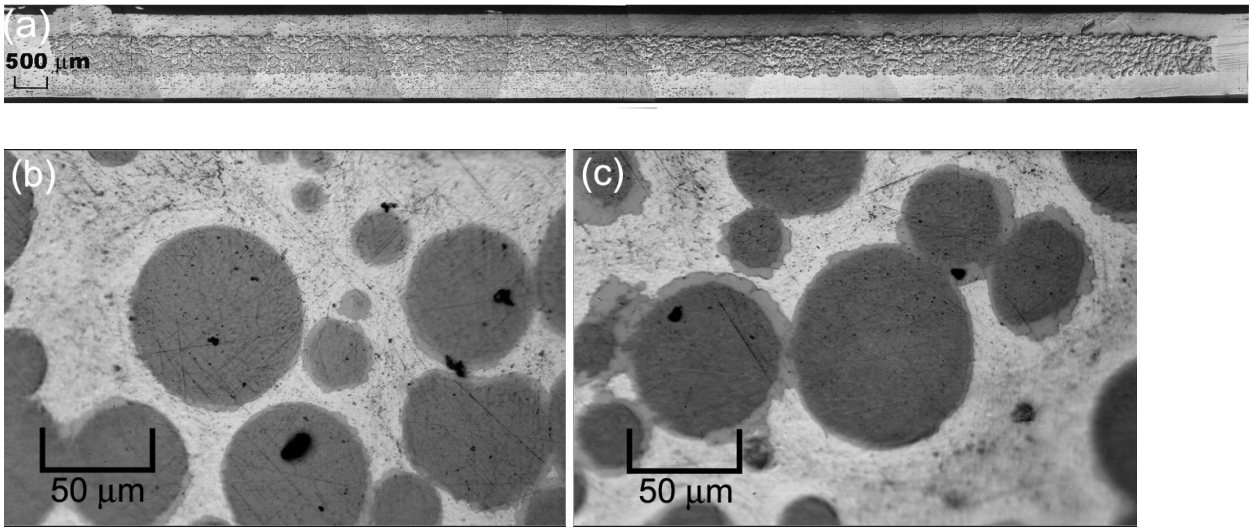

Figure 4.31: Optical metallography images of plate R2R010 showing the a) cross-section of the plate, b) general microstructure of the low neutron flux side of the plate, and c) general microstructure of the high neutron flux side of the plate (63)

a) b)

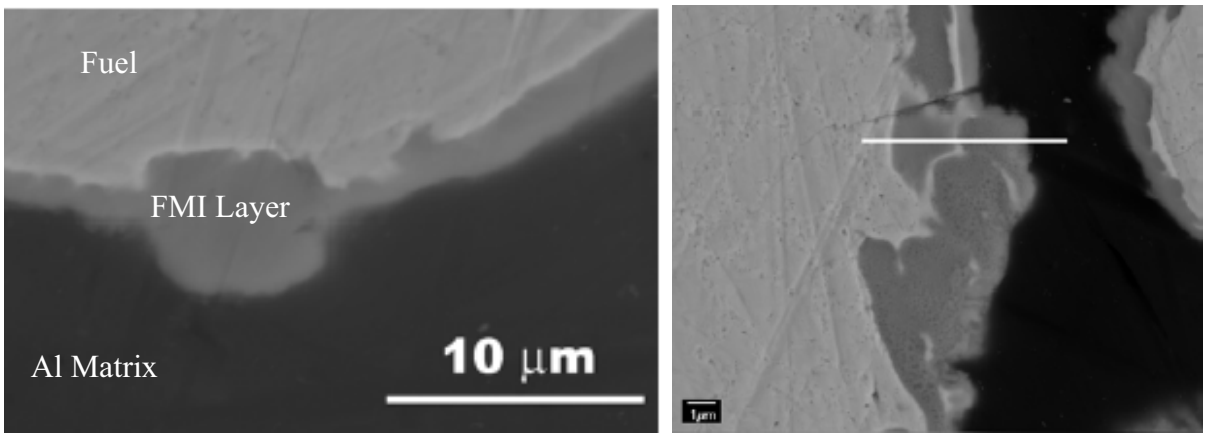

c)

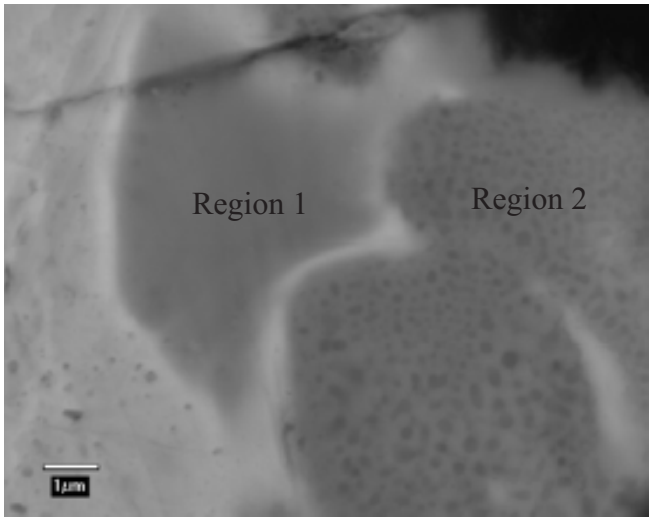

Figure 4.32: Backscatter electron images of plate R2R010 a) low neutron flux side, b) high neutron flux side with corresponding EDS line scan, and c) high magnification image of image b) (64)

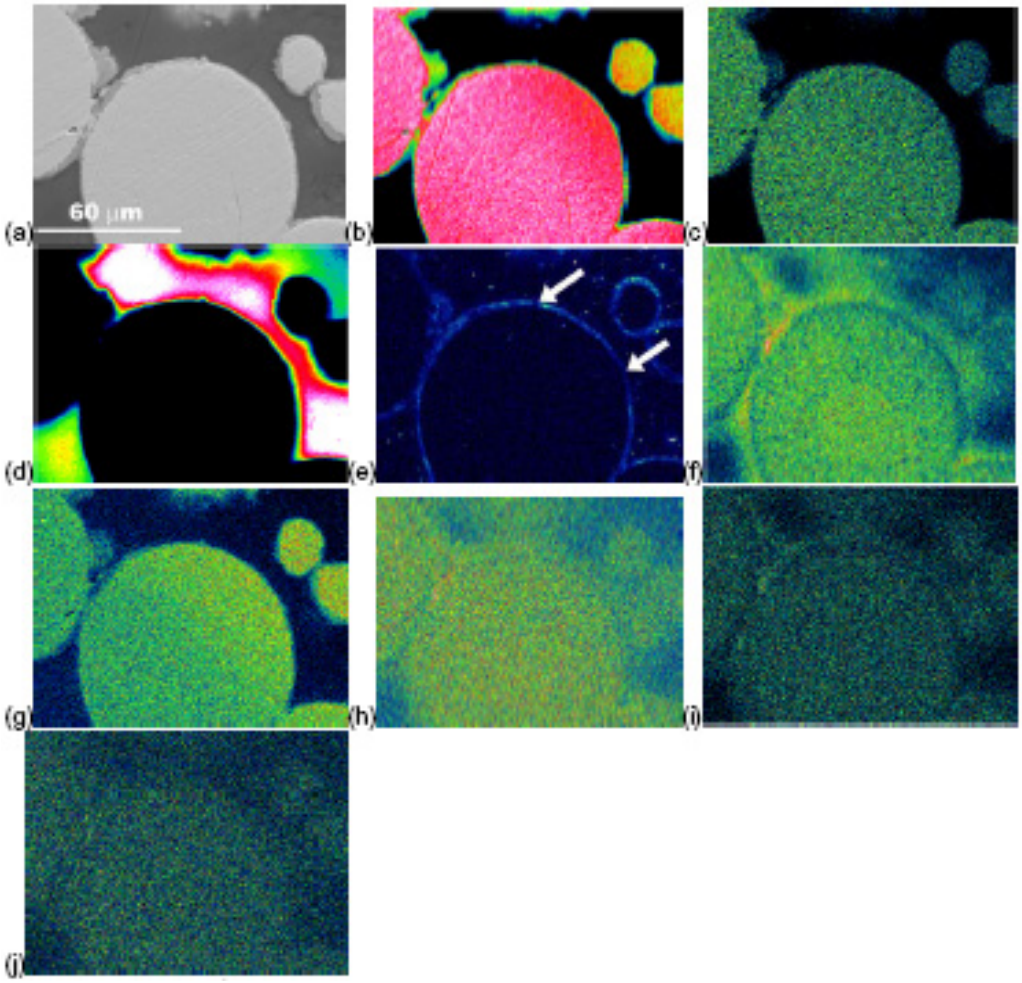

Figure 4.33: X-ray maps of the high neutron flux end , punch B, of plate R2R010: a) SEI, b) U, c) Mo, d) Al, e) Si, f) Xe, g) Kr, h) Cs, i) Nd, and j) Ru. In the Si map, Si enrichment is seen around the fuel particles, the FMI region, and are noted by the arrows. (64)

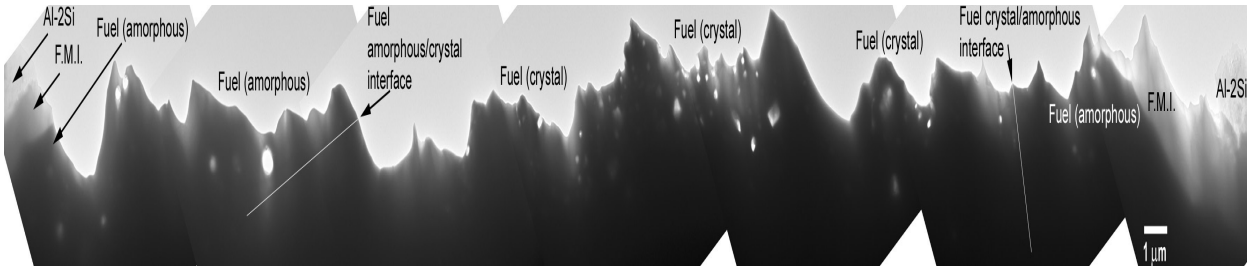

Figure 4.34: Montage of a typical fuel kernel in RERTR-6 and -7 L.Flux showing the key microstructure areas including the Al-2wt%Si matrix, the FMI layer, the amorphous rim fuel region, large fission gas bubbles, and the crystalline fuel region. Note that an interface line is shown to identify the general area in which the fuel transitions from an amorphous to crystalline structure.

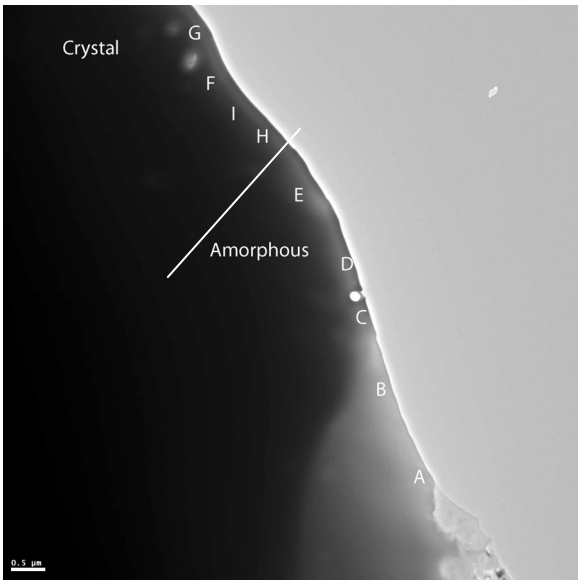

Spot	Al	Si	Mo	U	(U/Mo)/(Al+Si)	Region
A	67.8	13.4	5.2	13.6	0.23	FMI
B	42	31.5	7.2	19.3	0.36	FMI
C	11.3	13.6	17.5	57.6	3.02	A. Rim
D	9.4	10	19.5	60.8	4.14	A. Rim
E	11.6	5.9	15.4	67.1	4.71	A. Rim
H	9.3	9.5	18.9	62.3	4.32	A. Rim
I	8.6	2.7	21	67.7	7.85	Fuel
F	8.4	1.5	21	69.1	9.1	Fuel
G	10.7	2.7	18.9	67.7	6.46	Fuel

Figure 4.35: BF image showing the crystal fuel region, the amorphous rim region, the FMI layer, and the Al matrix. EDS spot compositions in at% are shown and their chemical compositions and atomic ratios are provided

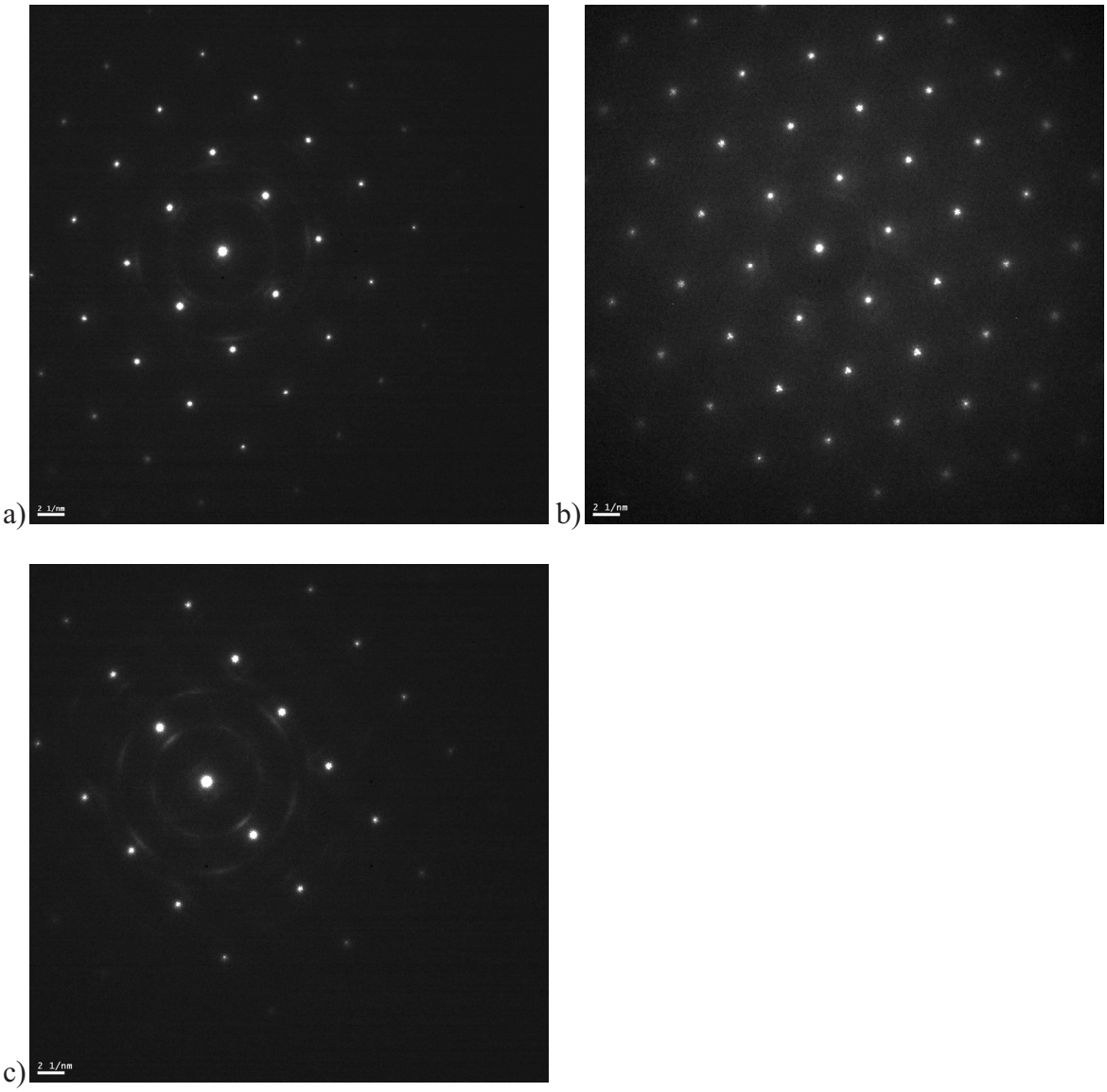

Figure 4.36: SAD images of the BCC U-7wt%Mo fuel kernel with a close up of diffraction spots showing satellite spots: a) z=[100], b) z=[111], and c) z=[110]

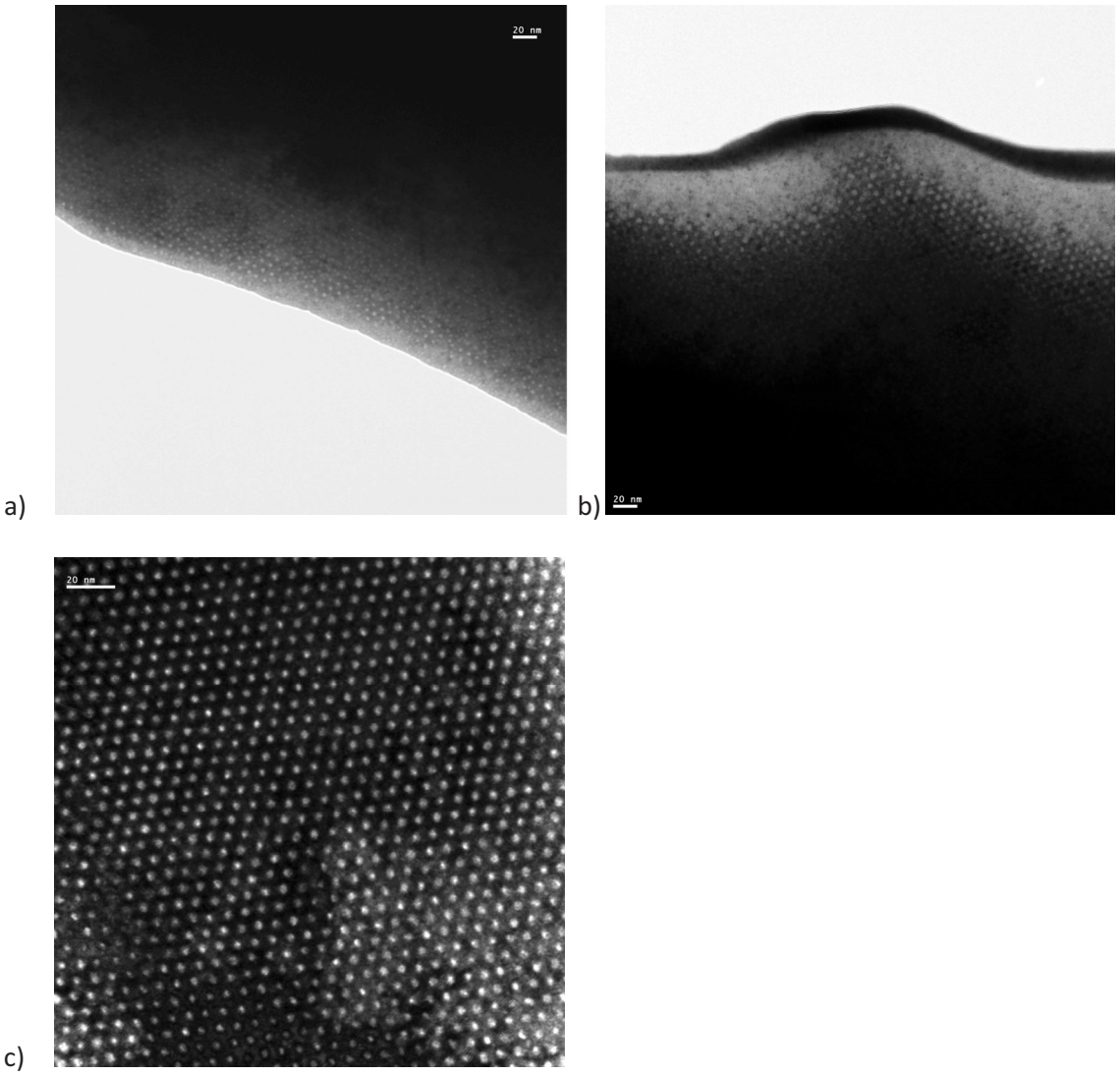

Figure 4.37: BF images of the bubbles superlattice at a) z=[100], b) z=[111], and c) z=[110]

a) 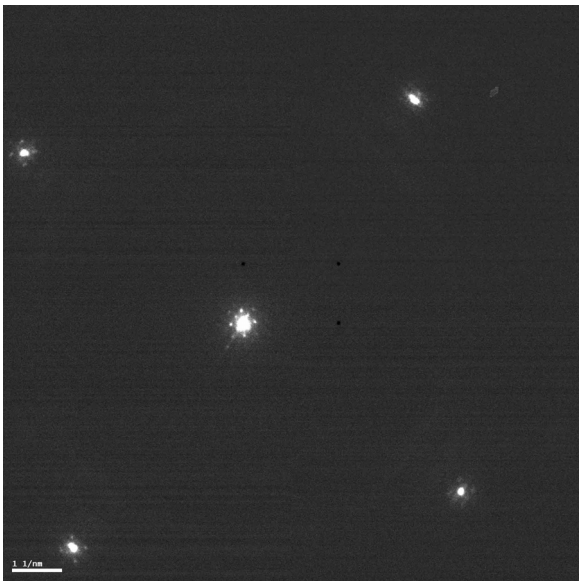

b) 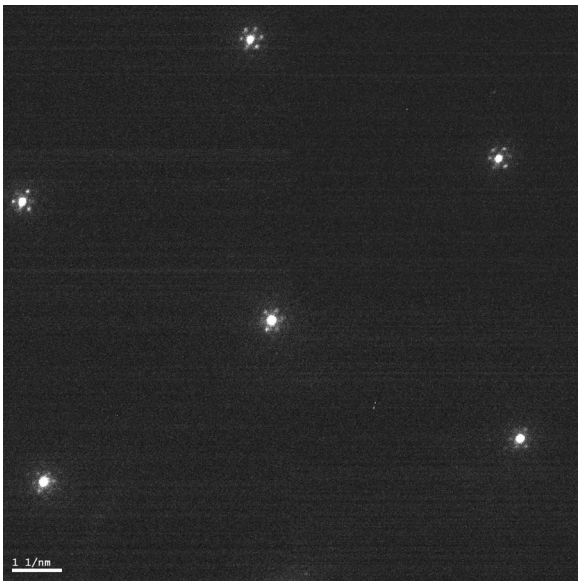

c) 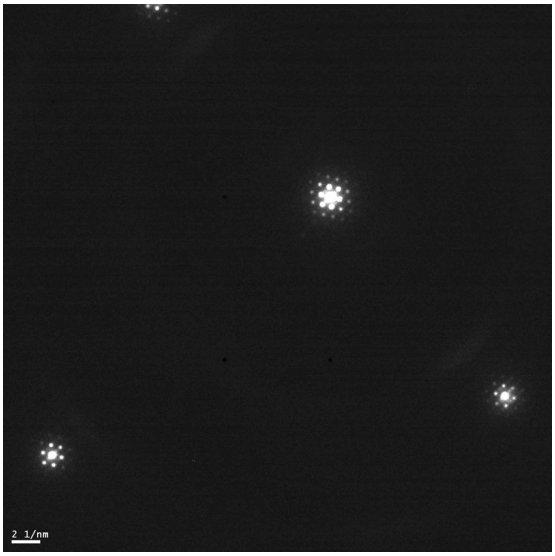

Figure 4.38: Close up images of the diffraction spots of the BCC U-7wt%Mo showing satellite spots in a) z=[100], b) z=[111], and c) z=[110]

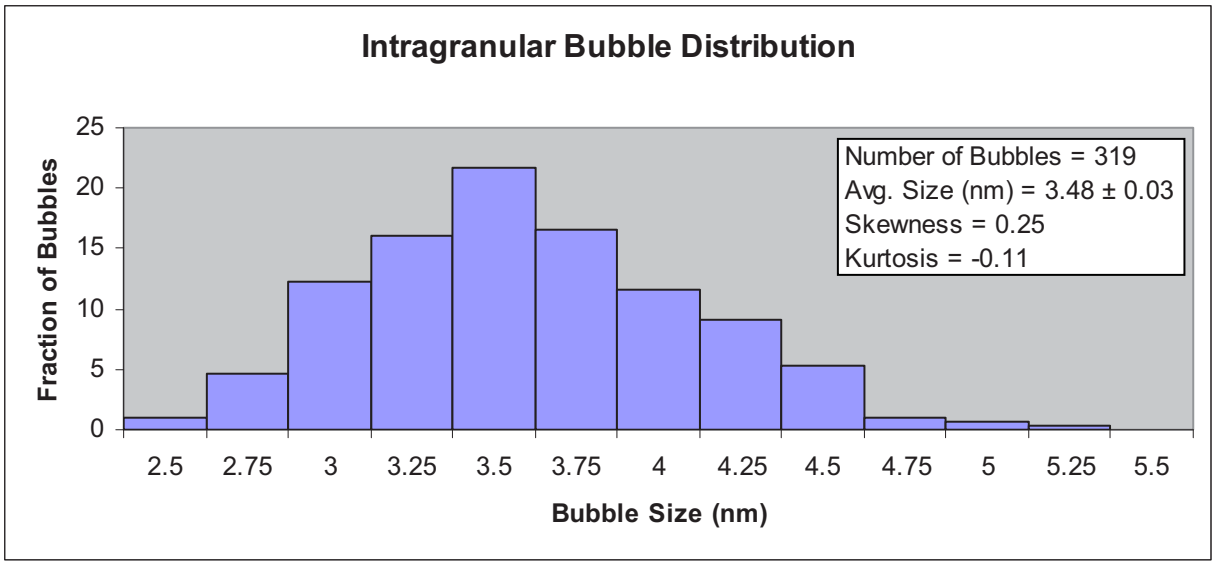

Figure 4.39: Intragranular bubble size distribution in the crystal U-7wt%Mo fuel

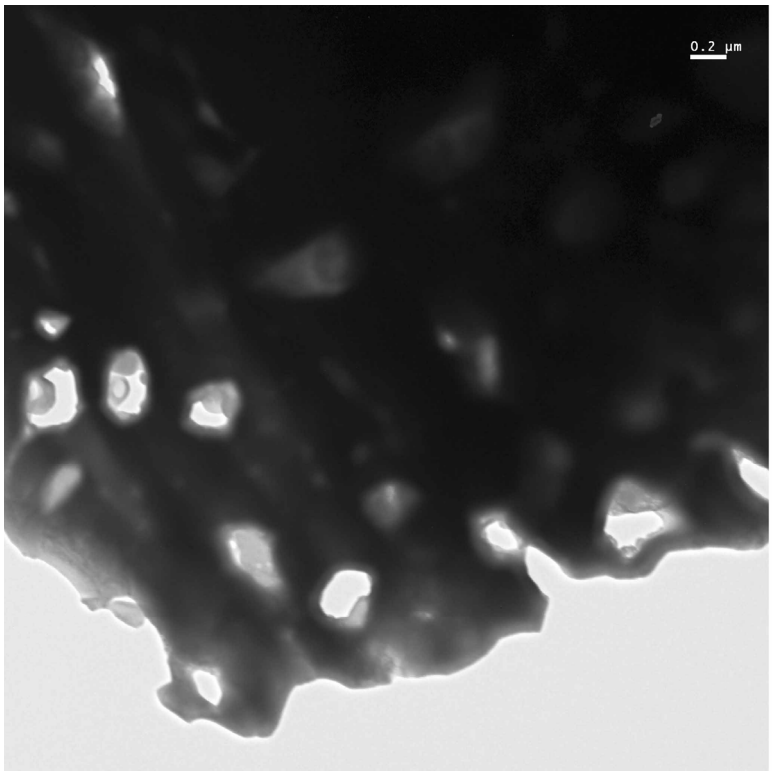

Figure 4.40: Intergranular type bubbles/fission product features in the crystalline region of the U-7wt%Mo fuel kernels

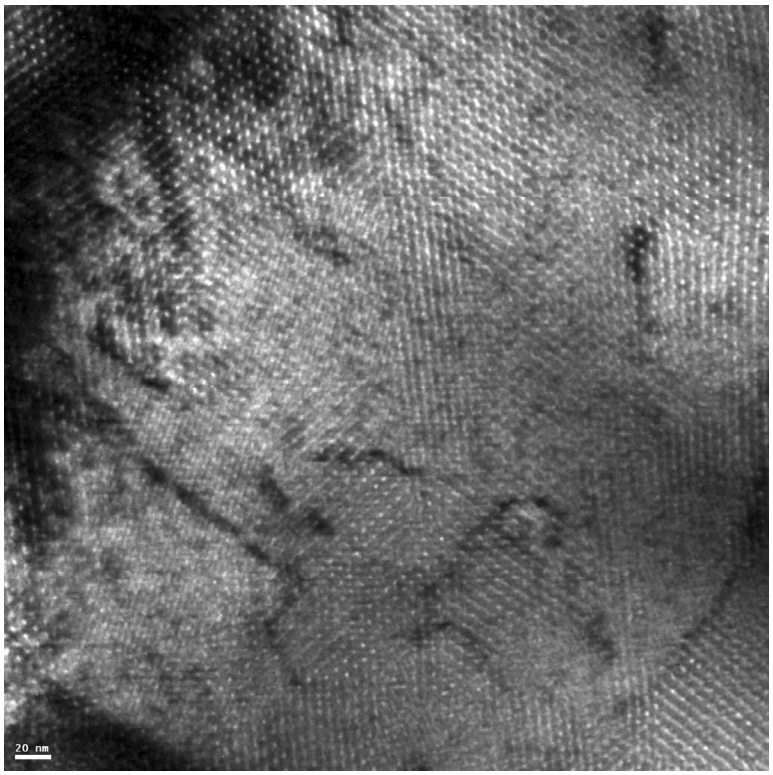

Figure 4.41: BF images at a g=200 condition near z=[110] showing the dislocation microstructure in the U-7wt%Mo bulk. Note that the superlattice bubble structure is still visible around the dislocations

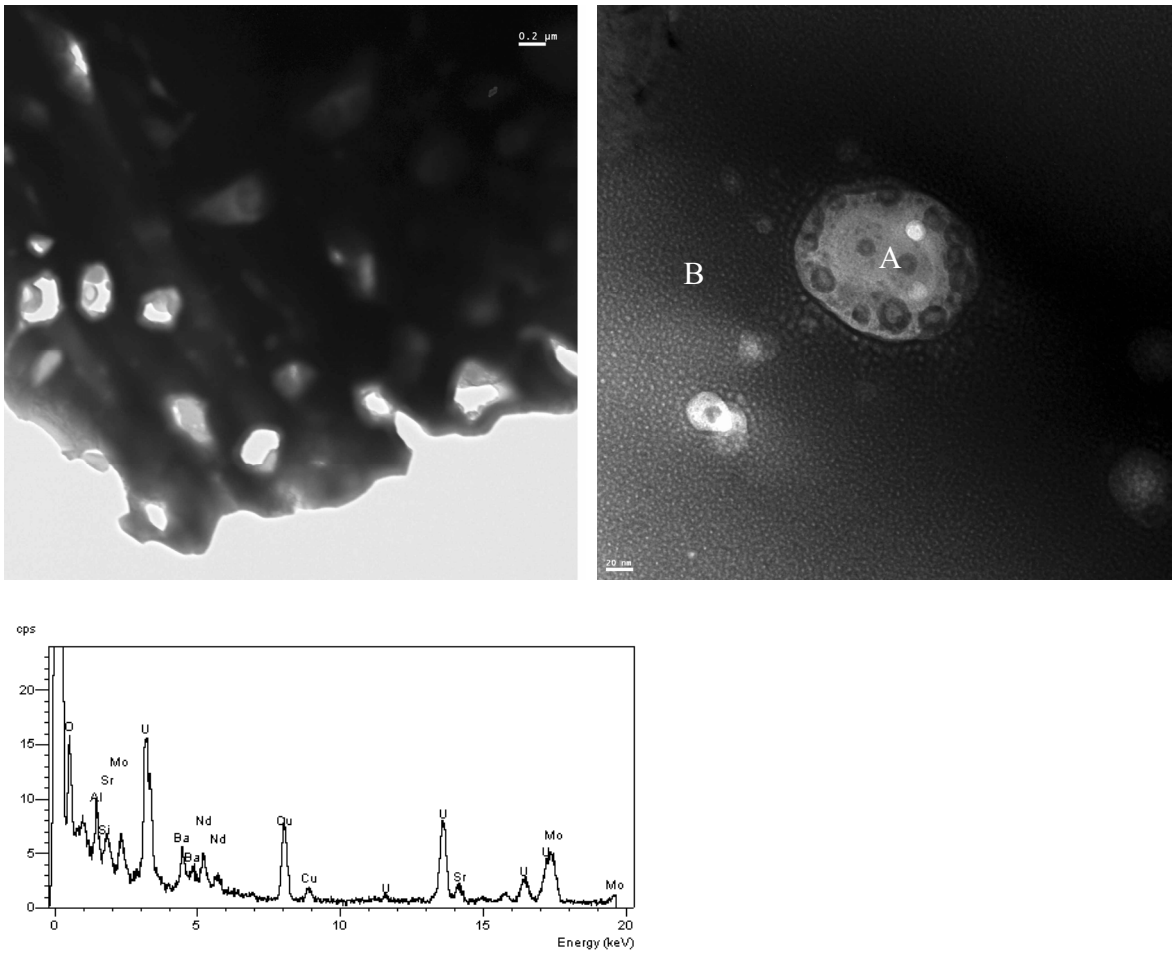

Spot	Sr	Y	Mo	Ba	Nd	U
A	17.5	1.8	14.7	7.7	33.9	24.3
B	2.9	0	25.9	0.7	0	71.1

Figure 4.42: a) Area which has a high density of fission gas bubbles/precipitate features are present and a close up of one of the features with its EDS spectrum and chemical composition measurement in at%.

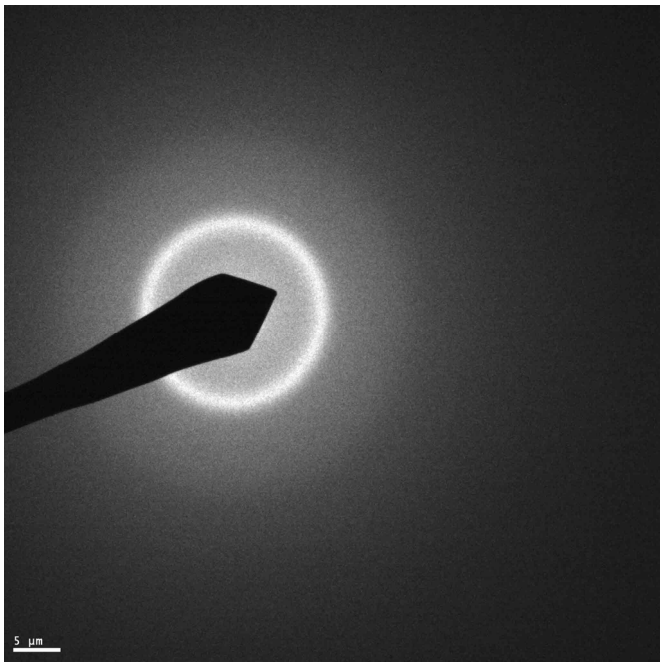

Figure 4.43: Typical SAD pattern of the FMI layer showing the amorphous structure

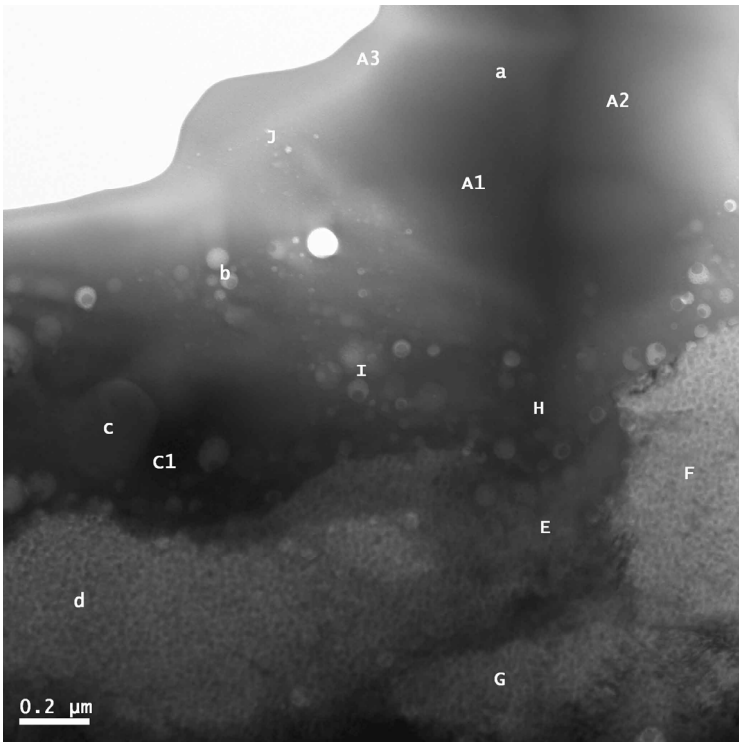

	Al	Si	Mo	U	Atomic Ratio
A	83.6	3.5	3.7	9.8	6.45
A1	78.2	9.9	2.5	9.4	7.40
A2	74.5	9.2	5.5	10.7	5.17
A3	73.4	8.9	4.8	11	5.21
B	79.6	8.5	3	9	7.34
C	93.9	4.8	0.7	0.7	NA
D	91.2	7.2	0.78	0.2	NA
E	91.8	5.3	1.1	0.2	NA
F	91.5	6.3	0.6	0.3	NA
G	90.6	7.8	0.6	0.2	NA
H	87.9	6.8	2.2	0.4	NA
I	89.7	5.6	2.1	2.6	20.28
J	82.9	4.2	3.3	9.7	6.70

Figure 4.44: BF image of an FMI layer, EDS spot compositions at the indicated locations, and atomic ratio values at the FMI locations. EDS values in at%

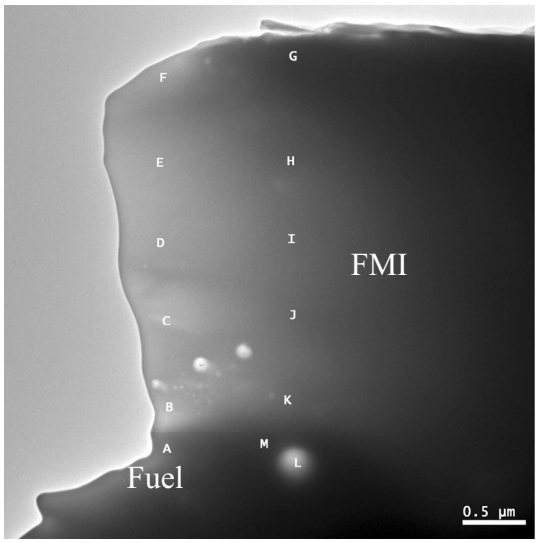
G
F
E
H
D
I
FMI
C
J
B
K
A
M
L
Fuel
0.5 µm

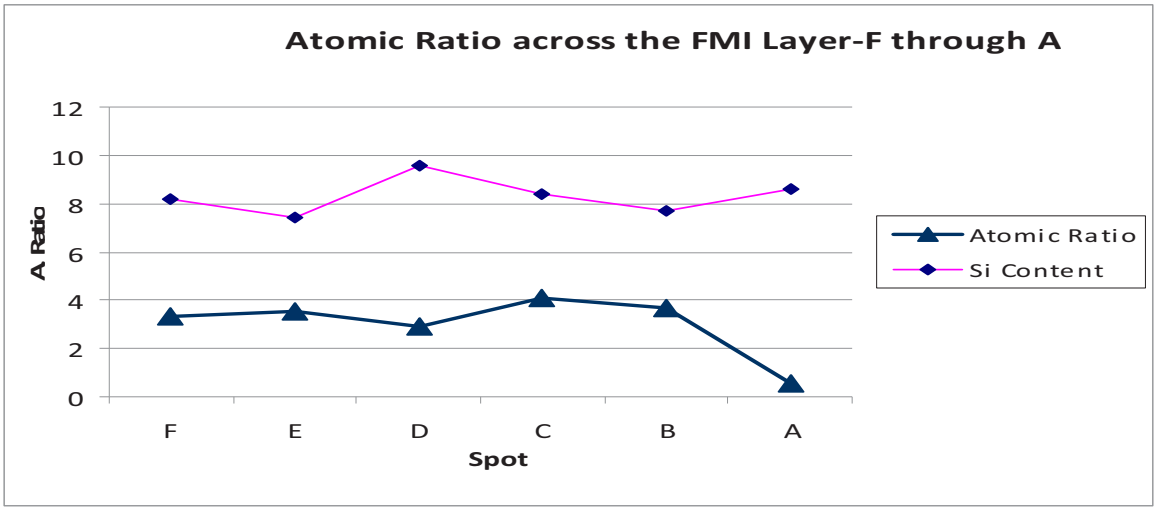
Atomic Ratio across the FMI Layer-F through A
A Ratio
12
10
8
6
4
2
0
F
E
D
C
B
A
Spot
Atomic Ratio
Si Content

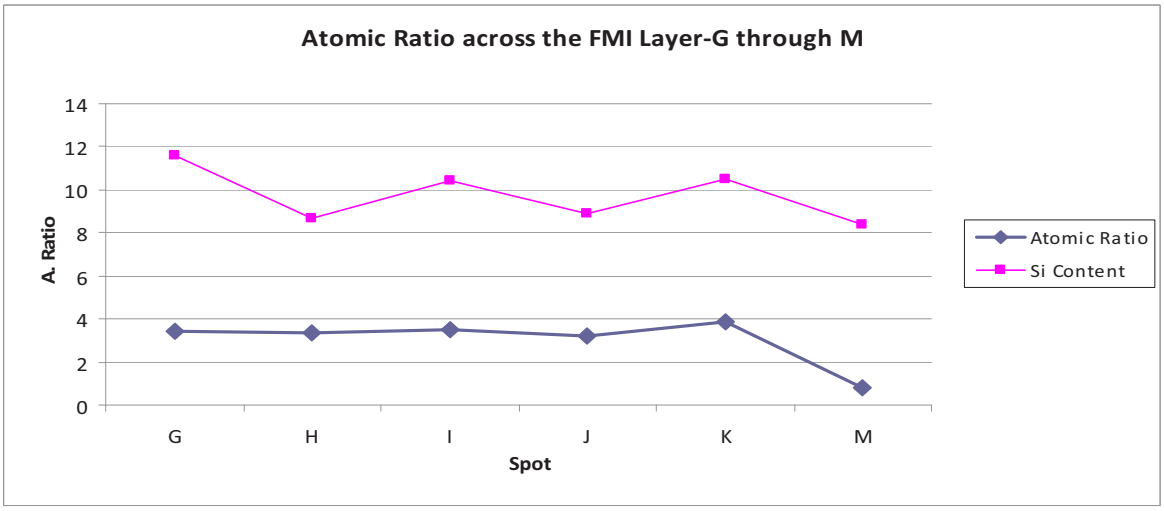
Atomic Ratio across the FMI Layer-G through M
A. Ratio
14
12
10
8
6
4
2
0
G
H
I
J
K
M
Spot
Atomic Ratio
Si Content

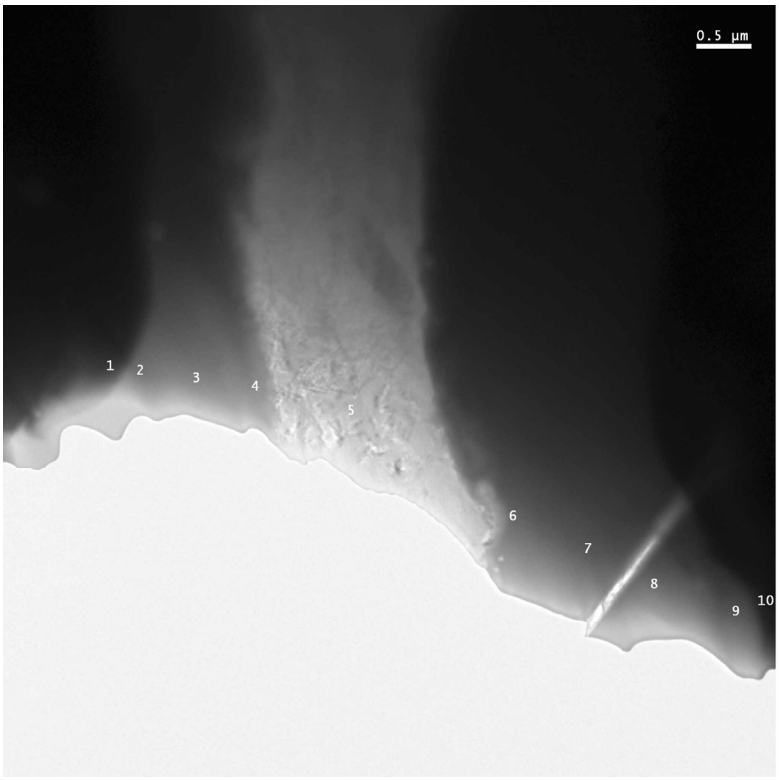

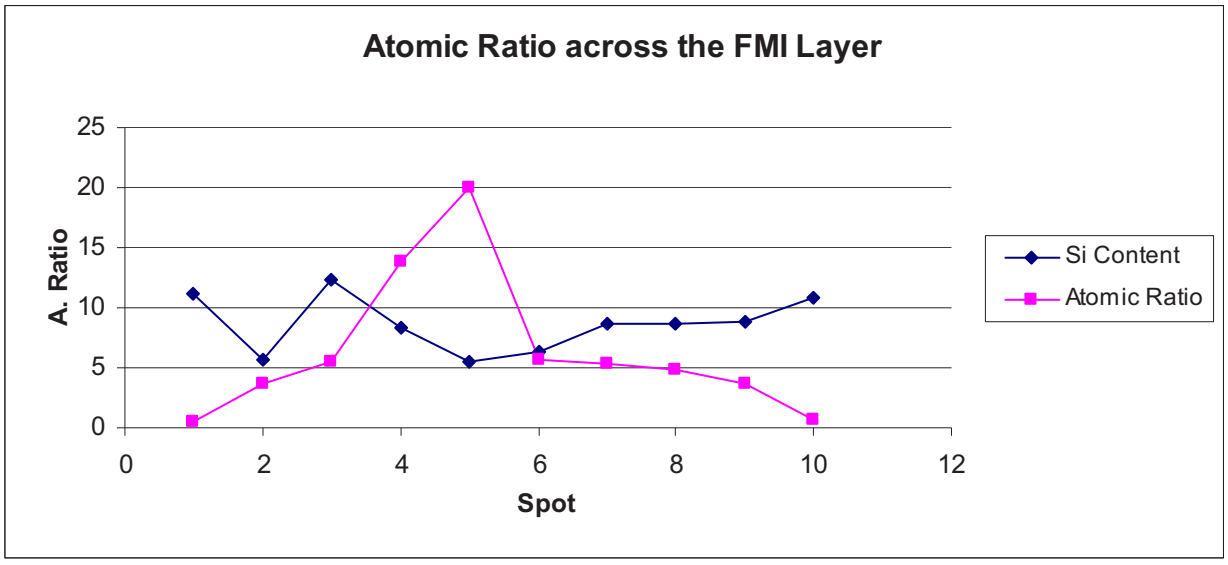

Figure 4.45: EDS spot scans across the FMI and their corresponding atomic ratio profiles. Included in the atomic ratio profiles is the measured Si content at the specific location.

a)

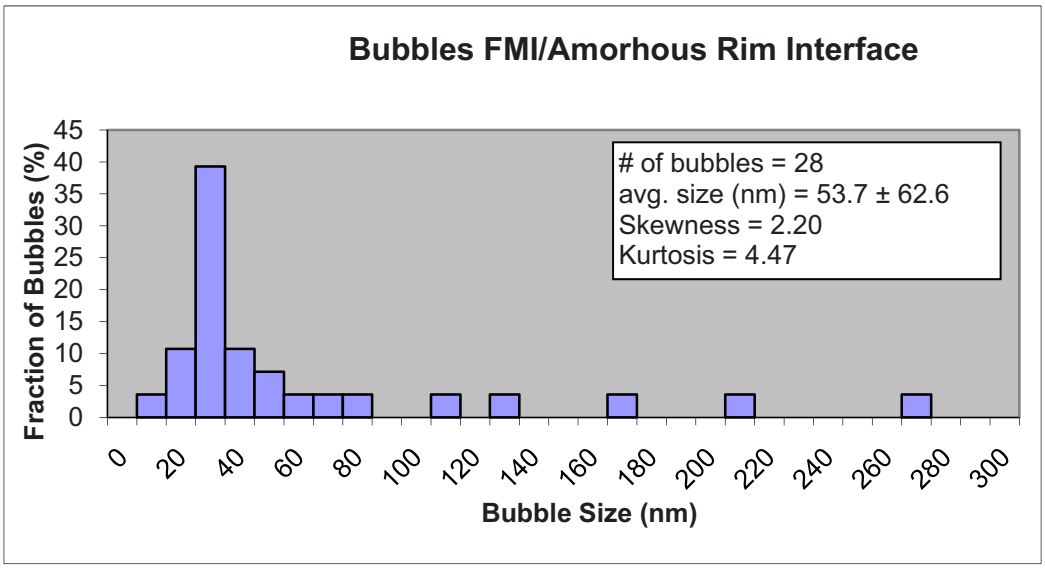
Bubbles FMI/Amorhous Rim Interface
Fraction of Bubbles (%)
45
40
35
30
25
20
15
10
5
0
# of bubbles = 28
avg. size (nm) = 53.7 ± 62.6
Skewness = 2.20
Kurtosis = 4.47
0
20
40
60
80
100
120
140
160
180
200
220
240
260
280
300
Bubble Size (nm)

b)

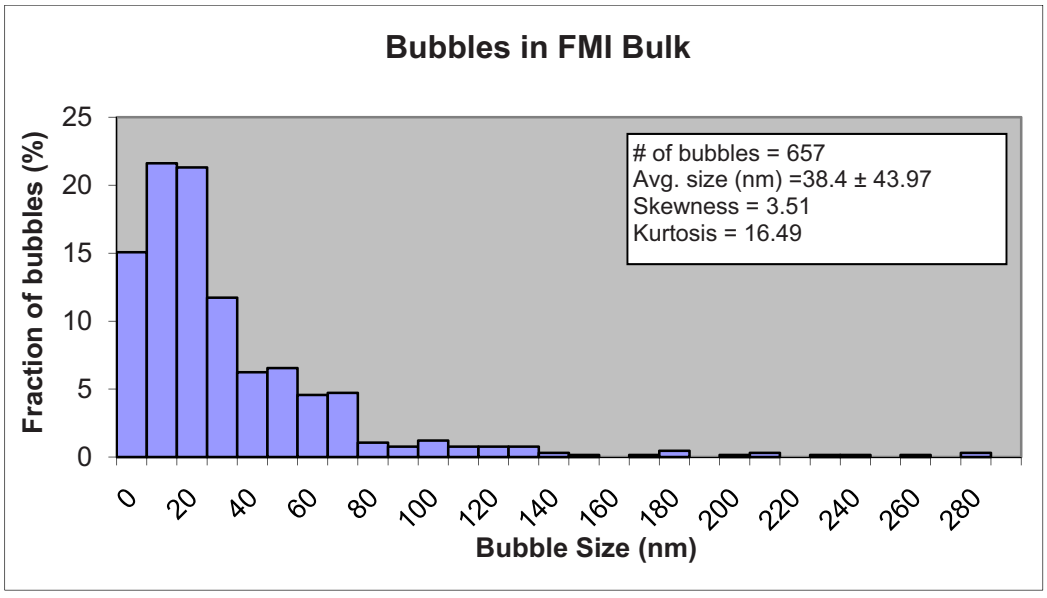
Bubbles in FMI Bulk
Fraction of bubbles (%)
25
20
15
10
5
0
# of bubbles = 657
Avg. size (nm) =38.4 ± 43.97
Skewness = 3.51
Kurtosis = 16.49
0
20
40
60
80
100
120
140
160
180
200
220
240
260
280
Bubble Size (nm)

c)

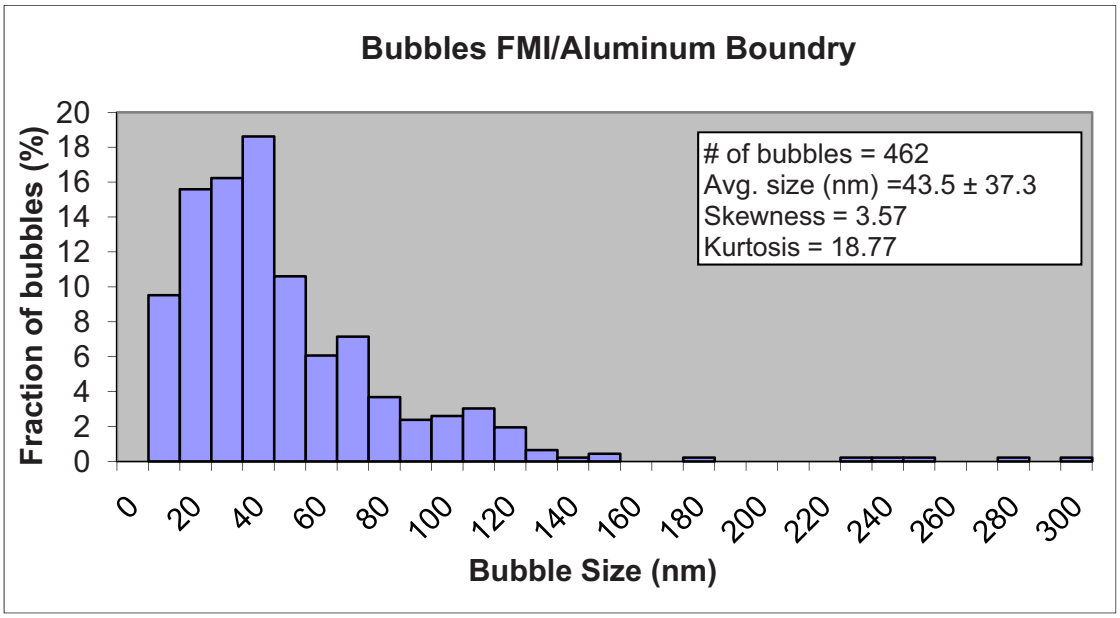

d)

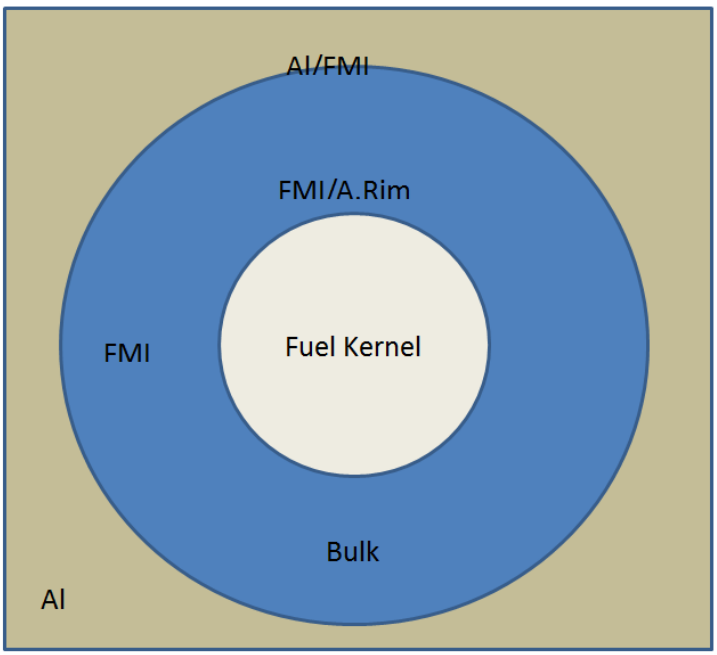

Figure 4.46: Bubble distributions and sizes at a) the FMI layer/amorphous rim interface, b) the bulk of the FMI layer, c) the FMI layer/Al-2wt%Si interface, and d) schematic showing the key areas of interest in the fuel particle.

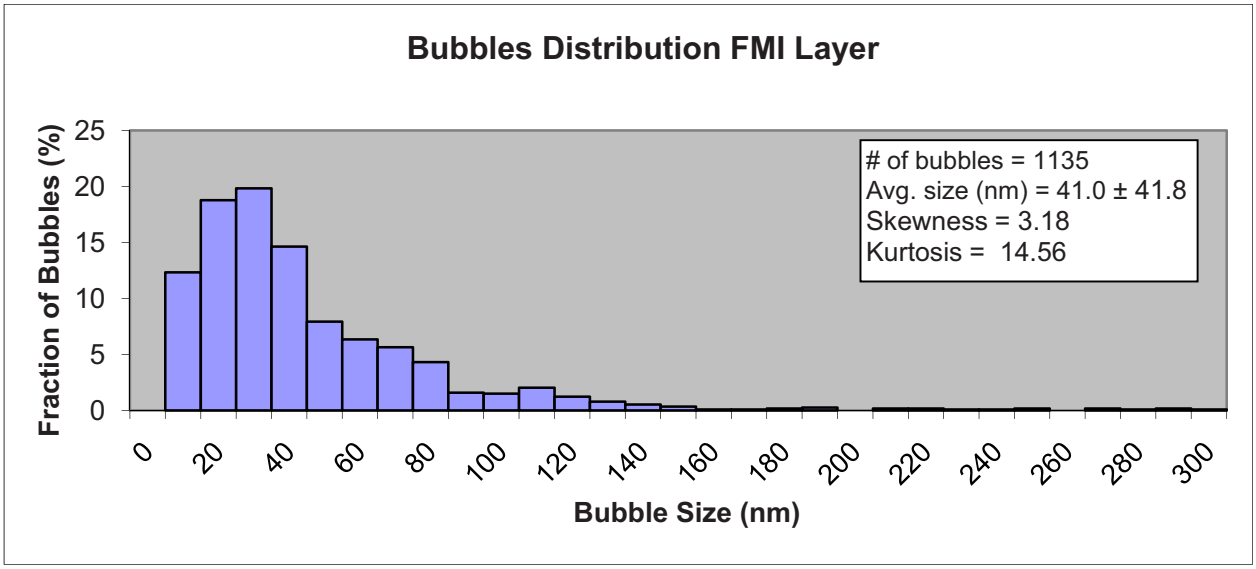

Figure 4.47: Fission gas bubble distribution throughout the entire FMI neglecting specific location of the bubbles

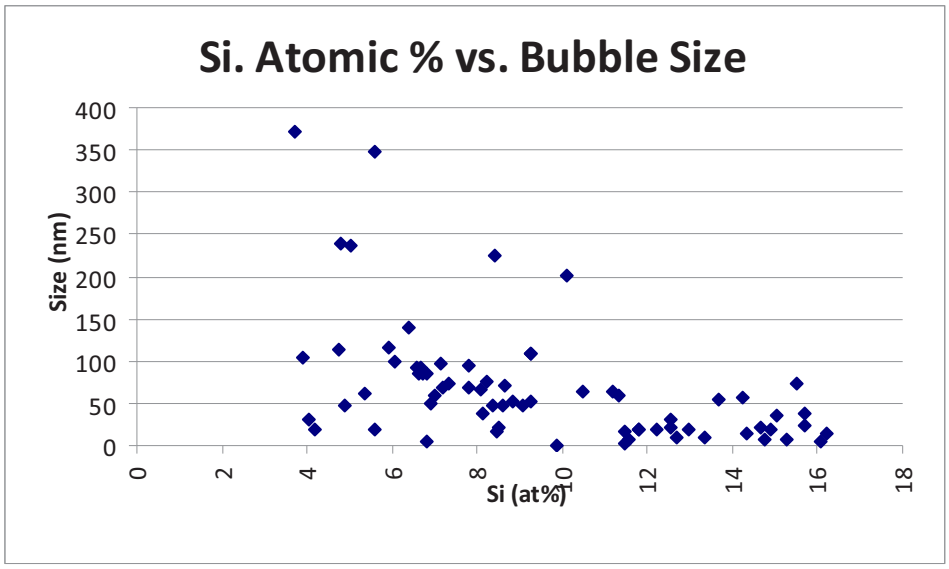

Figure 4.48: Measured Si content (at%) vs. fission gas bubble size independent of bubble location in the FMI layer. Measurements were obtained next to or on the bubble.

a) 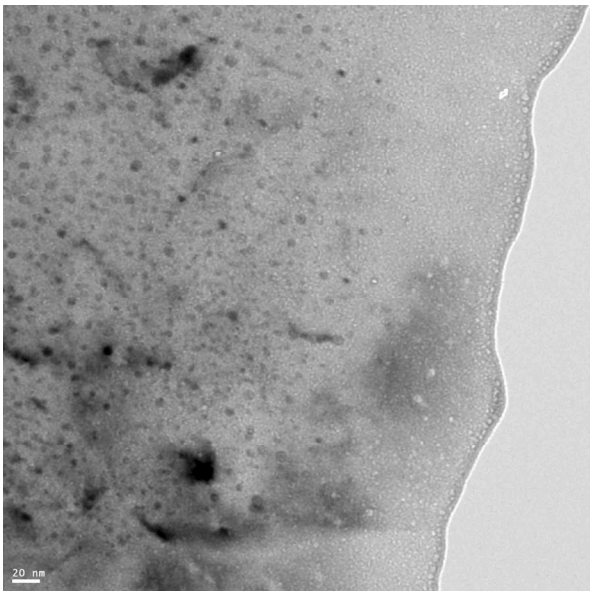

b) 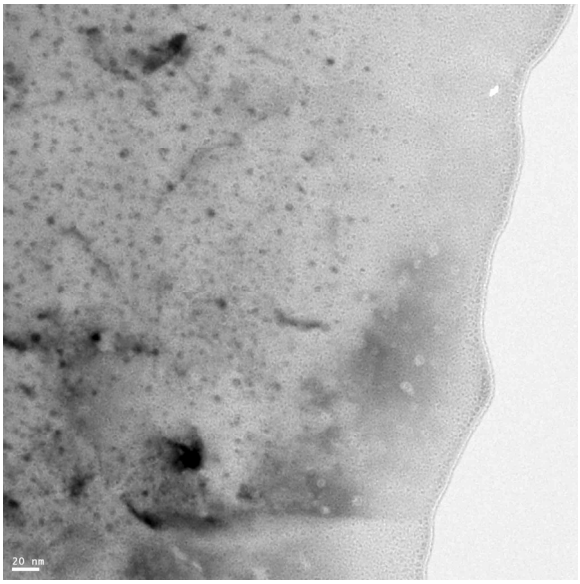

c) 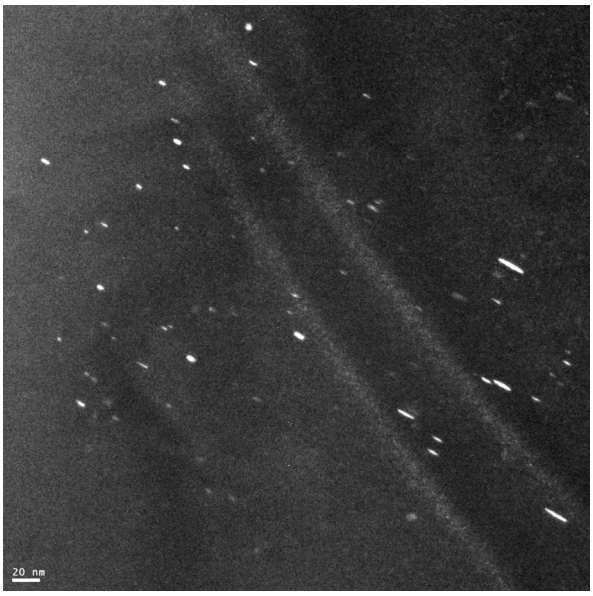

Figure 4.49: BF images of the Al-2wt%Si matrix in an a) underfocus condition and b) an overfocus condition showing Si precipitates (dark phase) and small voids (light phase), and c) WBDF image showing faulted loops in the Al matrix

a)

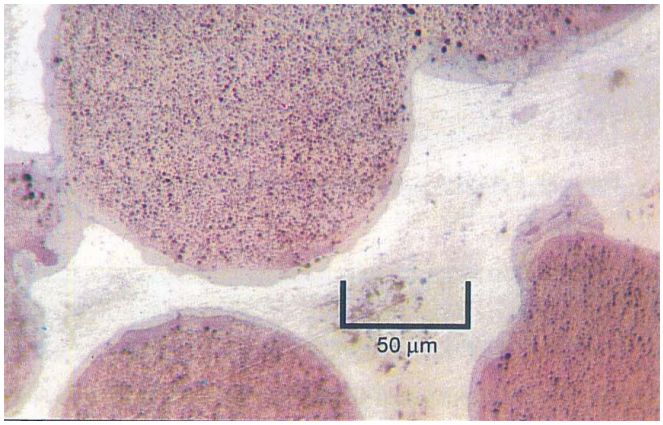

b)

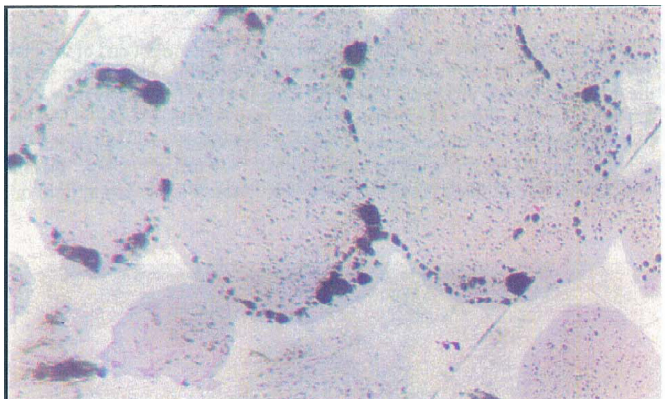

Figure 4.50: OM images of a) the low flux of plate R2R040 and b) the high flux end showing the distribution of the fission gas bubbles (63).

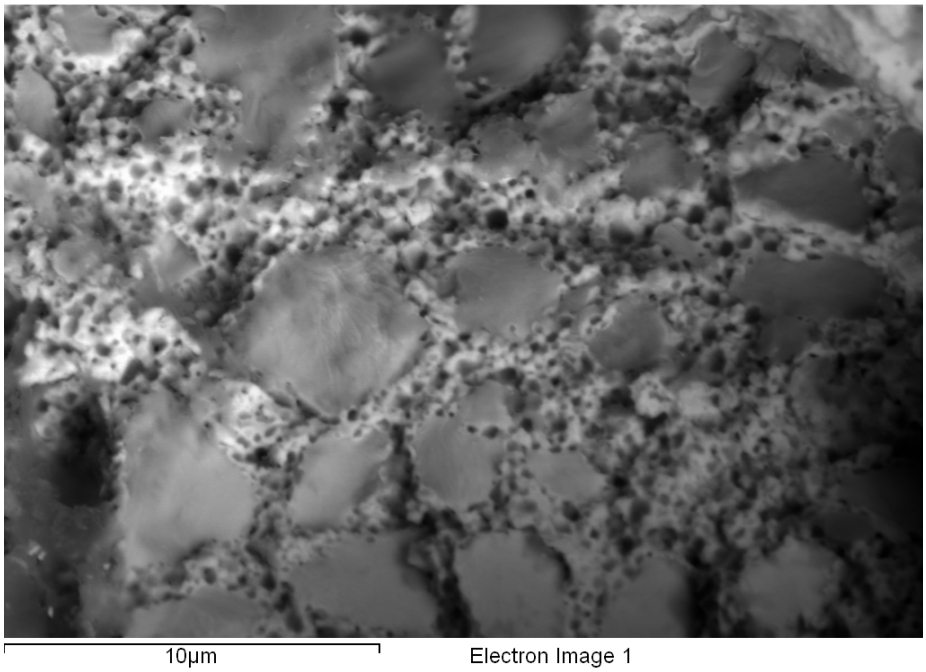

Figure 4.51: SEM image of a fracture surface of RERTR-7 L. Flux showing a high density of intergranular bubbles at the grain boundary interfaces.

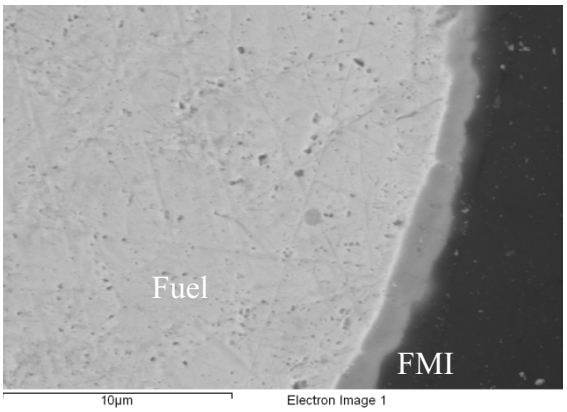

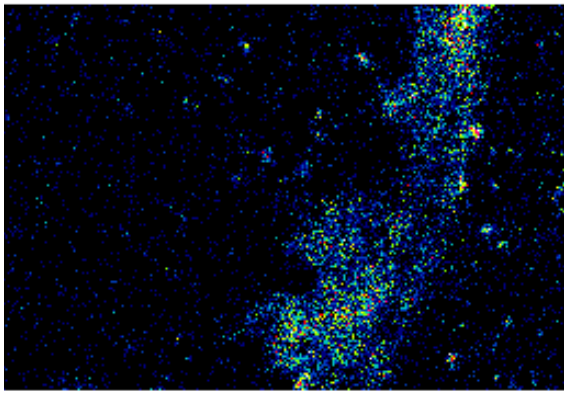

Figure 4.52: SEI image of a fuel particle showing the FMI layer and the Si WDS spectrum of the area showing a high Si content protruding into the amorphous rim region of the fuel particle.

a) b)

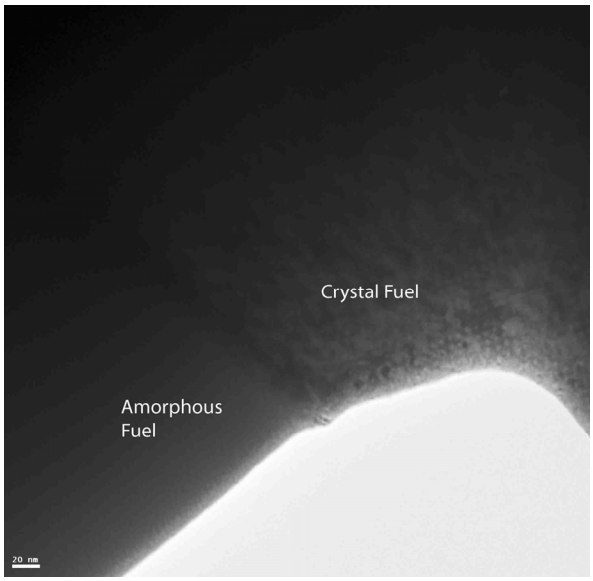

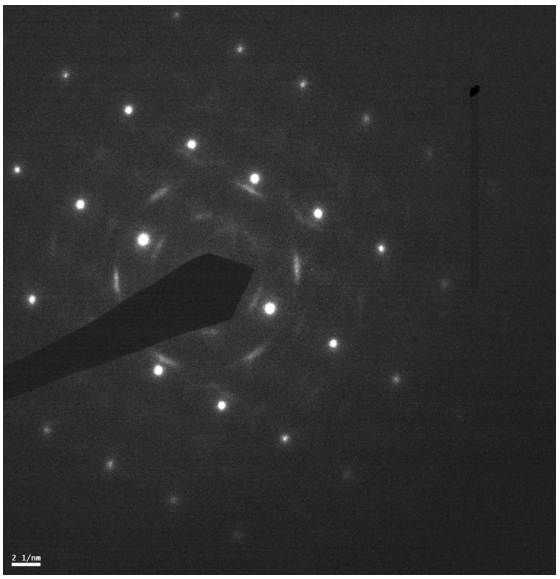

c)

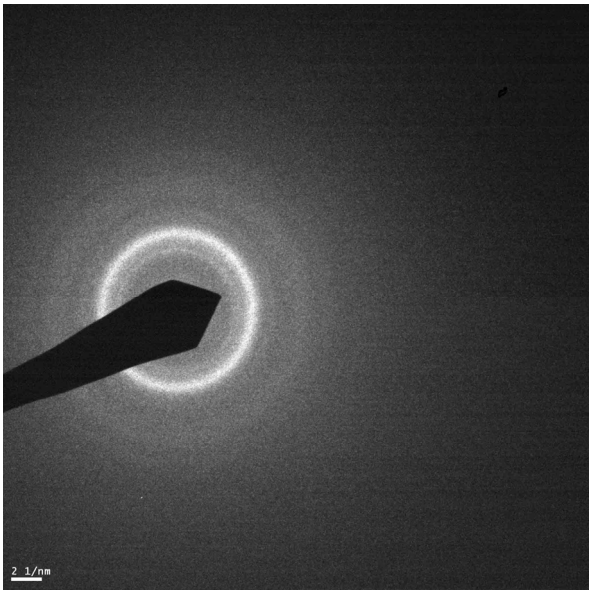

Figure 4.53: a) BF image of the amorphous rim/crystal interface. Notice the superlattice bubble formation on the crystal part of the image. b) Electron diffraction pattern from the crystal fuel. c) SAD ring pattern of the amorphous fuel rim region.

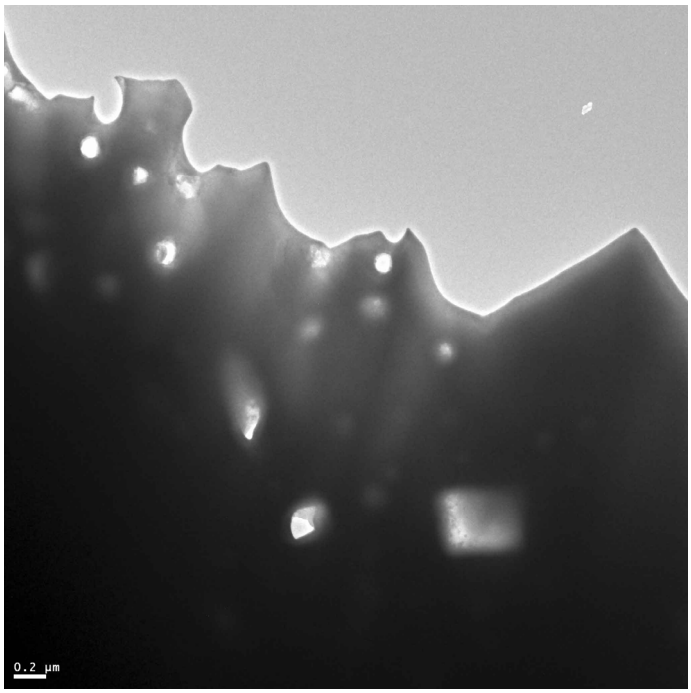

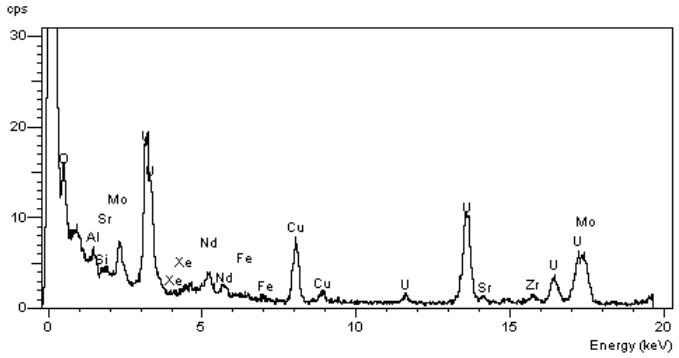

Figure 4.54: a) Fission Gas bubbles with fission product features in the bulk of the U-7wt%Mo fuel. Notice the various geometries. Included is an EDS spectrum of a fission product feature. Notice the counts from Nd, Sr, and Zr, indicating a high concentration of fission products.

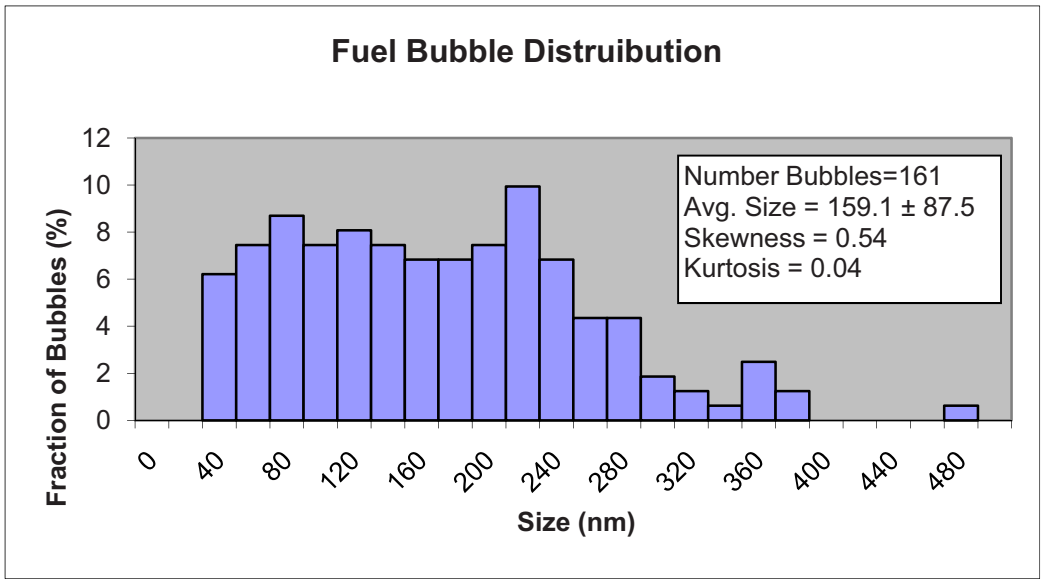

Figure 4.55: Size and distribution of the intergranular bubbles present in the fuel region. This is includes bubbles from both the amorphous rim and the crystalline fuel region.

a) b)

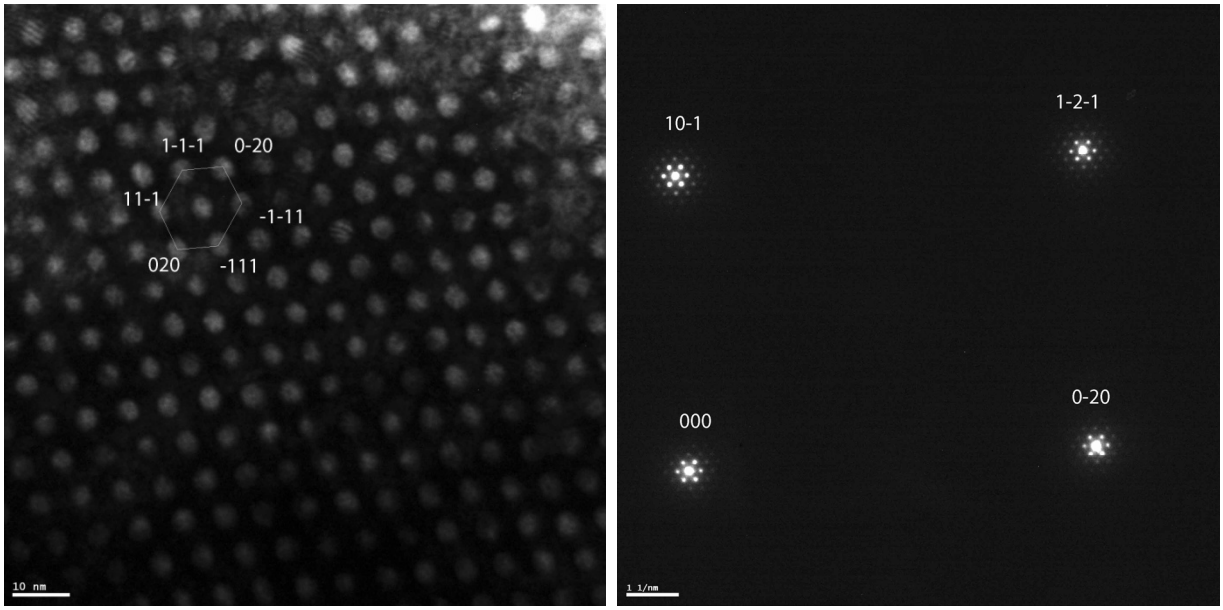

Figure 4.56: a) BF image of the intragranular bubbles at a z=[011]. The bubbles are in an FCC [011] alignment as seen in the outline. b) Electron diffraction pattern of the bulk BCC U-7wt%Mo at a z= [011] condition showing satellite spots orientated in a FCC [011] pattern around the BCC spots

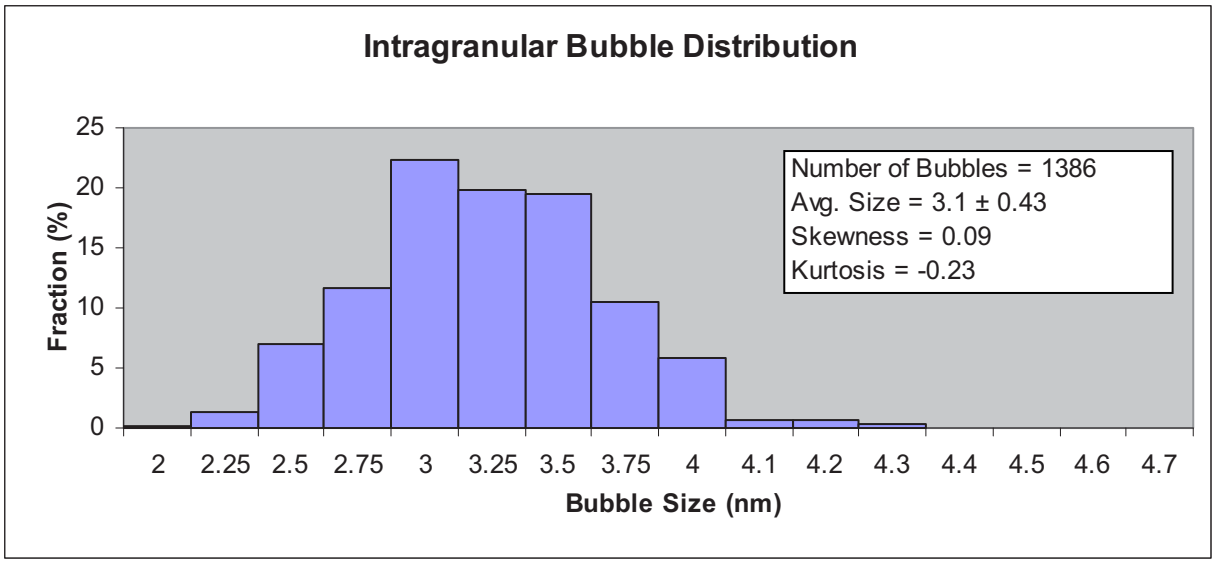

Figure 4.57: Intragranular bubble size and distribution in the crystalline area of the fuel.

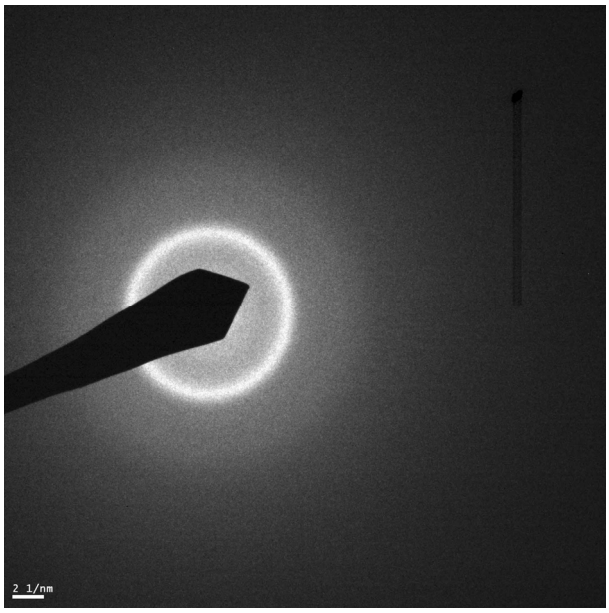

Figure 4.58: Ring pattern of the FMI layer showing the amorphous character

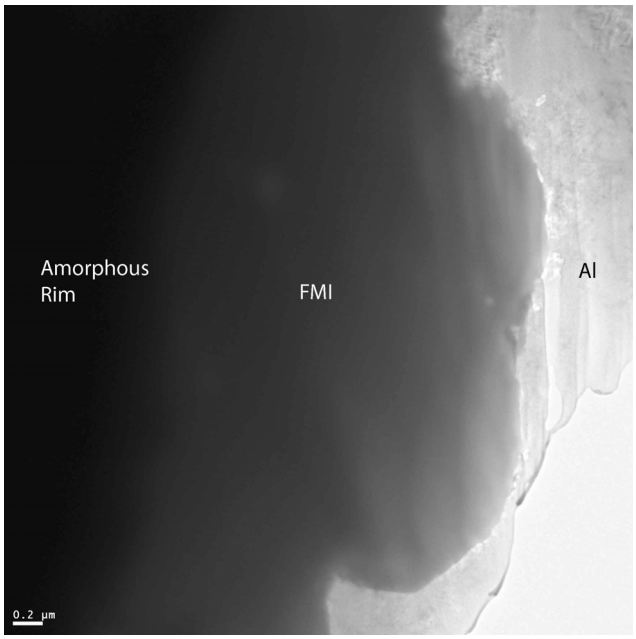

Figure 4.59: BF image of the FMI layer showing the variation in the thickness

a)

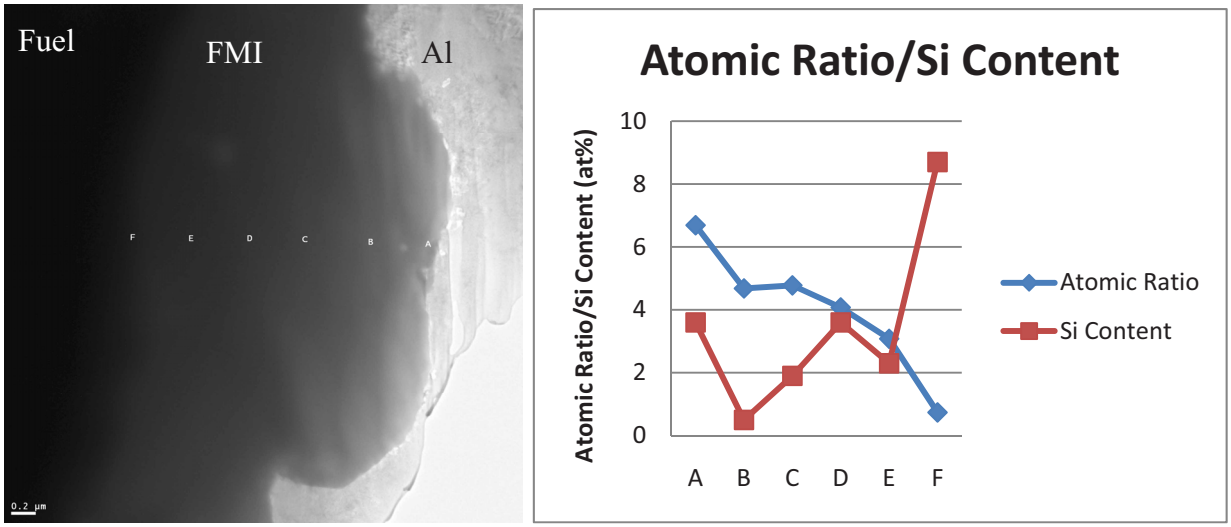

b)

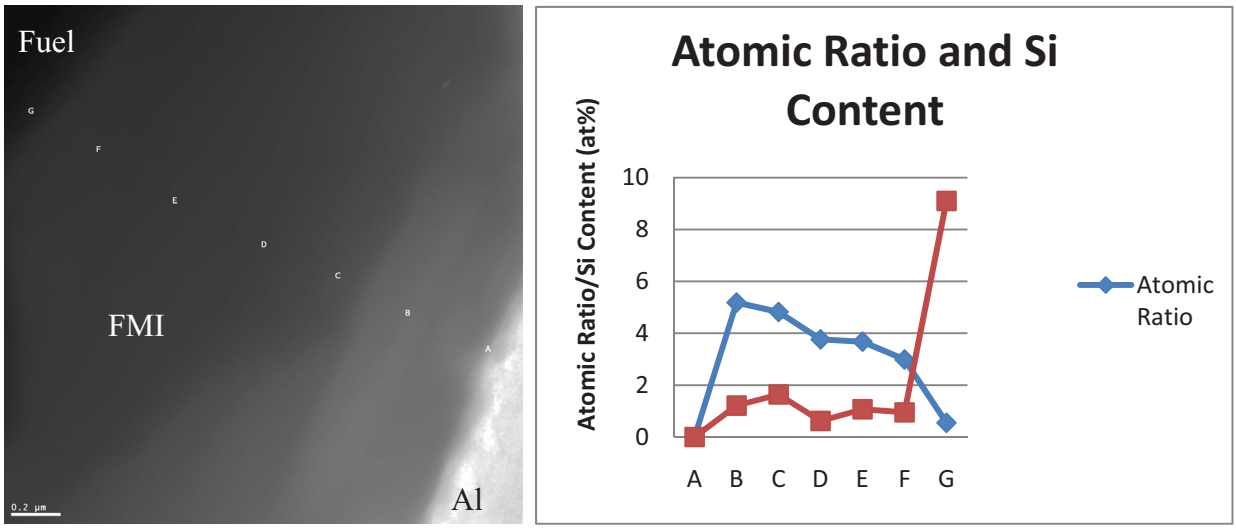

Figure 4.60: BF images of the FMI layer with EDS line scans and their corresponding atomic ratio plots

a)

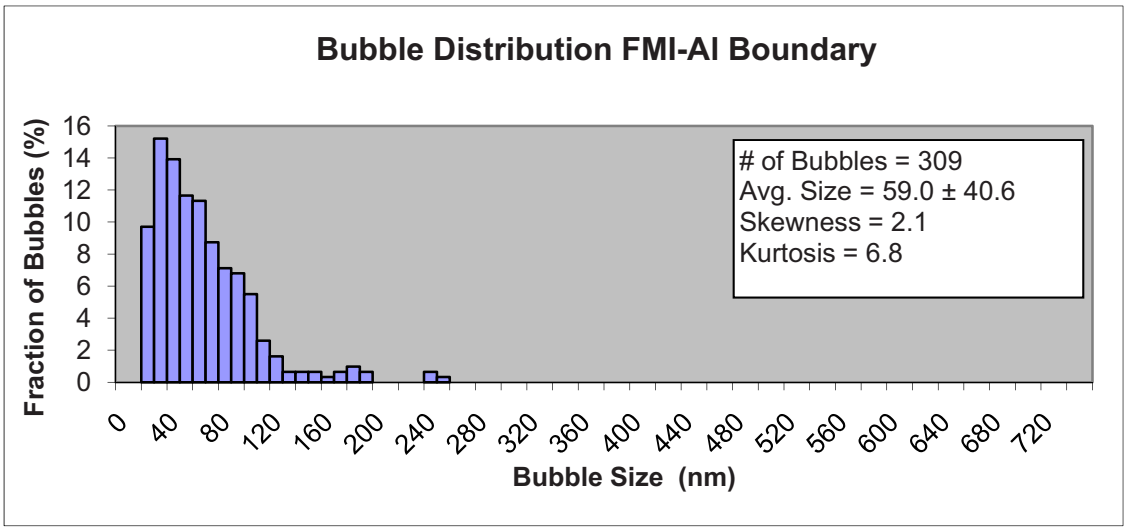
Bubble Distribution FMI-Al Boundary
Fraction of Bubbles (%)
16
14
12
10
8
6
4
2
0
0 40 80 120 160 200 240 280 320 360 400 440 480 520 560 600 640 680 720
Bubble Size (nm)
# of Bubbles = 309
Avg. Size = 59.0 ± 40.6
Skewness = 2.1
Kurtosis = 6.8

b)

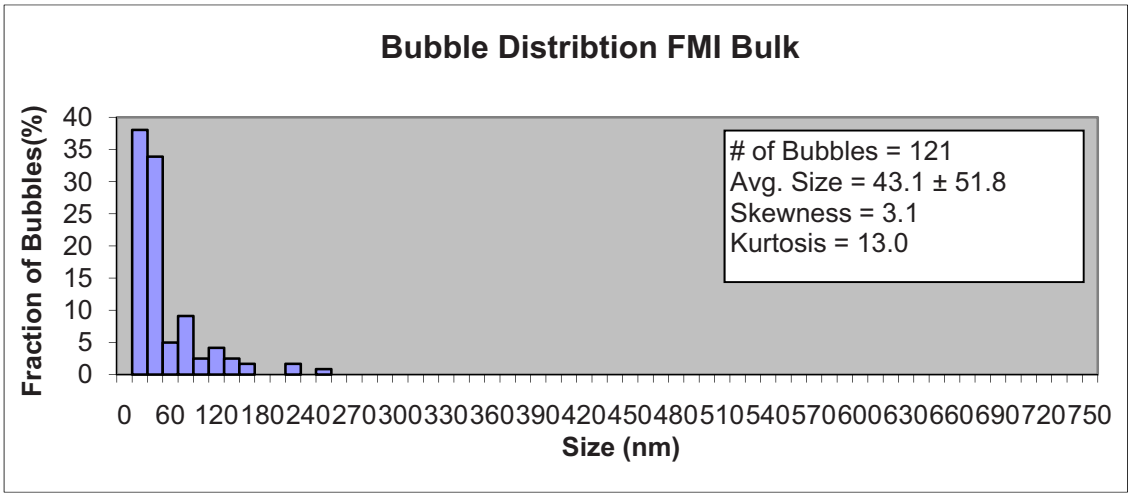
Bubble Distribtion FMI Bulk
Fraction of Bubbles(%)
40
35
30
25
20
15
10
5
0
0 60 120 180 240 270 300 330 360 390 420 450 480 510 540 570 600 630 660 690 720 750
Size (nm)
# of Bubbles = 121
Avg. Size = 43.1 ± 51.8
Skewness = 3.1
Kurtosis = 13.0

c)

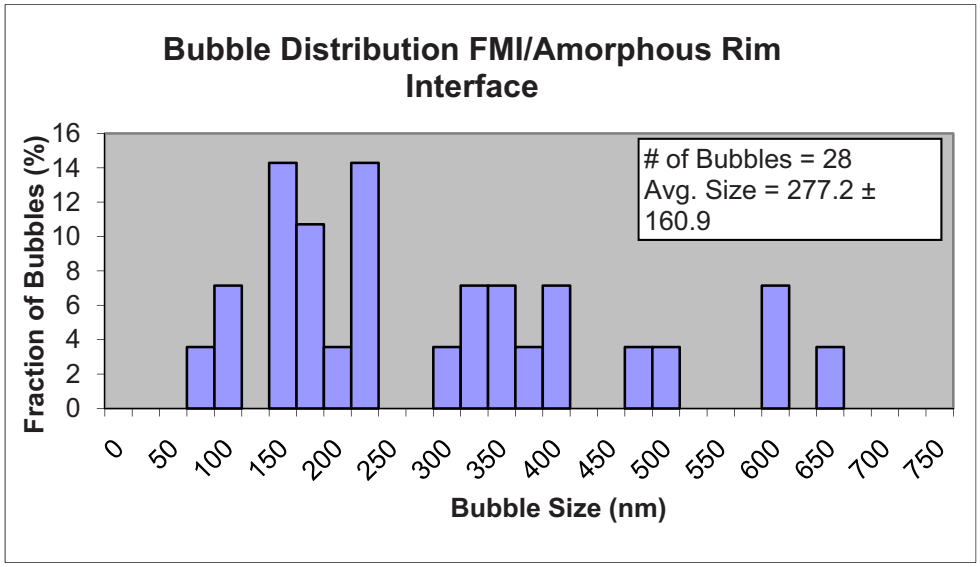

d)

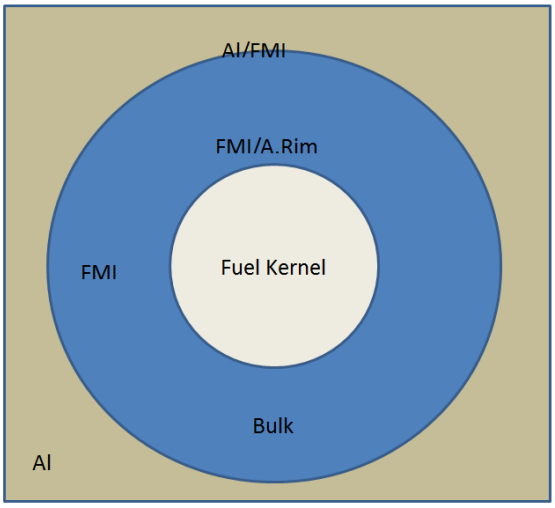

Figure 4.61: Size and bubble distributions of the a)FMI/Al interface, b) the FMI bulk, c) the FMI/fuel interface, and d) schematic of the key areas of interest in the fuel particle.

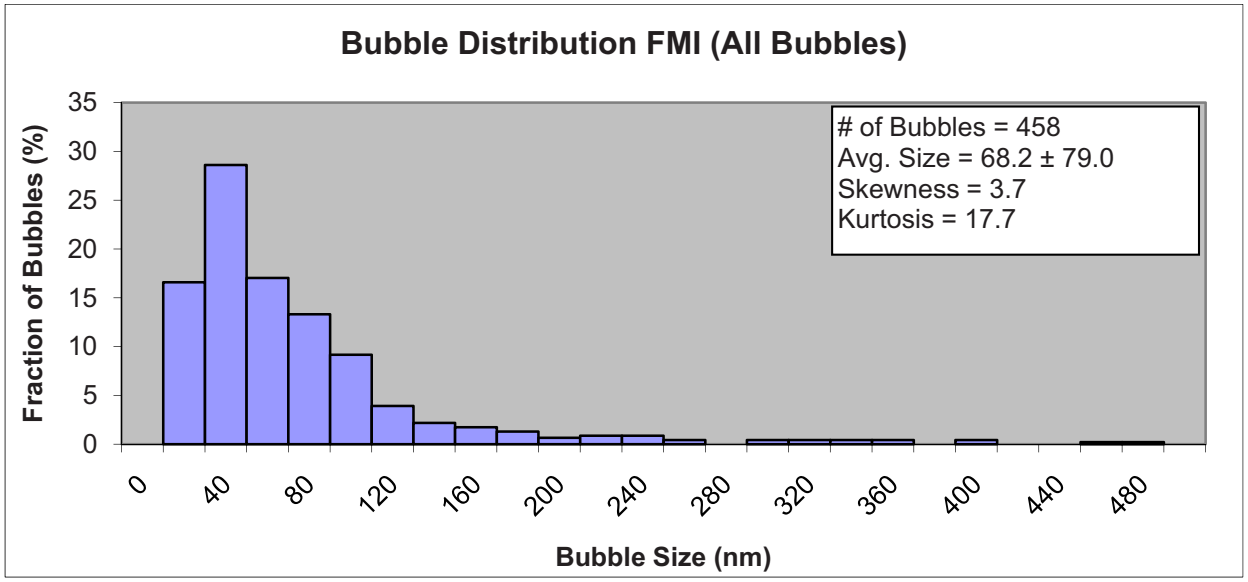

Figure 4.62: Size and bubble distribution of all bubbles present in the FMI regardless of bubble location.

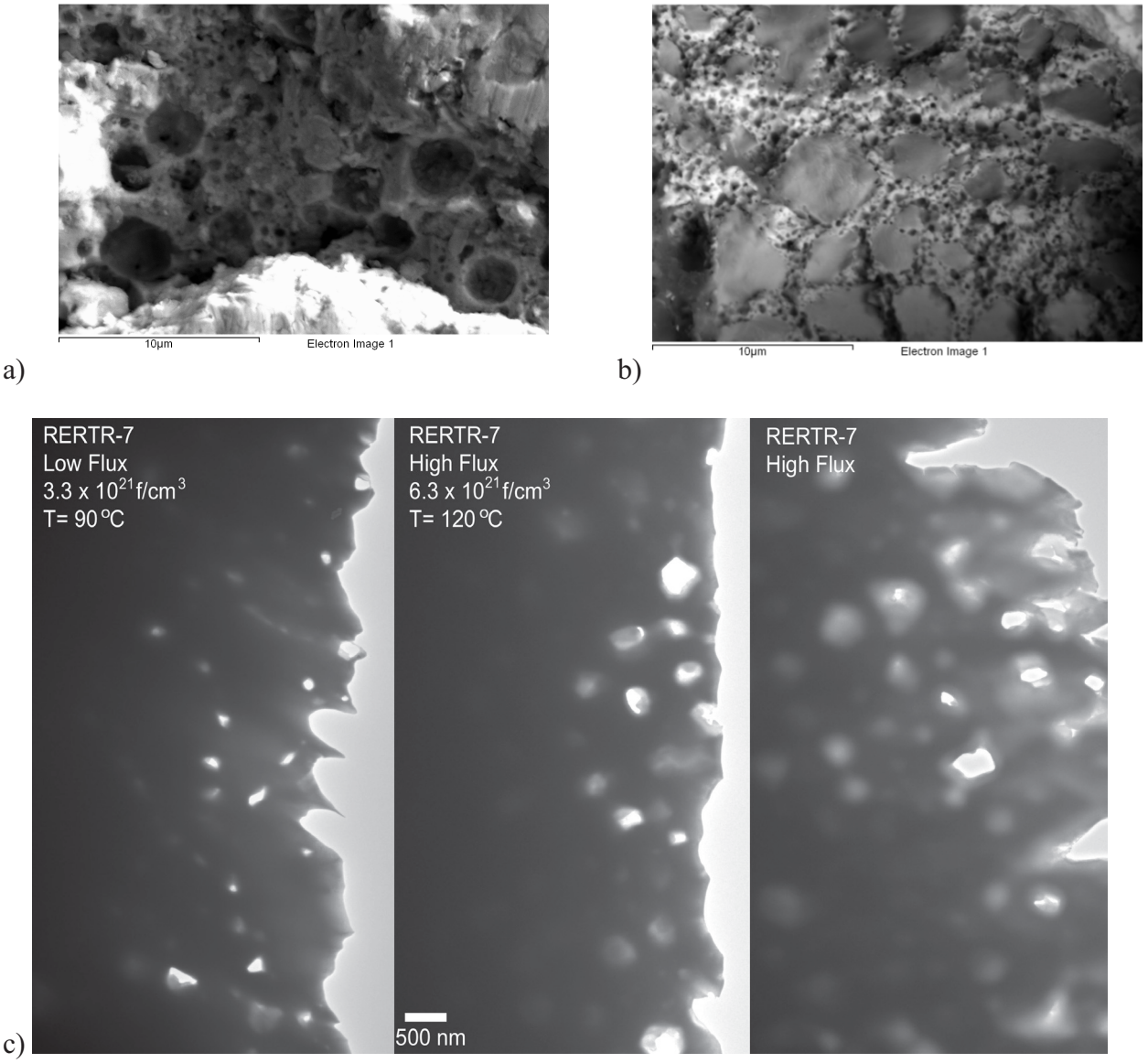

Figure 4.63: a) SEM image of a fracture surface of RERTR-7 H.Flux showing a large distribution of bubbles throughout, b) SEM image of a fracture surface of RERTR-7 L.Flux, and c) BF images of the intergranular type bubbles in RERTR -7 L.Flux and H.Flux.

a)

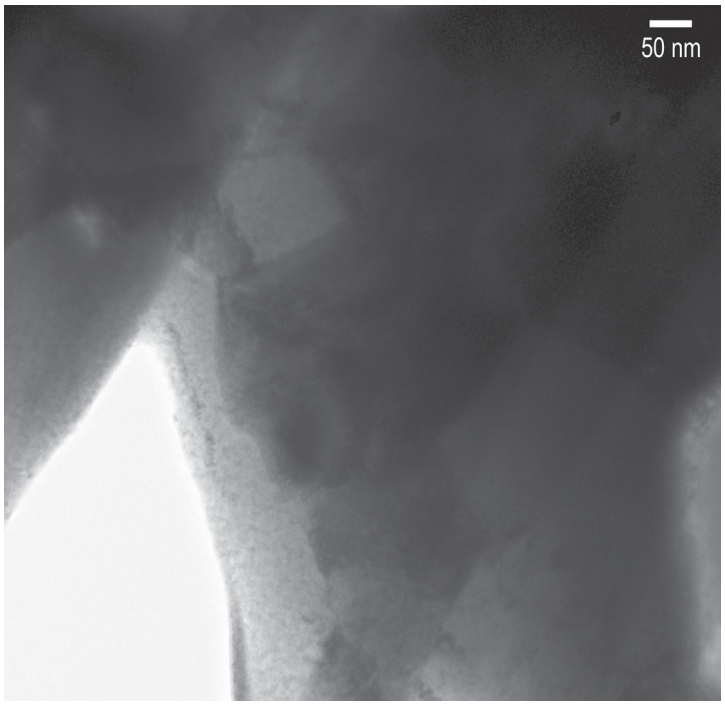

b)

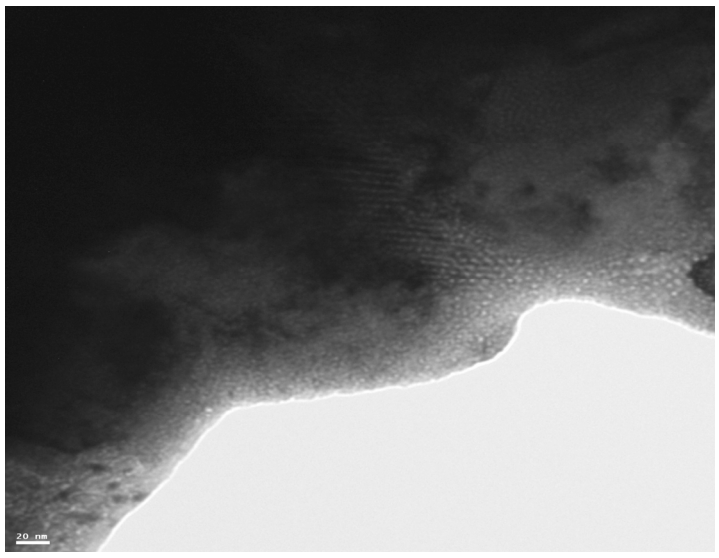

Figure 4.64: a) BF image of the fuel grains in RERTR-7 H. Flux and b) residual bubble superlattice in the fuel grains

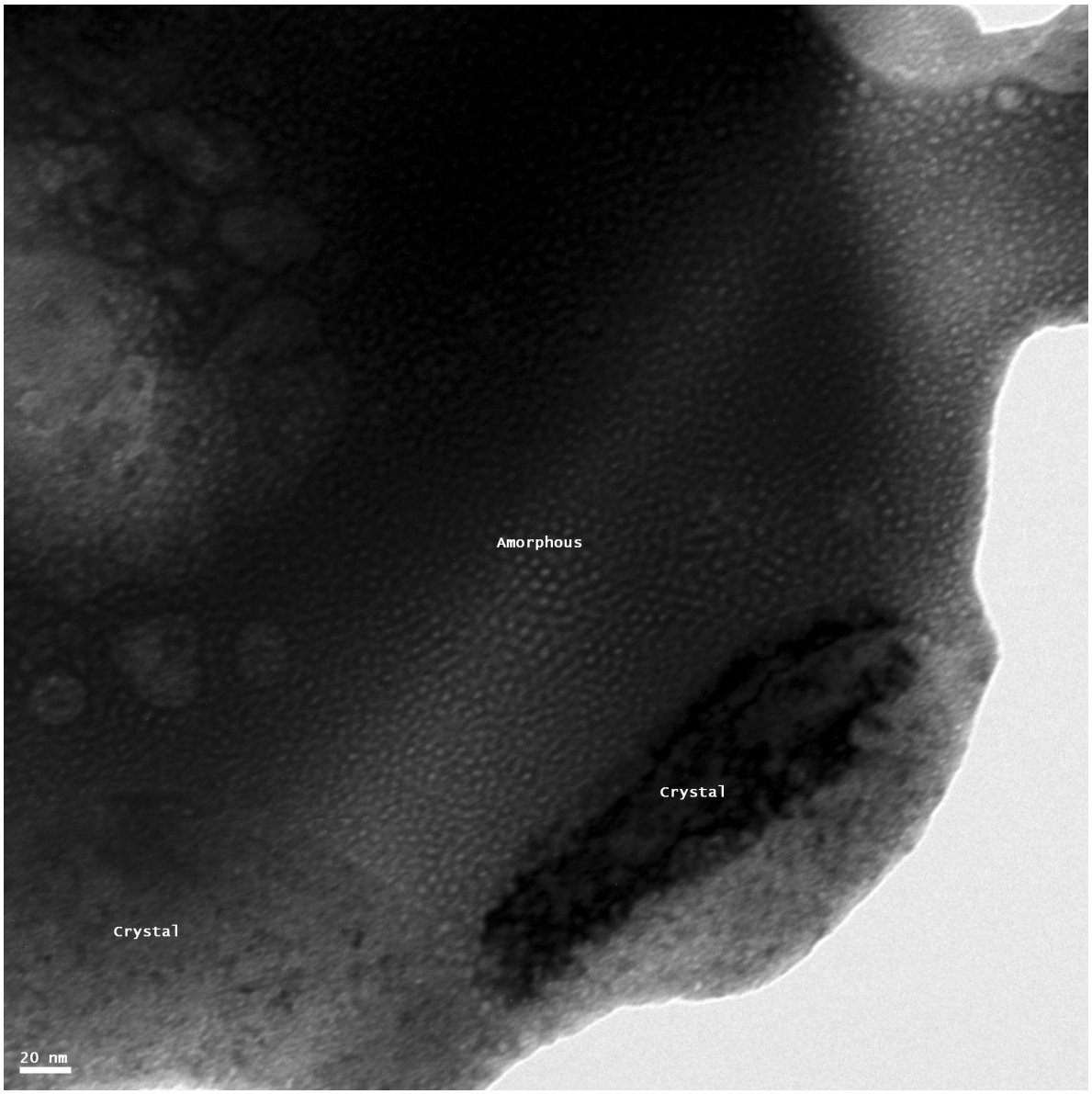

Figure 4.65: BF image of the crystal fuel region where a grain has undergone amorphization. Note that the bubble superlattice was still present in this location and some residual ordering is present.

Figure 4.66: Montage of BF TEM images showing a typical amorphous rim microstructure in RERTR-7 H.Flux.

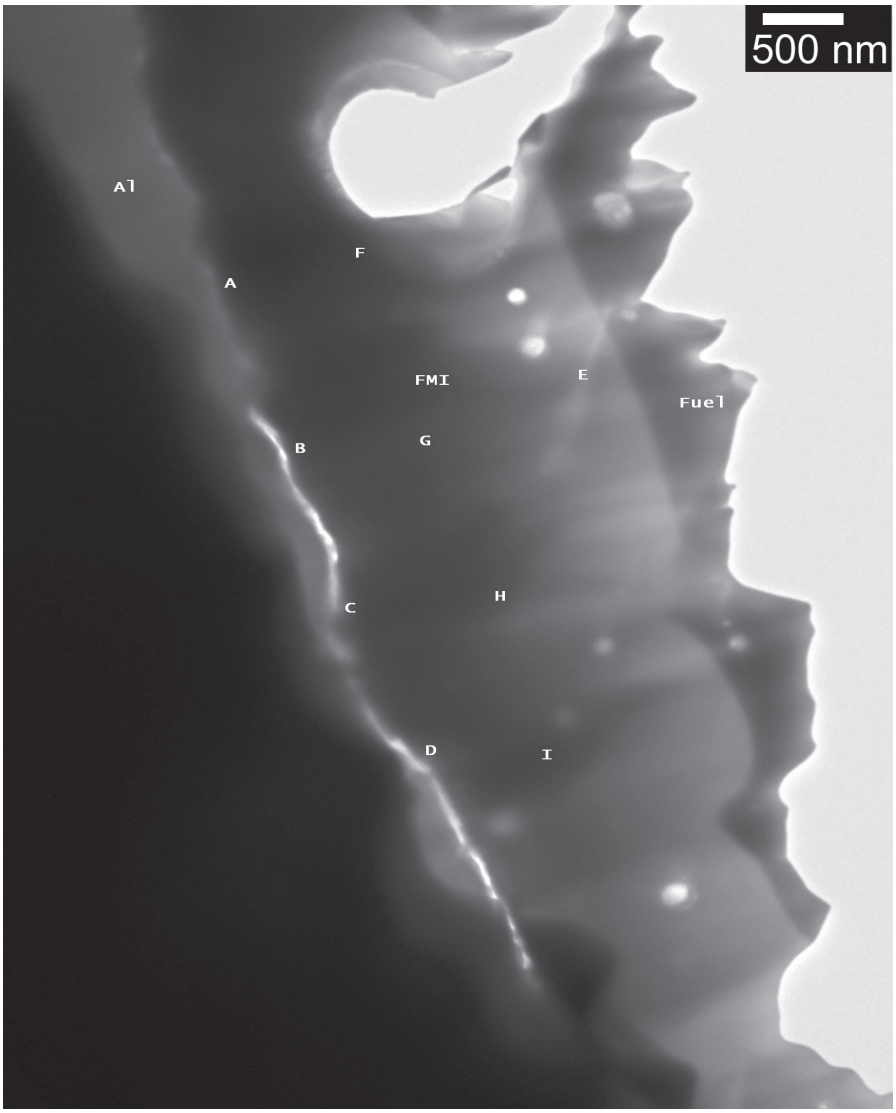

Figure 4.67: Cracking along the FMI layer/Al matrix interface in RERTR-7 H.Flux. Note the letters were used to correspond to EDS measurements.

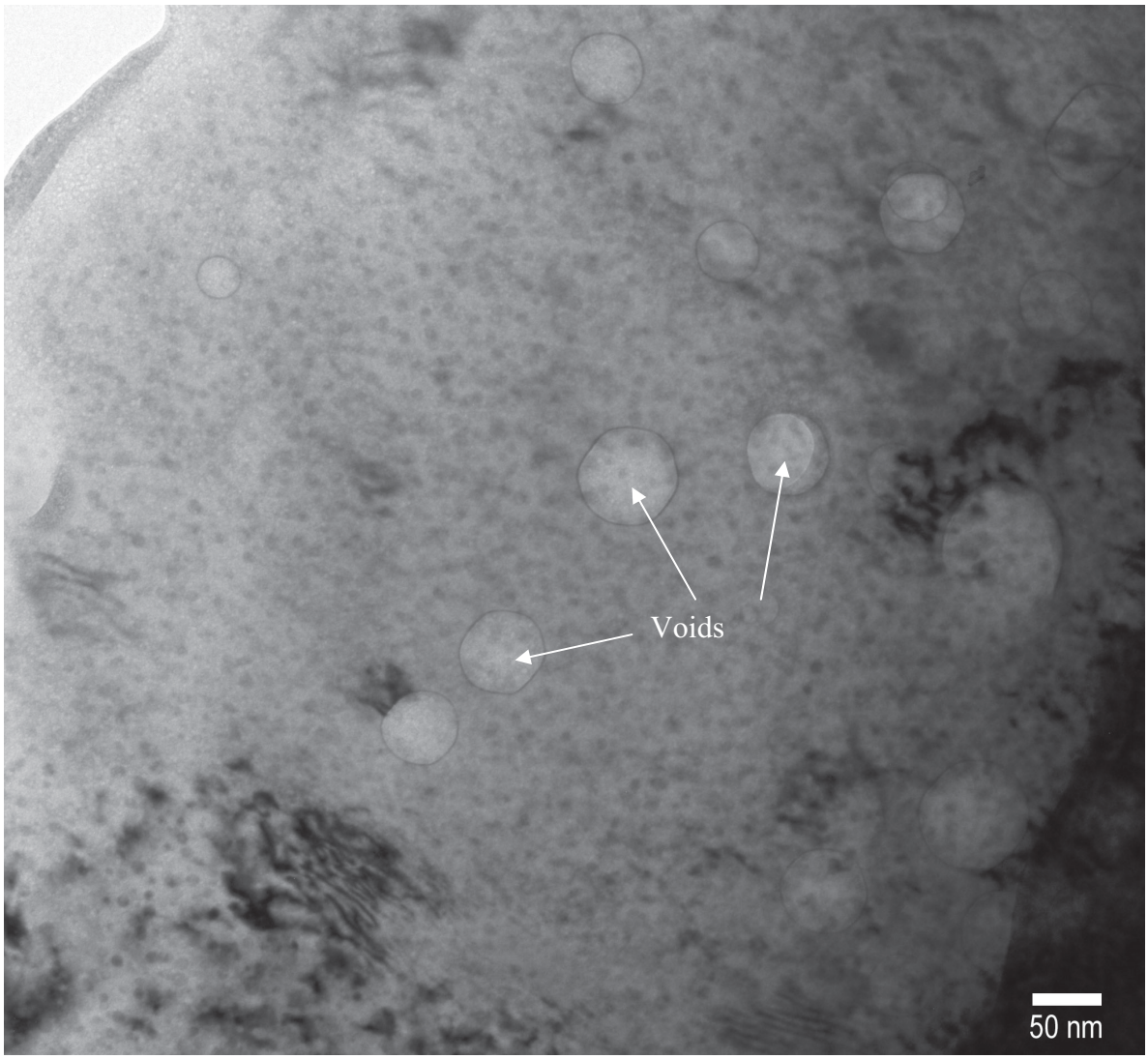

Figure 4.68: BF image showing Si precipitates and voids in the Al matrix. The Si precipitates, ~10 nm, are the uniformly distributed dark features throughout the whole image and form from Al transmutation during irradiation. The voids are the light circular features roughly 50 nm in size.

Chapter 5 : Experimental Discussion

Three specific questions are the focus of this study of U-7wt%Mo/Al-2wt%Si dispersion fuel:

- How does the Si content in the FMI layer affect the growth rate of the FMI layer, how does it affect the FMI's microstructure which goes amorphous, and how does it suppress the bubble growth in the FMI layer?
- Why does the rim between the FMI layer and the crystalline fuel region go amorphous, how is its microstructure affected by irradiation, and how the amorphous rim region differs from the amorphous FMI layer?
- How does the bubble superlattice form in the crystalline fuel region?

The discussion will be focused on these questions.

Figure 5.1 a) and b) are provided to help guide the discussion of a) where the Si is residing in the fuel particle after fabrication and b) where the Si is residing during irradiation. The figure shows the key regions that form in these steps and also shows where the Si is residing and at what compositions. A quick discussion of what is happening in the figures will be provided to help understand the discussion provided later. In Figure 5.1a) after fabrication, Si and Al will have diffused into the crystalline fuel particle due to thermal diffusion. A FMI layer that is nano-crystalline, as seen in RERTR-9A and -9B, with a chemical composition around $(U,Mo)(Al,Si)_3$ will form between the matrix and the crystalline fuel particle. Near the fuel, the FMI layer is Si enriched, up to 50 at%, with the FMI layer near the Al matrix being Al rich. Si precipitates will still be present in the Al matrix away from the fuel particles.

Figure 5.1 b) shows a schematic of the fuel system microstructure the after irradiation of the dispersion fuel. The Al matrix shows 10 nm sized Si precipitates that continually supply Si to the FMI layer. The FMI layer is completely amorphous with varying chemical compositions. The composition ranges from $(U,Mo)(Al,Si)_{2-7}$ depending on location. The $(U,Mo)(Al,Si)_2$ is near the amorphous rim region and $(U,Mo)(Al,Si)_7$ region occurring near the Al matrix. Between the FMI layer and the crystalline fuel region, an amorphous rim region has formed that has a chemical composition of $(U,Mo)_{3-4}(Al,Si)$ with only a small amount of Al present 1-10at%. This layer has a Si concentration of up to 20 at%. Large fission gas bubbles are present in this layer. Si and Al are continuing to diffuse into the crystalline fuel by primarily cascade mixing, thus increasing the amorphous rim thickness. The crystalline fuel region shows a bubble superlattice with random intergranular bubbles along the grain boundary. In RERTR-7 H.Flux, the fuel has/is undergoing recrystallization and small pocket of amorphous fuel is present with no significant Si or Al present. This indicates that there are two possible mechanisms in the crystalline fuel region that can drive the region amorphous: radiation induced recrystallization and a Si-modified crystalline region adjacent to the FMI layer.

5.1: How does the Si content affect the microstructure in the FMI layer?

The Si concentration affects three primary properties of the FMI layer; the chemical composition, amorphization of the FMI layer, and the gas atom diffusion and bubble growth in the FMI layer. The reasons for how the Si affects these specific properties are discussed below.

Figure 5.2a) is also provided to follow how the Si specifically affects the FMI layer's chemical composition, why it is amorphous, and the gas atom diffusion and bubble growth. Figure 5.2b) is provided to follow how the amorphous rim forms and how the Si affects the formation of the amorphous rim.

One of the key questions/issues in this study is how the Si content in the FMI layer plays a role in suppressing undesired FMI layer growth and bubble growth. Additionally, prior to this study, the specific microstructure of the FMI layer was unknown after fabrication. As a reminder, Table 5.1 provides Si locations and FMI microstructure of a pure Al matrix and Si-modified Al matrix after key points in the life of the fuel. The discussion of how the Si content affects the FMI layer microstructure will be presented in the following sections: section 5.1.1: a brief reminder of why Si was added to the matrix, section 5.1.2: what is the FMI layer's microstructure after fabrication, section 5.1.3: reasons why the FMI layer is amorphous, and section 5.1.4: how the covalent bonds help suppress bubble growth.

5.1.1: Background on why Si was added to the Al matrix

The FMI layer in the U,Mo/Al dispersion fuel from the RERTR-1 thru -5 irradiation campaigns was shown to not be stable at high burnup, showing large micron sized bubble growth in the FMI layer and uncontrolled FMI layer growth (19) (29). The large bubble growth is a precursor for large bubble interlinking, which leads to pillowing of the fuel and breakaway swelling in the fuel. The uncontrolled FMI layer growth leads to undesirable consumption of the Al matrix.

This decreased volume of Al matrix affects the overall temperature of the fuel by decreasing the overall thermal conductivity of the fuel. This decrease in thermal conductivity is due to the FMI layer having a much lower thermal conductivity than the Al matrix (53). The decrease in thermal conductivity leads to an increase in the overall fuel temperature. This leads to increased diffusion rates of defects and in turn leads to more Al matrix being consumed, creating a self-reinforcing process.

Si was added to the Al matrix in the RERTR-6 and following campaigns in an effort to control the FMI layer instability. This was done to create an FMI layer with a chemical composition similar to $U(Al,Si)_3$. The Si was also added to suppress the formation of UAl_4 and $U_6Mo_4Al_{43}$, the two phases believed to show undesirable bubble formation. From the Kr irradiations, $U_6Mo_4Al_{43}$ was shown to form large gas bubbles and is likely the phase driving large fission gas bubble formation in a U-Mo/Al dispersion fuel. $U(Al,Si)_3$ is a phase that is present in the FMI layer in the U_3Si_2/Al silicide dispersion fuel. Irradiation of the silicide dispersion fuel to a high burnup shows that the FMI layer, $U(Al,SI)_3$, is relatively stable at high burnups, showing minimal FMI growth and very little bubble growth (RERTR2010GAN). SEM analysis of the punches from the RERTR-6 and -7 L. Flux U-7wt%Mo/Al-2wt%Si dispersion fuel shows that the Si addition to the matrix helped stabilize the FMI layer to an acceptable level, reducing bubble growth throughout the FMI layer and the FMI layer thickness (51). Discovering the reason why Si limits the FMI growth and bubble growth was one of the primary reasons why TEM analysis was completed on the RERTR-6, -7 L. Flux, -9A and -9B punches.

EDS was used to determine the Si content in specific regions of the FMI layer. Note that the Si measured by EDS is semi-quantitative, providing an idea of the relative chemical composition in an area. One primary goal of the TEM studies was to determine the specific Si content in different regions, primarily around fission gas bubbles and at FMI layer interfaces. Prior to this study, it was not completely known where the Si was residing in the fresh fuel and the irradiated fuel.

5.1.2: FMI layer microstructure after fuel fabrication

RERTR-9A and -9B TEM analysis of the as-fabricated, unirradiated fuel showed that the Si preferentially diffuses into the FMI layer out of the Al matrix during fabrication due to thermal diffusion. Prior to discussing the Si content in the as-fabricated FMI layer, the structure of the FMI layer will be discussed. The FMI layer developing during fabrication in RERTR-9A and -9B due to the elevated temperatures from the rolling process was shown to form crystalline nano-sized grains, ~30 nm. Due to the short time at elevated temperatures during fabrication, the crystalline grains do not have sufficient time to grow into larger micron sized grains of $(U,Mo)(Al,Si)_3$ type compositions.

The nano-crystalline structure seen in RERTR-9A and -9B is consistent with results seen in diffusion couples between DU-7wt%Mo fuel and an Al-5wt%Si matrix (69). These diffusion couples were annealed at 600˚C for 24 hours. This led to FMI layer thicknesses ranging from 265-542 μm, much larger than the FMI layers seen in RERTR-9A and -9B which were ~2-3 μm.

Note that in RERTR-9A and -9B, the fuel during fabrication is held at 450˚C for roughly 45 min. Perez showed that the FMI layer formed during diffusion couple experiments consisted of a nano-crystalline structure with a $(U,Mo)(Al,Si)_3$ type phase, similar to the FMI layer formed during fabrication of RERTR-9A and -9B.

The Si content can range up to 70 at% in the FMI layer with the FMI forming a Si and Al rich region in a $U(Al,Si)_x$ type composition. Perez also showed that the FMI layer is Si enriched near the fuel region and the FMI layer is Al rich near the Al-matrix (69). This can be seen in

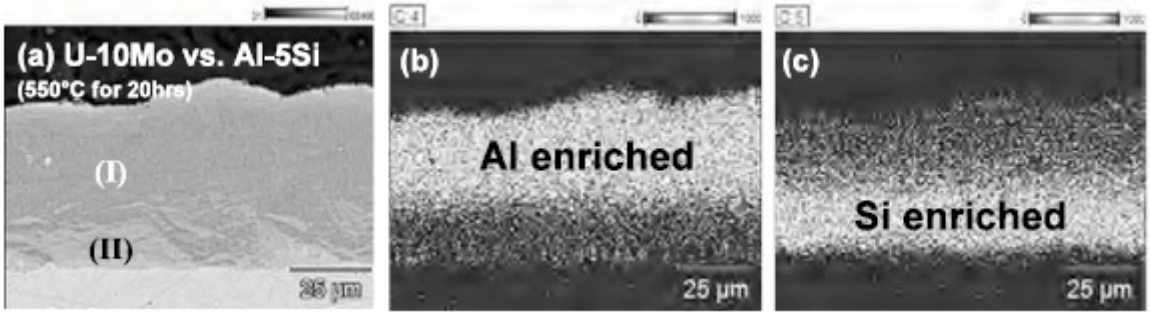

Figure 5.3 (69) . This shows that the Si atoms have a higher affinity for the U-Mo compared to Al. This is consistent with thermodynamic calculations conducted by Ryu (45), which showed that the magnitude of heat of formation for USi_3 is higher than UAl_3, -132.2 to -104.6 kJ/mol respectively. Additionally, Leeners (70) showed that an irradiation of a U slug that was surrounded by Al and an AlSi alloy showed that the Si diffused through the Al zone and formed a USi_3 type interaction layer next to the U slug and a $U(Al,Si)_3$ outside of the USi_3.

EDS analysis of RERTR-9A and -9B shows that the Si content present in the FMI layer can be as high as 50 at%. This high Si content is desired to help drive the FMI layer towards a $(U,Mo)(Al,Si)_3$ type phase, which is similar to the known stable FMI layer phase $U(Al,Si)_3$ that suppresses fission gas bubble growth and undesirable FMI layer thicknesses. The reason for the

high Si content in the FMI layer is due to its insolubility in the Al matrix and its affinity of (U,Mo). Si moves in two locations: it can form as large precipitates away from the fuel kernels, very similar to those seen in RERTR-9A and -9B, and the Si diffuses into the FMI layer when near the fuel kernels. The denuded Si zone, ~10 μm, can be seen in Figure 5.4 (71). Figure 5.5 shows the phase diagram for Al-Si (72). There are no phases that form between Al and Si at the irradiation temperatures, <200°C, of the U-Mo fuel, showing the insolubility of the Si in Al. The diffusion coefficient of Si through Al at 100˚C is 6.9×10^{-17} cm^2/sec and $\sim 10^{-8}$ cm^2/sec at 450˚C. (73). Assuming a $\sqrt{4Dt}$ relationship to describe the distance the Si can diffuse, the Si should be able to diffuse over 100 μm over the 45 minute hot rolling step at 450˚C. Note this calculated 100 μm diffusion is higher than the 10 μm precipitate free zone seen in Figure 5.4. One reason for this difference could be the broad variation in diffusion coefficient values in the literature. An order of magnitude difference in the reported diffusion coefficient value will lead to the correct value. Another potential mechanism that explains the difference is the bias for the Si to either diffuse to the fuel particle or form large precipitates. When comparing the size of the precipitates in RERTR-9A to the Al-2wt%Si powder sample, the -9A precipitate size is significantly higher compared to the Al -2wt%Si powder sample. This bias towards sinks could explain why the Si doesn't travel as far as calculated.

5.1.3: Why the FMI layer is amorphous

Following irradiation, the FMI layer, shown in schematic form in Figure 5.1b), was shown to be completely amorphous, as seen in the RERTR-6 and -7 L.Flux samples. Other FMI layers

similar to the FMI layer seen in RERTR-6 and -7 L. Flux have also been seen to be amorphous. Specifically, work at the INL on a U_3Si_2/Al silicide dispersion fuel shows that the $U(Al,Si)_3$ FMI layer is amorphous in character after irradiation (23). Additionally, the FMI layer formed in UAl_x/Al dispersion is amorphous (74). The UAl_x phase composition is composed of a mixture of UAl_2, UAl_3, and UAl_4 phases. These results show that Al and Si content have an effect on the ability of the FMI layer to remain crystalline during irradiation.

The covalent bonds formed with Al and/or Si affect the material's ability to undergo amorphization (6). Si-Si bonds have a significant effect on the FMI layer ability to remain crystalline. Si-Si bonds are primarily covalent in nature, though no bond is completely ionic or covalent; they are a mixture of both in various amounts. Equation 5.1 below shows an expression to determine the ionic vs. covalent nature of bonds between elements using the elements electronegativity (75). This expression uses the electronegativity of the elements to determine the covalent bonding of a material. In general, elements residing on the right side of the periodic table, i.e. Cl, F, O, C, tend to form covalent directional bonds when paired with like atoms. Si and Ge are intermetallics and behave very similar to the right side of the period table elements. The metallic elements tend to form metallic bonds when paired with each other. For a material to be ionic, the difference in electronegativity is the driving force. The higher difference in electronegativity, the more likely the atoms are to be ionically bonded. Table 5.2 shows the nature of the bonds that might form in the FMI layer, i.e. Si-Mo, Al-U, U-Mo, etc (76). Si-Si is assumed to be 100% covalent and other like element combinations, such as Al-Al are assumed to be metallic bonds. Note that, in addition to the bonds listed in Table 5.2,

tetrahedral bonds can also form in a material. For instance, Si-O-Si bonds are prevalent in SiO_2. Tetrahedral types of bonds might also be present in the FMI layer, such as Si-Si-Al or Si-Si-U bonds, though no evidence has been found to back this theory up and this analysis will limit the discussion to bonding between two atoms only.

$$\text{Covalent \%} = \exp\left(-0.25 \times \Delta E_n^2 \right) \qquad (5.1)$$

where ΔE_n is the difference between the two elements' electronegativity

Trachenko (6) compiled a collection of other's experimental results of materials that undergo amorphization. Trachenko showed that the Si-Si bonds prevent/slow reordering of the atoms from the highly energetic fission products and neutron damage cascades, creating short range disordering. The covalent bonds are directional and when other interstitials in the cascade are trying to move around or through the directional bonds to reach a specific lattice location, they need to provide enough energy to break the bond. If the atom cannot break the bonds, the atoms become pinned around the Si-Si bond, leading to short range disordering. A high enough concentration of covalent bonds can prevent the material from regaining its crystalline state. This value is unknown for this FMI layer as Si-Si bonds are not the only covalent bonds present in the FMI layer. If the minimum concentration is met, the bonds will slowly disorder the system, eventually leading to amorphization. At low concentrations, the bonds will affect the ordering of the system but not enough to force amorphization. At higher temperatures, atomic motion will increase and will be able to move around the Si-Si bonds.

In an ionic system, the atoms are electrostatically charged and for an atom to diffuse through this bond, it does not require the extra energy covalent bonded systems needed to reach a low energy lattice spot. The atoms in an ionic system are charged and are likely to reside next to atoms of opposite charges. This leads to some short range ordering and the ability of ionic systems to remain crystalline or resist amorphization.

With the U,Mo/Pure Al dispersion FMI layer undergoing amorphization without Si added to the matrix, another bond besides Si-Si bonds supports disordering of the FMI layer during irradiation and keeps it amorphous. Minasian (77) showed that U-Al bonds are partially covalent. The calculation of the covalent nature of the U-Al bond shown in Table 5.2 indicates that this bond is covalent, (~99% covalent). Additionally, knowing that U_3Si_2 fuels undergo amorphization during irradiation (23), U-Si bonds are assumed to contribute to the disordering of a system. The U-Al, U-Si, and Si-Si covalent bonds are likely the driving force for why the FMI layer in a U,Mo/Al,Si dispersion fuel is undergoing amorphization. To show the effect of Al content on driving the system amorphous, Table 5.3 shows various U-Al phases and their Al content that have been shown to undergo amorphization. Aluminum was added to the table, but due to metallic bonding, Al should not go amorphous and was shown not to in RERTR-6 and -7 L.Flux. Note that the Kr irradiations of the DU-alloys in this study showed that UAl_4 and $U(Al,Si)_3$ remained crystalline to a dose of 100 dpa at an irradiation temperature of 200˚C. The reported UAl_4 and $U(Al,Si)_3$ phases listed in Table 5.3 were irradiated at a temperature of ~100˚C. Three possibilities of why UAl_4 and $U(Al,Si)_3$ do not undergo amorphization could be: the critical temperature for amorphization for UAl_4 and $U(Al,Si)_3$ likely resides somewhere between 100 ˚C

and 200˚C, the irradiation particle could affect the damage cascade and the materials ability to recover from a cascade, and/or the fission rate can affect the materials ability to undergo amorphization.

5.1.4: The effect of the covalent bonds on fission gas bubble growth

The covalent nature of the Si bonds affects the ability of the material to remain crystalline, but also affects the free volume associated with an amorphous material (78). Diffusion in an amorphous material is believed to occur by atoms squeezing into the free volume present in the amorphous structure. If the free volume is decreased, the diffusivity of atoms through the amorphous materials will be lower. This can be seen in the Doolittle equation 5.2 below (19).

$$\eta^{-1} = A \exp [C/V_f] \qquad (5.2)$$

where η is the viscosity, A and C are constants, and V_f is the free volume

The viscosity is related to the gas mobility of the diffusion of the gas atoms. A larger viscosity will mean lower diffusion and thus a smaller free volume in the amorphous material.

Si bonds have been shown to help reduce the free volume in the amorphous FMI layer (79). It is believed that the U-Al covalent bonded system doesn't reduce the free volume as effectively as the Si-Si bonded system, thus leading to the large fission gas bubbles seen in (19). The decrease in free volume in an amorphous material leads to a decrease in fluidity of the fission gas atoms. This in turn leads to the fission gas atoms residing in solution or as smaller bubbles,

which can hold higher gas pressures (2). This can be seen in Equation 5.3 (13), where a smaller bubble radius has a larger equilibrium pressure. Also, the decreased fluidity will help reduce bubble coarsening, leading to a decreased chance of forming the large non-uniformly distributed bubbles seen in the U,Mo/Al dispersion fuels in the FMI layer (19).

$$P=2\gamma/r \qquad [5.3]$$

where P is the pressure in the bubble, γ is the surface tension of the bubble, and r is the radius of the bubble.

Si content in the FMI layer is important to suppress fission gas bubble formation and to minimize the FMI layer thickness. Hofman (51) suggested that when the Si content is less than 5 at%, the FMI layer will behave like the FMI layer formed in the U,Mo/Al dispersion fuel. This FMI layer will increase in size and will start to form large fission gas bubbles with increasing burnup. $U_6Mo_4Al_{43}$, a known phase that forms in the FMI layer of U,Mo/Al dispersion fuel, was shown in the Kr irradiations to form large gas bubbles, a precursor for bubble inter-linkage and pillowing in the fuel. By adding Si, the $U_6Mo_4Al_{43}$ phase was not seen in RERTR-6 and -7 L.Flux and large bubbles were not seen in the FMI layer.

To verify the theory that Si content affects the bubble size, Si content around fission gas bubbles was measured using EDS in the RERTR-6 experiment and the Si content vs. bubble size in the FMI layer can be seen in Figure 5.6. There seems to be a general trend where, at low Si content, the bubble size is large when compared to the high Si content region. This analysis is

independent of bubble location in the FMI layer. Addition measurements would help with statistical analysis, but due to the challenges of sample preparation in these materials, additional measurements are difficult to achieve.

Figure 5.6 shows how the Si concentration, i.e. the Si-Si bonds, affects the amorphous free volume of the FMI layer and the fission gas bubbles' ability to form large bubbles. It appears that the low density of Si-Si bonds increases the free volume present in the FMI layer, allowing for increased gas diffusion in the layer. This increased diffusion allows for small bubbles to grow by coalescence with each other and/or for fission gas atoms to diffuse into the bubbles. It appears that around 10 at% the effect of the Si-Si bond density on bubble size is saturated or the reduction in free volume is saturated and diffusion of the gas atoms is slowed. With (51) suggesting that a Si concentration of 5 at% suppresses bubble and FMI layer growth, it appears that a Si concentration of 10 at% efficiently controls bubble growth. The 5 at% value reported by (51) likely helps in reducing the FMI layer growth. With SEM analysis showing that the FMI layer sizes are within acceptable levels, <10 μm, it appears that the Si in the FMI layer, ~2-10 at%, is suppressing FMI layer growth.

Summary of the key points discussed:

1: Si helps suppress the formation of UAl_4 and $U_6Mo_4Al_{43}$, driving the system to a $(U,Mo)(Al,Si)_{2\text{-}7}$ type phase which has been shown to resist bubble growth.

2: Si, along with Al, allow the FMI layer transition to an amorphous state during irradiation due to their covalent bonding nature.

3: The covalent bonding of Si-Si bonds helps reduce the free volume leading to decreased diffusion of fission gas in the amorphous FMI layer, mitigating bubble nucleation and growth. Al-Mo and Al-U bonds do not suppress the free volume enough to suppress bubble growth in the FMI layer.

4: A Si concentration of around 10 at% appears to minimize the FMI layer bubble size.

5.2: What is the amorphous rim?

With the discovery of the amorphous rim region in RERTR-6 and -7 L. Flux, questions arose as to why this region formed, why is it amorphous, how does its chemical composition affect fission gas behavior, and why do large (>10nm) fission gas bubbles form at the amorphous rim/FMI interface at high burnups. Theories will be presented to provide a consistent explanation to these questions. Note, please refer to Figure 5.1b) to understand where the amorphous rim is occurring in the fuel and Figure 5.2b) to understand how the Si affects key microstructure components of the amorphous rim.

5.2.1: Why is the amorphous rim amorphous?

RERTR-6, -7 L.Flux, and -7 H.Flux showed that the layer between the amorphous FMI layer and the crystalline fuel was amorphous and of different chemical composition when compared to the FMI layer. This layer was termed the amorphous rim region. The amorphous rim region had a

chemical composition that is composed primarily of U, Mo, Si, and Al in a $(U,Mo)_3(Al,Si)$ type of concentration . It is not completely known what the exact Al content is in this region. SEM analysis has shown that the amorphous rim includes about 1-2 at% Al. TEM analysis shows that it can reach a maximum concentration of 10at%. Where the FMI layer is mostly composed of Al, the amorphous rim has a significant amount of Si when compared to Al. Just as a comparison, the FMI layer has a chemical composition of $(U,Mo)(Al,Si)_{2-7}$ and the amorphous rim has a composition of $(U,Mo)_{3-4}(Al,Si)$.

Prior to discussing why the Si and Al was present in this region, the reasons why the amorphous rim region is amorphous will be presented. This is likely the same reason presented before in the FMI layer without the significant contribution of Al covalent bonds. With a significant Si content present in the amorphous rim region, Si likely plays a major effect on amorphization. As mentioned in the Si content discussion in the FMI layer region, Si-Si bonds particularly affect the crystalline structure of a material, supporting local disorder from the damage cascades on the short range. The higher density of Si-Si bonds in the material, the more likely that the material will not be able to recrystallize following the ongoing damage cascades in a nuclear fission environment, thus undergoing amorphization. It should be noted that if any Al is present in the amorphous rim, it can help with the disordering and eventually amorphization.

5.2.2: Why Si is present in the amorphous rim?

Various diffusion couples experiments show no indication of the amorphous rim region forming between the FMI layer and the crystal fuel region (36), (69). RERTR-9A and -9B fresh fuel punches, examined after fabrication and prior to irradiation, showed that there is no amorphous rim present, indicating that this region is forming due to the irradiation process. These results show that the amorphous rim forms by some radiation-induced process. Van de Berghe (1) showed that in a U,Mo/Pure Al dispersion fuel, the amorphous rim region is not evident around the fuel particle, indicating that the Si addition to the matrix has a major effect on the formation of the amorphous rim region during irradiation. Note that U-Al bonds in the FMI layer in a U-Mo/Pure Al matrix will help support local disordering, driving this FMI layer amorphous as seen by Van den Berghe (1).

From analysis of RERTR-9A and -9B, a large concentration of Si is present in the nano-crystalline FMI layer before irradiation (up to 50 at%). The FMI layer Si concentration was shown to decrease significantly after irradiation in RERTR-6, -7 L. Flux, and -7 H.Flux, with a maximum of 20 at% Si in the FMI layer after irradiation in parallel with the formation of an adjacent Si-rich amorphous rim. Si will have not diffused into the Al due to its insolubility with Al. This indicates that the Si has diffused from the FMI layer and into the amorphous rim region. Additionally, Al is present in the amorphous rim but at low atomic concentrations ~2-10 at%. Comparing the amorphous rim Si content to the FMI layer Si content, the Si content in the amorphous rim is roughly 5-10 at% higher than the FMI layer. Figure 5.1b) shows this concept in the Si distribution.

One important question to answer is how do the Si and Al atoms diffuse into the amorphous rim region. As mentioned before, no Si was observed in the crystalline fuel/FMI layer interface after fabrication as seen in RERTR-9A and -9B. Additionally, TEM analysis of a diffusion couple between Al-2wt%Si and U-7wt%Mo showed that the high temperature diffusion process did not create the amorphous rim region as seen in RERTR-6 and -7 L. Flux (69). This indicates that the amorphous rim region does not form by thermal diffusion. One key observation of the diffusion couple experiment is that Perez showed the Si enriched in the FMI layer near the crystalline fuel (69).

With elevated temperatures during fabrication and in diffusion couple experiments not creating the amorphous rim, the formation of the amorphous rim from the crystalline fuel is governed by some radiation induced process. It is not completely known how the Si is diffusing into the crystalline fuel region and forming the amorphous rim but two possible mechanism are radiation-induced cascade mixing and radiation enhance diffusion due to the production of point defects.

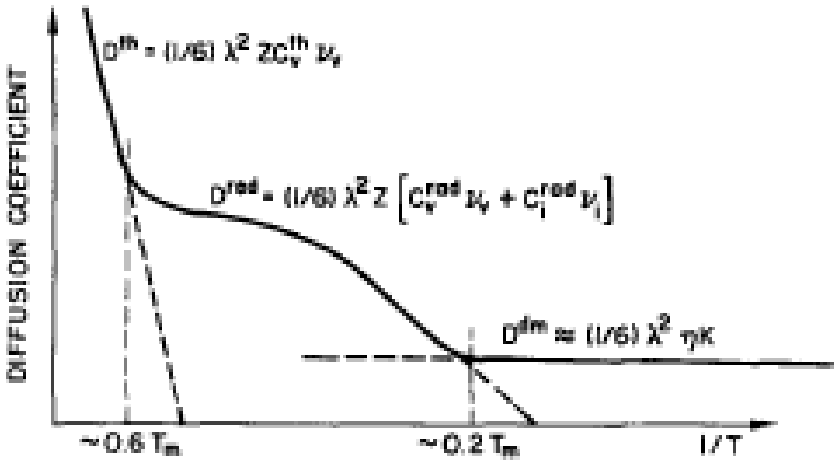

Figure 5.7 shows a simple diagram of what a typical diffusion coefficient vs. temperature profile is for an irradiated system. Two key temperature values are noted. These being ~0.6 T_m and ~0.2 T_m. Temperatures above 0.6T_m, thermal diffusion is the dominating process. Between 0.6 T_m and 0.2T_m, radiation enhanced diffusion is dominating. This is due to the mobility of the point defects being created due to the irradiation process. Below 0.2T_m, the system is dominated by diffusion mixing. Note that for RERTR-6 and -7L.Flux, the irradiation temperature is roughly 0.22T_m, indicating that both diffusion mixing and radiation enhanced diffusion are likely contributing to the diffusion coefficient. Calculations were done to see what the effect of both of the diffusion processes were on the distance Si travels into the crystalline region from irradiation. Mixing will be talked about first and then the radiation enhanced diffusion contribution.

It is assumed that the diffusion mixing will behave like a Gaussian distribution. From this, the full width half maximum, FWHM, of the distribution in a radiation cascade system is equal to:

$$FWHM = \sqrt{\frac{2}{3} R^2 F t} \tag{5.4}$$

where R is how far an atom is displaced during a cascade, F is the dpa rate, and t is the irradiation time

(80) showed that Si is displaced 2-3 nm from its lattice location during a single damage cascade. This value will be used for R in equation 5.5. The irradiation time is specific to the experiment, but for this analysis is assumed to 116 days. The dpa rate reported by Rest (81) can be described by equation 5.5 below:

$$dpa\ rate = B/f_r \qquad (5.5)$$

where B is a constant, $6x10^{23}$ $m^{-3}sec^{-1}$ and f_r is the fission rate of the fuel. Note that B is reported for both UO_2 and U_3Si_2 fuels.

Assuming a f_r value of $4x10^{20}$ $fiss/m^3sec$ and an irradiation time of 116 days, the predicted FWHM of the cascade mixing process is ~200 nm, much lower than the 4 μm size seen in RERTR-6 and -7 L.Flux.

Rest created an expression for radiation enhanced diffusion for UO_2 and U_3Si_2 fuels based on the irradiation temperature and fission rates. Appendix 1 shows the equations and parameters used to determine the radiation enhanced diffusion coefficient for a low temperature, high fission rate fuel. The radiation enhanced diffusion coefficient was determined to be $1.29x10^{-18}$ m^2sec^{-1}. Assuming a $\sqrt{4Dt}$ relationship to determine how far material will diffuse into a material after

some period of time, the Si will diffuse roughly 7 μm. Note that this calculation was for a UO_2 and U_3Si_2 fuel system. It is not clear if any parameters need to be changed for a U,Mo system.

Comparing the cascade mixing and the radiation enhanced diffusion contributions to Si diffusion into the crystalline fuel region, the radiation enhanced diffusion is the dominating process in the U,Mo fuel system. The cascade mixing process is an order of magnitude low while the radiation enhanced diffusion estimates the Si diffusion into the crystalline fuel to be on the correct magnitude, leading to the assumption that radiation enhanced diffusion is the primary mechanism for Si and Al atoms diffusing into the amorphous rim.

Another key question to understanding the amorphous rim is what Si concentration drives the crystalline fuel region amorphous. RERTR-7 L.Flux showed that at the crystal fuel/amorphous rim, the Si concentration is 2-3 at% on the crystalline side. It appears that a 2-3 at% concentration of Si-Si bonds is needed for the crystalline fuel region to undergo amorphization though additional work is needed to confirm this statement. Additionally, once the crystalline fuel undergoes amorphization, Si will preferential diffuse towards the amorphous rim from the FMI layer due to its high affinity to U (45). Si has also been shown to diffuse faster through Mo when amorphous when compared to crystalline Mo, showing how an amorphous material tends to have a higher diffusion rate when compared to a crystalline state (82).

It is believed that during the irradiation, the amorphous rim will slowly consume the crystalline fuel region, eating away the crystalline fuel grains by the four proposed Si diffusion/mixing

mechanisms. SEM results of RERTR-7 H. Flux showed that the amorphous rim has grown larger, ~8 μm, than the reported ~4 μm reported in RERTR-6, indicating that the Si is indeed slowly diffusing/mixing into the crystalline fuel region and driving the crystalline fuel region slowly amorphous. As a side note, the amorphous rim will slowly decrease the rate it consumes the crystalline fuel with increasing burnup. This is due to the finite Si concentration being distributed throughout the FMI layer and the amorphous rim region. Eventually, there will not be enough Si concentration (~2-3 at%) to diffuse into the crystalline fuel region and drive it amorphous.

It would be interesting to further investigate a U-Mo/Pure Al matrix system to a) verify that the amorphous rim region doesn't form between the crystalline fuel and the FMI layer and b) see how much Al is mixing into the crystalline fuel region at the FMI layer crystalline fuel interface. One would assume that mixing is occurring at this interface in this system and Al should be present in the crystalline fuel region. Knowing at what concentration Al drives the crystalline fuel amorphous would be beneficial.

5.2.3: What is the chemical composition of the amorphous rim region?

OM images of RERTR-7, Figure 5.8, at a fission density of ~9×10^{21} f/cm^3, show that large non-uniformly distributed fission gas bubbles are littering the FMI layer/amorphous rim interface. EDS analysis of RERTR-6 and -7 L. Flux of this interface provided some explanation of why this might be occurring. Prior to discussing these bubbles, note that on the high burnup side of

the fuel plate, the fuel is beyond the designated end of life operating burnup of $4.2x10^{21}$ f/cm^3. Even though the bubbles are forming at a burnup well beyond end of life operation, it is useful to understand why these bubbles are forming. The atomic ratio, x=(U+Mo)/(Al+Si), in U_xSi was used to help try to identify the phases across the amorphous layer. The atomic ratio at the FMI/amorphous rim interface was shown to be around x=3, indicating that the fuel has a composition close to $(U,Mo)_3(Al,Si)$. This composition is very similar to U_3Si.

One pressing question is why is the FMI layer have a chemical composition of $(U,Mo)(Al,Si)_3$ and the amorphous rim have a composition of $(U,Mo)_3(Al,Si)$? The amorphous rim has a composition that is primarily U_3Si. The FMI layer is primarily UAl_3. Comparing the heats of formation for these two phases at 298°C as reported by Ryu in (45), the heats of formation for U_3Si and UAl_3 are -134.0 and -104.6 kJ/mol. This shows that the system will want to form the U_3Si phase in the amorphous rim instead of the UAl_3 type phase. Note that Si will drive the heats of formation higher while Mo decreases the value. The Mo difference between the FMI layer and the amorphous rim is minimal.

U_3Si has been shown to form large micron sized fission gas bubbles at operational limit burnups (83). These bubbles are large and non-uniform in distribution, a common precursor for breakaway swelling. U_3Si_2 and USi show uniformly distributed fission gas bubbles that are significantly smaller in size when compared to U_3Si. U_3Si, U_3Si_2, and USi were recently shown to be amorphous (23) at research reactor operating parameters. The Si-Si bond concentrations in these three phases likely affect the free volume. A smaller free volume will lead to decreased

atom diffusion and thus affect the fission gas behavior in these amorphous phases. Birtcher (20), (18) conducted low temperature ion irradiations on U_3Si and U_3Si_2, tetragonal structures, to understand how the crystalline lattice parameter change as the material is undergoing amorphization. He showed that in U_3Si_2, the lattice parameter in all three crystalline directions decrease with increasing dose. This lowers the total free volume in U_3Si_2. In U_3Si, an increase in lattice parameter occurs in one direction and the other two directions decrease in value. This increase is faster than the decrease in other two lattice directions, leading to an total increase in free volume. The lower Si-Si bond concentrations in U_3Si are the reason free volume increases with dose and large non-uniform bubbles are present at high burnup.

The increased Si-Si bonds in U_3Si_2 and USi help form the uniformly distributed bubbles by reducing the free volume in the materials. With RERTR-6 and -7 L. Flux showing a similar atomic ratio in the amorphous rim as U_3Si and with it being amorphous, it is believed that the amorphous rim has similar fission gas behavior as U_3Si, producing the large micron sized bubbles seen in Figure 5.8 at high burnups.

Summary of key discussion points are:

1: Si and a small contribution of Al present in the amorphous rim is maintaining the amorphous nature of the region following radiation-induced cascade damage due to the covalent Si-Si bonding and any Al-covalent bonding that might be present

2: Si diffuses/mixes into the crystalline fuel by a combination of cascade mixing and radiation enhanced diffusion with the radiation enhanced diffusion being the primary mechanism.

3: A Si concentration above 2-3 at% is needed in the crystalline fuel to maintain an amorphous structure after radiation damage.

4: The amorphous rim region continues to grow with increasing dose, from 4 μm to 8 μm from RERTR-7 L.Flux to H.Flux.

5: The chemical composition of the amorphous rim is similar to U_3Si, a known fuel phase that forms large bubbles that interlink, a precursor for fuel failure. Note that the large fission gas bubbles appear beyond the expected life of the fuel. Bubbles are present at $9x10^{21}$ f/cm^3 and the life of the fuel is ~$4x10^{21}$ f/cm^3.

5.3: Why does a bubble superlattice form in the crystalline fuel?

With the formation of a bubble superlattice in the fuel, as seen RERTR-6 and -7 L.Flux, understanding how this ordered structure is formed is important. Defects, such as precipitates, voids, and bubbles have been shown to order in materials. In particular, how the bubble superlattice created during ion implantations and void superlattices form during fuel operation is key to understanding the ordered structure seen in RERTR-6 and -7 L.Flux. A review of how void and bubbles superlattices are formed is presented and these two defect lattices are compared to RERTR-6 and -7 L.Flux to help understand how the superlattices are forming.

In the early 1970's, the void superlattice phenomenon was first observed in Mo. Since then, various ordered superlattices have been seen in FCC, BCC, and HCP systems. These ordered

defects include voids, precipitates, and bubbles. For defect ordering to occur, four key steps generally need to occur in the systems though they are not necessarily required (4).

1: Agglomeration of vacancies into clusters (i.e. vacancy loops), perhaps directly during collisional phase of cascade cooling;

2: A bias for dislocations towards preferential absorption of interstitials over vacancies (i.e., absorption asymmetry);

3: An asymmetry in the production and diffusion of mobile point defects (i.e. production bias);

4: Some degree of anisotropy during the evolution of clustered defects. This could either be triggered by diffusional anisotropies of point defects, or by anisotropic elastic interaction between defect clusters during the latter stages of their evolution;

The focus of this discussion will be on void and bubble superlattices. Voids are defined as vacancy clusters and are empty cavities. Bubbles are fission gas stabilized voids. The differences between the two are voids tend to be faceted and bubbles are spherical. When the void has absorbed enough gas, it will lose its facets and become spherical. (84) provided a list of experiments in which void and bubble superlattices were seen in FCC and BCC materials, along with their irradiation parameters. The typical parameters of both the void and bubble superlattices from (84) will be provided prior to discussing how both the void and bubble superlattices form and can be seen in Table 5.4.

The ordered void superlattices are normally oriented with the host material. For example, a void superlattice will be in a BCC orientation in a BCC system. Void diameters have been shown to

vary from 1.6-78 nm. Void lattice parameters for the materials ranged from 10-145 nm. In general, the ratio of the void lattice parameter to void diameter is around 4-6. In the large diameter systems, the ratio is normally less than 3. Another key observation from the list of experiments is the irradiation temperatures. The range of temperatures that showed void superlattices ranges from 430-1050˚C. In general, these temperatures are within the void formation regime or $0.3T_m<T<0.5T_m$. This indicates that the void superlattices can form across a large range of temperatures. When irradiation temperatures are above $0.5T_m$, defects will have increased diffusion and the recombination of interstitials and vacancies will be higher.

Bubble superlattices generally form an orientation with the host material, but some variation has been seen (85). Typical bubble diameters range from 1.5 nm to 6 nm. Around 6 nm, the bubble superlattice was shown to collapse, allowing for the bubbles to coalescence together (65). Typical lattice parameters range from 4 nm to 12 nm. The ratio of the lattice parameter to bubble diameters is ~2-3. The range of temperatures at which the bubbles tend to form is between $0.15T_m<T<0.35T_m$. Once again, Table 5.4 summarizes the parameters at which voids/bubble superlattices form, the typical temperature ranges, the typical void/bubble diameters, the void/bubble lattice parameters, and the ratio for the lattice parameters to void/bubble diameters for the void and bubble lattices.

How does a void superlattice form:

As an irradiation begins in a material, vacancies and interstitials will be produced due to the damage cascades from charged/neutral particles. Depending on defect sinks strengths and

diffusion of the defects, vacancies can cluster together and form voids in the bulk of the material. Remember that for a typical void superlattice to form, one of the general criteria for formation is that there is a bias for interstitials to be preferentially absorbed in dislocations. This allows for vacancy clustering and formation of voids. At the beginning of void formation, the voids will be randomly distributed throughout the bulk of the material. With increasing dose, a void superlattice will start to form and mature with irradiation.

It is believed that the self-interstitial atoms, SIA, diffusion through the bulk is the likely driving force for void superlattice formation. As damage cascades are created, point defects, i.e. vacancies and interstitials, will be produced. These point defects can form clusters or loops or remain as a single point defect. SIA loops will move through the bulk along specific crystalline planes and have mobility at low temperatures. The planes are often the close packed planes of the lattice, such as the [111] direction in a BCC material. In a BCC material, this will lead to SIA fluxes in 8 primary directions. The SIA atoms will have an attraction to voids and will diffuse towards the voids. Smaller voids have a higher bias for the SIA (86). The SIA loops will be absorbed in the void and will cause the volume of the void to decrease. The vacancy flux on a void is related to the size of the voids. Larger voids will grow at the expense of smaller voids (87). The vacancy flux helps the void grow by the absorption of vacancies. These vacancy and SIA fluxes affect the growth rate of the void, either increasing or decreasing its volume.

In the random void distributed system, the distance between voids will vary in the 8 primary directions. As an example, Figure 5.9 shows three voids in a semi aligned system. The distance

between voids A and B is much smaller than between B and C. With a uniform distribution of defects being produced in the bulk, there will be a greater number of defects between void B and C when compared to A and B. This indicates that voids A and B will have less SIA loop shrinkage in A-B direction. In the B-C direction, a greater number of defects will need to be absorbed and this will change the void growth rate in this direction. A random void not aligned with other voids will see a high SIA flux and will shrink or will become aligned with other voids.

Additionally, as a void absorbs a SIA loop, it will adjust its center of gravity along the direction the dislocation loop was traveling. This shift in center of gravity is the driving force for the voids aligning themselves with voids moving towards other voids along the direction of greatest void separations. The voids' center of gravity will move along the 8 primary BCC directions until SIA flux and vacancy flux are equal in all 8 directions. When this occurs, the void should see 8 neighbor voids equally spaced around the void. The vacancy and SIA fluxes will be equal when the void superlattice is in equilibrium.

The void superlattice is highly dependent on many parameters. If certain parameters aren't met, the voids will remain random. First, if the four void superlattice parameters discussed above are not met, the voids will remain random. A key parameter is the anisotropy effects of the voids or point defects. If the point defects are not moving along specific planes, voids ordering will not occur and thus the superlattice will not form. In addition to the four void superlattice parameters, the chemical composition, fission rates, and precipitates present can all affect void superlattice formation.

How does a bubble superlattice form:

With fission gas, primarily Xe and Kr, being created in the fuel during irradiation at a production rate of ~0.247 atoms/fission (67), it is important to understand how the fuel particle stores the fission gas. The discussion will focus on a single bubble in the fuel and how it grows at the low irradiation temperatures, how the bubble moves throughout the fuel particle, what forces are acting upon the fuel, and finally why bubbles arrange themselves in the ordered superlattice as seen in RERTR-6 and -7L. Flux.

It is important to understand what is physically happening to a bubble in the fuel. As fission gas is created in the fuel, fission gas atoms will start to interact with each other, creating fission gas clusters. The clusters eventually accumulate more fission gas and vacancies that are in the matrix. Vacancies are present in the matrix due to fission product and neutron damage cascades. Fission gas and vacancies present in the material/fuel will diffuse slowly due to the low irradiation temperature and the very small temperature gradient across the fuel particle. In a low temperature, stress gradient free environment, interaction of the fission gas atoms and vacancies with the fission gas clusters/bubbles will likely be driven by random walk process or by bubbles moving throughout the matrix.

Understanding how the bubble moves through the fuel is also key to determining how the bubbles grow in the fuel. The proposed reasoning for the bubble growth and movement in the fuel is dislocation loop punching (88) (89). In this process, a dislocation loop is pushed into the

matrix by the energy stored in the over pressurized fission gas bubble. The dislocation loop comes from surface matrix atoms surrounding the bubble. The removal of surface atoms creates new volume in the bubble which, in turn, lowers the pressure in the bubble as the dislocation loop moves away from the bubble. The larger bubble volume lowers the energy stored in the bubble. This reduction in energy is the energy required to punch the dislocation into the matrix or the strain energy of the dislocation loop punch. Additionally, when a dislocation punch is created by the bubble, the bubble will displace itself half a burgers vector towards the dislocation loop, providing a mechanism for bubble movement in the fuel. The dislocation loop will be punched along crystalline planes, specifically on the low energy plane in the matrix. For a BCC host material, the dislocation will be punched on the low energy planes or the (110) family of directions.

The dislocation loop punching process can be seen in Figure 5.10. This cartoon shows the basic idea of how the punching process happens. Figure 5.11and Figure 5.12 show dislocation loop punches in an experimental setting. Notice how the punches in Figure 5.11 and Figure 5.12 are radiating away from the bubble in specific directions or along specific crystalline planes. Figure 5.11 and Figure 5.12 show that the dislocation loop punching process is not a single event. The punching process will happen repeatedly in a bubble. Though the pressure in the bubble is being released by the punching process, fission gas atoms, created by fission, will continue to diffuse into the fission gas bubble. This increases the pressure in the bubble and forces it to complete another dislocation loop punch to lower its stored energy.

Wolfer developed a model to simulate the energy required to punch a dislocation loop by a bubble (89). This model provides a very detailed analysis of the energy required to punch a loop and how the loop punching physically affects the bubble. Most of the following discussion will be focused on the results seen in this study, as it is believed that this is the driving force in ordering the intragranular bubbles. Different energy components were added to the model to simulate the typical energy interactions that occur by the bubble dislocation loop punches. Equation 5.6 shows the energy components required to punch out a dislocation loop. A brief explanation of each component is provided, as well as an explanation of how each component affects the bubble-dislocation loop punching event.

$$\Delta F(R)=F_{gas}(V,T)-F_{gas}(V_i,T)+E_L+\Delta E_s+E_p(p)-E_p(p_i)+E_{pL}(R)+\Delta E_{pL(R)}+E_{LL}(R) \qquad (5.6)$$

where $\Delta F(R)$ is the total change of the Helmholtz free energy. $F_{gas}(V,T)-F_{gas}(V_i, T)$ is the Helmholtz energy of the gas that is contained in the bubble before and after the dislocation loop punching. E_L is the total strain energy that is associated with the dislocation loop. ΔE_s is the change in surface energy from changing bubble sizes from the dislocation loop punch. E_p is the bubble strain energy before and after the punching. E_{pL} is the interaction energy associated with the dislocation loop interacting with the stress field of the bubble. ΔE_{pL} is the interaction energy associated with the dislocation loop interacting with the other bubbles in the matrix. E_{LL} is the interaction energy associated with dislocation loops interacting with other dislocation loops in the matrix.

The $F_{gas}(V,T)$ terms are related to the Helmholtz free energy of a gas. In the RERTR-6 and -7 L. Flux study, the gas stored in the bubbles are a distribution of fission gases. To fully use this model for fission gas, the composition of the gas would be needed to determine the exact gas chemical distribution in the fission gas bubbles. This energy contribution is highly dependent on the pressure of the bubble. The pressure of the bubble is always changing due to two primary components: fission gas atoms diffusing into the bubble due to the fission process and dislocation loop punching, lowering the pressure of the bubble.

The ΔE_s, the change in surface tension energy, is related to the bubble shape and volume. The volume of the bubble changes by various interactions. In the RERTR-6 and -7 L. Flux samples, the bubble shape is consistently spherical with no evidence of faceting. The volume contained in the bubble changes with the various points of the dislocation loop punching process. Wolfer showed that the bubble volume changes as the dislocation loop is driven away from the bubble. This can be seen in Figure 5.13 (89). The initial dislocation punch does not provide a significant increase in volume in the bubble and it is not until the dislocation loop has separated far enough from the bubble that the bubble volume increases a significant amount. These changes in volume affect the bubble shape slightly and will affect the ΔE_s value.

The E_L and E_{Im} terms, the strain energy associated with the dislocation loop, will increase in energy slowly as the dislocation loop is pushed away from the bubble. This is primarily due to the dislocation volume increasing in size as the loop separates from the bubble. Eventually the loop will reach its ideal volume and its energy contribution will become constant.

The E_{pL}, interaction energy between the bubble stress field and the dislocation loop is highly dependent on the separation distance of the bubble and dislocation loop. As the dislocation loop punch is created, it is generally near the surface of the bubble or around one burgers vector away from the surface of the bubble. At this distance, the interaction between the bubble and the dislocation loop is at its greatest and the increase in volume of the bubble is at a minimum. As the dislocation is driven away from the fission gas bubble due to the bubble stress field, the bubble provides a compressive stress as it moves away. As it continues to move away from the bubble, the interaction energy decreases quickly due the stress field falling off by a $1/r^3$ relationship. This decrease in energy will allow the volume of the bubble to expand and the increase in volume will slowly decrease the pressure inside of the bubble. Note that as the loop moves away from the originating bubble, the loop will start to interact with neighbor bubbles and add additional E_{pL} to the neighboring bubble, compressing the volume and increasing the bubble pressure inside the neighbor bubbles.

The ΔE_{pL} term is the addition of energy supplied by bubbles that are neighboring the bubble. This interaction energy is the greatest in a bubble superlattice situation as the energy is highly dependent on the distance between the bubbles. In a bubble superlattice, the spacing between bubbles will be closest and this term will have its greatest effect. Only nearest neighbors play a major role on this value. Bubbles farther than the nearest neighbor will not provide a significant energy contribution and were neglected in the Wolfer model.

The E_p term, or the bubble strain energy, drops off as the pressure in the bubble decreases. This is highly dependent on the separation distance of the bubble and the dislocation loop. As the dislocation loop moves farther away from the bubble, the bubbles volume increases and the bubble pressures decreases, leading to a lower bubble strain energy.

The ability of the dislocation to move away from the bubble will slow as additional dislocations accumulate around the bubbles. This is the loop-loop interaction term, E_{LL}. Dislocation loops from previous punches and other dislocation loops from neighbor punches will strongly interact with the new dislocation loop. The E_{LL} term will continue to increase with increased dislocation loop punches. This increased energy will force the bubble to have a larger pressure to complete future dislocation loop punches in this specific direction. This is the driving reason for the ordering of the bubbles and will be discussed later. Additionally, the dislocations can interact with other dislocations, forming larger ones. This reduces the density of the dislocations in the debris field and lowers the E_{LL} term.

Figure 5.14 (88) shows the effect of all of the energy components on the Helmholtz energy of the bubble as a function of dislocation loop separation distance from a 5 nm bubble. The goal of the bubble to perform the loop punching is to lower the energy of the bubble or lower the Helmholtz energy to a larger negative value. The terms that affect this value the greatest are E_L and E_{LL} terms. Figure 5.14 shows the E_L having the highest positive energy addition to the bubble. The increase in strain energy as the separation increases is due to the dislocation loop fully forming as it separates from the bubble.

The E_{LL} term for Figure 5.14 was set at the maximum value, assuming the maximum dislocation density in between two bubbles. This loop-loop interaction is the primary driving force for creating the bubble superlattice in RERTR-6 and -7 L. Flux. Bubbles will want to coalescence together; they will move towards each other by dislocation loop punching. This creates a large amount or increased density of dislocations between the two bubbles, which increases the effect of the E_{LL} term. A higher E_{LL} value will require a need to have a higher pressure in the bubble to punch in the direction of the other bubble. Eventually, the bubble will not be able to punch a dislocation loop and will move in another direction that is more energetically favorable. Eventually it will see another neighbor bubble, creating a dislocation debris field between those two bubbles before it reaches the bubble. This process continues until the bubble is surrounded by neighbor bubbles that are equally spaced, thus creating the bubble superlattice seen in RERTR-6 and -7 L. Flux.

The ability of the bubble to punch a dislocation loop is highly dependent on the energy imposed by the neighboring bubbles, i.e. the bubble density, the fission gas inventory inside the bubbles, and the dislocation debris field surrounding the bubbles. As bubbles start to approach each other, the energy in the bubble will be less negative. This can be seen in Figure 5.14, where the total energy of the system is less negative at 5nm compared to 50 nm. With the system less negative, it will be less likely to punch a dislocation loop. The primary interactions that are driving the energy less negative are the bubble-loop interaction and the strain energy associated with the dislocation loop. Not shown in Figure 5.14 is the effect of dislocation loop density or

the E_{LL} in system. It was assumed to be at a maximum value for this analysis. With the separation distance between bubbles reduced as the irradiation proceeds, the bubbles will punch out a significant dislocation debris field between the bubbles. The E_{LL} term likely plays a major role in preventing the loop punching to occur in the direction of the dislocation loops.

Note that this process only happens in a low temperature system. Defects such as the bubbles and dislocations will have much higher diffusion rates at elevated temperatures. This increased diffusion likely affects the E_{LL} term, where the dislocation density between two bubbles will be lowered and the bubbles will be allowed to diffuse much closer to each other or coalescence together, forming a larger bubble which has a lower surface tension and generally a lower pressure.

In the superlattice seen in RERTR-6 and -7L.Flux, the theories of both the bubble superlattice and the voids superlattice can be compared to better understand which theory is more applicable for RERTR-6 and -7 L.Flux. From RERTR-6, the bubble diameter was ~4 nm. This is on the low end of the void superlattice but in the middle of a typical bubble in a bubble superlattice regime. The lattice parameter of RERTR-6 was determined to be around 10 nm. This is on the low end of the void superlattice system but also high on the bubble superlattice system. The ratio between lattice parameter and bubble diameter was around 2-3. This ratio is very typical of a bubble superlattice system with void superlattice systems, showing a typical ratio of 4 or greater. The T_m for RERTR-6 is typical for a bubble superlattice formation regime, T_m=~0.25. With the temperature of the bubble superlattice residing in the bubble superlattice regime, the

lattice parameter to bubble ratio being similar to a bubble superlattice regime, and the diameter of the bubbles falling in the bubble superlattice regime, it is likely that the dislocation loop punching process is dominating the formation of the bubbles into the ordered superlattice.

Proving the dislocation loop punching process:

There are limitations in conducting dislocation analysis in RERTR-6 and -7 L. Flux. The bubble superlattice adds diffraction scattering and this scattering severely hampers the ability to image dislocations, such as the loops proposed to form in bubble dislocation loop punching. When the bubbles are at a diffraction zone, such as z=100 or 110, bubbles will be stacked on each other in the image and provide a clear image of the bubbles. When a two beam condition is created, such as g=200, the sample is tilted and the bubbles are no longer stacked on each other. This means the electron beam must penetrate through the bubbles without being scattered by the bubbles to properly image the dislocations that might/should be present between bubbles.

To know completely if the ordering of the bubble superlattice is occurring by bubble dislocation loop punching, the system would have to be in the random bubble morphology stage. In this system, the bubble density should be lower than a superlattice system and the bubble spacings should be much larger, allowing for the opportunity to better image dislocations that might be present between the two bubbles. It is unclear when exactly the bubbles will appear in a random state. A void system was shown to form at low doses or a few dpa (84). It was hoped that the Kr irradiation of the DU-7wt%Mo foils with Xe atoms would help fill in this hole but, due to the

heavy oxidation of the samples during sample shipment and irradiation, it was impossible see the small 2-3 nm size bubble in a random or ordered configuration.

Summary of key points:

1: Bubble sizes and spacing in RERTR-6 and -7 L.Flux indicate that the system is a bubble superlattice.

2: Dislocation loop punching is believed to be the driving force for the formation of the bubble superlattice as the bubbles sizes and spacing are consistent with the formation of a bubble superlattice and not a void superlattice.

Table 5.1: Key fuel lifetime steps and questions/unknowns of the effect of Si during these steps

Time in Life	**Si locations**	**FMI layer microstructure-Pure Al matrix**	**FMI layer microstructure Si-modified matrix**
Pre-Fabrication	As precipitates in the matrix	No FMI layer	No FMI Layer
After Fabrication	Matrix and the FMI layer	Unknown	$(U,Mo)(Al,Si)_3$ nano-crystals with varying Si and Al compositions (See Figure 6.1a))
Post Irradiation	Matrix, the FMI layer, and the amorphous rim	Large FMI Layer and bubble growth	Suppressed FMI Layer and bubble growth

Table 5.2: The covalent % of key bonds that could form in the FMI layer from Eq. 6.1. The values of electronegativity used for U, Mo, Al, and Si are 1.38, 2.16, 1.61, and 1.9 (76)

Bond	% Covalent
U-Mo	85.9
U-Al	98.7
U-Si	93.5
Al-Si	97.9
Al-Mo	92.7
Si-Mo	98.3

Table 5.3: Al type phases that undergo amorphization in dispersion fuels at low temperatures and their respective Al content.

Phase	Al Content at%	Amorphous?	Source
UAl_2	66	Yes	(74)
UAl_3	75	Yes	(74)
UAl_4	78	Yes	(74)
$U_6Mo_4Al_{43}$	79	Yes	This work
UMo_2Al_{20}	88	Yes	This work
Al	100	No	This work

Table 5.4: Typical parameters of a bubble and void superlattice

Defect Lattice	Temperature Range	Typical Diameters nm	Typical Lattice Parameters nm	Ratio of Lattice Parameter/Diameter
Bubble	0.15-0.35 T_m	2 to 6	6 to 12	2 to 3
Void	$0.3T_m$-$0.5T_m$	4 to 78	20 to 75	4 to 5

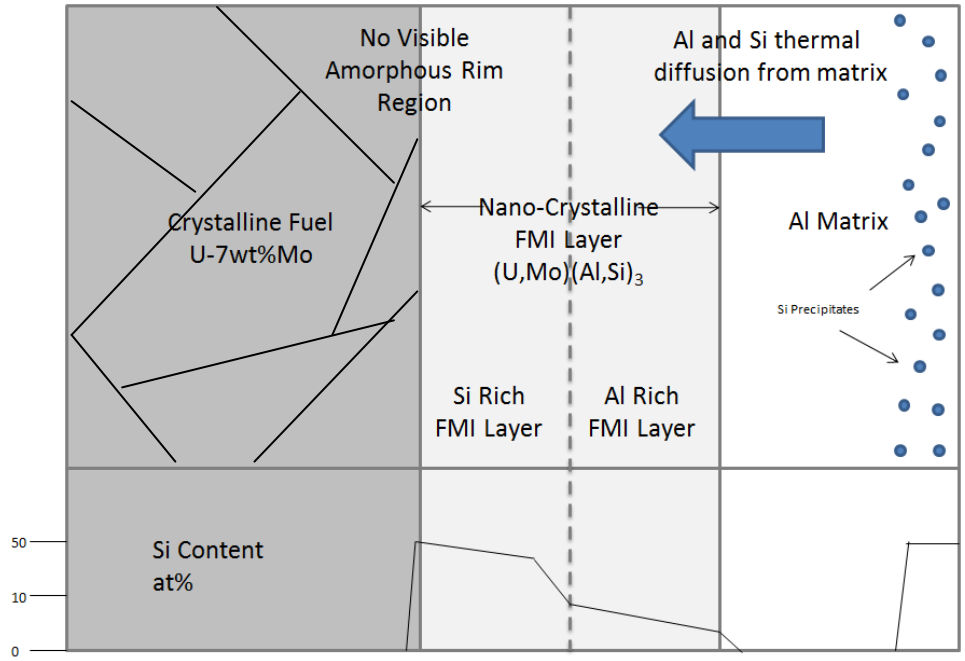
No Visible
Amorphous Rim
Region
Al and Si thermal
diffusion from matrix
Crystalline Fuel
U-7wt%Mo
Nano-Crystalline
FMI Layer
(U,Mo)(Al,Si)3
Al Matrix
Si Precipitates
Si Rich
FMI Layer
Al Rich
FMI Layer
Si Content
at%
50
10
0

a)

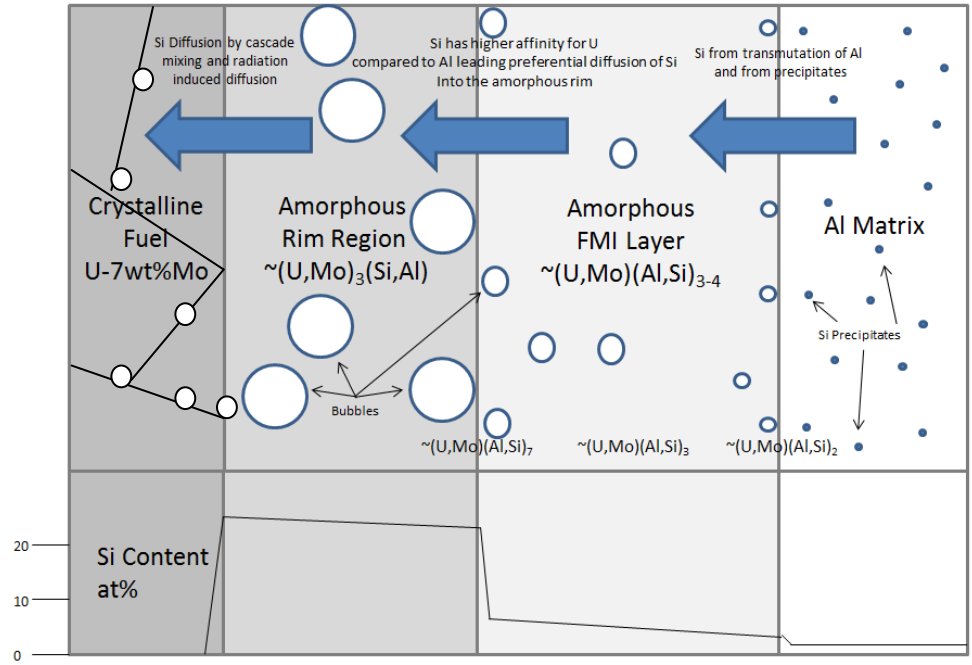
Si Diffusion by cascade
mixing and radiation
induced diffusion
Si has higher affinity for U
compared to Al leading preferential diffusion of Si
Into the amorphous rim
Si from transmutation of Al
and from precipitates
Crystalline
Fuel
U-7wt%Mo
Amorphous
Rim Region
~(U,Mo)3(Si,Al)
Amorphous
FMI Layer
~(U,Mo)(Al,Si)3-4
Al Matrix
Si Precipitates
Bubbles
~(U,Mo)(Al,Si)7
~(U,Mo)(Al,Si)3
~(U,Mo)(Al,Si)2
Si Content
at%
20
10
0

b)

Figure 5.1: Schematics showing the key regions formed in U-7wt%Mo/Al-2wt%Si dispersion fuel a) after fabrication and b) during irradiation. A representation of the Si content in each region is provided. Note that the amorphous rim region grows into the crystalline fuel region.

a)

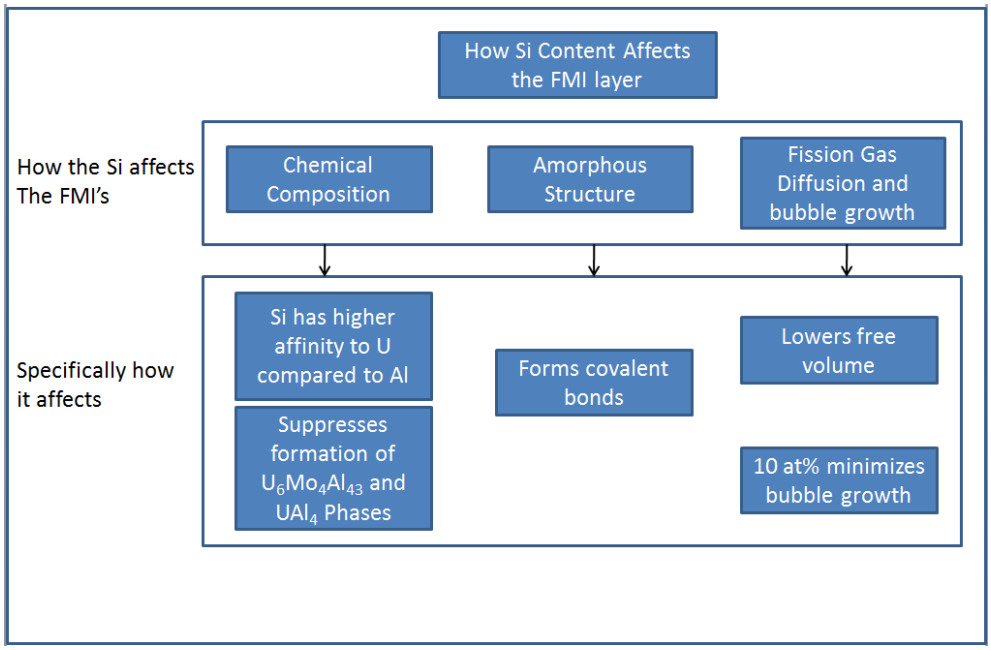

b)

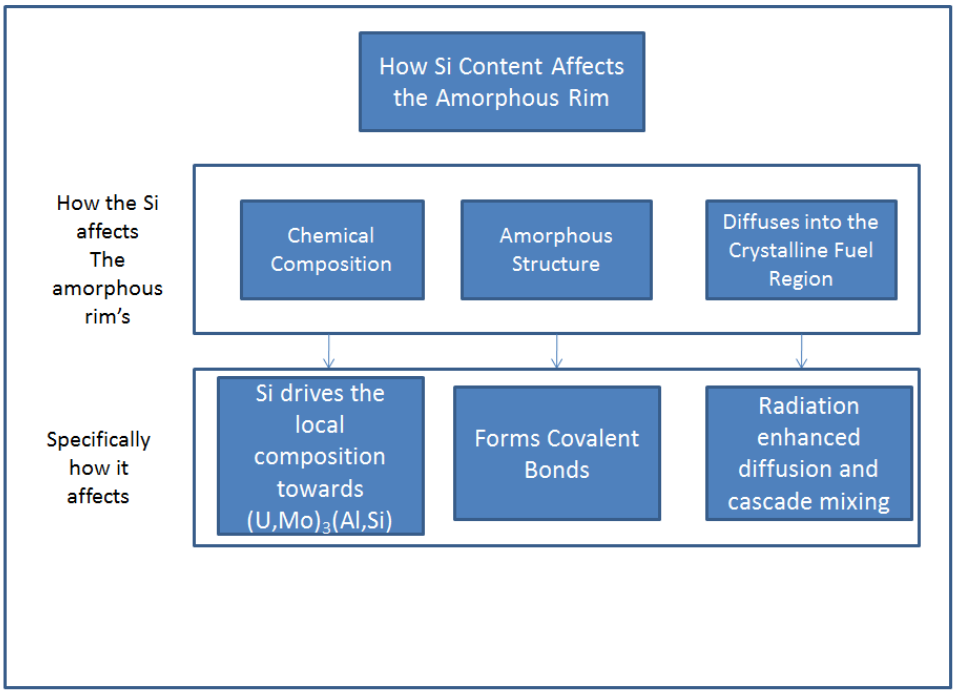

Figure 5.2: Schematics on how the Si affects the a) FMI layer and b) amorphous rim region

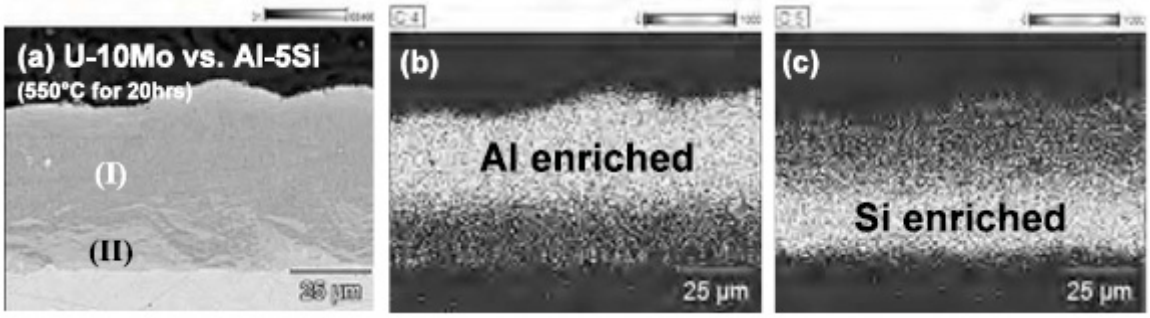

Figure 5.3: FMI layer from a diffusion couple experiment showing Si rich and Al rich regions in the FMI layer. (69)

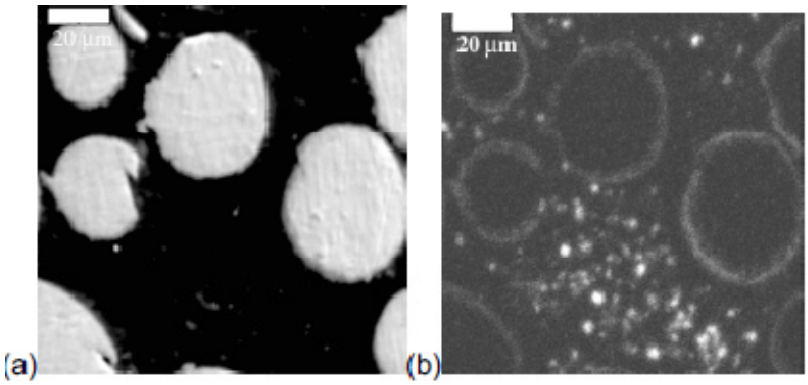

Figure 5.4: Si denuded region surrounding the fuel particle after fabrication: a) SEI image and b) its Si X-ray map. Notice how the Si precipitate density around the particles, ~10 µm, is very low. Additionally, the Si enriched FMI layer and amorphous rim region can be seen around the fuel particles as bright rings. (71)

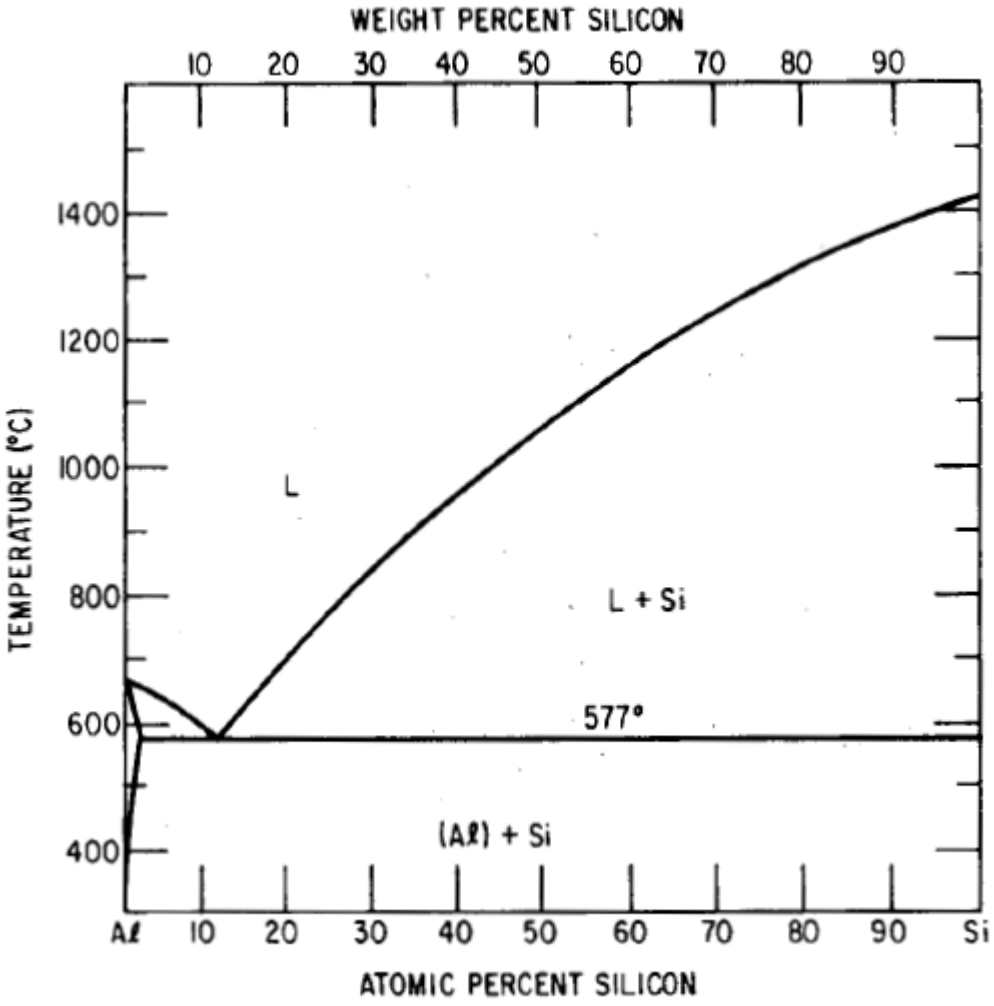

Figure 5.5: Al-Si phase diagram. Note how Si is insoluble in Al and ends up forming precipitates in the Al matrix (72)

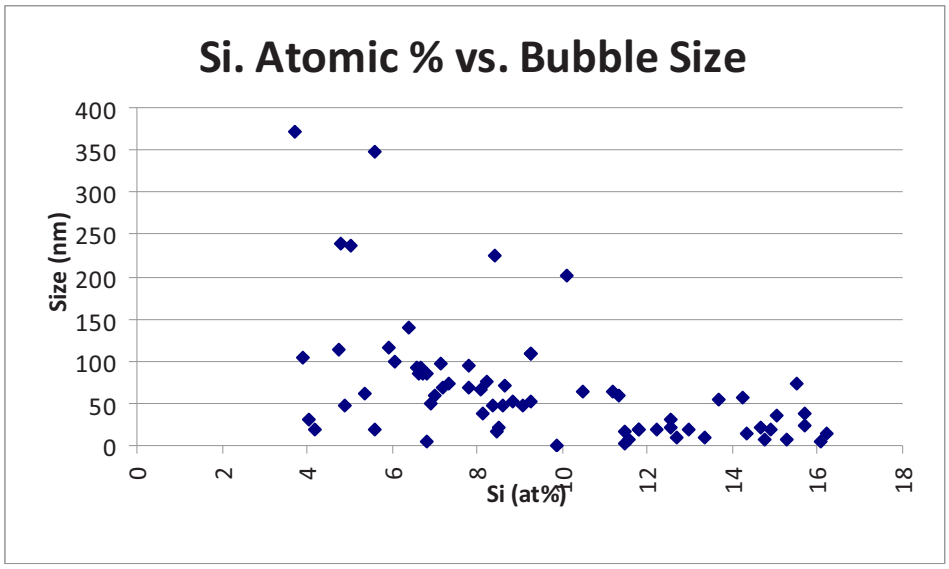

Figure 5.6: Si content vs. fission gas bubble size in the FMI layer. This analysis is independent of location in the FMI layer.

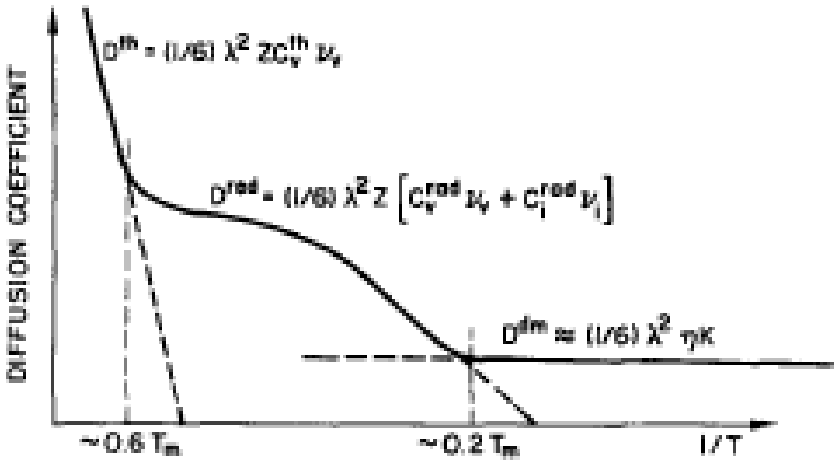

Figure 5.7: Simple diagram showing the diffusion coefficient vs. temperature profile in an irradiated material (90)

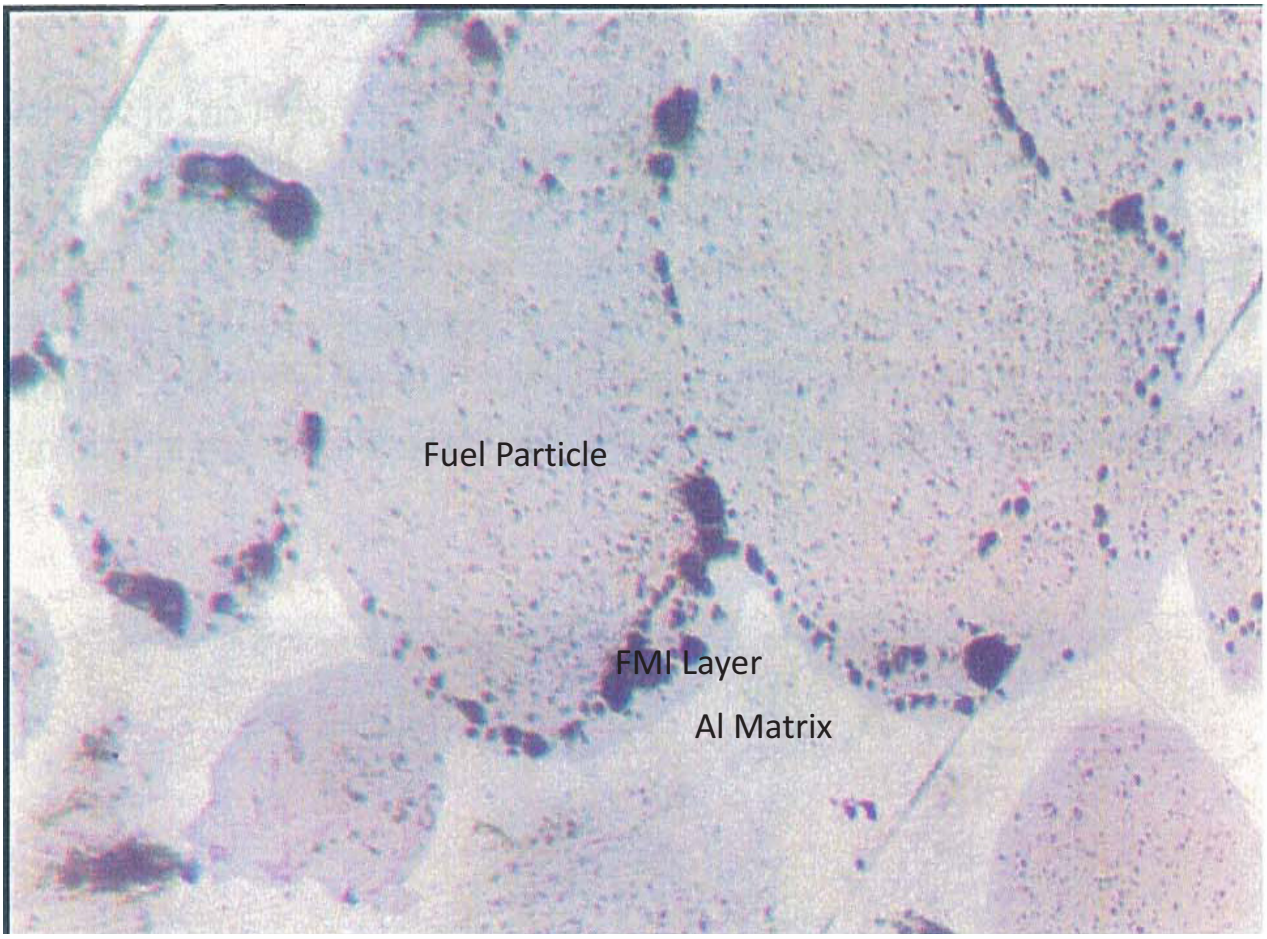

Figure 5.8: Optical microscopy images of RERTR-7 at a burnup of ~$9x10^{21}$ f/cm^3. Note the large fission gas bubbles that are present between the FMI layer and the amorphous rim region. Key regions are shown. (63)

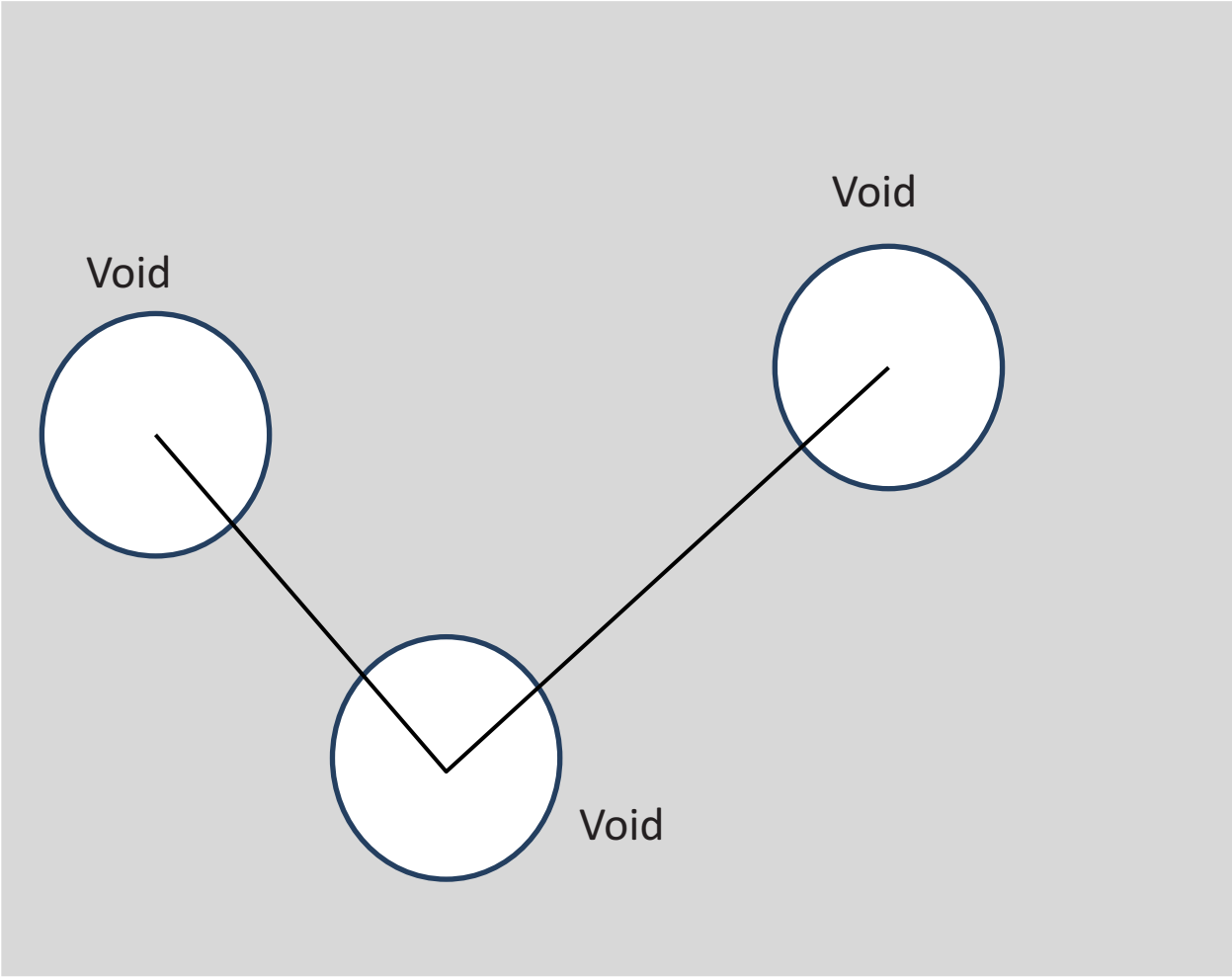

Figure 5.9: Voids starting to align along aligned planes

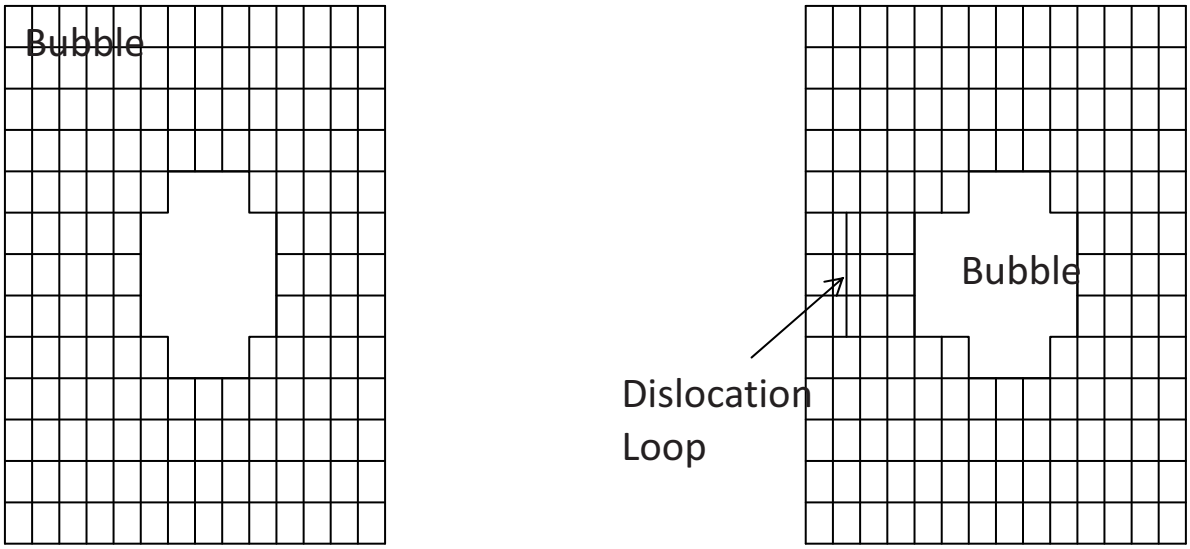

Figure 5.10: Cartoon showing how the dislocation loop process works. Note how the punched out dislocation loop causes the fission gas bubble to gain additional volume.

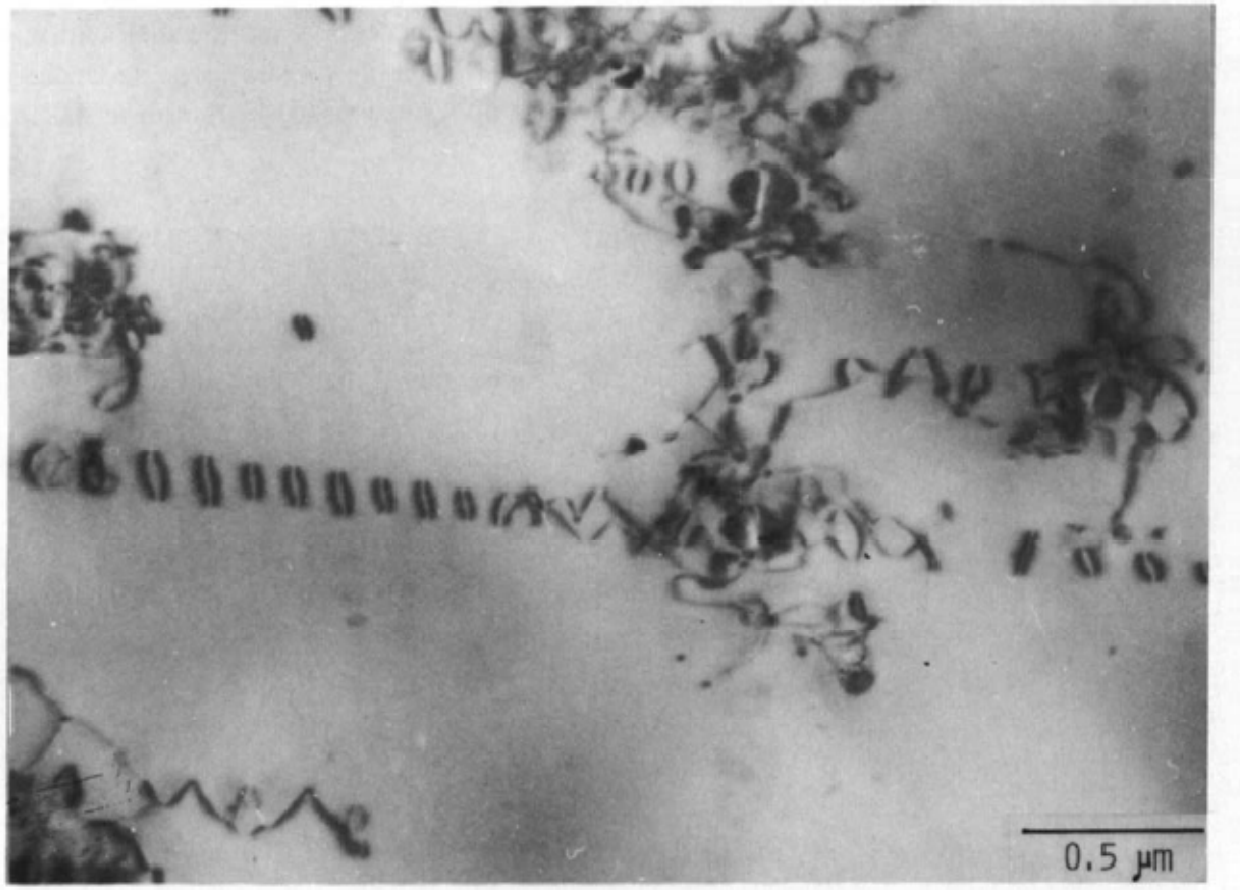

Figure 5.11: BF image showing dislocation punches radiating away from a bubble. Note how they radiate away from the bubble in a specific direction (91).

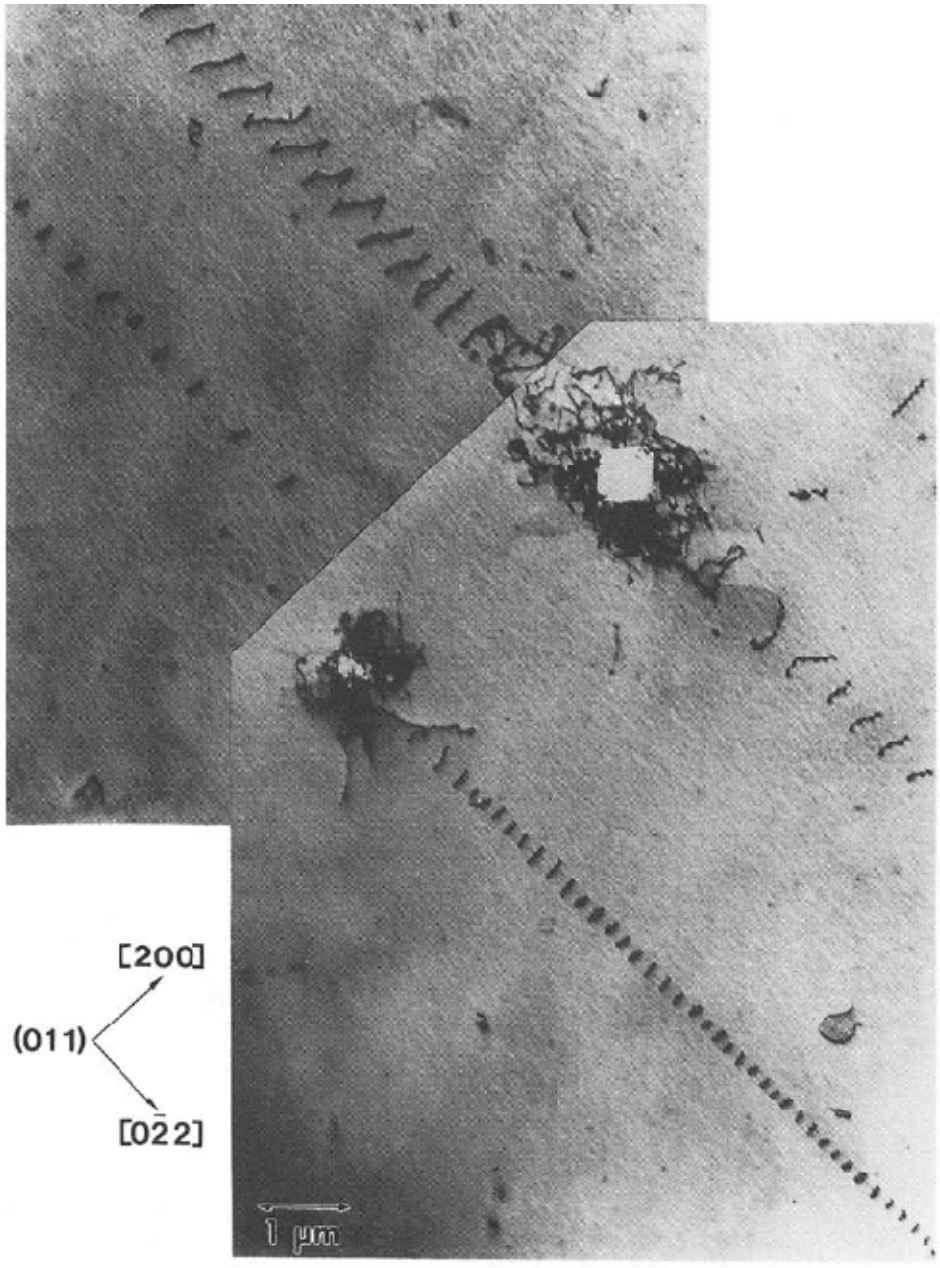

Figure 5.12: Dislocation loops event from two bubbles. Notice the directionality of the dislocation loops and the large dislocation debris field surrounding the bubbles (92).

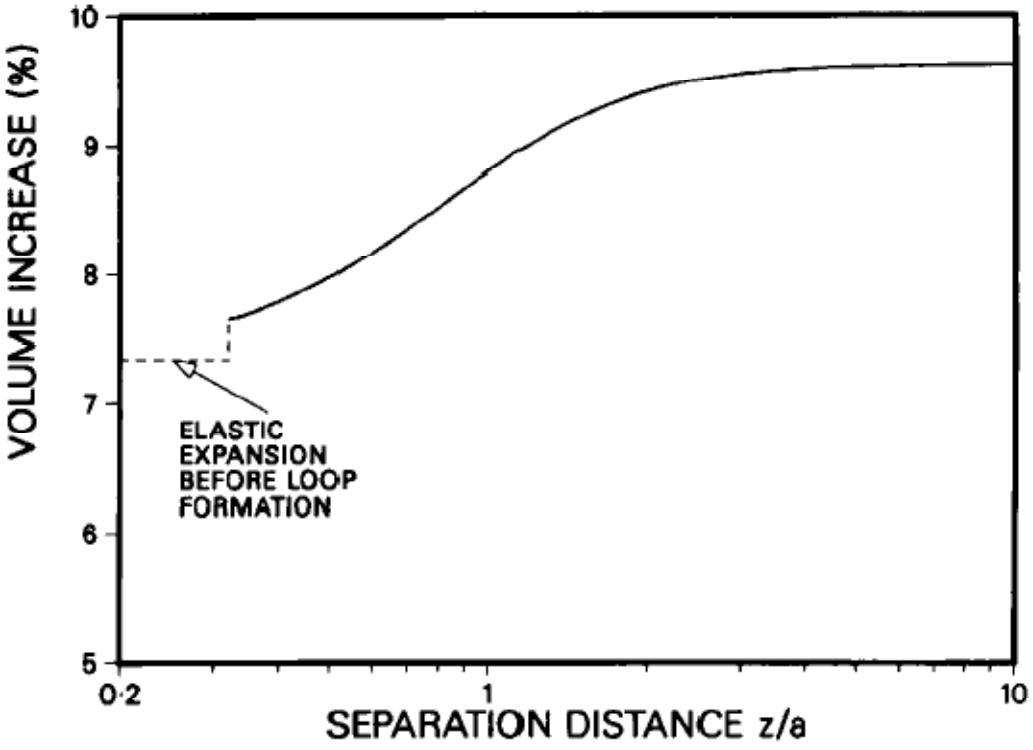

Figure 5.13: Bubble volume as a function of dislocation loop separation from the bubble. Notice how as the dislocation loop migrates farther from the bubble, the bubble volume increases. a is the bubble radius and is defined as 5 nm in this calculation. z is the separation distance between the bubble and the dislocation punch. (89)

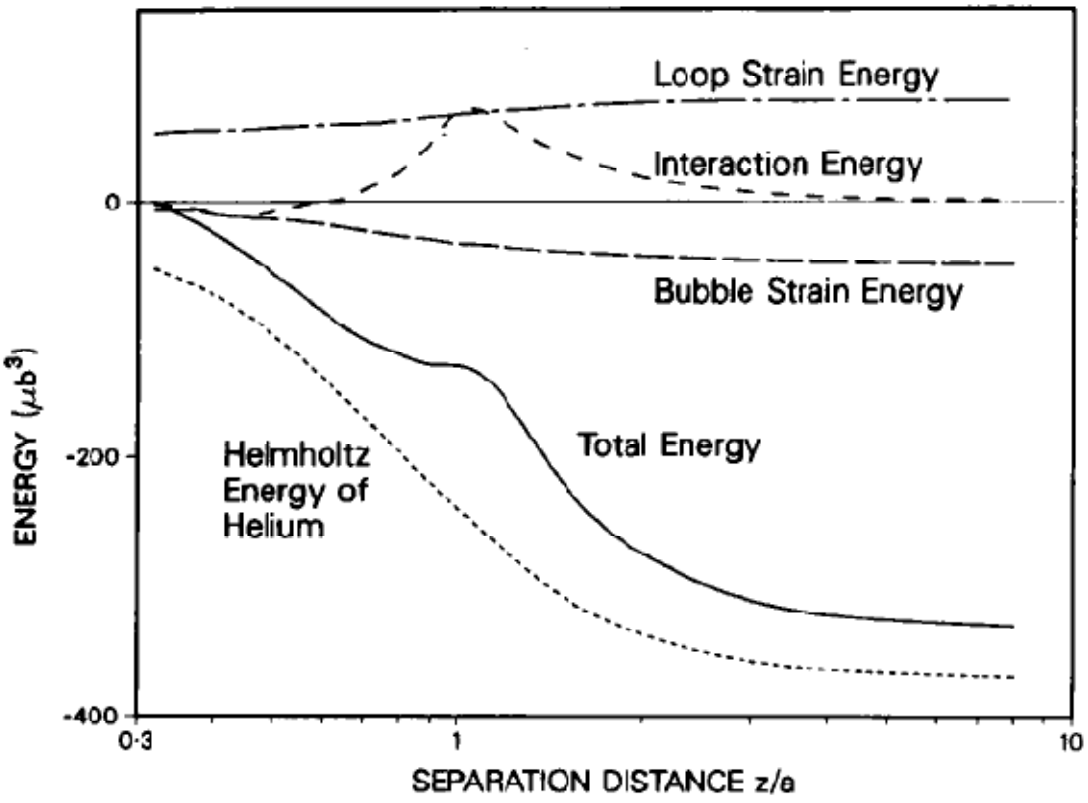

Figure 5.14: Calculation showing the bubble's Helmholtz energy as a function of dislocation loop separation from the bubble. a is the bubble radius and is defined as 5 nm in this calculation. z is the separation distance (88).

Chapter 6 : Intragranular Bubble Model

A model was created by Rest (3) to predict the size distribution of the intergranular and intragranular bubbles in a crystalline fuel. The model is being used to fit key intragranular bubble parameters, such as the bubble resolution rate, the bubble nucleation factor, and the gas atom diffusion coefficient. Because of the wide rage in bubble sizes, obtaining the distribution of experimental intergranular bubble requires both SEM and TEM analysis of the same sample, a procedure that is not yet perfected for analyzing highly radioactive fuel. TEM analysis is capable of imaging smaller intragranular bubbles. This chapter will proceed as follows: an explanation of what the key parameters are and how they affect bubble growth/shrinkage; a background of the model will be presented, focusing on the intragranular portion of the model; model results will be compared to experimental results to help fit key bubble parameters; a sensitivity analysis of the key parameters in the model will be provided; and a discussion of how these key parameters compare to literature results will be provided.

Explanation of the key parameters:

The bubble nucleation factor, f_n, is the probability that a two gas atom cluster will form a stable nucleus. This value is based on the presence of a vacancy at the two gas atom collision to help stabilize the newly formed bubble. If the vacancy is not there, the bubble will dissolve. Turnbull (93) reported that the f_n term is roughly equal to the vacancy bulk concentration.

The gas atom diffusion coefficient, D_g, is used to understand how fast fission gas atoms will diffuse through the material. Note that the fission gas in a fuel system is composed of many different elements and is composed primarily of Xe and Kr gas atoms, and the overall gas atom diffusion coefficient is a combination of the Xe and Kr gas diffusion coefficient.

The bubble resolution rate, b, is used to define the gas atoms that are knocked out of the bubble and back into solution by fission fragments. This process explains why bubbles can shrink or disappear during irradiation. This process has been shown to occur during irradiations in which UO_2 fission gas bubbles are shown to dissolve into smaller bubbles, indicating resolution occurring (15). Olander (13) reported that there are two primary theories of how this process works. One theory states that if a fission fragment interacts with any part of the bubble, all of the fission gas atoms are reintroduced back into solution, completely destroying the bubble. The other theory states that only part of the fission gas atoms are reintroduced back into solution, leaving a smaller bubble. The partial resolution of the bubble is the likely theory seen in the ordered bubble superlattice in RERTR-6 and -7 L.Flux. If a whole bubble was destroyed in a superlattice system, the ordered neighbor voids would relax into the free volume, creating slight disordering in the superlattice. This was not seen in RERTR-6 and 7 L.Flux, with long micron-sized ordering occurring in the fuel grains.

6.1: Model Background

A model has been developed by Rest and others to predict intergranular and intragranular bubble distributions seen throughout crystalline U-Xwt%Mo dispersion fuels (3). The full model predicts bubble size distributions, bubble densities, and the affect these bubbles have on the swelling of the fuel. Experimental data is important in setting key parameters in the model and results from Van de Berghe (1), RERTR-6, and RERTR-7 L.Flux are being used to establish the correct key parameters for the model. Due to the inability to obtain intergranular bubble size distributions experimentally, only the intragranular portion of the model will be used in this work. Below, a description of the intragranular model created by Rest is provided.

At the temperatures seen in the RERTR irradiations (T<500 K), the diffusion of gas atoms through the material, D_g, through the material is assumed to be athermal and proportional to the fission rate, $\dot{f}$ (fissions/cm^3-sec). Additionally, the gas-atom resolution rate b is assumed to be proportional to the fission rate at this temperature. The gas-atom diffusion coefficient and gas-atom resolution rate is given by:

$$D_g = D_o \dot{f} \quad 6.1$$

$$b = b_o \dot{f} \quad 6.2$$

b_0 and D_o are defined as the gas atom resolution parameter and the gas-atom diffusion parameter

The rate equation that describes the time evolution of the density of gas in intragranular bubbles is given by [1]:

$$\frac{d[m_b(t)c_b(t)]}{dt} = 16\pi f_n D_g r_g c_g^2(t) + 4\pi r_b(t) D_g c_g(t) c_b(t) - b m_b(t) c_b(t) \quad 6.3$$

where f_n is the bubble nucleation factor or the probability that two gas atoms will cluster, c_g and c_b are the gas-atom concentration in the fuel and gas bubble density in the fuel, r_b is the average gas-bubble radius, m_b is the average number of gas atoms present in the average bubble, D_g was the diffusion coefficient for the gas atoms in the material, and r_g is a gas-atom radius. Note that the c_g and c_b terms only pertain to the fission gas present in the bulk of a grain and doesn't include the concentration of bubbles and gas-atoms on the grain boundaries. The value of f_n is <1 due to the gas-bubble nucleation within the fuel matrix requiring the presence of vacancy clusters to become viable. The three terms on the right hand side of the equation describe the change in the density of the gas in the intragranular bubbles due to bubble nucleation. The first term describes the generation rate of the bubbles in the fuel during irradiation. The second term describes the generation rate of atoms in a bubble. The last term is related to the fission gas resolution due to irradiation.

Equation (6.3) can be denoted as the sum of two equations. These are the time evolution of the fission gas-bubble average density and average number of gas-atoms in a bubble:

$$\frac{dc_b(t)}{dt} = \frac{16\pi f_n D_g r_g c_g^2(t)}{m_b(t)} - \frac{b}{2} c_b(t) \qquad 6.4$$

$$\frac{dm_b(t)}{dt} = 4\pi r_b(t) D_g c_g(t) - \frac{b}{2} m_b(t) \qquad 6.5$$

The first term in the right hand side (RHS) terms in Eq. (6.4) represents the generation rate of the bubbles in the fuel during irradiation. The second term is the whole bubble destruction related to the resolution process. This assumes that if a fission fragment interacts with a bubble, the gas bubble will be destroyed with the gas atoms being re-deposited into solution in the fuel. The first term in Eq. (6.5) represents the generation rate of atoms in the bubbles, i.e. how fast fission gas atoms are diffusing into a bubble due to diffusion from the bulk. The last terms in Eq. (6.5) represents the gas-atom chipping from the bubbles from resolution. This is where some of the gas atoms in the bubble will be deposited back into solution from fission fragment interaction. Note that the bubble resolution rate is the same for a bubble that is destroyed by a fission fragment or partially destroyed. There is a critical bubble size in which complete bubble destruction will occur.

With a high irradiation induced gas-atom resolution rate, the bubbles produced stay in the nanometer range. The resolution rate affects the last terms in 6.4 and 6.5 or the whole bubble destruction and gas atom chipping of a bubble. As the irradiation continues, the density of the bubbles increases rapidly at the beginning of irradiation and at longer times, the density proceeds

to decrease drastically due to larger bubbles forming. Assuming long irradiation times, the left hand side of (6.4) and (6.5) can be assumed to be zero. The quasi-steady state solutions of (6.4) and (6.5) are given below:

$$c_b = \frac{16\pi f_n r_g D_g c_g^2}{b_g m_b(t)} \qquad 6.6$$

$$m_b(t) = \left(\frac{3b_v}{4\pi}\right)^{\frac{1}{2}} \left(\frac{4\pi D_g c_g(t)}{b}\right)^{\frac{3}{2}} \qquad 6.7$$

The amount of gas-atoms present in a bubble can be related to the average bubble size r_b by the using a modified Van der Waals gas-law relationship:

$$\frac{2\gamma}{r_b}\left(\frac{4}{3}\pi r_b^3 - h_s b_v m_b\right) = m_b k_b T \qquad 6.8$$

where b_v is the Van der Waals constant for Xe, T is the absolute temperature of the system, k_b is Boltzmann's constant, and h_s is a fitting parameter that, for a given T, makes the Van der Walls gas law relationship equivalent to a hard-sphere equation of state (94).

Assuming the bubbles are in the nanometer sized range, an approximate solution for equation 6.8 is:

$$r_b(t) = \left(\frac{3h_s b_v m_b(t)}{4\pi}\right)^{\frac{1}{3}} \qquad 6.9$$

The fraction of gas that diffuses into the grain boundary of the grains sized (d_g) can be approximated by:

$$f_s = \frac{8}{d_g}(D_g t)^{\frac{1}{2}} - \frac{6}{d_g^2} D_g t \qquad 6.10$$

Based on the amount of gas that diffuses to the grain boundary and imposing gas-atom conservation, where the sum of the gas in solution, the intragranular bubbles, and the grain boundaries is equal to the total amount of gas produced from fission, the concentration of gas-atoms c_g is approximated by:

$$c_g(t) = \frac{-(1+f_s) + [(1+f_s)^2 + 64\pi f_n r_g D_g \dot{f} \beta t / b]^{\frac{1}{2}}}{32\pi f_n r_g D_g / b} \qquad 6.11$$

where β is the number of gas-atoms created per fission event

The average number of gas atoms in the fuel per intragranular bubble is:

$$n_b(t) = \frac{c_g(t)}{c_b(t)} \qquad 6.12$$

The key calculations that are being fit to experimental parameters in this work are the bubble radius, r_b, and the bubble concentrations, c_b.

There are some limitations to using this model. One issue is that the gas atom diffusion coefficient is assumed to be athermal. All literature reported values discussed later have some temperature dependence on the gas-atom diffusion coefficient. With the experimental results of Van den Berghe (1), RERTR-6, and -7 L.Flux only having a temperature variation of 20˚C, it is

assumed that this athermal assumption has little effect on the model results. It would be interesting to see how a large temperature variation between samples, ~100˚C, would affect the model results.

Another limitation is the fact that the bubble superlattice is in an ordered superlattice. The model assumes that the bubbles are randomly distributed throughout the bulk. Using the experiment results, an attempt to add a component in the model incorporating the fact the intragranular bubbles are in a bubble superlattice will be added and explained later.

Provided next is how improvements to the model were made possible through the experimental results. This includes a step by step process of how the model was used to determine the key bubble parameters, i.e., the bubble nucleation factor, the gas-atom diffusion coefficient, and the bubble resolution rate.

With the intragranular model not incorporating the fact that the intragranular bubbles were in an ordered structure, a relationship was incorporated into the model to include this ordering. In section 4.11, a bubble yield calculation was completed to determine how much of the fission gas created during the irradiation would be tied up in the bubble superlattice. This calculation incorporated the fact that the bubbles were in an ordered FCC superlattice. From this calculation, it was determined that ~17% of the total fission gas created is not present in the intragranular bubbles and resides in the grain boundaries as intergranular bubbles and in solution in the fuel. Please note the potential error in the 17% value as discussed back in section 4.11. In

the model, equation 6.10 solves for the gas residing along the grain boundaries or f_s. Three specific parameters are used to solve for f_s. These being the irradiation time, the gas-atom diffusion coefficient, and the grain diameter. From the experimental results, the irradiation time and grain size of the fuel are known. Note that additional experimental grain size measurements would be statistically beneficial for the model. Solving equation 6.10 so that f_s is 0.17, the gas atom diffusivity, D_g, can be estimated to fit experimental results. D_o was found to be 1.5×10^{-42} m^5.

Knowing D_g and that f_s should be 0.17, the gas concentration, c_g, is found using equation 6.11. Note that the bubble resolution rate, b, and bubble nucleation factor, f_n, will have to be optimized to fit the model results to the experimental results. As it will be seen in the sensitivity analysis, the bubble nucleation factor, f_n, has no effect on the bubble diameter and only affects the bubble concentration. This c_g value can be implemented into equation 6.7 to find the total gas atoms present in the bubble. Once the gas atoms present in a bubble are known, the concentration of bubbles can be found using equation 6.6. Additionally, equation 6.9 can now be solved to determine the average bubble radius.

As it will be seen in the sensitivity analysis later, the bubble nucleation factor has little effect on the average bubble radius and the bubble resolution parameter can be optimized to fit the model results to experimental results. Once the gas atom diffusivity parameter and the gas resolution parameter are optimized to fit the experimental bubble diameters, the model bubble nucleation

factor can be optimized to fit the model bubble concentration to the experimental bubble concentrations.

Table 6.1 shows the flow chart on how the model was used to find the intragranular bubble diameters and the bubble concentration.

6.2: Model Results

The model created by Rest (3) was used to find key intragranular bubble parameters such as: the fission gas atom diffusion coefficient, the bubble nucleation factor, and the bubble resolution rate. Experimental results from Van de Berghe (1), RERTR-6, and -7 L.Flux were implemented in the model to find the key parameters. Additionally, a sensitivity analysis of the key parameters is provided as a function of bubble diameters and bubble concentrations. This sensitivity analysis shown later was completed on the fit model parameters. During the fitting of the model and the experimental results, the sensitivity of key bubble parameters was monitored to know which ones affect the model results significantly. Note that the irradiation and bubble parameters of Van de Berghe are not exactly known and are ballpark estimates. These parameters include the fuel grain size, bubble size, bubble spacing, and fission rate and densities.

As a reminder, to find the bubble resolution rate and the gas atom diffusion coefficient, the bubble resolution parameter and gas atom diffusion parameter each needs to be multiplied by the fission rate as seen in equations 6.1 and 6.2. The model results and sensitivity analysis will focus

on the bubble resolution parameter, b_o, and the gas atom diffusion parameter, $d_{o,}$ as the fission rates reported by Van den Berghe, RERTR-6, and -7 L.Flux differ in value. The b_o and D_o terms are assumed to be constant between the three experiments.

Table 6.1: Flow chart to determine the intragranular bubble diameter and concentration using the model developed by

Step	Equation	Solve For
1	6.10	D_g
2	6.11	c_g
3	6.7	m_b
4	6.6	c_b
5	6.9	r_b

Table 6.2 shows a list of the parameters used in the model, including the key parameter's values that were fit to experimental results. The bubble nucleation factor, f_n, was determined to $5.9x10^{-3}$. The gas atom diffusion parameter, D_o, was found to be $1.5x10^{-42}$ m^5. The gas resolution parameter, b_o, was found to be $7x10^{-20}$ m^3. Remember, to find the gas atom diffusion coefficient and the bubble resolution rate, the gas atom diffusion parameter and gas resolution parameter needs to be multiplied by the fission rate for the specific experiment.

Figure 6.1 shows the fit of model to experimental data. This includes the work done by Van de Berghe (1), RERTR-6, and RERTR-7 L.Flux. Note that in Figure 6.1, the bubble nucleation factor, the gas-atom diffusion parameter, and bubble resolution parameter were optimized to best fit the three experiments. The optimized values are those presented in Table 2.1. Figure 6.2, Figure 6.3, Figure 6.4, and Figure 6.5 show the sensitivity analysis on the key model parameters; the bubble nucleation factor, the gas atom diffusion coefficient parameter, and the bubble resolution parameter. With the fit for the model being in agreement with both RERTR-6 and -7 L.Flux, as seen in Figure 6.1, the sensitivity results will be conducted on only RERTR-6's irradiation parameters.

Figure 6.2 shows the sensitivity of the model on the effect of the fuel grain size on the bubble diameter. This sensitivity was included due to the fact that not enough fuel grains were measured for good statistical confidence. Figure 6.2 shows that the size of the grain size has significant influence on the bubble diameter, especially when the grain size is smaller than 3 μm.

This is due to smaller grain sizes leading to an increase of grain boundaries for the fission gas to diffuse to. Larger grain sizes will lead to a decrease in grain boundaries and thus more fission gas residing in the bulk of the grains.

Figure 6.3 shows the sensitivity of the model on the effect of the gas resolution parameter on the a) bubble diameter and the b) bubble concentration. As seen in the sensitivity analysis of the bubble diameter, a 10% difference in the resolution rate parameter can change the bubble diameter as much as 0.5 nm, a significant amount. The dependence of the bubble resolution parameter on the bubble concentration is less noticeable, but still affects the value significantly, though not as significant as the bubble nucleation factor. This sensitivity analysis of the bubble resolution rate shows the importance of having more data points in the fit to better help find the correct bubble resolution parameter.

Figure 6.4 shows the sensitivity of the model on the effect of the gas atom diffusion coefficient on the a) bubble diameter and the b) bubble concentration. The sensitivity analysis of the diffusion coefficient shows that both the bubble diameters and concentrations can change rapidly with small differences in value. Knowing that the amount of gas along the grain boundaries and the grain size affect the gas-atom diffusion coefficient, it is key to know from experimental results what the grain size is and to verify that the bubble yield calculation is correct.

Figure 6.5 shows the sensitivity of the model on the effect of the bubble nucleation factor on the a) the bubble concentration and the b) bubble diameter. As seen in the sensitivity analysis of the

bubble nucleation factor on the bubble diameter, large changes in the bubble nucleation factor do not affect the diameter. This shows that the gas-atom diffusion coefficient and the bubble resolution rate are the key parameters for determining the bubble diameter. The bubble concentration is strongly affected by the bubble nucleation factor and this term was modified to make the model bubble concentration match the experimental bubble concentration.

6.3: Model Discussion

This section is focused on discussion of the model results compared to literature value.

The sensitivity analysis of the bubble nucleation factor, f_n, shown in Figure 6.5, shows that f_n strongly affects the bubble concentrations and affects the bubble radius minimally over a couple orders of magnitude in value. As a reminder, the optimized bubble nucleation factor was $5.9x10^{-3}$. Veshchunov (93) reported that the bubble nucleation factor for UO_2 ranges from 10^{-5}-10^{-4}, which is roughly the vacancy bulk concentration. Additionally, work by Spino and Rest (94) on UO_2 reported that the bubble nucleation factor is $5x10^{-3}$, very close to the optimized model value of $5.9x10^{-3}$. This shows that the value determined by the model as fit to the new data of this work is in good agreement with the literature results.

The bubble resolution rate is found by taking the optimized bubble resolution parameter, b_o, and multiplying this value by the fission rate of the fuel. Note that the fission rates in fuel vary throughout the irradiation cycle due to burnup, and the rate also varies with location in the fuel.

An example of the latter is if the fuel plate is aligned radially in the reactor, such as the RERTR plates, the side close to the reactor will see a higher fission rate when compared to the side of the plate further from the reactor. Literature shows that the bubble resolution rate for UO_2 can vary from 10^{-2} to 10^{-5} sec^{-1} (93), (94). Olander reported that the resolution rate lies between 1.1 - 4.1 x 10^{-19} m^3 times the fission density (13). This range is due to the displacement energy used for the ejection energy of a gas atom from a bubble. The model bubble resolution rate value for the U-7wt%Mo fuel for RERTR- 6 is ~20.9 sec^{-1}, $7x10^{-20}$ m^3 times $3.8x10^{20}$ $fiss/m^3sec$. The bubble resolution rate is highly dependent on fission rate and research reactor fuels should show a higher bubble resolution rate due to the higher fission rates when compared to the UO_2 fuel values reported by Turnbull. Using the RERTR-6 fission rate as input to Olander's equation, the bubble resolution rate lies between 41 and 155 sec^{-1}. The models value is in agreement with Olander's analysis.

Turnbull performed an analysis to determine the diffusion coefficients of Xe and Kr at varying temperatures in UO_2 and showed that the diffusion coefficients for Xe and Kr at 200˚C were around $2x10^{-20}$ and $7x10^{-21}$ m^2 sec^{-1}, respectively. Note that the model is assumed to be athermal below 500K. The calculated value from the model using RERTR-6's fission rate is $5.7x10^{-22}$ m^2sec^{-1}. This is an order of magnitude lower than what Turnbull proposed for UO_2. A proposed reason for the difference could be the differences in structures for UO_2 and U-Mo fuel. UO_2 has a cubic fluorite structure (95) while U-7wt%Mo is a BCC structure. One structure might have increased diffusion properties compared to the other. As an example a BCC material tends to

have a higher diffusion coefficient than an FCC structure (96). Further investigation is needed to verify this theory.

Additional work is needed to better verify key bubble parameters. This includes additional measurements of the intragranular bubble distributions at various burnups. In addition to more bubble size distribution data points, grain size measurements at various burnups are needed.

Table 6.1: Flow chart to determine the intragranular bubble diameter and concentration using the model developed by (3)

Step	Equation	Solve For
1	6.10	D_g
2	6.11	c_g
3	6.7	m_b
4	6.6	c_b
5	6.9	r_b

Table 6.2: Literature and fitted key parameters from Rest's model (3)

Common Parameters	**Value**	**Reference**
# of Gas Atoms/Fission, β	0.25	Olander (13)
Gas Atom Radius, r_g	0.216 nm	Olander (13)
Van der Walls Constant, b_v	8.5×10^{-23} m^3/atom	Olander (13)
Fitting Parameter, h_s	0.6	Spine/Rest (94)

Irradiation Parameters	**Value**	**Reference**
Van de Berghe fission rate	4.08×10^{14} fiss/cm^3-sec	(1) (3)
Van de Berghe fission density	1.4×10^{21} fiss/cm^3	(1) (3)
Van de Berghe grain size	3.0 µm	(1) (3)
Van de Berghe Bubble Diameter	2.0 nm	(1)
RERTR-6 fission rate	3.80×10^{14} fiss/cm^3-sec	This work
RERTR-6 fission density	4.5×10^{21} fiss/cm^3	This work
RERTR-6 grain size	3.0 µm	This work
RERTR-6 Bubble Diameter	3.1 nm	This work
RERTR-7 fission rate	4.30×10^{14} fiss/cm^3-sec	This work
RERTR-7 fission density	3.30×10^{21} fiss/cm^3	This work
RERTR-7 grain size	3.0 µm	This work
RERTR-7 Bubble Diameter	3.51 nm	This work

Fitted Parameters	**Value**	**Reference**
Bubble Resolution Parameter, b_o	7×10^{-20} m^3	This Work
Gas-Atom Diffusion Parameter, D_o	1.5×10^{-42} m^5	This Work
Bubble Nucleation Factor, f_n	5.9×10^{-3}	This Work

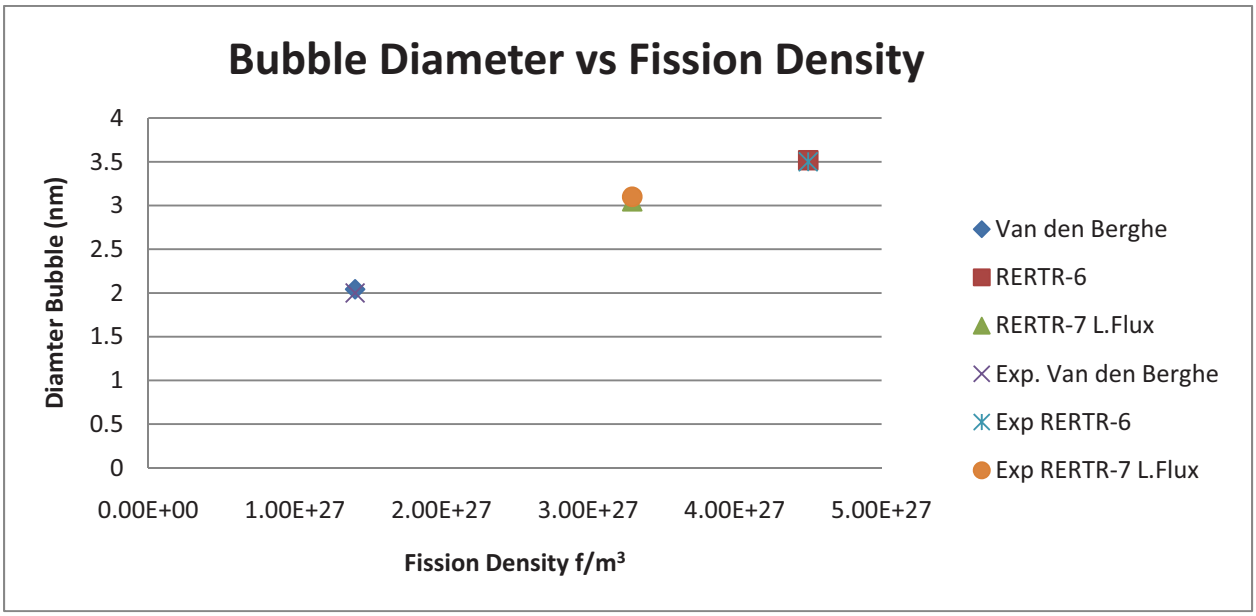

Figure 6.1: The model fit to experimental results

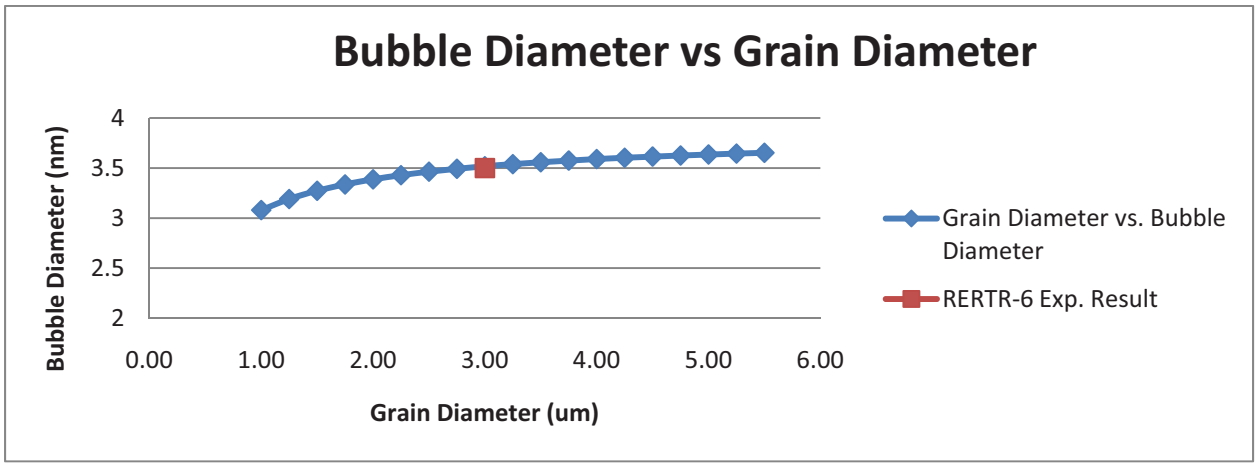

Figure 6.2: The effect of the grain diameter on the bubble diameter

a)

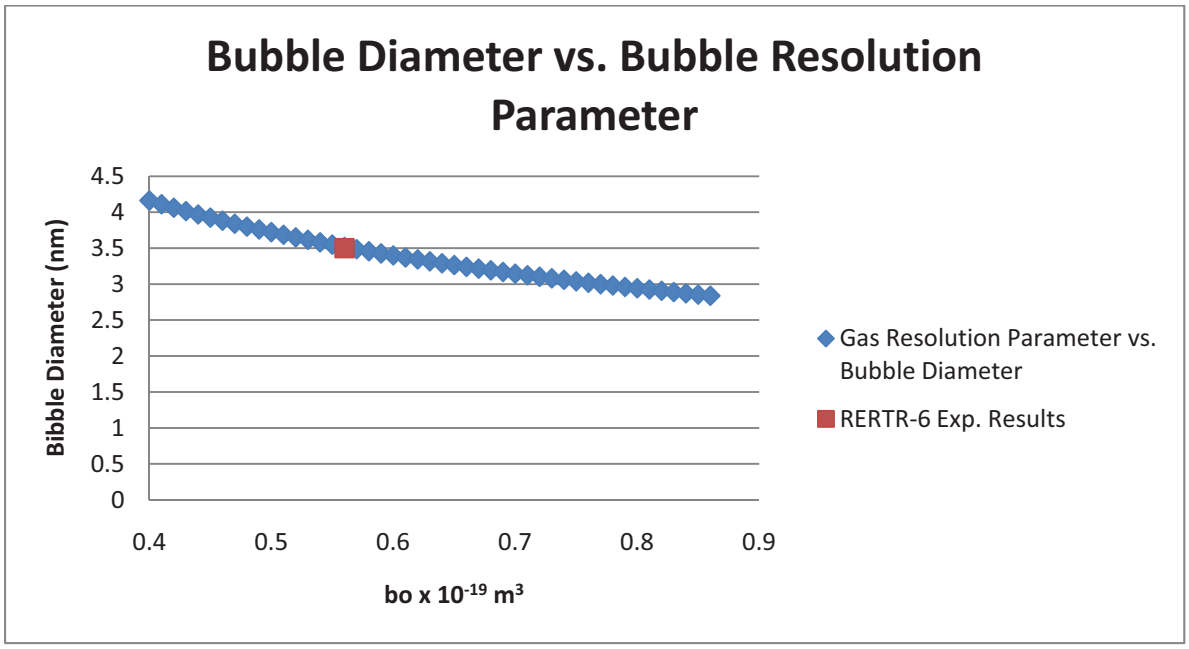

b)

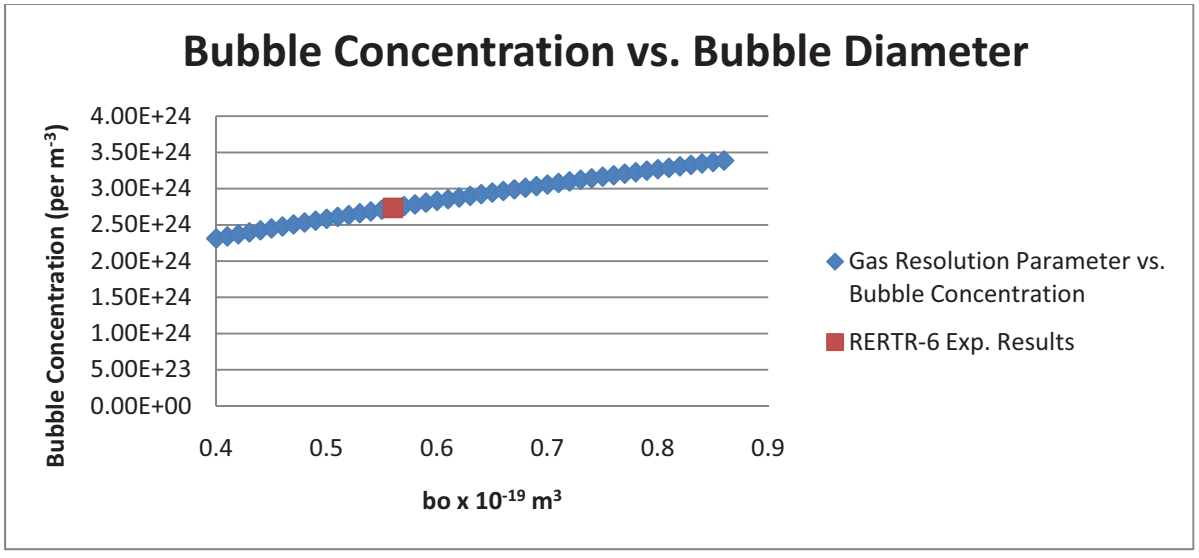

Figure 6.3: The gas resolution parameters vs. a) the bubble diameter and b) the bubble concentration

a)

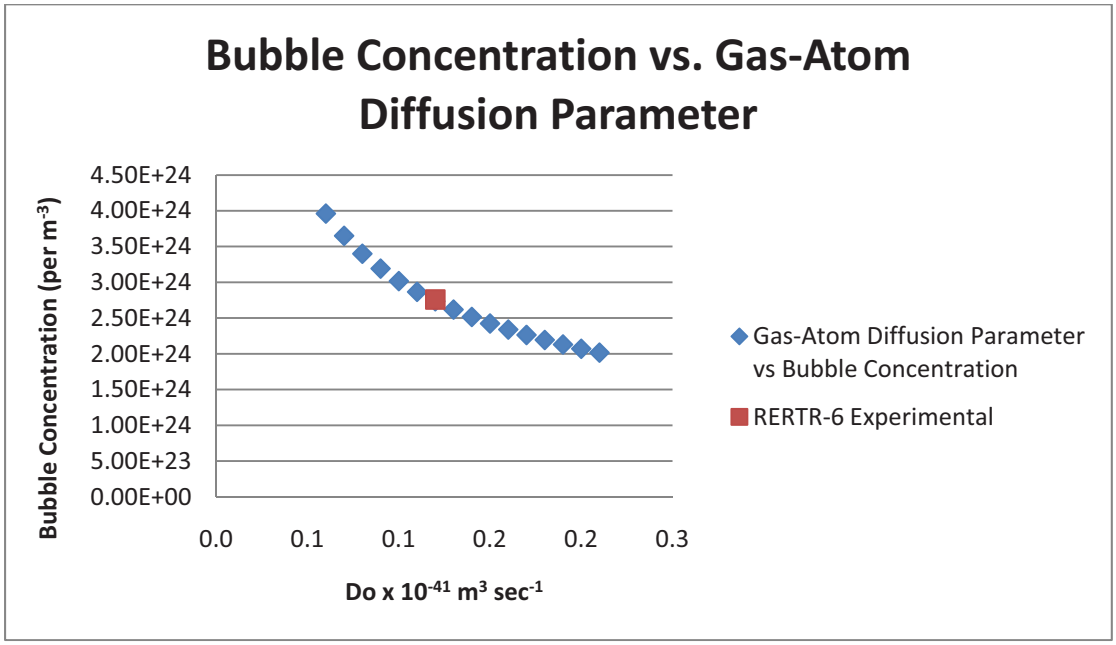

b)

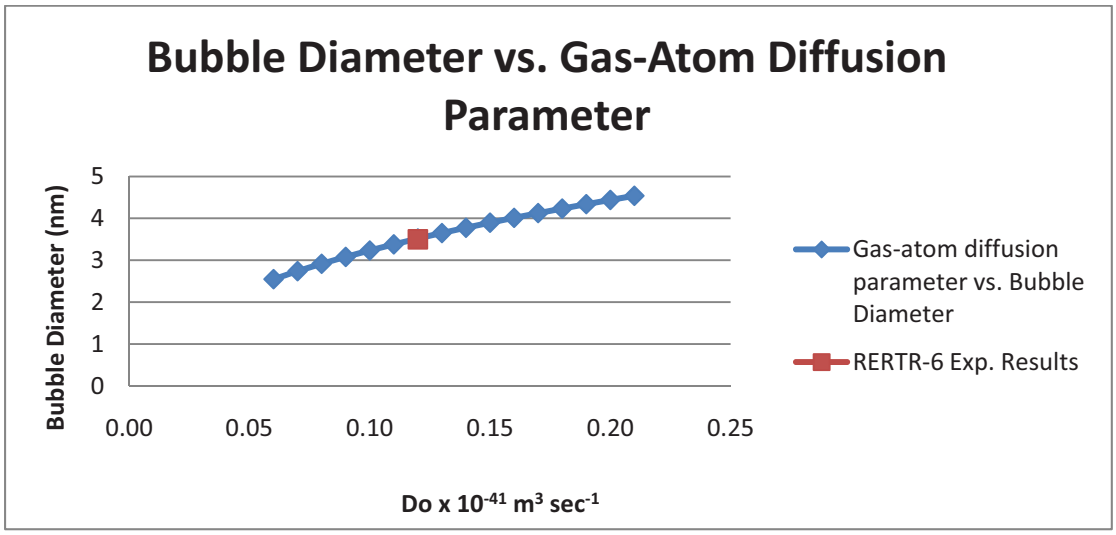

Figure 6.4: The gas atom diffusion parameters vs. a) the bubble diameter and b) the bubble concentration

a)

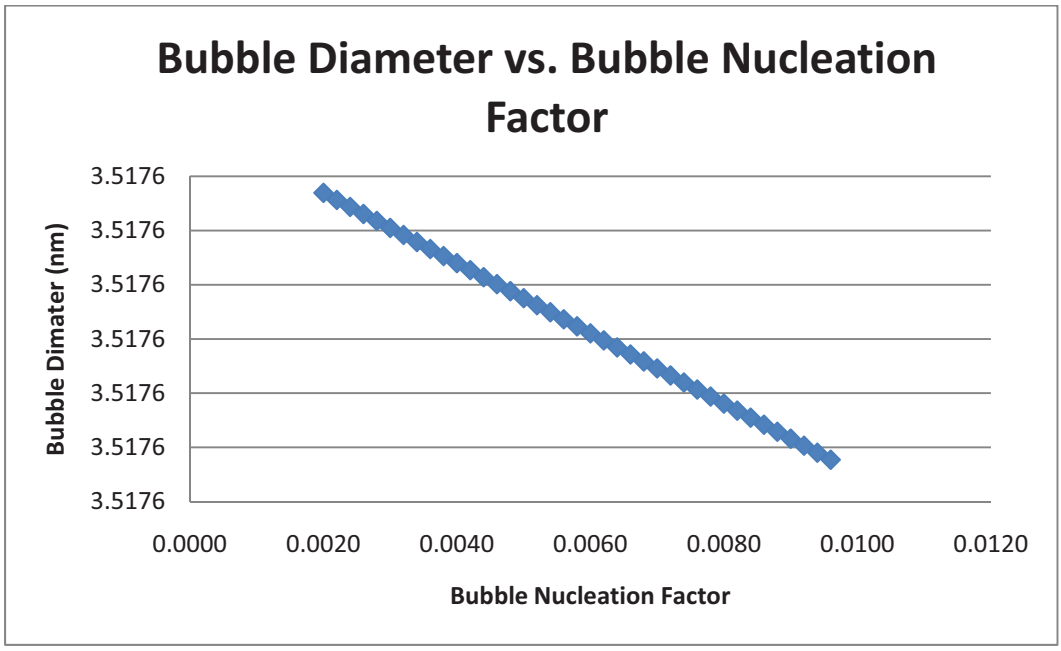

b)

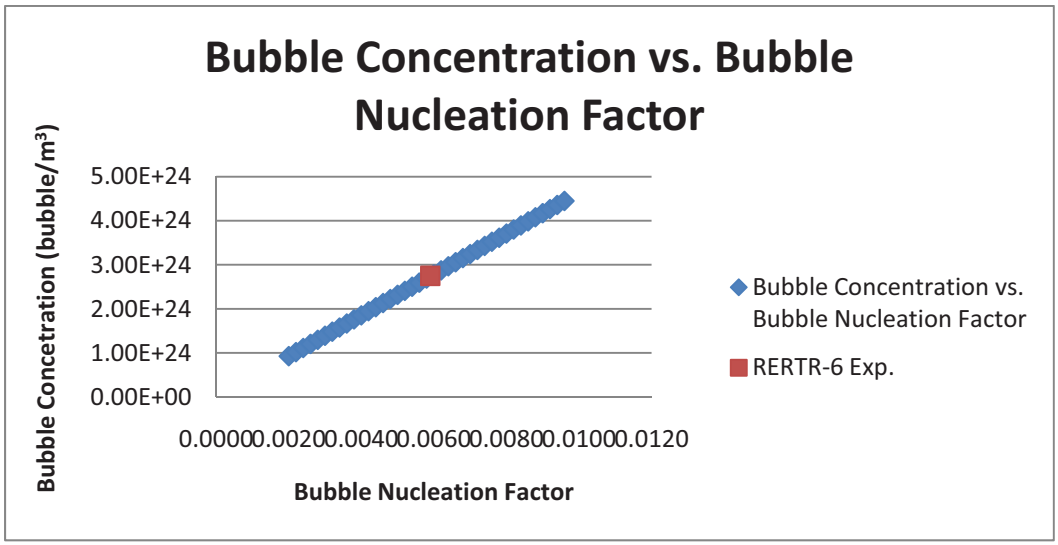

Figure 6.5: The bubble nucleation factor as a function of a) the bubble diameter and b) the bubble concentration

Chapter 7 : Conclusions and Future Work

The objective of this study was to understand the microstructure of U-7wt%Mo/Al-2wt%Si dispersion fuel after fabrication and during irradiation. This included understanding what the effect of the Si modified matrix has on the fuel particles, particular the FMI layer and amorphous rim. Key physical parameters of the ordered bubble superlattice were found at different burnups. An intragranular bubble model created by Rest (3)was used to help determine important key parameters, such as diffusion coefficients, the bubble nucleation factor, and bubble resolution rates. The following are conclusions drawn from this study.

1: The general microstructure of the U-7wt%Mo/Al-2wt%Si dispersion fuel consists of four regions: the Al-2wt%Si matrix, the FMI layer region, the amorphous rim region, and the crystalline fuel region. The amorphous rim region was a new region found by this study.
2: The Si-modified FMI layer was shown to be amorphous and does not show large interlinked bubbles like U-7wt%Mo/Al dispersion fuel. Si-Si covalent bonds help the system undergo amorphization. A Si concentration of 10 at% minimizes bubble growth in the FMI layer. Si was shown to suppress the formation of $U_6Mo_4Al_{43}$, a phase that was shown to form large fission gas bubbles in heavy Kr ion irradiations of the DU-alloys.
3: The amorphous rim region was shown to be amorphous, made up primarily of U, Mo, and Si in a $(U,Mo)_3Si$ chemical composition. A Si concentration of 2-3 at% or higher is required to drive the crystalline U-7wt%Mo fuel region amorphous. The amorphous rim region was shown to continue to grow with the thickness of the layer growing from 4 μm to 8 μm from RERTR-7

L.Flux to RERTR-7 H.Flux. The amorphous rim region was shown to have large undesired fission gas bubbles at a burnup well beyond end of life operation.

4: A bubble superlattice formed in the crystalline fuel region. A comparison of the bubble size and lattice parameter to typical void and bubble superlattices show that the system is indeed a bubble superlattice. The bubble superlattice was shown to be FCC in an orientation. Dislocation loop punching is believed to be the driving force for arranging the bubbles in the superlattice structure.

5: With the original intragranular bubble model not incorporating the ordered structure of the bubbles in RERTR-6 and -7 L.Flux, a component was added to the model to incorporate the superlattice. Using experimental results from RERTR-6, RERTR-7 L.Flux, and results from Van de Berghe [1], important bubble parameters, such as the bubble nucleation factor, the fission gas atom diffusion coefficient, and the bubble resolution rate were found the U-7wt%Mo fuel. These values are b_o=7 x 10^{-20} m^5, D_o= 1.5 x 10^{-42} m^5, and f_n=5.9x10^{-3}.

Future Work:

Recommended future work to better characterize the U-7wt%Mo/Al-2wt%Si dispersion fuel are listed below.

Experimental work:

1: Investigate low dose bubble superlattices to better understand the bubble superlattice. In particular, find the fluence where the bubbles are randomly distributed and verify if the

dislocation loop punching process is driving the bubbles into the ordered superlattice. This could include heavy ion implantations or low burnup neutron irradiated fuel.

2: Use a high resolution TEM to better understand the local Si concentration in the FMI layer and around fission gas bubbles. This can include X-ray mapping of the FMI layer.

3: Understand how the fission density affects the fuel grain size.

4: Obtain more bubble superlattice physical parameters at various fission densities to help determine where the bubble superlattice collapses.

Model work:

1: Understand how the fluence affects the grain size of the fuel and also obtain a better distribution of the grain sizes in the crystalline fuel region.

2: Obtain additional data points to better fit key bubble parameters such as the resolution rate, the fission gas diffusion coefficient, and the bubble nucleation factor.

Chapter 8 Bibliography

1. *Transmission Electron Microscopy Investigation of Irradiated U-7wt%Mo Dispersion Fuel.* **Berghe, S. Van den.** 2007, RERTR-2007 International Meeting.
2. *A Classification of Uniquely Different Types of Nuclear Fission Gas Behavior.* **Hofman, G. L.** 2005, Nuclear Engineering and Technology, Vol. 37 No. 4, pp. 299-308.
3. *Analysis of Intergranular Fission-Gas Bubble-Size Distribution in Irradiated Uranium-Molybdenum Alloy Fuel.* **Rest, J.** 2009, Journal of Nuclear Materials, Vol. 385, pp. 563-571.
4. **Was, G.A.** *Fundamentals of Radiation Materials Science.* Berlin : Spinger-Verlang, 2007.
5. *Threshold Energy Surface and Frenkel Pail Resistivity for Cu.* **King, W.E.** 1983, Journal of Nuclear Materials, Vol. 117, pp. 12-25.
6. *Understanding Resistance to Amorphization by Radiation Damage.* **Trachenko, K.** 2004, J. Phys.:Condens. Matter. Vol. 16, pp. 1491-1515.
7. **Duderstadt, J. J.** *Nuclear Reactor Analysis.* New Yotk : Wiley, 1976.
8. *Radiation Damage from Different Particle Types.* **Was, G.** 2007, NATO Science Series II: Mathmatics, Physics and Chemistry, Vol. 235, pp. 65-98.
9. *Radiation-induced segregation in multicomponent alloys: effect of particle type.* **Was, G. A.** Material Characterization Vol. 32, pp. 239-255.
10. *The Growth of Grain-Boundary Voids Under Stress.* **Hull, D.** 1959, Phil Mag, Vol. 4, Issue 42, pp. 673-687.
11. *Radiation-Induced Material Changes and Susecptibility to Intergranular Failure of Light Water-Reactor Core Internals.* **Bruemmer, S.M.** 1999, Journal of Nuclear Materials, Vol 274, pp. 299-314.
12. *Elevated Temperature Feretic and Martenstitic steels and their application to future nuclear reactors.* **Klueh, R. L.** 2004, Oak Ridge National Laboratory.
13. **Olander, D.** *Fundamental Aspects of Nuclear Reactor Fuel Elements.* Springfield, Virgina : TID-26711-P1, 1976.
14. *The Distribution of Intragranular Fission Gas Bubbles in UO2 During Irradiation.* **Turnbull, J.A.** 1971, Journal of Nuclear Materials, Vol 38, pp. 203-212.
15. *The Distribution of Intragranular Fission Gas Bubble in UO2 During Irradiation.* **Turnbull, J.A.** 1971, Journal of Nuclear Materials, Vol. 38, pp. 203-212.
16. *The Migration of Intragranular Fission Gas Bubbles in Irradiated Uranium Dioxide.* **C.Baker.** 1977, Journal of Nuclear Materials, Vol 71, pp. 117-123.
17. *Formation and Growth of Intragranular Fission Gas Bubbles in UO2 Fuels with Burnup of 6-83 GWd/t.* **Kashibe, S.** 1993, Journal of Nuclear Materials, Vol 206, pp. 22-34.
18. *Amorphization of U3Si by Ion or Neutron Irradiation.* **R.C.Birtcher.** 1997, Journal of Nuclear Materials, Vol. 244, pp. 251-257.
19. *Post-Irradiation Analysis of Low Enriched U-Mo/Al Dispersions Fuel Miniplate Tests, RERTR-4 and -5.* **Hofman, G.L.** 2004, RERTR 2004 International Meeting.
20. *Amorphization of U3Si2 by Ion or Neutron Irradiation.* **Birtcher, R.C.** 1996, Journal of Nuclear Materials, Vol 230, pp. 158-163.
21. *The RERTR Currenct Scpoe of Work for Reactor Conversions.* **Landers, C.** 2005, RERTR 2005 International Meeting.
22. *RERTR Fuel Development and Qualification Plan.* **D.M.Wachs.** 2007, INL/EXT-05-01017.

23. *TEM characterization of irradiated U3Si2/Al dispersion fuel.* **Gan, J.** 2010, RERTR-2010 International Meeting.
24. *Characterization of U-Mo Fussion Gas Bubbles on Grain Boundaries.* **J.Rest.** 2008, The 2008 International Meeting on the Research Reactor Fuel Management.
25. *PIE Results of the KOMO-3 Irradiation Test.* **Park, J.M.** 2008, The 2008 International Meeting on the Research Reactor Fuel Managment.
26. *Comparision of swelling and irradiation creep behavior f FCC-austenitic and BCC feretic/martenstitic alloys at high neutron exposure.* **Garner, F.** 2000, Journal of Nuclear Materials, Vol. 276, pp. 123-142.
27. *Selection and Microstructures of High Density Uranium Alloys.* **M.K.Meyer.** 1997, OSTI ID: 554785.
28. *U-Mo Fuels Handbook.* **Rest, J.** 2006, Argonne National Laboratory Internal Report.
29. *Irradiation Behavior of Uranium-Molybdenum Dispersion Fuel: Fuel Perfomrance Data from RERTR-1 and RERTR-2.* **M.K.Meyer.** 1999, RERTR 1999 International Meeting.
30. *Design of High-Density Gamma-Phase Uranium Alloys for LEU Dispersion Fuel Applications.* **Hofman, G.L.** 1998, RERTR-1998 International Meeting.
31. *Reaction Layer Between U-7wt%Mo and Al Alloys in Chemical Diffusion Couples.* **M.Mirandou.**
32. *U-Mo Foil/Cladding Interactions in Friction Stir Welded Monolithic RERTR Fuel Plates.* **Jr., D.D. Keiser.** 2006, RERTR-2006.
33. *Interdiffusion Behavior in Gamma Phase U-Mo Alloy Versus Al-6061 Alloy Couple Fabricated By Frication Stir Welding.* **Jr., D.D. Keiser.** 2007, Defect and Diffusion Forum, Vol. 266, pp. 131-148.
34. *Thermodynamic and Metallurgical Consideration to Stabilizing the Interaction Layers of U-Mo/Al Disperison Fuels.* **Y.S.Kim.** 2005, RERTR 2005 International Meeting.
35. *Charterization and Testing of Monolithic RERTR Fuel Plates.* **Jr., D.D. Keiser.** 2007, The 2007 Interntional Meeting on Research Reactor Fuel Management .
36. *Phase Stability and Diffusion Characteristics of U-Mo-X (X=Si, Al, Zr) Alloys.* **J.M.Park.** 2005, RERTR 2005 International Meeting.
37. *Phase Stability of U-Mo-Ti Alloys and Interdiffusion Behaviors of U-Mo-Ti/Al-Si.* **Park, J. M.** 2007, RERTR 2007 International Meeting.
38. *Progress of the KOMO-3 Irradiation Test For Various U-Mo Dispersion and Monolithic Fuels To Overcome the Interaction Problem in U-Mo/Al Dispersion Fuel.* **C.K.Kim.** 2005, RERTR 2005 International Meeting.
39. *Post-irradiation Analysis and Performance Modeling of Dispersion and Monolithic U-Mo Fuels.* **Y.S.Kim.** Prague, Czech Republic : s.n., 2007, RERTR-2007 International Meeting.
40. *Effect of Recrystallization in High-Burnup UO2 on Gas Reslease.* **Rest, J.** OSTI 4329433.
41. *Radiation-Induced Microstructural Chane in High Burnup UO2 Fuel Pellets.* **Nogita, K.** 1994, Nucl. Inst. Met. in Phys. Res. B, Vol. 91, pp. 301-306.
42. *Effect of Si and Zr on the Interdiffusion of U-Mo Alloy and Al.* **Park, J.M.** 2008, Journal of Nuclear Matierals, Vol. 374, pp. 422-430.
43. *Observation of the Nucleation and Evolution of Porosity in U-Mo Fuels.* **Hofman, G.L.** 2005, RERTR 2005 International Meeting.

44. *Interdiffusion Behavior in gamma-phase U-Mo Alloy Versus Al-6061 Alloy Couples Fabricated By Friction Stir Welding.* **Jr., D.D. Keiser.** 2007, Defect and Diffusion Vol. 266 , pp. 131-148.
45. *Heats of Formation of (U,Mo)Al3 and U(Al,Si)3.* **Ryu, H.J.** 2206, Journal of Nuclear Materials, pp. 52-56.
46. *An Investigation on the Irradiation Behaviour of Atomized U-Mo/Al Dispersion Rod Fuels.* **J.M.Park.** 2004, RERTR 2004 International Meeting.
47. *Progress of U-Mo Dispersion Rod Fuel Qualification Program in Korea.* **C.K.Kim.** 2002, RERTR 2002 International Meeting.
48. *Initial Assessment of Radiation Behavior of Very-High-Density Low-Enriched-Uranium Fuels.* **G.L.Hofman.** 1999, RERTR-1999 International Meeting.
49. *Characterization of the Interaction Products in U-Mo/Al Dispersion Fuel from In-pile and Out-of-Pile Tests.* **Ryu, H.J.** 2006, RERTR-2006 International Meeting.
50. *Post-Irradiation Examination of Uranium-7wt%Molybdenum Atomized Dispersion Fuel.* **Leenaers, A.** 2004, Journal of Nuclear Materials, Vol. 335, pp. 39-47.
51. *Results of Low Enriched U-Mo Dispersion Fuel Miniplates from Irradiation Test, RERTR-6.* **Hofman, G.L.** 2006, RERTR-2006 International Meeting.
52. *Identification of Phases in the Interaction Layer Between U-Mo-Zr/Al and U-Mo-Zr/Al-Si.* **Varela, C.L. Komar.** 2007, RERTR 2007 International Meeting.
53. *Modeling of High-Density U-Mo Dispersion Fuel Plate Performance.* **Hayes, S.L.** 2002, RERTR-2002 International Meeting.
54. *The UMUS Failure: Facts and Analyses.* **Huet, F.** 2003, The 2003 International Meeting on the Research Reactor Fuel Management.
55. *Analysis of Factors Influencing Formation of Pores and Pillows in UMo Fuel.* **Savchenko, A.M.**
56. *Heavy Ion Irradiation of U-Mo/Al Dispersion Fuel.* **Wieschalla, N.** 2006, Journal of Nuclear Materials , pp. 191-197.
57. *Uranium-molybdenum Nuclear Fuel Plates Behavior Under Heavy Ion Irradiation: An X-ray Diffraction Analysis.* **Palancher, H.** 2009, Jouranl of Nuclear Materials, Vol 385, pp. 449-455.
58. *Heavy Ion Irradiation as a Method to Discriminate Reseach Reactor Fuels.* **Palancher, H.** 2006, The 2006 International Meeting on the Research Reactor Fuel Mananagement.
59. **Jungworth.**
60. *Microstructural Analysis of Irradiated Atomized U(Mo) Dispersion Fuel in an Al Matrix with Si Addition.* **Leenaers, A.** 2008, The 2008 International Meeting on the Research Reactor Fuel Management.
61. **Ziegler, J.F.** Particle Interactions with Matter. *SRIM.* [Online] 2010. [Cited: Nov. 21, 2010.] srim.org.
62. **Stadelmann, P.** JEMS. *JEMS.*
63. *RERTR-7 Post-Irradiation Examination (PIE) Letter Report.* **Robinson, A.B.** 2007, INL/EXT-07013271.
64. *Characterization of the Microstructure of Irradiated U-Mo Dispersion Fuel with a Matrix that Contain Si.* **Jr., D.D.Keiser.** 2009, The 2009 International Meeting on the Research Reactor Fuel Management.

65. *A Temperature Threshold for Gas-Bubble Superlattice Formation in Molydbenum.* **Lawson, F.E.** 1998, Journal of Nuclear Materials, Vol. 252, pp. 34-42.
66. *Determination of Fission Gas Yields from Isotope Ratios.* **Mogensen, M.** 1983, International J. of Mass Spec. and Ion Physics, Vol. 481, pp. 389-392.
67. —. **Mogensen, M.** 1983, International Journal of Mass Spectrometry and Ion Physics, Vol. 48, pp. 389-392.
68. *Number of gas atoms per bubble.* **Cost, J.R.** s.l. : Journal of Nuclear Materials, Vol. 67.
69. *Interdiffusion in Diffusion Couples: U-Mo vs. Al and Al-Si.* **Perez, E.** 2009, INL/CON-09-17105.
70. *The Effect of Silicon on the Interaction Between Metallic Uranium and Aluminum: A 50 Year Long Diffusion Experiment.* **Leenaers, A.** 2008, Journal of Nuclear Materials, Vol. 381, pp. 242-248.
71. *Results of Recent Microstructural Characterization of Irradiated U-Mo Dispersion Fuels with Al Alloy Matrices that Contain Si.* **Jr., D.D. Keiser.** 2008, The 2008 International Meeting on the Research Reactor Fuel Management.
72. *A Study of the Uranium-Aluminum-Silicon System.* **Dwight, A.E.** 1982, ANL-82-14.
73. *Low Temperature Characterization of Al-Si Diffusion Kinetics.* **Dugan, M. Patrick.** 1988, Superlattices and Microstructures, Vol. 4, No. 4/5, pp. 565-570.
74. *Transmission Electron Microscopy Investigation of UAlx Based MTR Fuel.* **Renterghem, W. Van.** 2010, The 2010 International Meeting on the Research Reactor Fuel Management.
75. **Mitchell, B. S.** *An Introduction to Materials Engineering and Science.* Hoboken, New Jersey : Wiley-Interscience, 2004.
76. **Winter, Mark.** WebElements. *Webelements.com.* [Online] The University of Sheffield and Webelements Ltd, UK, 1993-2010. [Cited: November 20, 2010.] www.webelements.com.
77. *A Heterobimetallic Complex with an Unsupported Uranium(III)-Aluminum(I) Bond: (CpSiMe3)3U-AlCp* . **Minasian, S.G.** 2008, J. Am. Chem. Soc., Vol. 130, pp. 10086-10087.
78. *Structural Relaxation and Self Diffusion in Covalent Amorphous Solids: Silicon Nitride as a Model System.* **Schmidt, H.** 2007, Journal of Applied Physics, Vol. 102.
79. *From High Enriched to Low Enriched Uranium Fuel in Research Reactors.* **Berghe, S. Van Den.** 2010, The 2010 International Meeting on the Reasearch Reactor Fuel Manangement.
80. *Ion Beam Mixing in Metallic and Semiconductor Materials.* **Mastasi, M.** 1994, Materials Science and Engineering, R12, pp. 1-52.
81. *Effect of Recrystallization in High-Burnup UO2 on Gas Release during RIA-Type Transients.* **Rest, J.** 1994, ANL/ET/PP--84776.
82. *The Effect of Mo Crystallinity on Diffusion Through the Si-on-Mo Interface in EUV Multilayer Systems.* **Bruijn, S.** 2009, Defect and Diffusion Forum Vols. 283-286, pp. 657-661.
83. *Post-irradiation Examanination of AlFeNi Cladded U3Si2 Fuel Plates.* **Leenaers, A.** 2008, Journal of Nuclear Materials, Vol. 275, pp. 243-251.
84. *Theory and Experiment of Nanostructure Self-Organization in Irradiated Materials.* **Ghoniem, N.M.** 2002, Journal of Computer-Aided Materials Design. Vol. 8, pp. 1-38.
85. *Importance of Stress in Bubble Ordering in the Helium Gas-Bubble Superlattice in Copper.* **Johnson, P.B.** 1987, Nature, Vol. 329, pp. 316-318.

86. *A Mechanism of Formation and Properties of the Void Lattice in Metals Under Irradiation.* **Dubinko, V.I.** 1989, Journal of Nuclear Materials, Vol. 161, pp. 57-71.
87. *Ordering of Voids and Gas Bubbles in Radiation Environments.* **Krishan, K.** 1982, Radiation Effects, Vol. 66, pp. 121-155.
88. *Dislocation Loop Punching in Bubble Arrays.* **W.G.Wofer.** 1989, Philosophical Magazine A, Vol. 59, pp. 87-103.
89. *The Pressure for Dislocation Loop Punching by a Single Bubble.* **Wofer, W.G.** 1988, Philosophical Magazine A, Vol. 58, pp. 285-297.
90. *Ion Bombardment Effecfts on the Near-surface Composition During Sputter Profiling.* **Lam, N.Q.** 1988, Surface and Interface Analysis, Vol. 12, pp. 65-77.
91. *Hydrogen Implantation Effects in the Subsurface Layer of Aluminum-Bubble Pressure and Surface Modifications.* **Kamada, K.** 1989, Journal of Nuclear Materials, Vol. 169, pp. 141-150.
92. *Hydrogen Bubbles in Metals.* **Condon, J.** 1993, Journal of Nuclear Materials, Vol. 207, pp. 1-24.
93. *On the Theory of Fission Gas Bubble Evolution in Irradiated Fuel.* **Veshchunov, M.S.** 2000, Journal of Nuclear Materials, Vol. 277, pp. 67-81.
94. *Matrix Swelling Rate and Cavity Volume Balance of UO2 Fuels at High Burnup.* **Spino, J.** 2005, Journal of Nuclear Materials, Vol. 346, pp. 131-144.
95. *First-Principles Calculation of Point Defects in Uranium Dioxide.* **Iwasawa, M.** 2006, Materials Transactions, Vol. 47, pp. 2651-2657.
96. **Mehrer, H.** *Diffusion in Solids.* Berlin : Springer-Verlag, 2007.
97. *Observation on the Irradiation Behavior of U-Mo Alloy Dispersion Fuel.* **G.L.Hofman.** 2000, RERTR-2000 International Meeting.
98. *Study of Decomposition and Reactions with Aluminum Matrix of Dispersed Atomized U-10 wt%Mo Alloy.* **Lee, J. S.** 2002, Journal of Nuclear Materials, Vol 306, pp. 147-152.
99. *Characterization of the Reaction Layer in U-7wt%Mo/Al Diffusion Couples.* **Mirandou, M.I.** 2003, Journal of Nuclear Materials, Vol 323, pp. 29-35.
100. *The Diffusion Coefficients of Gaseous and Volatile Species During the Irradiation of Uranium Dioxide.* **Turnbull, J.A.** 1982, Journal of Nuclear Materials, Vol. 107, pp. 168-184.
101. *Ion mixing.* **Matteson, S.** 1983, Ann. Rev. Mater. Sci, Vol. 13, pp. 339-362.
102. *Self-Organization of Cavities Under Irradiation.* **Dubinko, V.I.** 1994, Appl. Phys. A. Vol. 58, pp. 21-34.
103. *Pavel Medvedev.* **Communication, Personal.** 2010.
104. *Dynamics of irradiation-induced grain subdivision and swelling in U3Si2 and UO2 Fuels.* **Rest, J.** 1994 , Journal of Nuclear Materials, pp. 187-202.
105. **Doolittle, J.** Journal of Applied Physics, Vol. 22, p. 1471.
106. *Matrix Swelling Rate and Cavity Volume Balance of UO2 Fuels at High Burnup.* **Spino, J.** 2005, Journal of Nuclear Materials, Vol. 346, pp. 131-144.
107. *Reaction Layer in U-7wt%Mo/Al Dispersion Couples.* **Mirandou, M.I.** 2004, RERTR 2004-International Meeting.
108. *Full-Sized Plates Irradiation with High UMo Fuel Loading-Final Resuts of ISIS-1 Experiment.* **Huet, F.** 2003, RERTR 2003 International Meeting.

109. *Course of Pin Fuel Test in WWR-M Reactor Core.* **Zakharov, A.S.** 2004, RERTR 2004 International Meeting.
110. *Nitrogen Diffusion in Amorphous Silicon Nitride Isotope Mulitlayers Probed by Neutron Reflectometry.* **Schmidt, H.** 2006, Physical review Letters, Vol. 96.

Appendix 1:

For a relatively low temperature system, $<0.3T_m$, and high fission rates, the radiation enhanced diffusion coefficient, D_{red}, is described by:

$$D_{red} = (\frac{\xi a^2 v_v \Omega}{\pi r_{iv} B})^{0.5} * e^{\frac{-\varepsilon_v}{2kT}} \sqrt{\dot{f}}$$

where a is the lattice parameter of the fuel, Ω is the atomic volume, $\dot{f}$ is the fission density, r_{iv} is the radius of the recombination of point defects volume, B is a conversion factor, v_v is the vacancy migration energies, ξ is a preexponential factor that accounts for deviations from diffusion in a pure solvent, k is the Boltzmann's constant, T is the temperature in K, and ε_v is the migration energy for a vacancy-solute pair.

The table below shows the parameters used to determine the D_{red} value. These parameters were incorporated for U_3Si_2 and UO_2 fuels. The fission rate, lattice parameter, atomic volume, and temperature were RERTR-6's parameters.

Property	Value
εv	0.9 eV
riv	$2x10^{-10}$ m
ζ	0.1
vv	$5x10^{-13}$ s^{-1}
B	$6x10^{23}$ $m^{-3}sec^{-1}$
a	0.34 nm
Ω	0.0396 nm^3
T	373
f rate	$4x10^{20}$ $fiss/m^3sec$

D_{red} was determined to be $1.29x10^{-18}$ m^2sec^{-1}